AFRL-RV-PS-
TR-2016-0130
Vol. III

AFRL-RV-PS-
TR-2016-0130
Vol. III

A DESIGNER FLUID FOR ALUMINUM PHASE CHANGE DEVICES

Volume III of III
Performance Enhancement in Copper Heat Pipes

Qi Yao and Ivan Catton

University of California, Los Angeles
420 Westwood Plaza, Room 43-132
Los Angeles, CA 90095-1597

17 Nov 2016

Final Report

AIR FORCE RESEARCH LABORATORY
Space Vehicles Directorate
3550 Aberdeen Ave SE
AIR FORCE MATERIEL COMMAND
KIRTLAND AIR FORCE BASE, NM 87117-5776

DTIC COPY
NOTICE AND SIGNATURE PAGE

This report is the result of contracted fundamental research deemed exempt from public affairs security and policy review in accordance with SAF/AQR memorandum dated 10 Dec 08 and AFRL/CA policy clarification memorandum dated 16 Jan 09. This report is available to the general public, including foreign nationals. Copies may be obtained from the Defense Technical Information Center (DTIC) (http://www.dtic.mil).

AFRL-RV-PS-TR-2016-0130, Vol. III HAS BEEN REVIEWED AND IS APPROVED FOR PUBLICATION IN ACCORDANCE WITH ASSIGNED DISTRIBUTION STATEMENT.

//SIGNED//   //SIGNED//
ANDREW WILLIAMS   PAUL HAUSGEN, Ph.D.
Program Manager   Technical Advisor, Spacecraft Component Technology

//SIGNED//
JOHN BEAUCHEMIN
Chief Engineer, Spacecraft Technology Division
Space Vehicles Directorate

BSC REPORT DOCUMENTATION PAGE

1. REPORT DATE	2. REPORT TYPE	3. DATES COVERED
17-11-16	Final Report	29 Jun 2015 - 29 Sep 2016

4. TITLE AND SUBTITLE

A DESIGNER FLUID FOR ALUMINUM PHASE CHANGE DEVICES, Vol. III of III
Performance Enhancement in Copper Heat Pipes

5a. CONTRACT NUMBER
FA9453-15-1-0318

5b. GRANT NUMBER

5c. PROGRAM ELEMENT NUMBER
62601F

6. AUTHOR(S)

Ivan Catton

5d. PROJECT NUMBER
8809

5e. TASK NUMBER
PPM00020770

5f. WORK UNIT NUMBER
EF126504

7. PERFORMING ORGANIZATION NAME(S) AND ADDRESS(ES)

University of California, Los Angeles
420 Westwood Plaza, Room 43-132
Los Angeles, CA 90095-1597

8. PERFORMING ORGANIZATION REPORT NUMBER

9. SPONSORING / MONITORING AGENCY NAME(S) AND ADDRESS(ES)
Air Force Research Laboratory
Space Vehicles Directorate
3550 Aberdeen Ave SE
Kirtland AFB, NM 87117-5776

10. SPONSOR/MONITOR'S ACRONYM(S)
AFRL/RVSV

11. SPONSOR/MONITOR'S REPORT NUMBER(S)
AFRL-RV-PS-TR-2016-0130, Vol. III

12. DISTRIBUTION / AVAILABILITY STATEMENT
Approved for public release; distribution is unlimited.

13. SUPPLEMENTARY NOTES

14. ABSTRACT
The deposition mechanisms and dry-out dynamics of a designer fluid were investigated experimentally in a flat grooved heat pipe. Generated coatings were observed during heat pipe operation. The fluid deposits demonstrated enhanced liquid spreading. The coating was found to creep up onto the fin tops and increase evaporative surface area. The overall thermal resistance was lowered and the maximum heat transport was increased. A numerical heat pipe model was developed for a grooved wick. Measurements of the coating geometry on coverage were used as empirical closure to represent the designer fluid. The theoretical and experimental temperature distributions matched well. Uncertainties in the closure properties were the major source of error.

15. SUBJECT TERMS
inorganic aqueous solution <and> heat pipe, spacecraft, satellites, thermal control, two-phase heat transfer

16. SECURITY CLASSIFICATION OF:			17. LIMITATION OF ABSTRACT	18. NUMBER OF PAGES	19a. NAME OF RESPONSIBLE PERSON
a. REPORT	**b. ABSTRACT**	**c. THIS PAGE**	Unlimited	218	Andrew Williams
Unclassified	Unclassified	Unclassified			**19b. TELEPHONE NUMBER** *(include area code)*

Standard Form 298 (Rev. 8-98)
Prescribed by ANSI Std. Z39.18

(This page intentionally left blank)

Table of Contents

ii

List of Figures

v

Approved for public release: distribution is unlimited.

List of Tables

ACKNOWLEDGMENTS

DISCLAIMER

The views and conclusions contained herein are those of the authors and should not be interpreted as necessarily representing the official policies or endorsements, either expressed or implied, of Air Force Research Laboratory or the U.S. Government.

1 Summary

Heat pipes and other phase change devices have vast application to thermal management systems due to their efficient heat transfer capabilities. Current trends for improving the thermal performance of heat pipes have been focused on optimization of different wick geometries, to give the most efficient liquid transport while lowering the overall thermal resistance of the device. Advances in manufacturing have opened research to high capillarity micro- and nano-structured wicks. The choice of working fluid has been limited in the past. However, recently discovered advanced working fluids can offer several advantages. A novel working fluid for phase change heat transfer devices was investigated at University of California, Los Angeles (UCLA). The Inorganic Aqueous Solution (IAS) has shown significant thermal performance enhancement due to surface augmentation but the deposition mechanisms of the IAS surface coating haven't been fully observed or understood. The goal of this work was to observe the deposition and wetting dynamics of the fluid during operation in a heat pipe and use information from those experiments to develop a predictive thermal and hydrodynamic model of flow in a heat pipe. In this work, a background in phase change heat transfer and advanced working fluids is first presented. Three tasks, coating characterization, heat pipe experiment, and heat pipe modeling are outlined. Deposition mechanisms of a new working fluid were examined through accurate flat heat pipe experiments. Surprising observations of the deposition patterns in a grooved wick yielded valuable insight into the fundamental heat transfer concepts in which the fluid enhances heat pipe thermal performance. The role of interesting dynamics of the fluid, including the role of advective flow in a heat pipe, or the creeping nature of salt deposits, in enhancing heat transfer were identified. These observations were then utilized to develop a heat pipe model to study the effects of the

deposition on heat pipe thermal resistance and dry-out limit theoretically. Strategic application of experimental closure to the model lead to even more interesting findings. Important information regarding the dry-out dynamics of flows with and without coatings was learned that will help develop the fluids.

2 Introduction

Thermal management has become a significant obstacle in developing many technologies. From electronics to space systems, contemporary design continuously demands high powered components to be small and lightweight leading to high heat fluxes and significant challenges. Recent increases in heat dissipation accompanied by a desire to reduce system size require very effective heat transfer devices that can transport more energy per unit area. Cooling systems are necessary to prevent damage to expensive high heat flux components due to high temperature or temperature fluctuations. The goal of a thermal management design is to maintain acceptable system temperatures to avoid decreases in performance, reliability, and lifetime of the components.

Heat pipes and other phase change heat transfer devices offer many important advantages as a thermal management device and have been of interest for years. Their multitude of uses have been summarized is various texts such as Reay and Kew [1] and Faghri [2]. These devices utilize phase change to efficiently transfer energy over comparatively long distances through the transport of vapor. Because phase change occurs isothermally, these devices are able to maintain extremely low temperature differences across their length resulting in extremely high effective thermal conductivities. The enthalpy of vaporization allows large quantities of energy to move from the evaporator section to condenser section. The lightweight and high performance of heat pipes drastically reduces the footprint of these devices in the overall system. The passive nature of these devices also eliminates the need for any input power that's required for other cooling devices [2]. A schematic of heat pipe operation is displayed below in Figure 1.

3
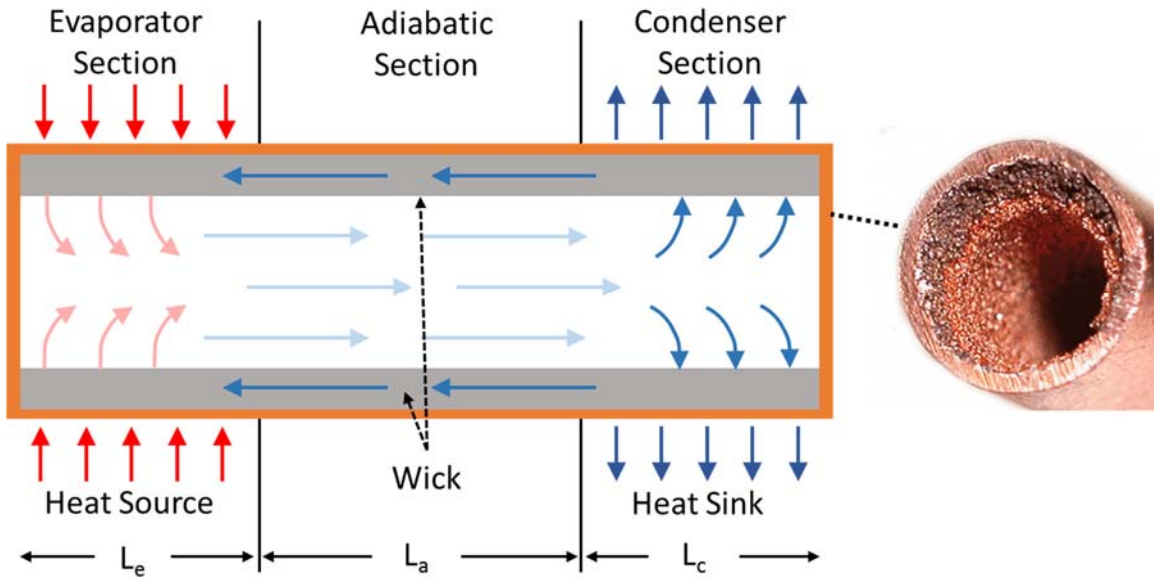
Figure 1: Schematic of heat pipe during operation

When the working fluid is evaporated and condensed in another section of the heat pipe the condensate is transferred back to the evaporating region by a capillary structure or wick. The properties of the wick such as pore size, permeability, porosity, and thermal conductivity determine the operating limits of the heat pipe.

2.1 Heat Pipe Operation

This section summarizes the basic hydrodynamic and thermal considerations in heat pipes given in common heat pipe texts like Chi [3]. A typical heat pipe is comprised of a hollow metal shell filled with a small amount of working fluid creating a device that is extremely lightweight. Phase change devices operate on a thermodynamic cycle where thermal energy is converted into kinetic energy and back to thermal energy through phase change of the working fluid. When one section of the device is heated, the working fluid evaporates. Due to a pressure difference, the vapor travels to the other end of the device, condenses, and rejects heat from the device. The liquid is returned to the evaporator section by a capillary structure attached around the inside of the metal

4

shell. The tube or shell is typically vacuumed to lower the saturation temperature of the working fluid and eliminate the interfacial resistance to evaporation created by air. Phase change devices will typically near the saturation temperature of the working fluid so that the majority of input heat is transferred as latent heat by evaporation of the working fluid. This allows heat pipes to transfer energy across a distance nearly isothermally.

2.2 Hydrodynamics

The operation of a heat pipe relies on capillary pressure differences in the wick created by the curvature of the menisci formed in the small pores. The wick allows the device to operate passively and in any orientation, even against gravity. Wickless heat pipes, or thermosiphons typically must be gravity-assisted to function (i.e. they must be heated from the bottom). Examples of common wicks are shown below.

Figure 2: Different types of wicks; Sintered copper (left), Axial grooves (center), Screen mesh (right)[4]

Phase change and increased temperature in the heated section of the heat pipe lowers the liquid pressure and increases the vapor pressure in that region of the device. The flow of liquid from the condenser to the evaporator, and vapor from the evaporator to the condenser, creates

pressure drops in the form of frictional losses and gravitational head. An illustration of the pressure variation in a heat pipe can be found in Figure 3.
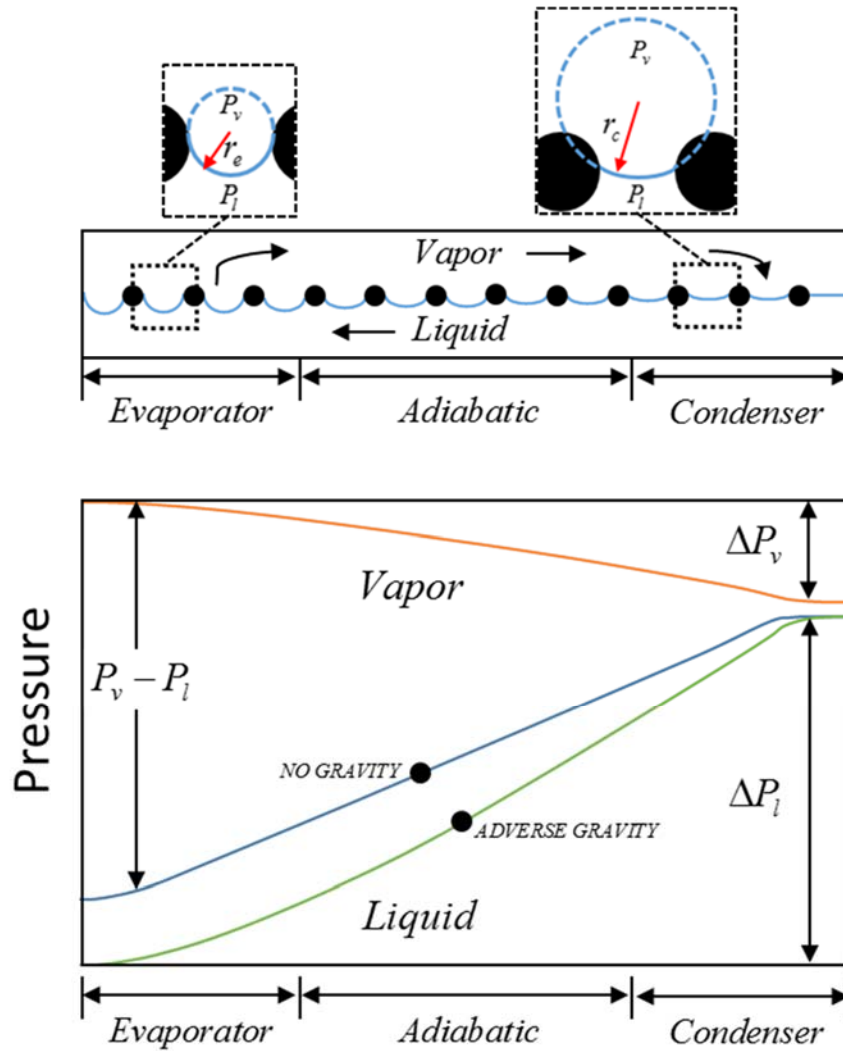
Figure 3: Pressure variation along a heat pipe

In the small pores of the wick, the pressure difference between the liquid and vapor phases, or capillary pressure, is determined by the curvature of the liquid/vapor interface. The shape of the liquid-vapor interface is dependent on the liquid's surface tension and the solid-liquid adhesion force [2]. The capillary pressure is given by the Young-Laplace equation,

$$P_c = P_v - P_l = \sigma\left(\frac{1}{r_1} + \frac{1}{r_2}\right) \qquad (1)$$

where r_1 and r_2 are the principal radii of curvature of the meniscus surface. Changes in liquid and vapor pressure along the heat pipe are compensated through axial variation of the meniscus curvature.

The capillary pressure difference between the evaporator and condenser must exceed all other pressure drops in the heat pipe for liquid to return to the evaporator as described in Equation (2),

$$\Delta P_c \geq \Delta P_v + \Delta P_l + \Delta P_g \qquad (2)$$

where ΔP_c is the difference in capillary pressure between the evaporator and condenser, ΔP_l and ΔP_v are the liquid and vapor pressure drops between the evaporator and condenser, and ΔP_g is the gravitational head of the working fluid. If this condition is not met, liquid will not reach the evaporator and the thermal resistance of the device will increase dramatically. The liquid and the vapor pressure drops increase with heat load due to the increase in flow rate and will eventually exceed the wick's maximum capillary pumping capability. This failure is referred to as "dry out."

A simple model for the maximum heat transport of a heat pipe, provided by Reay et al. [1] demonstrates the effects of different heat pipe parameters on capillary performance. As fluid evaporates in the heated section, the meniscus recedes in the wick pore which decreases the solid/liquid contact angle and the curvature at the liquid/vapor interface $\left(r = \cos\theta / r_{pore}\right)$. The condenser is flooded with condensing fluid so that the contact angle is much larger. Applying the Young-Laplace equation to the evaporator region and condenser region yields,

7

$$\Delta P_c = 2\sigma\left(\frac{1}{r_e} - \frac{1}{r_c}\right) \tag{3}$$

assuming the pores are uniform and symmetric. The vapor pressure drop is typically negligible compared to the liquid pressure drop so that any decrease in liquid pressure reduces the contact angle and curvature of the menisci. Thus, the liquid pressure in the condenser will be larger than in the evaporator inducing a flow to evaporator. Assuming a flat interface in the condenser, the maximum capillary pressure difference is,

$$\Delta P_{c,\max} = \frac{2\sigma}{r_e} = \frac{2\sigma\cos\theta_e}{r_{pore}} \tag{4}$$

The liquid pressure drop in the wick can be expressed with Darcy's law for flow in porous media, given by Equation (5). If the heat pipe is inclined with the evaporator above the condenser, the gravitational head is expressed in terms of the inclination angle, given in Equation (6).

$$\Delta P_l = \frac{\mu_l \dot{m} L_{eff}}{\rho_l K A_w} \tag{5}$$

$$\Delta P_g = \rho_l g L_{eff} \sin\phi \tag{6}$$

The effective length is used to account for the lower velocity near the ends of the heat pipe. Knowing that the heat transport is $Q_{\max} = \dot{m} h_{lv}$, the maximum heat load can be determined,

$$Q_{\max} = \left(\frac{\rho_l \sigma h_{lv}}{\mu_l}\right)\left(\frac{A_w K}{L_{eff}}\right)\left(\frac{2}{r_e} - \frac{\rho_l g L_{eff} \sin\phi}{\sigma}\right) \tag{7}$$

Though this is a very simplistic model, the effect of the fluid properties and geometry of the wick is immediately apparent. The first term is known as the figure of merit, M, which is used to quantify a working fluids performance potential for different temperatures.
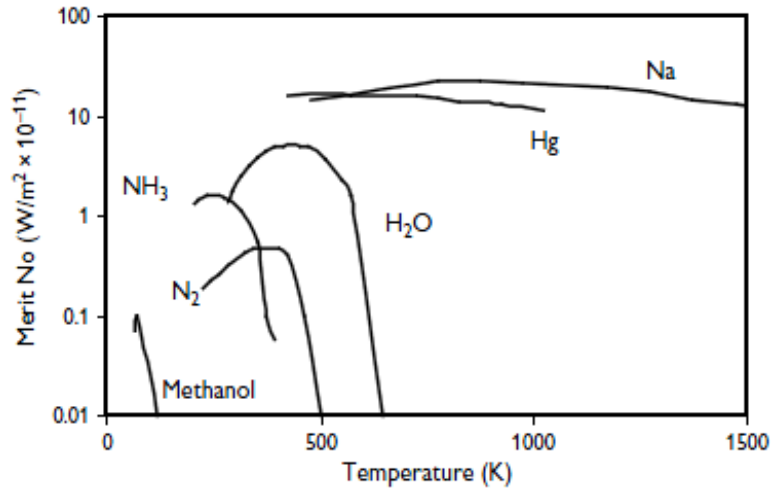
Figure 4: Figure of Merit [1]

High surface tension, latent heat, and density along with low viscosity are valuable and explains why water is so commonly used in heat pipes. However, water is limited by its freezing point for low temperature environments which is why ammonia and alcohol which also have lower latent heats are used for refrigeration and aerospace applications [3]. It is also limited for high temperature applications because the latent heat of water cannot handle the high heat fluxes where sodium can. Equation (7) also shows the competing properties of a wick. Reducing the pore size of a wick will increase the maximum capillary pumping power but will decrease the permeability.

Different types of wicks are favored for different applications as they vary in cost, permeability, capillarity, and performance. Grooves widely used in space applications where lower capillarity isn't an issue in absence of a gravitational head and the device can benefit from the high permeability, reliability and low cost of this type of wick. For electronics cooling, where the

9

cooling area is typically very small, sintered wicks are preferred due to the need for high performance and uniform liquid spreading over the evaporator [5].

The design of these devices is based on the selection of wick geometries, shell materials, and working fluid. The shell material is chosen based on its thermal and structural properties. Copper and aluminum are common due to their high thermal conductivities where titanium is used for its strength. Compatibility with the working fluid must also be considered. Water is a very common working fluid due to its high enthalpy of vaporization, specific heat and surface tension but reacts with aluminum to creates a non-condensable gas (NCG) that will cause a heat pipe to fail. Water is typically used with copper although the lightweight of aluminum makes it desirable for space applications. Other working fluids like methanol or ammonia have less appealing thermal properties but are able operate at lower temperatures than water.

2.3   Organization of the Report

This work covers a large scope of material so each major section is separated into a separate chapter with its own background. A general literature review and motivation for the research is presented in Chapter 2. Basic heat pipe operation is discussed with regard to the potential of advanced working fluids. Current methods and strategies for achieving performance enhancement in heat pipes as well as advanced working fluids are presented. Previous studies on the advanced working fluids studied in this report is discussed as a source of motivation for the following work.

Chapter 3 introduces the advanced working fluids studied in this work and provides a background into the chemistry of the fluid. This includes review of surface wetting and deposition mechanisms for specific inorganic aqueous solutions. The diffusion process of ionic constituents

in a heat pipe is analyzed. Qualitative tests of evaporating droplets are presented and the fluids used the rest of the study are summarized.

Chapter 4 is focused on the design and testing of a modular flat heat pipe used to compare the working fluids and observe deposition patterns on a grooved wick. Important aspects of instrumentation, charging the working fluid, and reliable experimental procedure are presented. Images of different concentrations and constituents captured with microscope camera are analyzed.

Chapter 5 deals with theoretical modeling of the flat grooved-wick heat pipe created in Chapter 4. The differences in current heat pipe models are summarized to explain why modeling capillary flow of advanced working fluids required a unique approach. The development of a coupled hydrodynamic and thermal model is presented. Governing equations, assumptions, solution procedure, are outlined. Experimental closure from Chapter 4 is used to represent flow in the deposits left by the working fluids. Model results are compared to experimental data and used to explain the performance enhancement mechanism seen during the experiments.

Concluding remarks and some suggestions for future work can be found in Chapter 6. An Appendix is included at the end of the document that contains additional experimental data, detail on uncertainty calculations, and the MATLAB code used to implement the model.

3 Literature Review

Some more specific heat pipe fundamentals are introduced to prepare the reader for the following chapters. Current trends and approaches to improving the performance of phase change devices are summarized to give insight into the potential for advanced working fluids. A brief history of the working fluids studied in this work is discussed and the overall goals of the report are outlined.

3.1 Heat Transfer

3.1.1 Thin Film Evaporation

The efficiency seen in phase change heat transfer devices is a result of the large heat transfer coefficients seen in thin film evaporation. The phase change at the interface does not require a large superheat like nucleate boiling [6], especially under a vacuum present in a heat pipe. However, small liquid menisci must form in the pores of heat pipe wicks where evaporation occurs. Wayner et al. [7]][[8] and other researchers such Mirzamoghadam [9] determined that the extended meniscus can be separated into three regions based on the interfacial forces and fluid flow shown in Figure 5.
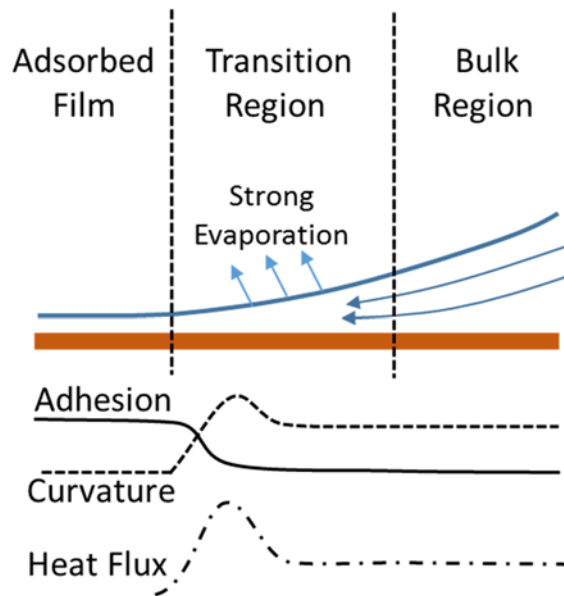
Figure 5: Schematic of a wetting meniscus

The *adsorbed film* is a non-evaporating region where liquid is adsorbed on the wall due to strong intermolecular forces between the solid wall and liquid molecules. In the *transition region* or evaporating thin film region the intermolecular forces are much lower. The liquid/vapor interface has a curvature which drives flow into the region. In the *bulk region* or intrinsic region, the intermolecular forces are negligible and the curvature of the interface becomes constant.

Large heat transfer coefficients are realized in the interline region due to a decrease in intermolecular forces and a small conductive resistance through the thin film. The transition/interline region exists over a very small length (<1μm) but heat transfer coefficients remain high as long as the film is thin. Wang et al. [10] model thin film evaporation in a microchannel with radii ranging from 2.5 μm to 210μm. They demonstrated that a thin film (<1μm in thickness) contributes over 50% of the heat transfer of the entire meniscus for the 210 μm radius channel and 97% for the 2.5 μm channel. Stephan and Busse [11] calculated the heat transfer in a

1 mm wide trapezoidal groove by solving the conduction equation in the walls and bulk liquid. The micro region was found to contribute 45% to the total heat transfer. Cheng and Dong [12] used the Galerkin method to solve conduction in a rectangular microgroove in combination with thin film evaporation. The contribution of the thin film was investigated as a function of contact angle and superheat. For a maximum film thickness of 2 μm and a 0° contact angle the thin film contributed over 90% of the heat transfer. The percentage dropped to 78% for a 60° contact angle. This film evaporation is an important design aspect for enhancing the evaporation efficiency in phase change devices

3.1.2   Thermal Resistance

A typical representation of the thermal resistances in a heat pipe is shown in Figure 6. The preferred pathway is through evaporation/condensation. The other possible pathway is axial conduction. This resistance is very large due to the thin wall and resulting cross-sectional area to length ratio. Prasher et al. [13] found that the of the vapor space is usually very low. He claimed the low vapor flow thermal resistance is responsible for isothermal transfer of energy seen in phase change devices. The temperature differences are directly related to pressure drop in the vapor through the Clasius-Clapeyron equation. Faghri [2] demonstrated the resistance of the liquid/vapor interface to be very small and that it can typically neglected for heat pipe analysis. He argues that conduction resistance through the wall and wick of the heat pipe in the evaporator and condenser section of the heat pipe is the primary cause of temperature drop along the heat pipe.

Approved for public release: distribution is unlimited.

Thermal Resistance	[K/W]
Wall	~10^{-3}
Wick	~10^{-2} - 10^{-1}
Interface	~10^{-4}
Vapor	~10^{-6}
Axial	~10^{1} - 10^{2}
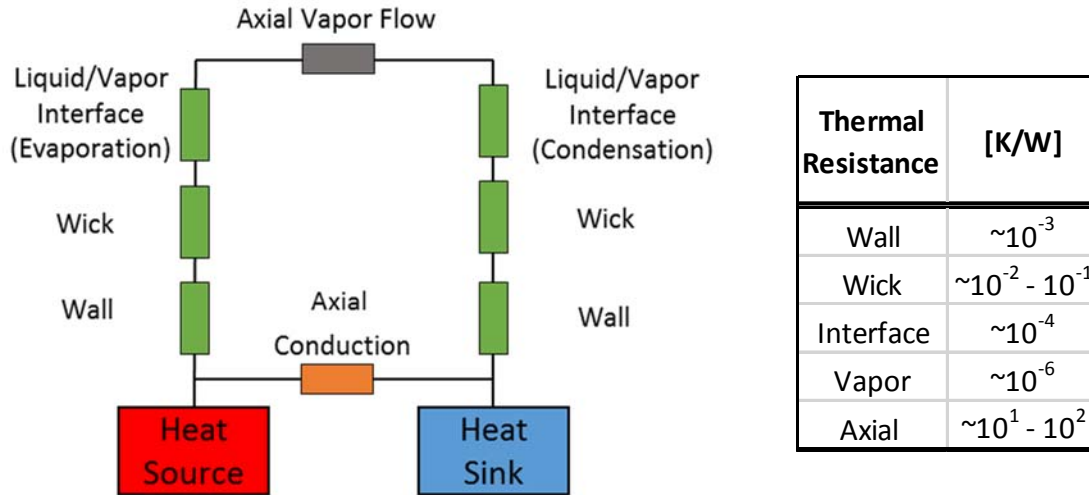
Figure 6: Thermal Resistances in a heat pipe [1]

The wall is designed to its minimum reliable thickness for manufacturing and structural integrity, leaving the wick as the focus efforts to improve thermal performance. The purpose of the wick is to drive internal flow and promote phase change through the generation of capillary pressure. The high thermal conductivity of the metal in the wick is advantageous, although the low thermal conductivity of the liquid that fills the pores drastically reduces the effective thermal conductivity. The characteristics of a wick with a low flow resistance (large flow area, porosity, thickness) are the same characteristics that increase thermal resistance

Heat transfer in a sintered wick of spherical particles and a rectangular groove is illustrated in Figure 7. For the sintered media the effective thermal conductivity can be estimated by weighting the individual materials with the porosity,

$$k_{eff} = \varepsilon k_{liquid} + (1 - \varepsilon) k_{solid} \tag{8}$$

For a porosity of 0.5, copper thermal conductivity of 390 W/m·K and water thermal conductivity of 0.6 W/m·K, the effective thermal conductivity is ~ 195 W/m·K.

15
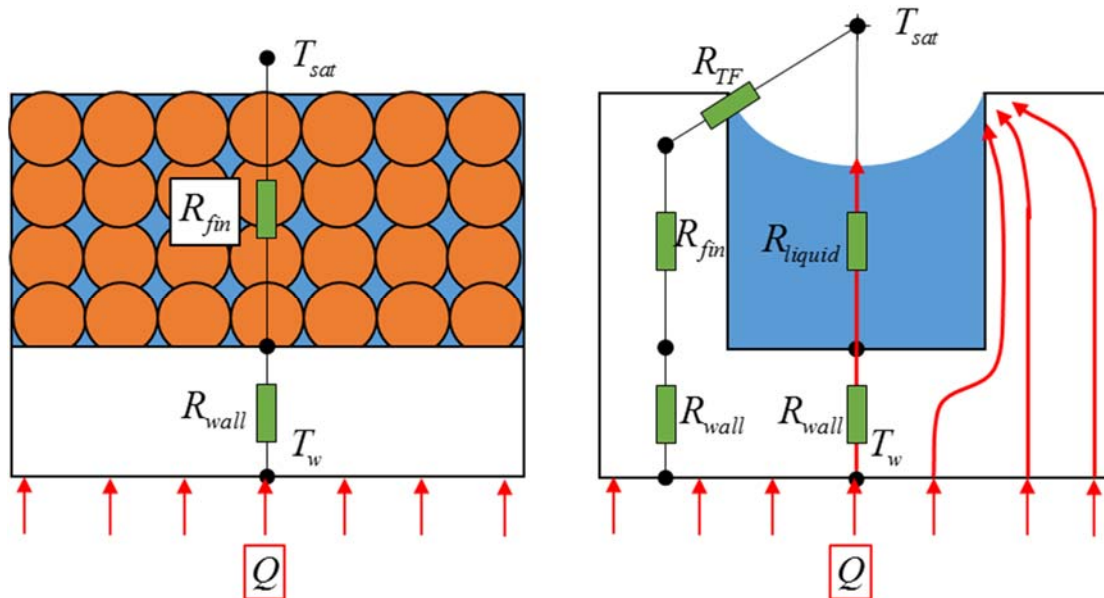
Figure 7: Thermal resistances (left) and heat flow path (right) in a rectangular grooved wick

The groove is slightly more complicated due to its non-uniform geometry though it has the same porosity (above the wall). Chi [3] argued that the discrepancy between the thermal resistance of the metal and liquid create a conjugate heat transfer problem that drastically increases the thermal resistance of the wick. The bulk liquid in the groove not only has low thermal conductivity but creates just two thin film regions near the top of the fins. Heat is forced to conduct around the liquid. Chi [3] provides an estimate for the effective thermal conductivity of a groove. For a square copper/water groove, the effective thermal conductivity is 1.91 W/m·K, which is significantly lower than the result if using Equation (8). Grooved heat pipes are utilized for permeability but suffer from lack of evaporative surface area and thin film regions.

3.2 Performance Enhancement

Various approaches have been taken to improve the performance of phase change devices. In a review, Plawsky [14] noted the ultimate goal of was to improve both the overall heat transfer

16

coefficient and liquid transport capability. Combinations of different structures, or composite wicks, were investigated as a method of increasing capillary pressures and permeability to promote liquid flow while creating geometry favorable for thin film evaporation. tested a sintered grooved composite wick and found increases in A variety of different wick structures have been combined such as groove, sintered particles, screens, and meshes [15-19]. Specific liquid transport structures or arteries have also been implemented to directly reduce the length liquid needed to travel [20-23].

Grooves with a sintered layer have been investigated several times [24, 25]. Wang and Catton [26] modeled a triangular groove with a sintered layer and found that the increase in evaporative surface area increased the overall heat transfer coefficient up to six times. As mentioned before, grooves especially benefit from the increased evaporative surface area due to lack of wetting on the top of the fin.

Others have investigated the use of wick structures with pore size distributions at two different length scales [27-29]. The small pores provide capillary pressure and area for thin film evaporation while taking advantage of the lower flow resistance in the large pores. Semenic [30] studied the dry-out behavior of sintered bi-porous wicks in a vapor chamber and found the large pores aided in vapor transport out of the wick while opening the small pores in the interior for evaporation.

Micro- and Nano-structured surfaces have also been a major area of research [14]. The implemented geometries are simple, consisting of pin fin arrays, posts, nano-wires, and nano-tubes [31-33]. The structures are designed to be on the order of the thin film region, vastly increasing

the thin film area and reducing the overall thermal resistance. Nano-structures are limited by permeability but have been successfully combined with larger structures as a composite wick [34].

Nano-structures show great potential for enhancing traditional wicking structures for heat pipes. Cost, reliability, and manufacturing capabilities are still obstacles to implementation. Cleveland [35] estimated that materials used for nano-fabrication can erode heavily in di-ionized water eliminating any long term use.

3.3 Advanced Working Fluids

Although much effort is given to optimizing wick geometry, the recent development of an advanced working fluids has led to its considerable attention. Working fluids are traditionally chosen for heat pipes based on their operating temperatures and thermophysical properties. Enhancing the fluid itself can increase performance in the desired temperature range without any modifications to the wick.

The enhancement effects of a working fluid can be two-fold. The fluid affects performance through the merit number, which is just a function of its thermophysical properties. It can also affect the heat pipe by augmenting the wick surface, creating favorable wetting or additional wicking capabilities caused by changes in surface chemistry. Surface characteristics and augmentation caused by chemical deposition can also have wicking capabilities. A lower contact angle and surface wicking will add capillarity to the heat pipe as well as improve efficiency of evaporation of the thin film.

3.3.1 Binary Fluids

Binary Fluids, a mixture of two working fluids, have been utilized to widen operating ranges and increase performance. Kiatsiriroat et al. [36] compared water to a water/ethanol mix

and showed that the Water/ethanol mix showed superior performance at lower temperatures and inferior performance at higher temperatures due to the fact that ethanol has a lower saturation temperature than water but less favorable physical properties. Savino et al. [37]experimented with dilute aqueous solutions of long chain alcohols such as n-heptanol. The authors showed that the surface tension of aqueous solutions of alcohol chains longer than four carbon atoms have a positive gradient with temperature when the temperature exceeds a certain value. This is advantageous because the typical negative surface tension gradient works against flow to the evaporator. This is known as the Marangoni effect. The heat pipe could benefit from increased surface tension and the positive Marangoni effect.

3.3.2   Nanofluids

Nanofluids are another type of heat transfer fluid that is created by suspending nanoparticles in typical working fluids. Nanoparticle materials are typically chemically stable metals such as copper, gold, silver and metal oxides. Numerous nanofluid studies have demonstrated enchantments of Critical Heat Flux (CHF) in pool boiling [38]. These fluids were originally of interest for two phase heat transfer due to their increases, though modest, in thermal conductivity and other changes in thermophysical properties. However, many studies concluded that the surface modification from the deposition of nanoparticles created a much greater enhancement through an increase in surface wetting and capillarity [39]. They concluded that significant CHF enhancement of nanofluids during pool boiling was a consequence not only of increased surface wettability, but also of improved capillarity resulting from the surface deposition of nanoparticles. The CHF of a nanofluid is enhanced by its improved ability to actively wet the heater surface, thanks to the porous structure of the thin nanoparticle layers [40].

19

Nanofluids have also been shown to increase the thermal performance in heat pipes and capillary grooves [41]. Liu et al. [42]tested the performance of CuO nanofluids in inclined grooved heat pipe and achieved a 60-80% decrease in thermal resistance and doubled the dry-out power. Solomon et al. [43] studied nanoparticle coated screen wicks to delineate the effect of changes in thermophysical properties and the surface coating. A clean screen wick and a nanofluid performed the same as a screen wick that was coated in nanoparticles and tested in a heat pipe with DI water. Both out-performed water in thermal resistance by 40%. They concluded that all the performance enhancement was due to the wick deposition and that changes in fluid properties were negligible.

Numerical investigations by Do and Jang [44] for nanofluids in a rectangular grooved heat pipe predicted over 100% improvements in overall heat transfer coefficients though they were never validated. They assumed the nanofluids produced a uniform porous coating over the evaporating section similar to the geometry modeled by Wang and Catton [26] for a groove covered by a porous coating. The performance increases were also attributed to the extended evaporating area. However, a parametric study of the coating thickness revealed that careful design is necessary. Excess thickness and low thermal conductivity of the coating material can potentially cause a reduction in performance.

3.4 History of IAS-Based Designer Fluids

The focus of this work is branch of advanced working fluids that are Inorganic Aqueous Solutions (IAS). Early investigative work by Amouzegar [45] spawned out of discrepancies with an alleged solid-state 'superconducting heat transfer medium' known as the Qu-tube. The Chinese Professor, Dr. Yuzhi Qu, and claimed in a patent [46] thermal conductivity orders of magnitude larger than currently possible. This led to various inconclusive and contradictory studies by several

universities and government institutions which were summarized by Yao [47]. Amouzegar disproved the possibility of such solid-state device. However, the fluid was tested as a phase change working fluid and showed success in various tests.

The fluid was recreated based on composition studies from the Naval Research Laboratory (NRL) that was described by Amouzegar [48] and patented by UCLA [49] as a designer working fluid for phase change heat transfer devices. The fluid has shown to lower thermal resistance in various devices and extend performance limits. Reilly et al. [50] investigated the thermal performance of IAS fluids in bi-porous sintered wicks and demonstrated significant decreases in thermal resistance and attributed the enhancement to deposits left on the wick surface shown in Figure 8.
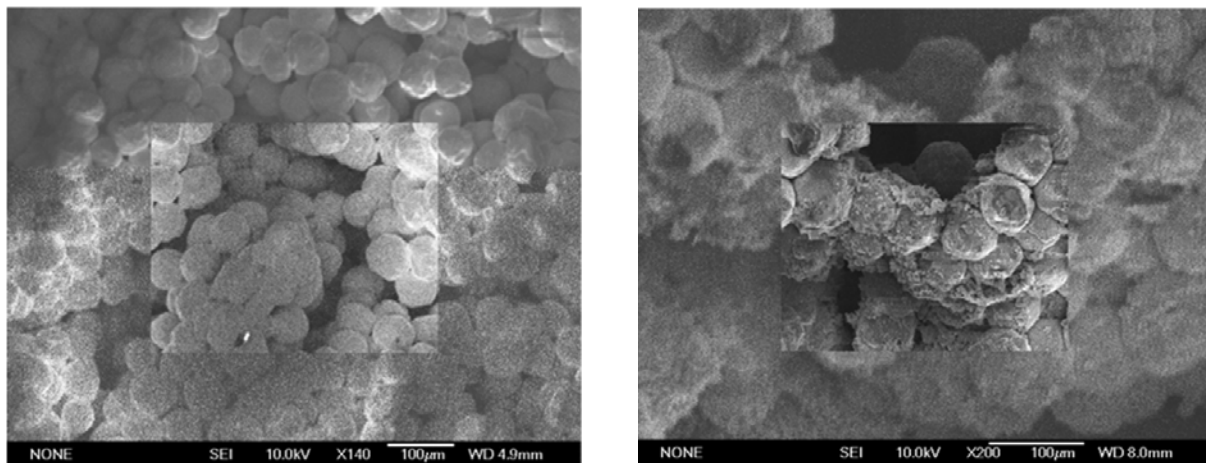
Figure 8: SEM image of a sintered copper wick before testing with IAS (left), and after testing (right). Deposits formed in the crevices of the sintered copper [50].

Karimi et al. [51] studied IAS in a thermal ground plan and saw thermal resistance decreases by about 20%. Stubblebine et al. [52] tested the fluid in aluminum devices as a means of preventing the formation of non-condensable gases and found that IAS aluminum devices could achieve similar performance to copper/water devices. The performance enhancement and reduction in

21

thermal resistance in all these studies was attributed to wetting enhancements due to surface augmentation left by the fluid.

The first goal of this work was to further explore the deposition mechanism of these fluids and observe their behavior inside an operating heat pipe. So many studies have hypothesized about superior wetting and surface augmentation, yet the deposition mechanism or flow dynamics in a wick of a heat pipe had never been observed *during* operation. Developing a heat pipe experiment to accurately measure thermal performance and view the wick in situ presented significant design and instrumentation challenges. The next chapter gives a detailed background on the chemistry of IAS and its unique characteristics to provide further motivation for this work.

4 Chemical Background and Analysis

This chapter gives an overview of the working fluids studied in this work. The bulk fluid concentrations and properties are discussed. The physical and chemical processes involved in generating a coating are analyzed. Visual characterization of the coating crystals and patterns review spreading mechanisms that could contribute to heat transfer enhancement.

4.1 Electro-chemical analysis

When the first IAS was originally developed, the complex chemical nature was addressed by Yao [47]. The original IAS discussed in his work labeled IAS #1 and will be referred to as IAS 1.1 with a separate nomenclature for this work. In reference to this report, the first number refers to the ratios of ionic constituent's concentrations, and the number after the decimal designates the overall molar concentration multiple of the original fluid. For example, IAS 2.2 has different mix ratios than IAS 1.1 but twice the concentration as IAS 2.1.

Yao [47] includes a very detailed analyses of the constituents and how to create the fluid. Each ionic constituent and compound was analyzed using Pourbaix diagrams, Gibbs free energy calculations, and equilibrium constants to determine which forms of the ions were stable and present in the solution. The summary and conclusion of Yao's work is presented in the following section as a necessary background to understanding the performance enhancement possibilities of such fluid for phase change heat transfer applications.

4.1.1 Chemical Constituents

The inorganic compound concentrations developed by Yao[47] and Amouzegar [45] are tabulated below in Table 1. The table on the left shows the compounds used to make that fluid. The table on the right shows concentrations of the ionic constituents.

Table 1: IAS 1 Chemical compounds (left) and ionic constituents (right) of the IAS #1.1 from Yao [47]

Chemical Compounds	Molecular Weight (g/mol)	Molar Concentration (mmol/L)	Mass Concentration (g/L)		Ion	Molecular Weight (g/mol)	Molar Concentration (mmol/L)	Mass Concentration (g/L)
$KMnO_4$	158.034	2.8	0.44		K^+	39.10	61.28	2.396
$K_2Cr_2O_7$	294.185	29.24	8.6		Ca^{2+}	40.08	13.24	0.531
CrO_3	99.99	19.13	1.91		Sr^{2+}	87.62	0.86	0.075
Ag_2CrO_4	331.73	0.033	0.011		Na^+	22.99	14.59	0.335
$Sr(OH)_2$	121.63	0.86	0.1		Mg^{2+}	24.31	0.58	0.014
$Ca(OH)_2$	74.093	13.24	0.98		Ag^+	107.87	0.07	0.007
$Mg(OH)_2$	58.3197	0.58	0.034		MnO_4^-	118.94	2.80	0.333
$NaOH$	39.997	14.59	0.58		CrO_4^{2-}	115.99	77.64	9.006
		Total	12.655					

The bulk inorganic solution is relatively dilute, with slightly over 12 grams of compounds added to a liter of water, with most of the weight deriving from the oxygen elements present in the permanganate, chromate, and hydroxide compounds. The molar concentration of each particular elemental ion, shown on the right of Table 1, is extremely low.

4.1.2 Chemical Processes

Yao's chemical analysis included several chemical reaction simulations on the original fluid. There were several key findings about the chemical behavior of the fluid and its dependence on multiple variables such as temperature and pH. The designer fluids considered in this study have the most of the same ionic constituents as the original IAS, shown in Table 2. Following

Approved for public release: distribution is unlimited.

suggestions by Yao, silver and magnesium were eventually removed due to their extremely low concentrations which is discussed in Section 4.7.

Table 2: Ion constituents of designer fluids

Designer Fluid Ions	
Positive Ions	Negative Ions
Na^+	MnO_4^-
K^+	
Mg^{2+}	$Cr_2O_7^{2-} \leftrightarrow HCrO_4^-$
Ca^{2+}	
Sr^{2+}	CrO_4^{2-}
Ag^+	

In an aqueous solution, the ionic forms of chromium, hydrogen chromate ($HCrO_4^-$), chromate (CrO_4^{2-}), dichromate ($Cr_2O_7^-$), and chromic acid (H_2CrO_4) can exist [53, 54]. The equilibrium concentration of each species is determined by the overall concentration of chromium and the pH of the solution. The individual concentrations are shown in Figure 9 as done by Yao [55] for the original UCLA IAS. The equilibrium constants and concentrations were calculated with a chemical analysis software OLI Analyzer. At a pH near 6.2 the chromium ions are distributed between chromate, dichromate, and hydrogen chromate with a negligible concentration of chromate acid. This diagram is based on equilibrium constants at 25 °C. If the temperature is increased, the concentration of dichromate decreases which is buffered by an increase in hydrogen chromate. The concentration of chromate does not change significantly with temperature.
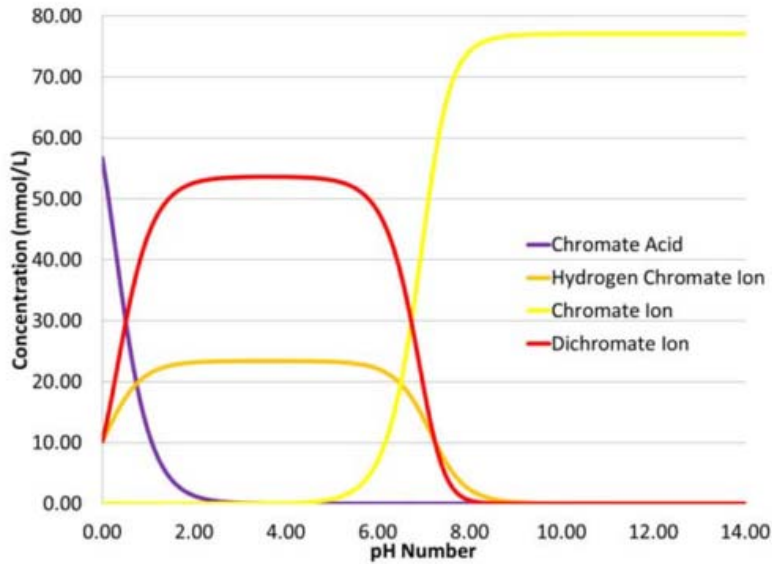
Figure 9: Predominance diagram for chromate[55]

Of the three oxidizers, the negative ions, permanganate (MnO_4^-) is the strongest and should react with copper before the chromium (VI) compound [56]. This redox reaction forms a permanent oxide layer comprised of manganese (IV) oxide (MnO_2) and copper (I) oxide (Cu_2O) as was also shown by Amouzegar [45]. For such a reaction, hydrogen ions are consumed which will increase the pH of the fluid. The increase will be slight, to 6.28, due to the low concentration of permanganate in the fluid.

$$6Cu(s) + 2H^+(l) + 2MnO_4^-(l) \rightarrow 3Cu_2O(s) \downarrow + 2MnO_2(s) \downarrow + H_2O(l) \qquad (9)$$
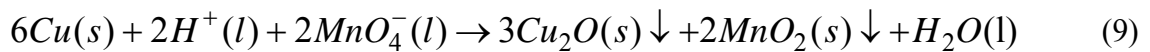
A higher pH adjusts the chromium balance of the fluid. However, the change in pH is limited due to the natural buffering effect of the chromium balance. For example, as the pH increases, hydrogen chromate separates into hydrogen ion and chromate ion to combat the increase. Yao performed a variety of tests to show that this reaction occurs first and that oxidation due to chromium (VI) is extremely slow and negligible for copper devices.

Besides the oxidation reaction, some chemicals are deposited due to solubility limits. The chromium balance is important in determining which compounds are deposited. The solubility of chromate salts is dependent on the concentration of the positive salt ions, in this case sodium, magnesium, strontium, calcium, sodium, and potassium, and the concentration of the different chromate ions.

The solubility limit is typically described as a solubility product, K_{sp}. This quantity is the product of the concentration of each ionic constituent, which for calcium chromate forms

$$K_{sp} = \left[Ca^{2+}\left(aq\right) \right]\left[CrO_4^{2-}\left(aq\right) \right] . \qquad (10)$$

Changes in the concentration of the chromium ions due to the balance will affect the equilibrium product and if the solubility product, K_{sp}, is reached. By examining the K_{sp} of different chromium salts, the chromate salt solubility products are orders of magnitude lower than those of dichromate and hydrogen chromate compounds. Therefore, it is reasonable to assume the positive ions will combine with chromate and deposit before the other compounds.

Table 3: Ksp Data for chromate compounds in IAS

Compounds	K_{sp} @ 25C	Solubility [g/L]
$CaCrO_4$	7.10E-04	4.16
$SrCrO_4$	2.20E-05	0.96
$NaCrO_4$	6.26E+02	3477.4
K_2CrO_4	1.36E+02	629.1

Table 3 shows the large discrepancy in K_{sp} for the different chromate compounds. The four possible positive ions (Na^{2+}, Sr^{2+}, Ca^{2+}, K^+), can be split into two groups. The solubility of calcium and strontium are extremely low and also decrease with an increase in temperature. As heating and evaporation occur, these ions form the majority of the solubility forced deposits. OLI Simulations

performed by Yao [55] showed that potassium chromate will reach solubility as the surface dries due to its large K_{sp}. Sodium chromate, which is a hygroscopic salt, was found to stay hydrated until the water is completely evaporated. The formation of the chromate salts is shown below.

$$Ca^{2+}(aq) + CrO_4^{2-}(aq) \leftrightarrows CaCrO_4(s) \downarrow \tag{11}$$

$$Na^{2+}(aq) + CrO_4^{2-}(aq) \leftrightarrows NaCrO_4(s) \downarrow \tag{12}$$

$$Sr^{2+}(aq) + CrO_4^{2-}(aq) \leftrightarrows SrCrO_4(s) \downarrow \tag{13}$$

$$2K^{+}(aq) + CrO_4^{2-}(aq) \leftrightarrows K_2CrO_4(s) \downarrow \tag{14}$$

It's important to note that the solubility data described in this section only describes bulk fluids with single compound solutions. The mixture is very complex and the solubility behavior of the overall solution will differ slightly from the solutions of each compound.

To summarize the following conclusions were made in this section:

1. Magnesium and Silver are removed do to their low concentration and solubility

2. Permanganate is the primary oxidizer and reacts with the copper surface to form manganese oxide and copper oxide

3. Chromium balances pH with chromate, dichromate, hydrogen chromate and chromate acid

4. Chromates have the lowest solubility of all possible chromium compounds

5. Calcium and strontium chromate solubility decreases with increases in temperature

6. Potassium chromate and sodium chromate are deposited only during dry-out of the surface

This electrochemical analysis remains important for understanding deposition mechanisms but there are many other factors contributing to the coating created in a dynamic system such as a heat

pipe. The understanding of the chemical composition of the coating is important for design of the fluid but the effects on heat pipe performance are the focus of this work.

4.2 Wetting

Surface wetting is a vastly studied subject. This section will provide a review of different types of wetting and how these types are combined and utilized with aqueous solutions on copper surfaces.

Amouzegar [45] demonstrated that chromate and permanganate salts in general are hydrophilic and thermal performance increases in phase change heat transfer devices previously were attributed to the highly wetting nature of this coating as well as the surface roughness created by the redox reaction of permanganate. She argued that the hydrophilicity is due to a combination of effects which include, the Wenzel effect, hemi-wicking, and hygroscopy which will be discussed throughout this section.

Supowit et al. [57] used a goniometer (First Ten Angstroms, FTÅ 4000A) to obtain contact angle measurements of water droplets on differently treated surfaces to observe the effect of the IAS coating on wetting properties of a droplet. The contact angle of the water droplet on each specimen was measured using a Drop Shape Analyzer method so that the "effective" contact angle was being measured. The effective contact angle describes the surface chemistry but also other microscopic impacts such as the Wenzel effect, hemi-wicking, and hygroscopy. The augmentation was done by placing three 10μL droplets of IAS on the coupon and evaporating the liquid. The heating and evaporation leaves a coating as a result of drying and chemical reaction with the copper. After the bare copper coupon and the IAS treated coupon were tested a third was prepared.

The IAS treatment procedure above was performed and then the coupon was gently rinsed in water so that most of the water soluble coating was removed.
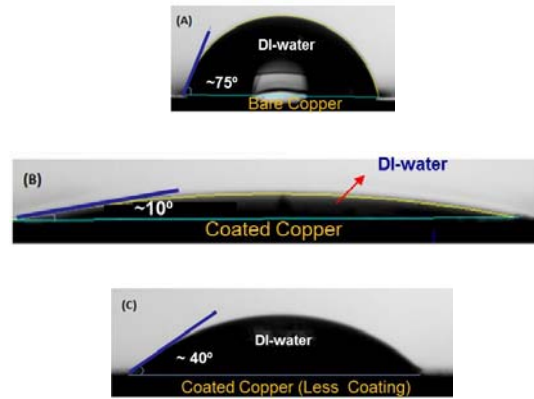
Figure 10: Contact angle measurements for water on a bare copper surface (top), IAS coated surface (middle), and washed IAS coated surface (bottom)[57].

The contact angle is drastically reduced from 75º to 10º on the IAS treated surface. The rinsed surface reduced the contact angle as well but by about 50% less. The spreading effect of the soluble porous coating was very evident. Though the porous surface structure is removed for the third measurement, the surface roughness created by the passivation reactions of IAS were still favorable to wetting. Without the IAS passivation, copper would form copper oxide if heated in air making the surface less hydrophilic. It was clear that the severe reduction in the contact angle in (B) is due to a combination of surface chemistry and structure effects.

There are many studies on the effect of surface energy and surface structure on the spreading of liquid. As described by the Wenzel and Cassie models, the wettability of a surface can be tuned by changing its morphology as well as surface energy. In the Wenzel regime, the liquid fills the grooves or pores of a rough surface, which reduces the effective contact angle according to

$$\cos\theta_a = r\cos\theta_s \ .$$

(15)

30

The Wenzel relation predicts that roughness enhances wettability. If the factor is larger than 1, a hydrophilic solid ($\theta < 90\circ$) becomes more hydrophilic when rough ($\theta^* < \theta$). Conversely, a hydrophobic solid ($\theta > 90\circ$) shows increased hydrophobicity ($\theta^* > \theta$.). In the Cassie regime, gas pockets are formed underneath the liquid effectively forming a composite surface made of the gas and solid. The apparent contact angle is then governed by the chemical heterogeneity of the surface as

$$\cos\theta_a = f_s \cos\theta_s + \left(1 - f_s\right)\cos\theta_c \ . \tag{16}$$

These simple models serve to demonstrate the most basic form of wetting and reduction in contact angle, a favorable effect for phase change heat transfer. Any form of surface augmentation that reduces the contact angle in a heat pipe would increase the capillarity through decreasing the maximum radius of curvature as well in increase the length of the thin film region.

4.2.1   Hemi-wicking

Patterns on a hydrophilic solid at a scale much smaller than the capillary length (above which gravity dominates surface tension effects) can induce superhydrophilicity. The Wenzel effect causes roughness to enhance hydrophilicity. However, the structures may also guide the liquid in a manner similar to wicking. This phenomenon is different than classical wicking, a process called hemi-wicking: As the film progresses in the microstructures, it develops an interface with air. Bico et al. [58] developed the idea that for some surface structures and roughness, liquid may penetrate into the surface features due to a capillary effect and further enhance the wetting properties and effective contact angle. There is a critical angle θ_c that determines whether liquid will imbibe into a surface morphology,

$$\cos\theta_c = \left(1 - \phi_s\right) / \left(r - \phi_s\right) \tag{17}$$

31

where ϕ_s is the solid fraction of the structure. If the contact angle on a smooth surface is less than the critical angle the liquid will penetrate in to the surface structure. The apparent contact angle can then be estimated by,

$$\cos\theta^* = 1 - (1 - \phi_s)\cos\theta .\tag{18}$$

This additional spreading phenomenon was termed "hemi-wicking" and has been used to predict spreading of liquid. Hay and Dragila [59] used this concept to predict the invasion velocity of liquid into a roughness. An example of "hemi-wicking" is depicted below.
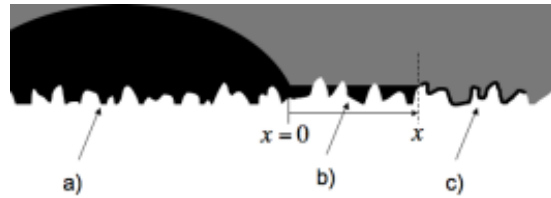
Figure 11: Spreading of a fluid droplet. a) Liquid droplet, b) Liquid "Hemi-wicking" into surface structure, c) Precursor film

The capillary effects were further studied in another visual experiment. A flat copper plate was coated with IAS as described above. The plate was heated slightly above saturation temperature to ~105 °C. The plate was then dipped into a pool of IAS heated to ~90 °C. Upon contact with the plate, the liquid formed a meniscus with a clearly visible macroscopic contact line. The liquid continued to travel up the plate via the porous IAS structure. As the liquid evaporated from the coating it was replenished with fluid from the bulk. As the power was increased the capillary height decreased as shown in Figure 12.
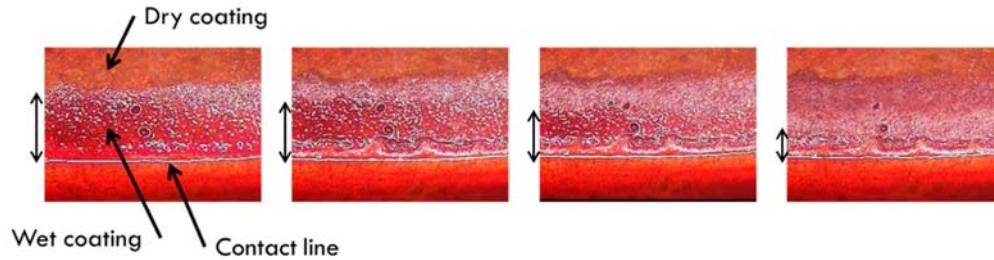
Figure 12: Vertical capillary wicking of IAS coating

This test reveals further proof that the IAS coating has wicking ability and can transport fluid beyond the contact line. The ability of IAS to create a micro-wick enhanced liquid spreading which generally has benefits for evaporative heat transfer. Studying this spreading behavior is necessary to optimize the use of IAS. Surface structure geometry and a relation to capillarity, wetting, and evaporations is desired to predict evaporative heat transfer from the coating.

4.2.2 Hygroscopy

Regardless of surface geometry, salts are generally hydrophilic because they are soluble in water, i.e. the salts will absorb water. Some salts are so extremely water-soluble and so easily hydrated that they are said to be hygroscopic. Sodium chromate is hygroscopic and rapidly absorbs water from air until a solution is formed. Amouzegar [45] hypothesized the advantage of the strong absorption forces of hygroscopic salts. This wetting mechanism is very complex and different than any other type of wicking used in traditional phase change devices. It was argued that he strong solvation forces, due to a water concentration differential, present with dry hygroscopic compounds create an additional pressure head that can aid in surface wettability.

4.3 Deposition Mechanisms

The analysis thus far has developed an understanding of the concentrations and solubility limits of the ionic constituents in the IAS fluid. The process by which these chemicals are deposited

33

inside a heat pipe can now be addressed. The use of inorganic salts in heat pipes as way to aid in the spreading of liquid must can be applied only after the deposition of the salts is understood.

The previous oxidation and solubility analysis describe an equilibrium state, with no evaporation or flow velocity. The results of deposit mass are based on a simplified system with the bulk solution covering a specified copper surface area. Though oversimplified, this analysis remains important for understanding roles of different ionic constituents. However, there are several other factors contributing to the coating created in non-equilibrium environments. In a phase change heat transfer device, evaporation and hydrodynamic forces can greatly affect the deposition pattern of the fluid constituents. Figure 13 shows a grooved heat pipe wick during operation with the original IAS fluid that will be covered in detail in the experimental section of this report. The grooves in the evaporator section are covered with deposits while the copper surface in the adiabatic region is visible. It's clear that the deposition and surface augmentation is highly non-uniform and covers the top of the groove fins as well as the groove itself.
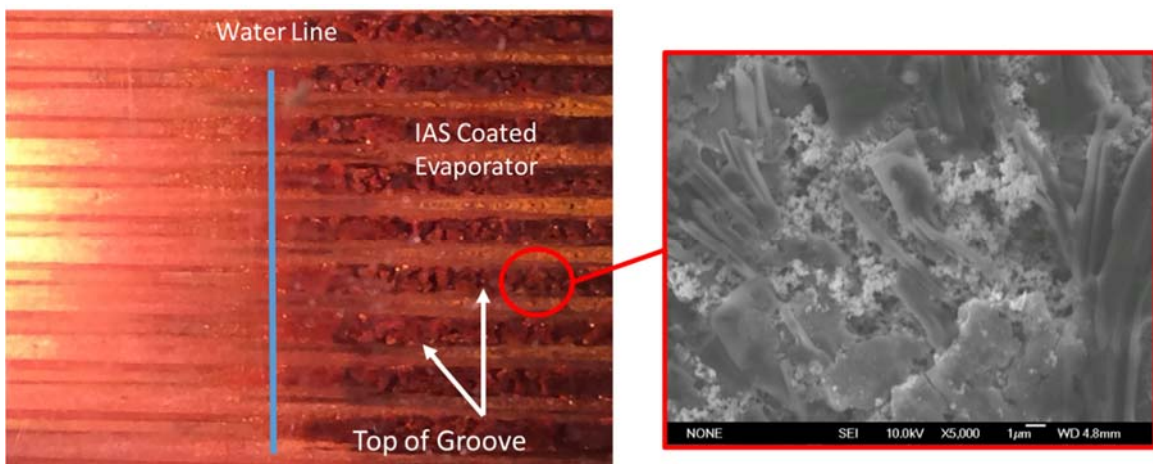
Figure 13: Representative heat pipe coating

34

From this result it's obvious that evaporation/condensation cycle in the heat pipe had a great effect on the deposition mechanisms of the working fluid and that the deposits primarily appear in the region where evaporation occurs.

4.3.1   Deposition by Solutions of Colloidal Particles

Deposition of particles by evaporating fluids has been studied for a variety of applications. The studies primarily focus on the behavior of an evaporating droplet due to its simplicity. As with most small scale phase change, evaporation occurs primarily from the contact line [7]. The meniscus creates a capillary induced flow that replenishes liquid at the edge as it evaporates. Deegan et al. [60] demonstrated that when the liquid contains colloidal particles for example, advection of the bulk fluid can cause the particles to accumulate and deposit near the contact line, a process known as the "coffee stain." It was argued that the criteria for ring effect was pinning of the droplets contact line and evaporation from the droplet edge. With a pure droplet, the drying occurs in two phases [61]. In the first phase, the diameter of the droplet is constant and the contact angle decreases as the fluid evaporates. In the second phase, after reaching a critical angle, the droplet unpins and the diameter decreases with a constant contact angle as the liquid core shrinks toward the center.

Deegan et al. [62] argued that colloidal deposits create a substrate-solvent interaction from surface roughness and chemical heterogeneities that keep contact line pinned. If the contact line were to recede as the droplet evaporated, the deposit would be uniform. Maenosono et al. [63] observed this two phase behavior with a colloidal suspension of nanoparticles, though the authors suggested that the small liquid meniscus between particles at the edge of the droplet created a capillary pressure that could be considered a suction force for liquid entering the porous deposit

35

of particles at the ring edge. The capillary effect explained the stronger pinning observed than without the deposits. This additional capillarity agrees with the analytical model of Adachi et al. [64] which demonstrated that the deposits would dry out first due to the expedited evaporation by the extended thin film monolayer of particles. The extended thin film plays a similar role to that of interline region of an evaporating meniscus which has much greater efficiency than the bulk region.

Hu and Larson [65] observed that Marangoni convection due to variation in surface tension can affect the deposition pattern. In some cases, the convection causes the particles to flow back and deposit near the center of the droplet. Ristenpart et al. [66] demonstrated analytically and experimentally that differences in thermal conductivities of the substrate and droplet determines the Marangoni direction. The effect of nanoparticle sizes and number densities on evaporation characteristics was studied by Chon et al. [67]. Droplets with the same volume concentration of small gold particles and large aluminum oxide particles were examined. The droplets with the larger quantities of small particles had a more uniform deposition than droplets with larger particles, which had a distinct ring-like deposit. The uniformity of the small gold particle deposits was attributed to an increase in viscosity as a result of the increased concentration of nanoparticles near the evaporating edge. The higher viscosity effectively choked the outward flow to the rim and decreased evaporation spreading the nanoparticles out.

Berteloot et al. [68] investigated the coffee stain effect microscopically and found interesting modulation effects due to stress caused by loss of volume from evaporation. An analytical model was developed an analytical model based on a packing limit and wedge shaped deposition. The deposit growth was found to be a function of the evaporation rate, contact angle,

and ratio of the packing limit to initial concentration. The ratio of packing limit to initial concentration can be used to gauge the growth rate and overall size of the deposit. In a rigorous full numerical simulation, Bhardwaj et al. [69] looked at the cause of de-pinning among other effects. It was demonstrated that magnitude of the receding angle of the bulk meniscus determined whether the droplet would de-pin. A small angle would avert de-pinning and a large receding angle would induce it.

A multitude of other studies have examined different fluids, evaporation conditions, and effects of different parameters though only a few related works have been discussed. In summary, particles are forced pushed to the edge of evaporating droplets due to advective forces and the size, nature, and concentration of the particles have significant effects on evaporation and wetting dynamics.

4.3.2   Deposition by Salt Solutions

The study of colloidal deposits is extensive and relatively well researched, but the deposit patterns and crystal growth created by electrolyte solutions similar to IAS is still a relatively unexplored area of research. The majority of research dedicated to salt crystallization has been related to damage of porous materials such as rocks, sandstone and common building materials like concrete and common salts such as sodium chloride and sodium sulfate [70-72]. The evaporation of sessile droplets of electrolyte solutions has been studied macroscopically for information regarding precipitation but little focus on the resulting patterns and the effect the deposits have on the wetting and spreading of liquid.

Crystallization patterns of evaporating water drops containing dissolved salts are different from the stains reported for evaporating colloidal suspensions. This happens because the salts

crystallize and grow during the drying. The overall evaporative behavior is similar to droplets of colloidal particles in that the evaporation is fastest near the edge of an evaporating drop, and consequently the solvent lost by evaporation around the edge must be replenished. This causes an outward flow in the droplet that brings fluid from the center to the edge of the droplet carrying with it any solutes which crystalize at the edge, possibly forming a ring-like stain.

Ion transport in solution is governed by competing forces of bulk advection and molecular diffusion. The advection is created by the evaporation rate of the solvent, and the diffusive flow is a result of the ionic concentration gradient. The ratio of the rate advective to the rate of diffusive transport is the Peclet number which can be used to identify the dominate mode of transport. For example, small diffusion coefficients and high evaporation rates would lead to a Peclet number far greater than one, and thus domination of advection over diffusion. Strong advection would concentrate the salt ions near the edge of the droplet.

However, nucleation of crystals and the formation of deposits is based on a local solubility limit instead of a packing limit. If the solubility limit is reached locally, crystal nucleation will occur. The irregularity of crystal growth, which can be fractal or dendritic by nature is also much more chaotic than a packing of colloidal particles. The variety of different electrolytes also have differing effects on solution properties such as surface tension, viscosity, vapor pressure due to varying solubility and ionic effects [73].

The location of crystal nucleation was found to be critical by Shahidzadeh et al. [74] through experimentally investigation of sodium chloride and calcium sulfate solutions. For NaCl, Pe > 1 (advection dominant) but the remaining deposits were unexpectedly uniform. The NaCl crystals were observed to form at the liquid-vapor interface. The protruding crystals created a

capillary pressure that transported the crystals inward toward the center of the droplet. For CaSO₄, it was estimated that Pe < 1 (diffusion dominant) yet a ring-like stain was deposited. These crystals started at the solid-liquid interface and remained there. The CaSO₄ crystallites, in the form of many small nano crystals originated from the precursor film extending from the macroscopic drop. The formation of this crystalline pathway enhanced wettability and beyond the initial radius.

Other interesting findings also highlight the uniqueness of salt deposits. The calcium sulfate droplets were found to have higher evaporation rates than the sodium chloride droplets. The difference was attributed to the much higher solubility of NaCl. The abundance of NaCl reduces the water vapor pressure by 25% at saturation while the difference in water vapor pressure of the CaSO₄ solution is negligible. The liquid-vapor surface tension of NaCl is also significantly above that of water, increasing the static contact angle.

It's clear that salt solutions introduce many other variables that effect the deposition pattern during evaporation. The goal of using salt solutions such as IAS in a heat pipe is to enhance wetting and spreading in the evaporator without inhibiting evaporation. This can be accomplished as long as the crystalline deposits occur at the interline. This requires advection dominant flow of ions, substrate-attached crystals, and moderate solubility to limit changes in thermophysical properties. In addition, the type of crystals can be used to create spreading, a phenomenon is called "creeping" which is discussed in the following section.

4.3.3   Creeping of Salt Solutions

Though solutions of colloidal particles have demonstrated small scale spreading due to intermolecular forces [75], salt solutions have well-known ability to "creep." Creeping, a phenomenon by which crystallites can extend or spread beyond the initial liquid contact line, was

Approved for public release: distribution is unlimited.

first reported by Washburn [76]. It was suggested that liquid is transported due to capillary action by the pores between the crystallite deposits as well as the space between the deposits and the substrate. Hazelhurst et al. [77] observed spreading in a variety of salt solutions but argued that the liquid is transferred over the crystallites due ability of the solid solute to preferentially wet the substrate.

The idea of a self-amplifying creeping process is unique in the area of wetting and is only made possible by the complicated growth mechanisms of crystals. Naturally, Crystallization occurs in a fractal or dendritic nature due to a morphological instability [78]. Salt crystals have the unique ability to spout protrusions which can grow more quickly than the rest of the crystal. In addition, the solution is transported, not particles, so that only space for the liquid is necessary for proper spreading.

Van Enchevort and Los [79] experimentally confirmed with several inorganic salts that liquid can be transported along the top of the crystal, "top supplied creeping," TSC) or between the crystallites and substrate ("bottom supplied creeping," BSC). TSC results in branching, widespread deposits while BSC leads to more compact crystals. $K_2Cr_2O_7$ and $(NH_4)_2Cr_2O_7$ demonstrated wide branching patters on smooth glass due to both TSC and BSC. However, a more hydrophobic Teflon substrate eliminated creeping because the liquid would not move to the periphery of the crystallites.

The wetting conditions for each type of growth was developed theoretically. The criteria for both cases depend on a combination of the interfacial energies between solution, substrate, crystals, and air. Though the condition for each type of creeping is different, poor wetting of the solution to the substrate, typically prevents either type of creep. It was also observed that some

40

crystallites were formed in the bulk and did not adhere to the surface. Once a few stuck to the substrate, creeping initiated. With salts, deposits are formed based on solubility so that they need not form at the solid surface. The crystallite-substrate surface energy needs to be low to promote attachment and creeping.

The details of creeping of salt solutions are still not well understood. Crystal growth depends on evaporation, surface energy, occurrence of secondary nucleation, crystal size and shape, and others making it practically impossible to form a complete quantitative description though the understanding of the conditions that promote creeping are valuable.

4.3.4 Summary

Sureshkumar [41] showed that Nanoparticle suspensions have been widely used to improve the performance of heat pipes yet, the detailed deposition of the nanoparticles is typically ignored and assumed uniform.

The literature review of evaporation driven deposits of inorganic salts or colloidal particle revealed that under certain conditions, that solutions can induces unique wetting and spreading of liquid unlike colloidal suspension. Salt deposits are based on solubility not a packing limit. The domination of advection over diffusion can lead to deposits near the evaporating interline region and the crystals can spread liquid over initially dry areas.

The use of IAS to increase the performance of a heat pipe stems from its ability to deposit on the surface of the wick and increase wetting. The goal is to understand this particular fluid and how conditions in a heat pipe play a role in the deposition patterns. The behavior of inorganic salts in a heat pipe can be expected to be quite different from that of a droplet. It's important to analyze the flow conditions with regard to the chemicals and concentrations present to determine the

possible ways to utilize the salt deposits to enhance wetting. In addition, IAS is composed of a variety of ionic constituents making the crystallization behavior even more complex.

The Peclet number must be examined for a heat pipe with the diffusion coefficients of the different solutes in IAS. Solubility must be examined together with the Peclet number and initial concentration in the IAS fluids. Calcium chromate has the lowest solubility and lowest diffusion constant. The previous analysis shows that the other compounds would not be deposited due to their high solubility. However, if the initial concentration is large enough, the local concentration of other ions may still exceed that larger solubility limit.

Creeping was also shown to be heavily dependent on wetting of both the solution and the crystallites. The choice of wick material is limited to copper in this work but creating a wick surface that favors wetting must also be investigated. Amouzegar [45] and Yao et al. [55] both suggested previously that the oxidation reaction possibly creates a foothold for chromate salts to adhere.

4.4 Concentration Analysis

The evaporation/condensation cycle in a heat pipe and evaporation from a wick present a different scenario compared to the finite liquid volume and flat surface of the evaporating droplets discussed above. The differences were analyzed with respect to the heat pipe geometry investigated later in this work.

The chemicals in IAS are inorganic and have much higher boiling points than water yielding a vapor from IAS that is almost pure water vapor [56]. Pure water is condensed on one side of the heat pipe and flows back to the evaporator due to a difference in capillary pressure, so that there

is constant axial flow toward the evaporator. The liquid then evaporates from the liquid menisci in the wick.

First, the axial flow along the heat pipe was analyzed following some simplifications outlined by Yao [47]. The chemical concentration profiles were used to determine if the solubility limit is reached. A 1-D diffusion model was used to estimate the chemical concentration profiles along the axial flow path, shown in Figure 14. Species #1 represents the chemicals in IAS and Species #2 represents water.
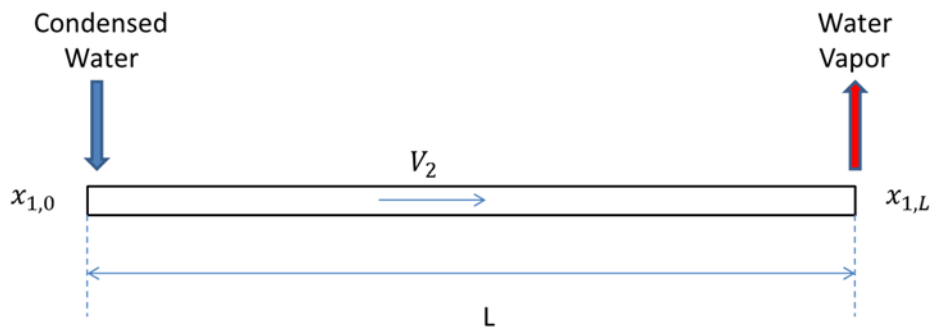
Figure 14: 1-D diffusion model

Fick's law for a two species system combines the advective molar flux and diffusive molar flux,

$$N_1 = x_1 \cdot (N_1 + N_2) - cD_{12}\nabla x_1 \tag{19}$$

where

The heat pipe was taken to be at steady state. This requires the chemical concentration profile to be constant so that the total molar flux of Species #2 was zero. The water species had a constant flux and bulk velocity due the cycle of evaporation and condensation. For a dilute solution,

$$\begin{aligned} N_2 &= v_2 \cdot c \\ N_1 &= 0 \end{aligned} \tag{20}$$

These conditions simplify Fick's law so that the advective flux balances the diffusive flux of the chemicals. The chemicals are advected with the velocity of the water.

$$x_1 N_2 = c D_{12} \nabla x_1 \tag{21}$$

The result is a simple first order differential equation that can be solved directly for the mole fraction of the chemicals assuming both boundary conditions are known. The equation was integrated from a location l, to the beginning of the evaporator section at L.

$$\frac{N_2}{c \cdot D_{12}}(l - L) = \ln\left(\frac{x_1}{x_{1,L}}\right) \tag{22}$$

The solution takes a more useful form if the non-dimensional Peclet number is introduced,

$$x_1(l) = x_{1,L} \cdot \exp\left[Pe\left(\frac{l}{L} - 1\right)\right] \tag{23}$$

where the Peclet number is the ratio of advection forces to diffusive forces.

$$Pe = \frac{advective\ force}{diffusive\ force} = \frac{L v_2}{D_{12}} \tag{24}$$

The molar concentration profile is now a function of only location, the concentration in the evaporator, and the Peclet number. Yao integrated this model with a model of a thermosiphon to solve for the concentration profiles of each chemical constituent. The results demonstrated that the chemicals will be heavily concentrated in the evaporator region due to the strong advective forces, or a large Peclet number. Analysis of the Peclet number provides insight into the behavior of the chemicals in a solution on a specific length scale. The flat heat pipe developed later in this work contains rectangular grooves that have a cross section of 500μm x 500 μm and a length of 0.1m. With an input power of 50 W the axial fluid velocity can be estimated as $v_2 \square 3mm/s$. For all

44

the relevant chemicals in IAS, the diffusion coefficients, taken from a study by Yuan-Hui and Gregory [80], and Peclet numbers are shown in Table 4 [80].

Table 4: Diffusion coefficient at 25 °C

Ion	D_{12} [$10^{-6}cm^2$/s] @ 25°C	Peclet Number
K^+	19.6	1.53E+05
Ca^{2+}	7.93	3.78E+05
Sr^{2+}	7.94	3.78E+05
Na^+	13.3	2.26E+05
CrO_4^{2-}	11.2	2.68E+05

The Peclet numbers are extremely large. As a result, advection is dominant in this flat heat pipe geometry, and all the chemicals are transported into a very small region near the meniscus where the solubility limits will be reached and coating will be generated. For example, $l/L = 0.99$, the concentration is on the order of $x_{1,L} \times 10^{-44}$. This analysis is enough to conclude a strong domination of advective flow and that the entire chemical mass of chemicals can be assumed to exist in the evaporator.

The cross section of the grooved wick was also analyzed. Even though the ions are transported to the evaporator, the length scale in the groove is much smaller than the axial distance from the condenser to evaporator. In a droplet the volume of solvent decreases, reducing the contact angle until the edge de-pins. Unless the heat pipe is failing, the shape of the liquid menisci in the wick will remain relatively constant. The evaporating region in a heat pipe contains many menisci, and in the case of a rectangular grooved wick, the menisci are relatively orderly. Here,

the geometry and scale is much more similar to that of a droplet. The grooves had a radius of 250μm. The Peclet number calculations for this length scale are shown in Table 5.

Table 5: Pe numbers at the groove length scale

Ion	D_{12} [$10^{-6}cm^2/s$] @ 25°C	Peclet Number
K^+	19.6	3.83E+02
Ca^{2+}	7.93	9.46E+02
Sr^{2+}	7.94	9.45E+02
Na^+	13.3	5.64E+02
CrO_4^{2-}	11.2	6.70E+02

The Peclet numbers were still very large, on the order of $\sim10^2$. The concentration at $l/L = 0.99$, is on the order of $x_{1,L} \times 10^{-6}$. It isn't until the length scale is on the order of a micron that the Peclet number becomes unity.

The solubility limits of the chromate compounds can be reached at low temperatures due to the large increases in local concentration due to advective flow. For calcium, strontium, and even potassium chromate, it can be assumed that most of the mass will be deposited near the thin film of the meniscus where most evaporation takes place. Even though potassium chromate is far more soluble that calcium and strontium chromate, the flow velocity still creates a local spike in concentration large enough reach the solubility limit. Unless the salt is extremely hygroscopic, the solubility only affects the initial concentration, and thus the total volume of coating, that can be used.

4.5 Deposit Investigations

Though evaporating droplets differ from a heat pipe, they can provide qualitative insight into the role and behavior of different salts. Like, the studies above, droplets of different solutions were examined to identify differences in spreading of each component of IAS. Separate solutions of each possible chromate salt and potassium permanganate were created at the concentration each had in the original fluid. For the chromate solutions, concentrations were based off of the molar concentration of the positive ion since there is an abundance of chromate ions. The evaporation process and resulting coating pattern of the evaporating droplets were observed.

$9\mu L$ droplets were dried in open air on copper coupons with a mirror finish using a heating plate at $60°C$. This droplet volume and temperature were chosen to compare to the grooved heat pipe wick tested later in this work. Each groove in the wick holds $8.125 \mu L$ so that the mass of chemicals was close to that of a single groove. The process was timed to calculate the evaporation rate and video captured using a microscope charged-coupled devices (CCD) camera. The test was repeated three times for each fluid. The individual solutions were then compared to the deposition pattern of the original solution and water.
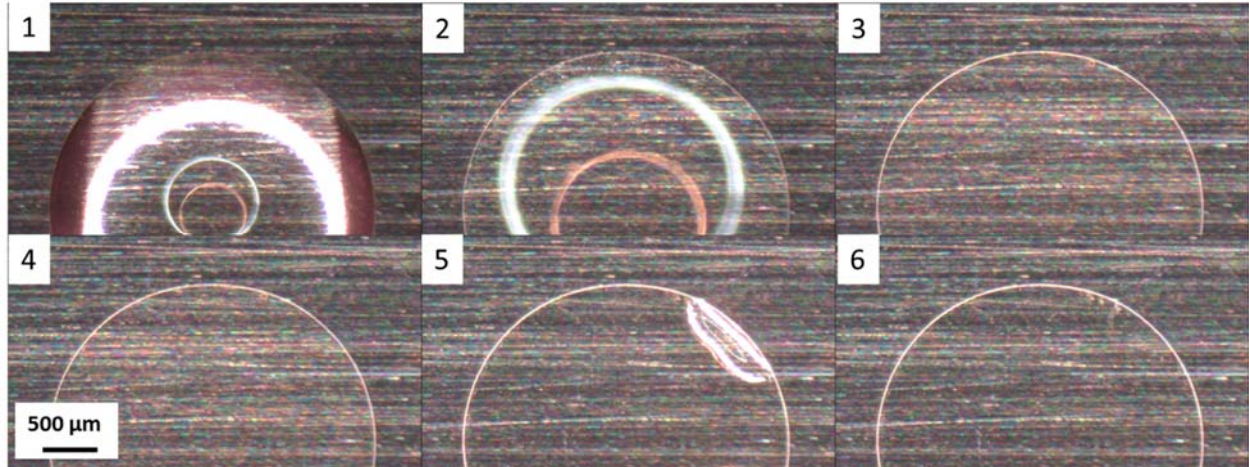
Figure 15: Evaporating water droplet

Figure 15 shows the evaporation process for water. The pictures were taken in 5 second intervals from the final time (stage 6) except stage 1 which was taken 15 seconds prior to stage 2. The stages are described in the list below.

1. Full droplet

2. Initial coating formation

3. Droplet becomes flat

4. Droplets interface becomes concave

5. Droplet begins to dry-out

6. Full dry-out

The water droplet remained pinned for the entire test. The droplet becomes flat in stage 3-4 and then eventually snaps apart in stage 5. The abrupt dry-out occurred because the capillary force of the meniscus stretched the liquid film. Though DI water was used a small amount of ring deposit was left on the surface. This contamination was most likely due to particulates in the air falling on the droplet during preparation.

IAS has far more interesting behavior. In stage 2, a coating began to form around the edge of the droplet. As discussed above, the evaporation occurs primarily form the edge of the droplet causing the concentration of ionic constituents to increase. The solubility limit is reached and deposits begin to form. This was a result of the domination of advective forces over diffusive forces. However, even though there was a "coffee-ring" a significant amount of chemicals was deposited in the center of the droplet. The coating continues to grow until the droplet is flat in stage 3 and then begins to expand outward radially as the droplet becomes concave in stage 4. The edge continues to expand in stage 5 as the droplet begins to dry-out from the center.

The expansion of the edge coating, and center dry-out signify spreading capability of IAS as well as a powerful suction force. The capillary and solvation forces associated with the coating pull all of the remaining liquid toward the evaporating meniscus. The snapping effect seen with was did not occur due to the coating in the center of the droplet which provided a transition force for the surface tension of the liquid film.
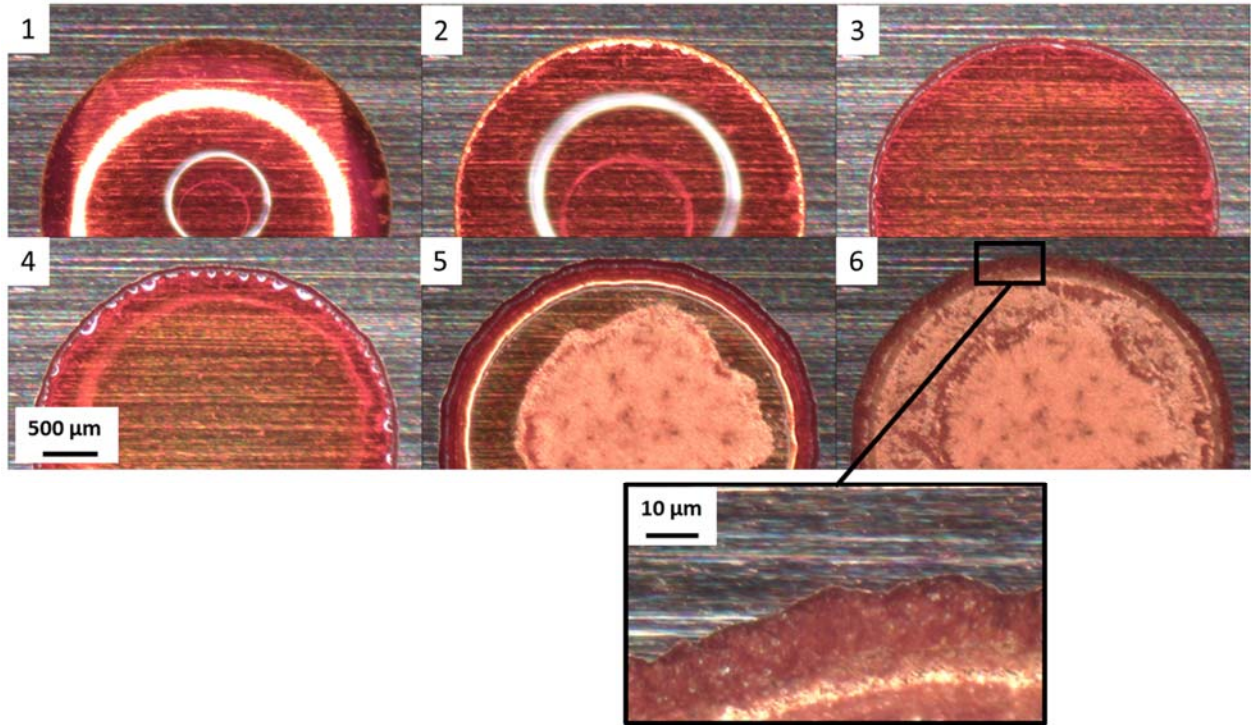
Figure 16: Evaporating IAS droplet

The potassium permanganate droplet also began to form a coating in stage 2, seen in Figure 17. In stage 3 the several branched protrusions emanated from the pinned edge of the droplet. Liquid flowed from the droplet out through the branches and continued to evaporate. The as the liquid supply diminished the protrusions still grew and dry-out again occurred from the center of the droplet. The protrusions were a result of the oxidation reaction of permanganate and copper. The chemical reaction created manganese oxide and copper oxide which changed the roughness and chemistry of the surface and led to liquid spreading.
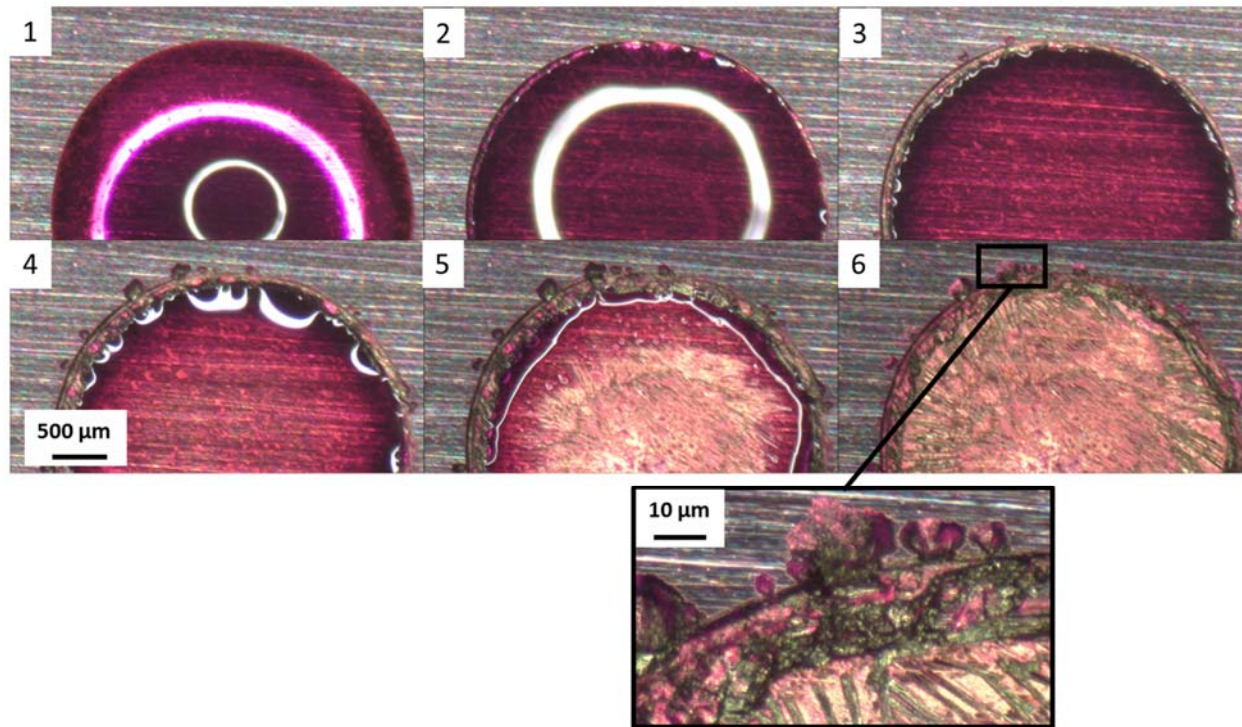
Figure 17: Permanganate evaporating droplet

The first chromate solution tested was potassium chromate, a high solubility chromate salt and the stages of evaporation are shown in Figure 18. With this solution, a coating at the edge was formed as well. There was a large buildup of deposits but the edge remained pinned in the same location for the entire test. Dry-out again occurred from the center, suggesting a strong suction force from the coating. In the magnified image, the edge is very defined unlike that of the spreading edge of IAS and potassium permanganate.

Strontium chromate is shown in Figure 19. This solution was as clear as water due to the very low concentration of strontium in the IAS fluid. A small coating formed at the edge of the droplet but once the droplet becomes a flat film, the interface snapped like it did for water. The capillary force of the edge and coating stretched the liquid film. The bare surface on the interior of

51

the droplet failed to provide and intermediate force for the film to maintain continuity and gradually dry-out.
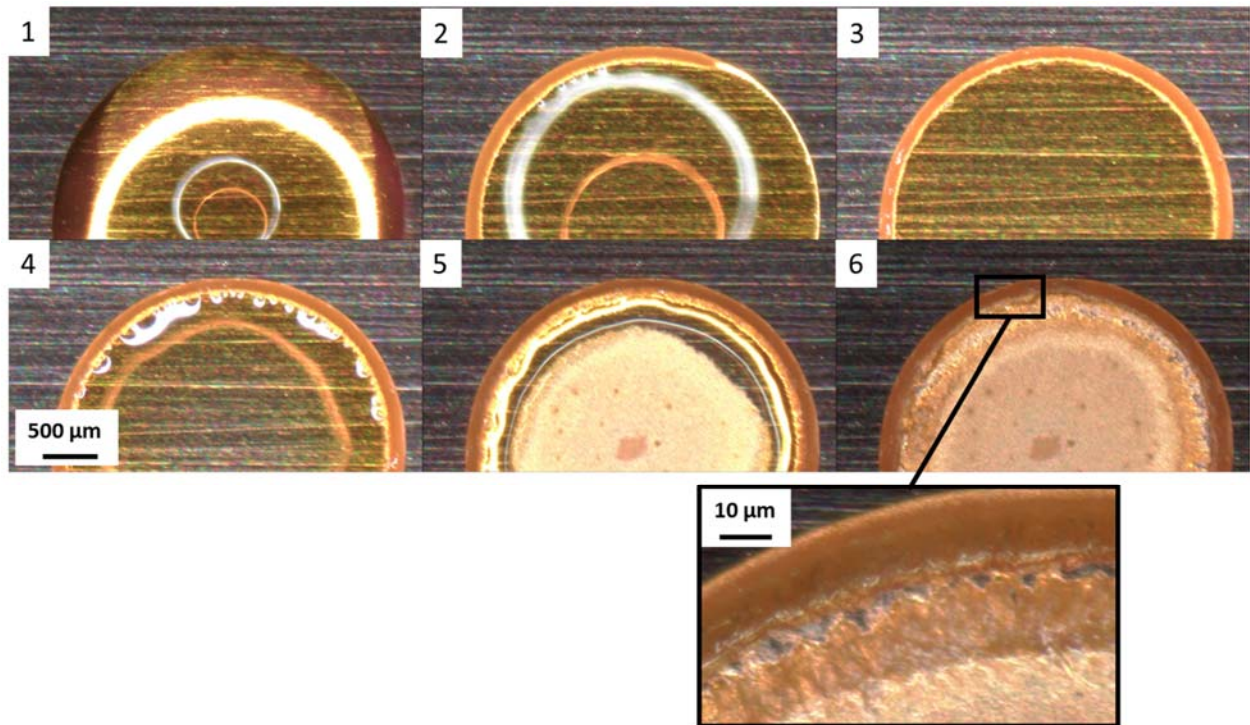
Figure 18: Potassium chromate droplet
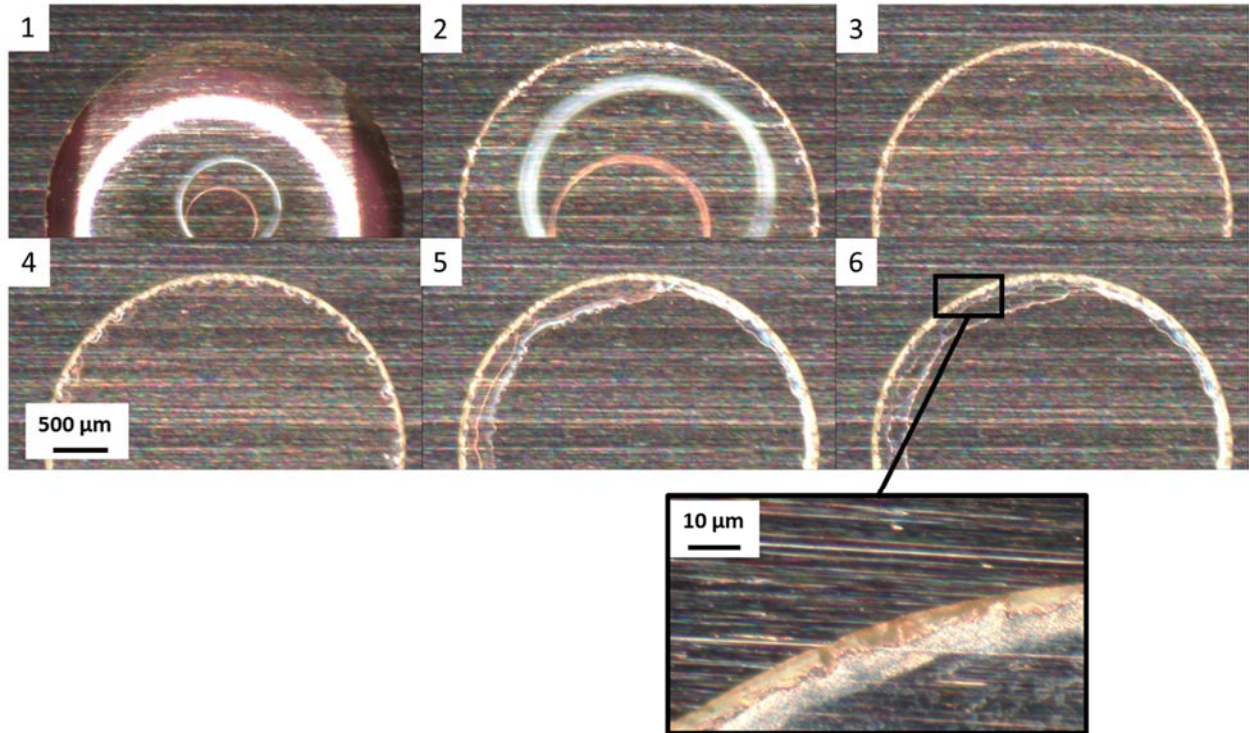
Figure 19: Strontium chromate droplet

The calcium chromate solution shown in Figure 20 behaved similar to potassium chromate. A large round deposit formed on the edge of the droplet but no creeping or spreading occurred. The droplet dried out from the center due to interior deposits. A seventh stage was included for this solution due the way the liquid dried in the coating. Liquid was trapped, or fully enclosed inside the coating. Comparing stage 6 and stage 7 the color of the coating on the right side of the edge is slightly darker due to the water inside. Though the center had completely dried out, a liquid slug remained on the interior of the cylindrical deposit mound and gradually dried out over a few seconds after the rest of the droplet. This entrapment could possibly due to the way the calcium chromate is formed, its low solubility, or deposit structure.
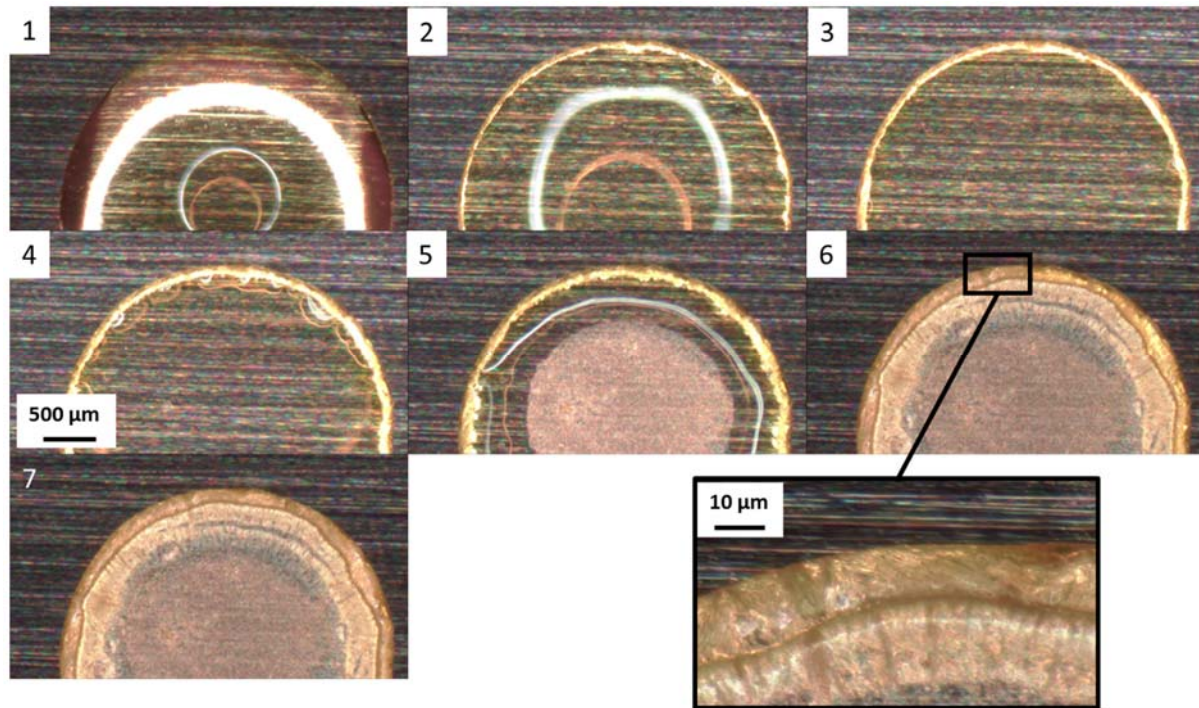
Figure 20: Calcium chromate droplet

The hygroscopic sodium chromate sequence is shown in Figure 21. Here, a small coating is formed during stage 2 and 3 near the magnitude of the strontium coating. Unlike any other solution tested, the sodium chromate solution begins to gradually dry-out from the edge, inward. The overall coating pattern is fairly uniform compared to the other solutions which have strong ring-like coatings. The edge of the droplet showed no sign of spreading.

54
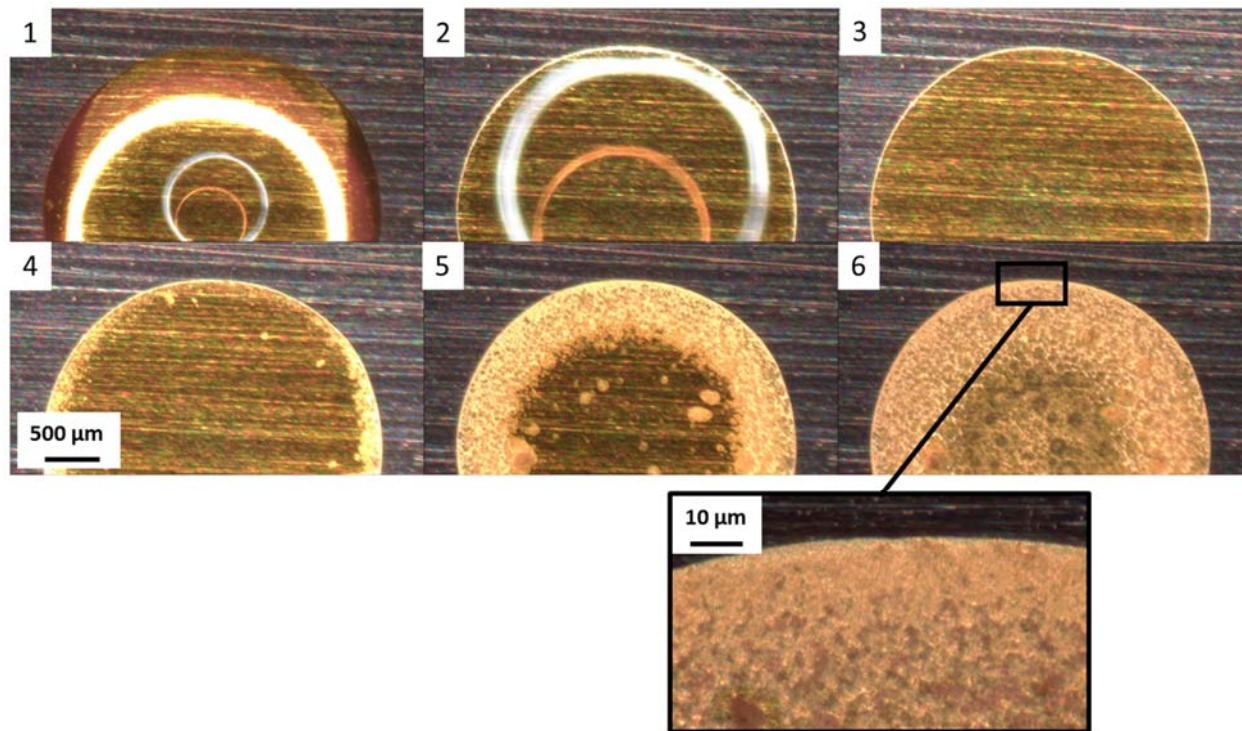
Figure 21: Sodium chromate droplet

The IAS and permanganate solutions were the only solutions to demonstrate creeping or spreading during evaporation. Highly magnified versions of the evaporation stages are shown in Figure 22 and Figure 23. At this magnification the creeping distance is more visible. The edge of the IAS solution moved uniformly almost 200μm from its original pinned position. The cylindrical deposit mound resembles that of the potassium chromate and calcium chromate coatings. The permanganate solution did not creep as far and the protrusions were unfortunately not included in the frame due to the high magnification. However, the potassium permanganate crystals (dark purple) are clearly visible in the solution (light purple). The crystals form at the edge but float in the solution. The liquid flows underneath the crystals and reacts with the surface creating a slight creep.
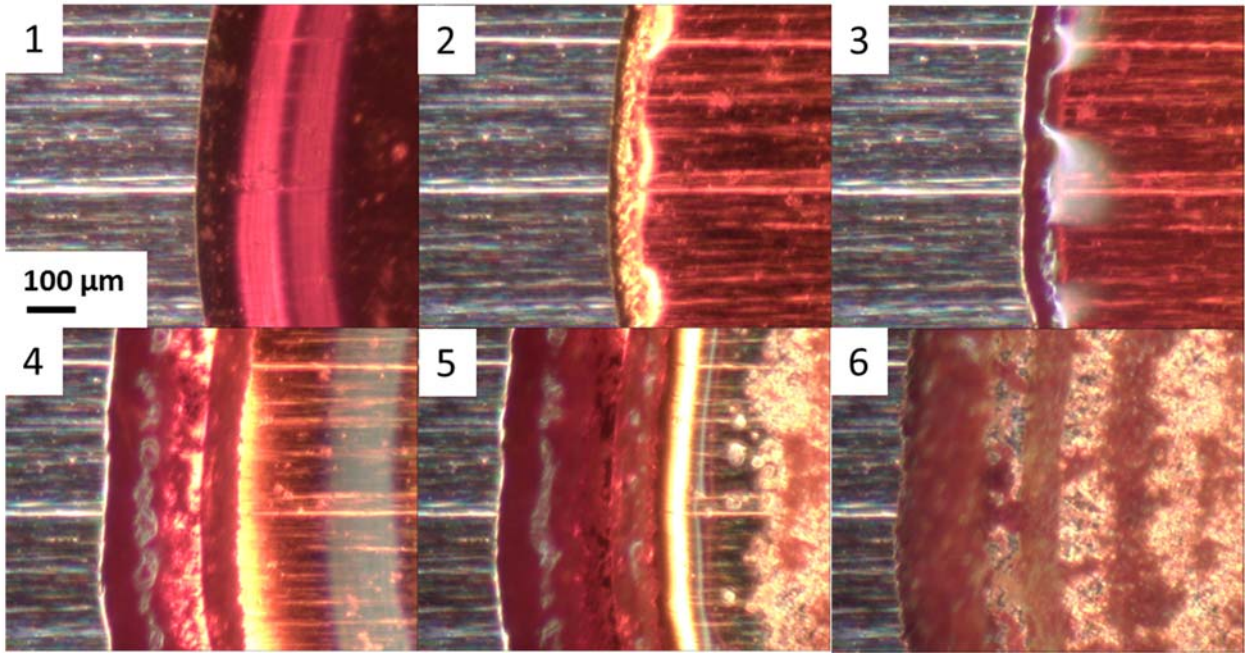
Figure 22: Magnified IAS droplet evaporation
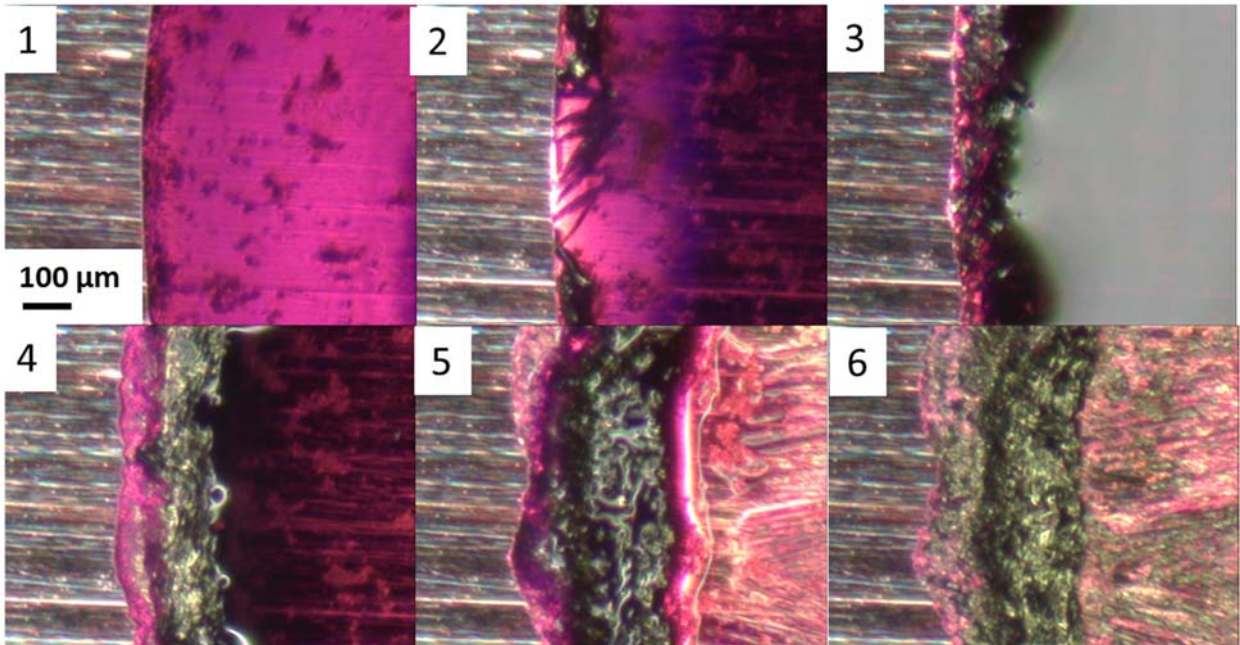
Figure 23: Magnified potassium permanganate droplet evaporation

The velocity in the droplet can be estimated using the evaporation rate, averaged over the experiment, and the surface area of the droplet cap as suggested by Shahidzadeh-Bonn et al. [74]. The calculated Peclet number ranged from 2-12 depending on the constituent. The experimental data is tabulated below.

Table 6: Droplet Test Data

Fluid	Water	IAS	KMnO4	KCrO4	NaCrO4	SrCrO4	CaCrO4
Total Time [s]	191.67	169.67	197.33	208.33	201.67	201.67	209.00
Initlal Volume [m^3]	7.65	8.35	8.43	8.73	8.08	7.83	8.62
Aveage Evaporation Rate [m^3/s]	3.99E-11	4.92E-11	4.26E-11	4.19E-11	4.01E-11	3.89E-11	4.12E-11
Estimated Velocity min [m/s]	3.52E-06	3.76E-06	3.22E-06	2.95E-06	3.21E-06	3.28E-06	2.97E-06
Estimated Velocity max [m/s]	7.03E-06	7.53E-06	6.44E-06	5.90E-06	6.42E-06	6.56E-06	5.93E-06
Diffusion Coefficient [m^2/s]	0.00E+00	2.00E-09	1.96E-09	1.96E-09	1.54E-09	7.94E-10	7.93E-10
Peclet number minimum	-	2.98	2.60	2.42	3.38	6.41	5.99
Peclet number maximum	-	5.95	5.21	4.85	6.76	12.83	11.99

These visual tests were a good indication of crystallization patterns of the different salts. The chromate salts all show some magnitude of the coffee-stain effect. Advection dominated diffusion and the ionic salts were carried to the edge of the droplet and crystallized there. Central crystals could be a result of lack of attachment to the surface or higher solubility. Although several chromate salts left a ring-like deposit, only potassium permanganate demonstrated the ability to creep.

57

4.6 Thermophysical Properties

Early hyporeport for explaining the performance of IAS involved differences in thermophysical properties due to the addition of the inorganic constituents. Amouzegar [45] experimentally measured surface tension, viscosity, phase change enthalpy, boiling point, freezing point, and density and found that the properties differed only slightly from de-ionized water. The data was within the experimental uncertainty of the testing methods used. It was concluded that the bulk properties could be assumed to be that of de-ionized water. The properties of IAS were also reviewed much more thoroughly by Yao [47]and the same conclusion was reached. In this work the properties of the IAS fluid will be assumed to be the same as water.

4.7 Present Working Fluids

The class of fluids used in this study, differ by exclusion of several compounds as well as overall concentration. The nomenclature for the fluids was discussed earlier. The IAS 2 fluids were created without Ag_2CrO_4 and the IAS 3 fluids excluded $Mg(OH)_2$. Stubblebine et al. [52] argued that the silver ions, though they may be important for aluminium passivation, are useless for performance enhancement in copper devices, especially at such low concentrations.

The IAS 2 fluids, shown in Table 7, were the first fluids tested in a heat pipe in this work and serve as a baseline for the relative overall concentration effect on the coating.

58

Table 7: IAS #2 fluids

| Compound | IAS Fluid Compound Mass [g/L] IAS | | | |
| | #2.1 | | #2.2 | |
	Theor.	Actual	Theor.	Actual
$KMnO_4$	0.4400	0.4420	0.8800	0.8833
$K_2Cr_2O_7$	8.5385	8.5385	17.0770	17.0888
CrO_3	1.9058	1.9163	3.8116	3.8374
$Sr(OH)_2$	0.1042	0.1062	0.2084	0.2103
$Ca(OH)_2$	0.9751	0.9801	1.9502	1.9519
$Mg(OH)_2$	0.0335	0.0367	0.0670	0.0679
NaOH	0.5508	0.5545	0.9364	1.1159
pH	6.2	6.18	6.2	6.37

The IAS 3 fluids were designed based around the overall concentration and ratios of the original fluid which is embodied by 3.1. This concentration was scaled up or down to study the overall effect of concentration. Two other fluids, the chromate only, or "yellow fluid," and the permanganate only, or "purple fluid," were designed to analyze effects of different ionic components on performance as in the droplet study. These fluids contained the chromate or permanganate components respectively at the concentrations in IAS 3.2. This larger concentration was chosen after preliminary testing covered later. IAS 3 is shown below in Table 8.

Table 8: Designer fluids studied in present work that were calculated in OLI (left), or measured with a scale (right)

| Compound | IAS Fluid Compound Mass Concentration [g/L] IAS | | | | | | | | | |
| | #3.025 | | #3.05 | | #3.1 | | #3.2 | | #3.3 | |
	Theor.	Actual	Theor.	Actual	Theor.	Actual	Theor.	Actual	Theor.	Actual
$KMnO_4$	0.1124	0.1127	0.2247	0.2248	0.4494	0.4497	0.8988	0.8989	1.3482	1.3489
$K_2Cr_2O_7$	2.1352	2.1350	4.2703	4.2716	8.5406	8.5413	17.0812	17.0831	25.6218	25.6200
CrO_3	0.4782	0.4773	0.9564	0.9572	1.9127	1.9360	3.8254	3.8371	5.7381	5.7401
$Sr(OH)_2$	0.0270	0.0280	0.0540	0.0539	0.1080	0.1100	0.2160	0.2210	0.3240	0.3220
$Ca(OH)_2$	0.2450	0.2445	0.4900	0.4800	0.9799	0.9808	1.9598	19.9550	2.9397	2.9383
NaOH	0.1707	0.1710	0.3206	0.3206	0.5427	0.5420	0.9352	0.9350	1.2912	1.2905
pH	6.2	6.21	6.2	6.23	6.2	6.25	6.2	6.23	6.2	6.21

All fluids used a target pH of 6.2. The only fluid with a different pH was the permanganate-only fluid in Table 9. This solution is naturally neutral and acid would have to be added to lower the pH. This could not be done because any acid would create NCG in the heat pipe and corrode the wick. The measure value is far off of the target value due to the large reported inaccuracy of the pH probe near neural pH of 7 or any other calibration value.

Table 9: IAS 3.2 Hybrid fluids

Compound	IAS Fluid Compound Mass Concentration [g/L]					
	IAS		Chromate-Only		Permanganate-Only	
	#3.2		#3.2		#3.2	
	Theor.	Actual	Theor.	Actual	Theor.	Actual
$KMnO_4$	0.8988	0.8989	-	-	0.8988	0.8988
$K_2Cr_2O_7$	17.0812	17.0831	17.0812	17.0810	-	-
CrO_3	3.8254	3.8371	3.8254	3.8250	-	-
$Sr(OH)_2$	0.2160	0.2210	0.2160	0.2159	-	-
$Ca(OH)_2$	1.9598	19.9550	1.9598	1.9590	-	-
NaOH	0.9352	0.9350	0.9304	0.9304	-	-
pH	6.2	6.23	6.2	6.22	7.08	7.51

5 Flat Heat Pipe Experiments

The first goal of the experiments was to obtain accurate performance measurements of a heat pipe using IAS fluids. The second goal was to observe the characteristics of deposits on the wick surfaces to gain insight into the physical mechanisms that contribute to performance enhancement.

The inherent characteristics of heat pipes make these types of experiments difficult. The metal casing materials used for heat pipe are opaque, hermetically sealed, and internally vacuumed. In studies that only required thermal resistance measurements, dry-out can be assumed when the thermal resistance dramatically increases [2]. However, this does not give any insight into the dynamics of liquid recession and dry-out. Particle deposition can be viewed after the test but important information about wetting is lost. In addition, the solubility of the compounds in IAS made preservation of the coating difficult.

In order to view inside the heat pipe, one wall must be transparent. Modular designs make charging and vacuum sealing much more difficult. Flat heat pipes sealed with O-rings have been utilized for this purpose by Wong and Chen [81] for grooved heat pipes and by Liou et al. [82] for sintered mesh flat heat pipes. Consistent degassing of the working fluid, charge volume, and vacuum pressure are also necessary criteria outlined by Reay and Kew [1] for accurate comparison. Dissolved non-condensable gas in the working fluid must be removed prior to charging so that the vacuum pressure inside the heat pipe is not affected during testing. The NCG can block condensation in part of the condenser and significantly impact thermal performance.

In this work, a modular flat heat pipe (FHP) apparatus with a transparent viewing plate was designed to quantitatively compare the thermal resistance and dry-out of the different working

fluids and observe the behavior of the working fluids during operation. A vacuum charging station was utilized to provide consistency between experiments. This chapter covers the experimental heat pipe performance results and observations of the IAS coating. The details of the experiment construction, testing procedure, instrumentation, uncertainty analysis, and charging the working fluid are also discussed.

5.1 Methods, Assumptions, and Procedures

5.1.1 Flat Heat Pipe Apparatus

The heat pipe test setup consisted of a vapor chamber with an internal volume measuring 3 cm x 13 cm x 1 cm. The top wall was a clear acrylic viewing window to observe liquid wetting, fluid deposits, and dry-out of the grooves. A stainless steel frame was sealed to the top window and grooved copper plate with Viton fluoroelastomer O-rings of durometer A90. A schematic of the chamber cross section is shown in Figure 24. The O-ring groove had a width of 4.83 mm and a depth of 2.85 mm, as suggested in the Parker O-Ring Handbook [83].
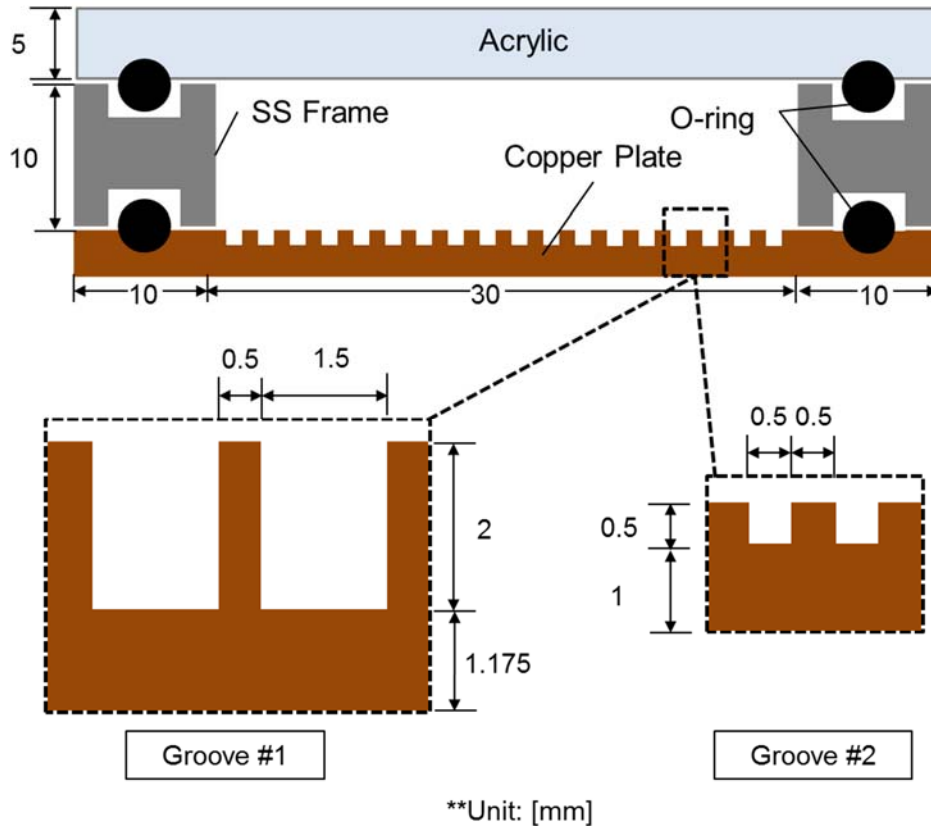
Figure 24: Schematic of the flat heat pipe cross-section for two different grooved wick geometries

Two different sized grooved wicks were tested. The first grooved plate had 15 large rectangular grooves measuring 1.5 mm wide by 2 mm milled in a 3.175 mm thick plate. This groove size, while relatively large, was chosen for machinability, low cost, and dry-out visualization. The second grooved plate was 1.5 mm thick with square 0.5 mm (500μm) grooves.

5.1.2 Instrumentation

Ten Type-T thermocouples were attached to the back side of the grooved plates with thermal adhesive as shown in Figure 25. The condenser section of both wicks was 3cm x 3cm. The evaporator section in the first wick with the larger grooves had 1cm x 3 cm evaporator section and

the second wick had a 3 cm x 3cm evaporator section. The smaller groove geometry and larger evaporator area were chosen for the second wick to reduce the boiling limit relative to the capillary limit. More details are given later.
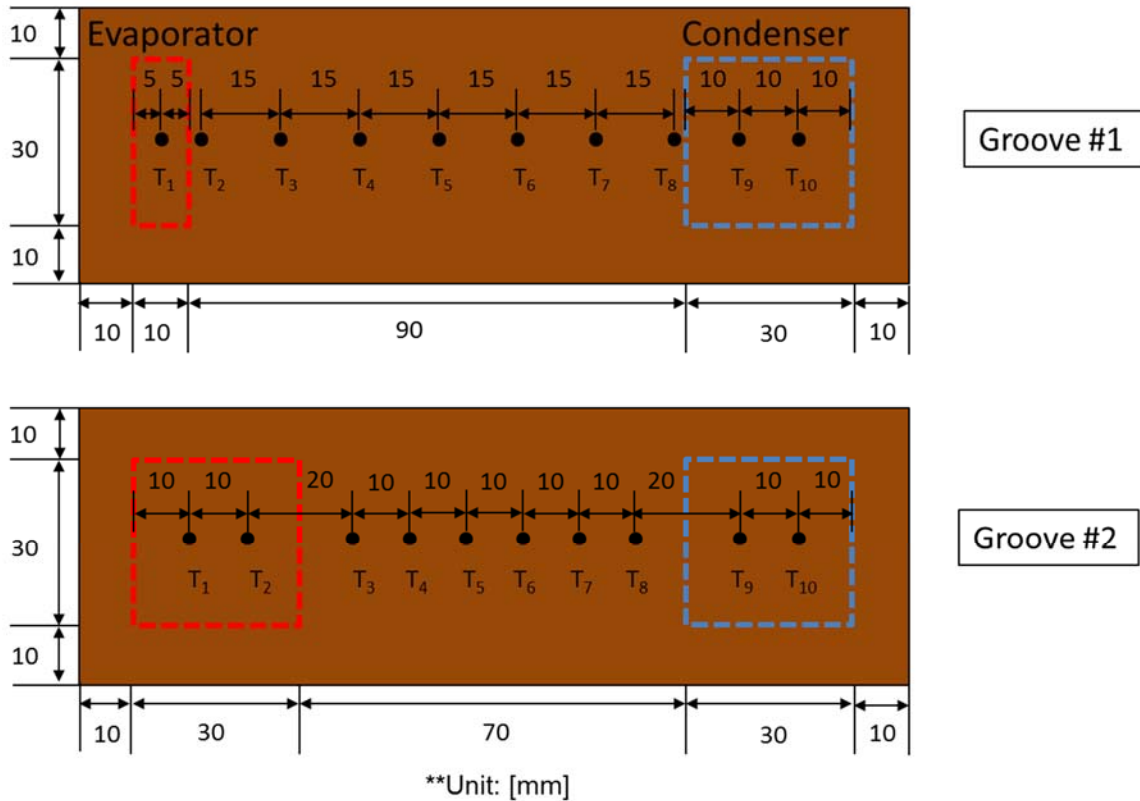
Figure 25: Thermocouple map for groove #1 (top) and groove #2 (bottom)

A schematic of the FHP apparatus is shown in Figure 26 for the first grooved wick. Heat was applied to the heat pipe via a copper block embedded with two 200 W cartridge heaters controlled by a direct current (DC) power supply. The wick plate was soldered to a copper heating stem and cooling block to ensure good thermal interfacing and consistency between experiments. The stem had a 3 cm x 1 cm cross section and was 3 cm long to allow the input power to be measured via Fourier's Law. Thermocouples were spaced at 1.5 cm along the stem with the top thermocouple adjacent to the plate. The cooling block was 3 cm x 3 cm and cooled by ice water

pumped by a peristaltic pump at 3.47 mL/s. The low flowrate allowed the inlet and outlet temperatures to differ enough to perform calorimetry. Another thermocouple was soldered into the steel frame to measure the vapor temperature. On the condenser end of the stainless steel frame, the charging tube was attached. A 1/8'' stainless steel charging tube connected to a needle valve and was soldered to the frame. A KF-flange vacuum fitting was attached to the other end of the valve to mate with the charging station described in the next section.
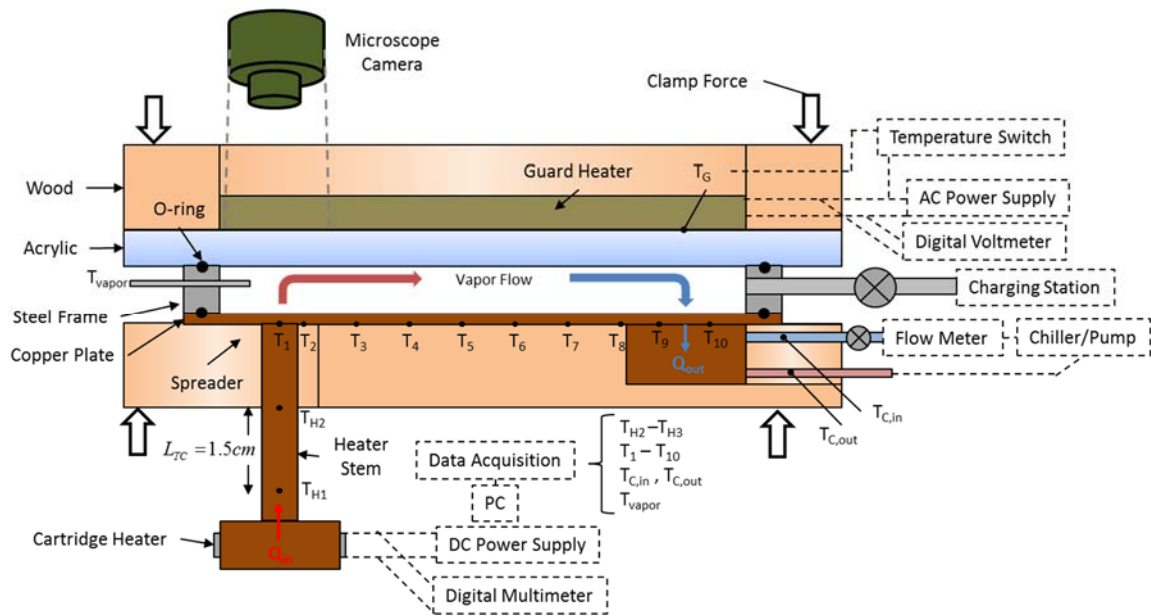
Figure 26: Schematic of flat heat pipe apparatus, heating stem configuration, and instrumentation for the first wick tested

The stainless steel frame was clamped between the viewing window, a top wooden pressure piece, and the grooved copper plate as shown in Figure 26. The wood piece assisted in spreading the force of the clamps to help uniformly distribute pressure along the O-rings. In order to prevent condensation on the viewing window, a heater block, variable alternate current (AC) power supply, and temperature controller were used as a guard heater to keep the window temperature and vapor temperature equal. A Scienscope CCD camera with stereo zoom optics was used to view inside of

the heat pipe. The heat pipe inclination angle was measured using a digital angle gauge with a resolution of ±0.1°.

A high accuracy Agilent 34401A 6½ digit multimeter was used to measure the voltage from the thermocouples with the assistance of an Omega thermocouple selector switch. The manual temperature measurement method was chosen over a modern data acquisition (DAQ) board to eliminate noise and errors in cold junction compensation (CJC), the primary source of error in temperature DAQ boards.

To measure the voltage of the thermocouple the two leads must be connected to the selector switch. This unavoidably creates two more junctions of dissimilar metals and generates additional voltage as shown in Figure 27.
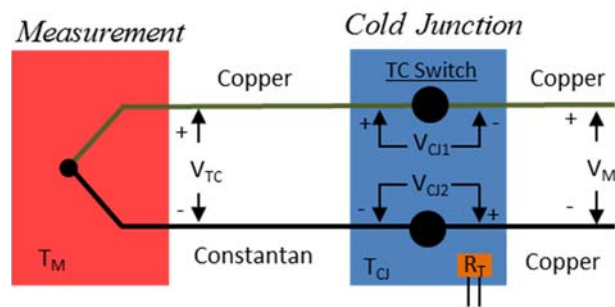
Figure 27: Additional voltage created when measuring thermocouple voltage with a thermocouple switch. A thermistor used to measure the temperature of the cold junction is shown in orange

The voltage read is then a combination of the thermocouple voltage at the point of measurement and the voltage across the reference or cold junction. Since the thermocouple voltage is sensitive to the temperature difference across both ends, the reference temperature must be known and isothermal. A thermocouple measurement system must be calibrated for a constant cold junction temperature. Maintaining a constant temperature at the cold junction is difficult. One way to simplify obtaining the measurement is to create and intermediate cold junction using an ice

bath [84]. The same metal is in contact with the switch connecter so that no additional voltage is generated (V_{CJ1} and V_{CJ2} are zero) as shown in Figure 28. The measured voltage is purely from the two thermocouples. Precise calibration tables for a zero degree cold junction developed by National Institute of Standards and Technology (NIST) are widely available [85].
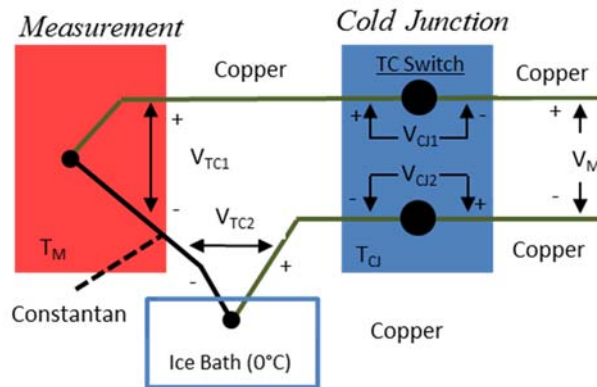
Figure 28: How to use an ice bath as a reference junction

Maintaining the cold junction at zero degrees was impractical for this application. The concept of Cold Junction Compensation was used to extract the true temperature by accounting for the non-zero voltage generated as the cold junction temperature varies [84]. The NIST calibration curve was formed at a 0°C cold junction temperature so the measured voltages with a different cold junction must be adjusted. The actual temperature of the thermocouple switch connection points was measured separately by a high accuracy Omega 10kΩ thermistor and Omega (CN16DPT-220) thermistor meter as shown in Figure 29. The voltage for the cold junction corresponding to what the thermocouple would measure was found from the NIST inverse calibration curve. This voltage was essentially what the system would have measured if the cold junction was at 0°C and measuring T_{CJ}. This voltage was added to the measured voltage if T_{CJ} was greater than the cold junction from the NIST calibration and vice versa.
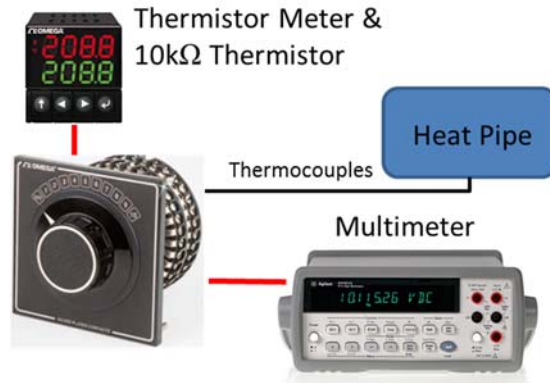
Figure 29: Thermocouple measurement system

The thermocouple switch was encased in a box with fiberglass insulation to create an isothermal environment for the switch leads.

<u>Uncertainty in Temperature Measurements</u>

Analysis of calibration and measurement uncertainty was performed based on the Root of Sum of Squares (RSS) method developed by Kline and Mclintock [86]. The NIST ITS-90 Type-T calibration curve was utilized for the thermocouple measurements [85]. The uncertainty in this calibration curve was ±0.03 °C. The NIST data was based on a 0 °C reference junction so the voltages read by the multimeter had to be adjusted based on the reference temperature of the thermocouple switch. The temperature of the thermocouple switch was measured using an Omega 10 kΩ thermistor and an Omega CN16DPT-220 temperature controller each with a ± 0.2 °C uncertainty. The Agilent multimeter had a reported uncertainty of ±0.0035% of the DC voltage readings. The Omega Type-T thermocouples had an inherent uncertainty of 0.5 °C. The uncertainty in the calibration curve, thermocouples, multimeter, and reference temperature measurement was combined using the RSS method to find the overall uncertainty in each temperature measurement. The total uncertainty of the temperature measurements was calculated

68

to be ±0.58 °C. The uncertainty in a temperature difference was calculated as the RSS of two individual temperature measurements, and was determined to be ± 0.81°C.

5.1.3 Charging the Working Fluid

For meaningful comparison between working fluids, a reliable and consistent method for charging the working fluid was required. For each test, the flat heat pipe needed to be vacuumed and charged with a consistent volume of fluid. The importance of degassing the working fluid is paramount for phase change devices. Release of unknown amounts NCG post-charge would decrease the performance of the flat heat pipe and obscure any performance enhancement of the different working fluids tested. Variations in charge volume can also add uncertainty into the heat pipe experiments. Flooding of the wick can significantly alter the local thermal resistances in different parts of the wick due to addition of a liquid film or block. The charge volume can also affect the dry-out limit. Pooling of liquid can change the effective length the working fluid has to travel to the evaporator which would increase the maximum power the heat pipe can handle.

Various charging techniques have been investigated by others and most consist of a system of valves, vacuum pumps, and degassing chambers [87-89]. Typically, the device was evacuated with a vacuum pump. The working fluid was stored in a chamber that was periodically vacuumed to remove NCG's. The valve between the chamber and heat pipe was then opened to fill the device.

The same charging station used by Yao [47] was used to charge the flat heat pipe in this work. A schematic of the station is shown below in Figure 30 and a list of parts in Table 10 . Two vacuum pumps were used in different sections of the system. Pump 1 (Alcatel) was used to de-gas the working and dry the vacuum lines from previous charges. The second pump (Varian) was used to evacuate the heat pipe before it was filled with the working fluid. The working fluid was stored

and de-gassed in a glass chamber which was stirred with a magnetic stirrer. The chamber was

vacuumed with Pump 1 intermittently, through valves #1, #2, and #4, until the gas bubbles were

no longer visible.
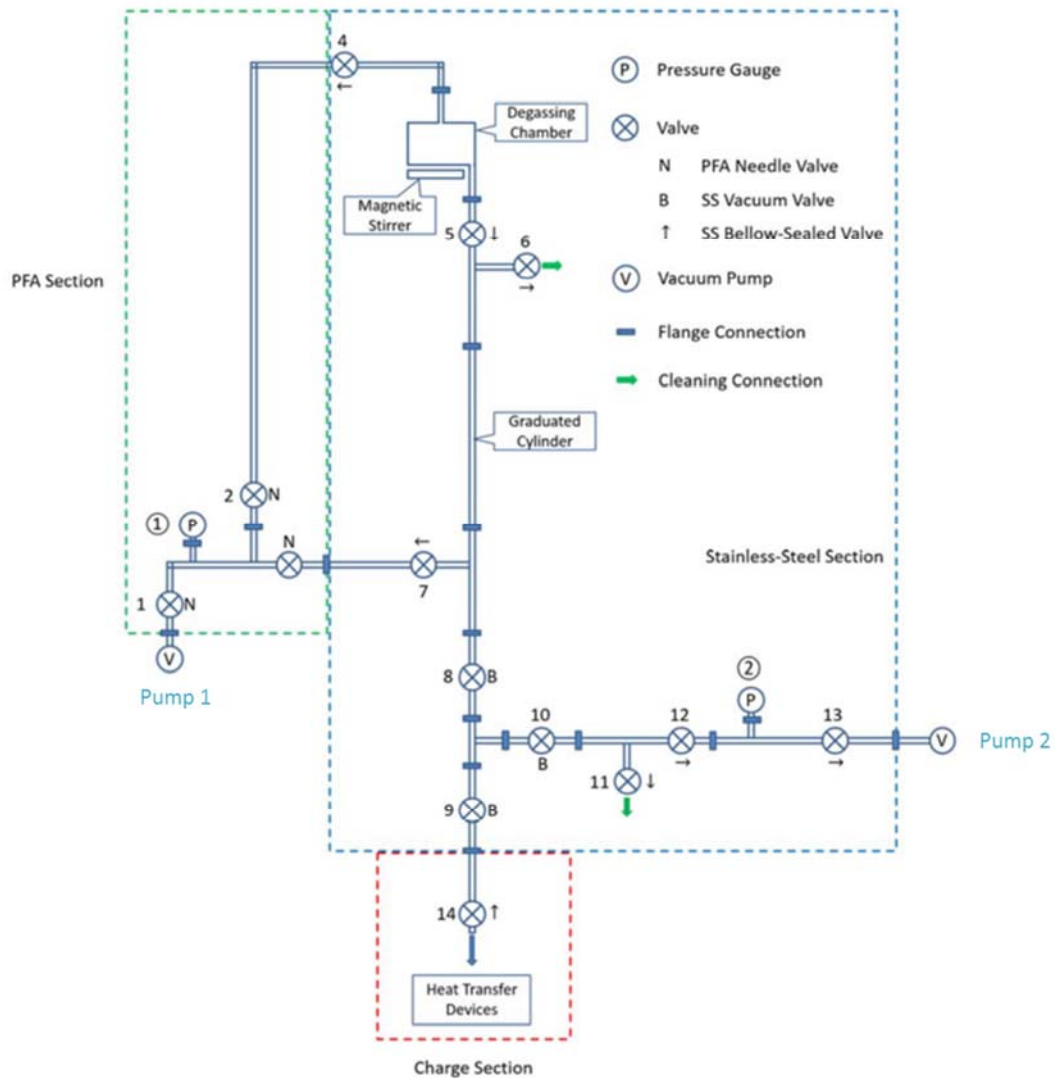
Figure 30: Charging station schematic [47]

The working fluid was left under vacuum overnight, and then the chamber was evacuated

one more time before charging to remove any residual gas. Pump 2 was used to evacuated the heat

pipe and dry the vacuum lines through valves #5, #8, #9, #10, #12, #13, and #14. An Omega

vacuum pressure transducer was used to detect leaks. The transducer's 5 PSI range over 100 mV provided a high sensitivity to changes in pressure.

Once the pressure in the device and lines stabilized valve #10 and #14 (attached to heat pipe) were closed. Valve #5 was slowly opened and the line was filled with de-gassed working fluid and the level was noted on the transparent glass graduated cylinder. The graduated cylinder had a resolution of ±0.1mL. Valve #14 was finally opened and the working fluid began to fill the device. Valve #14 was closed when the desired amount was charged.

Table 10: Important parts of the charging station [47]

Category	Vendor	Part #	Description
Pressure Gauge	McMaster Carr	3840K8	Digital Vacuum Gauge, Polycarbonate Case, 29.9"Hg-0
	Omega	PX409-005AV	5 Psi High Accuracy Transducer, mV/V Output, Cable Connection
Valve	Swagelok	SS-6BK	Stainless Steel Bellows-Sealed Valve, Gasketed, PCTFE Stem Tip, 3/8 in. Swagelok Tube Fitting, SC-11 Cleaned
		SS-2H	Stainless Steel Bellows-Sealed Valve, Welded, SS Stem Tip, 1/8 in. Swagelok Tube Fitting
		PFA-4RPS6	PFA Needle Valve, 3/8 in. Swagelok Tube Fitting
	Ideal Vacuum	P103568	Ball Valve, Manual, ISO-KF Interface, NW-16 Vacuum Fittings, Stainless Steel
Vacuum Pump	Ideal Vacuum	P102308	Old Alcatel Adixen 2005SD Dual Stage Rotary Vane Vacuum Pump, Ultimate Total Pressure 2×10^{-3} mbar, Pump Speed $5.4 m^3/h$
		P102295	New Varian DS302 Dual Stage Rotary Vane Vacuum Pump, Ultimate Total Pressure 2×10^{-3} mbar, Pump Speed $11.6 m^3/h$

The charge volume was determined based on the volume of the grooves in the heat pipe wick. The volume of the large grooves in the first wick was 5.85 cm³. The heat pipe was charged with 7 mL which corresponds to a ~20% excess. This volume was chosen to be consistent with similar tests done by Amouzegar [45] as well as compensate for the possibility of liquid trapped in the corners of the frame and copper plate. The volume of the grooves in the second wick was

71

0.98 m. The heat pipe was charged with 2 mL, which corresponds to a 100% excess. Deciding to increase the excess was first due to the resolution of the graduated cylinder. The resolution of ±0.1mL is $\pm10\%$ of the groove volume. Increasing the charge reduced this to $\pm5\%$. The excess fluid was also meant to counter the reduction in overall chemical mass contained in the working fluid by changing from the large grooves to the small grooves. As long as the charge volume was consistent for each charge, the expected decrease in thermal performance as a result of pooling of the liquid in the condenser was considered inconsequential with regard to comparison of different working fluids and observation of the chemical deposition in the evaporator.

5.1.4   Test Preparation and Procedure

In the preliminary tests, the plate was thermally connected to the heater stem and condenser block with thermal grease and pressure from the clamps that compress the O-rings. Inconsistency with the thermal contact necessitated a new strategy. To overcome this obstacle, the grooved plates were soldered to the heater stem and condenser block. The same grooved plates were used for every test by thoroughly cleaning the grooves between tests (this was also far more cost-effective considering the large number of proposed tests). Ideally, a new grooved plate would be used for each test to avoid any effects of corrosion from the IAS fluids. This possibility was taken under consideration and an extra water test was repeated to examine this uncertainty. Though the grooves showed signs of corrosion, the performance was unchanged. Details are included in the Appendix.

The grooved copper plate was first cleaned with ethanol to remove any oil or vacuum grease that might have contaminated the sample during handling. The plate was then washed with a 6M solution of hydrochloric acid to remove any oxides and generate a clean copper surface. The surface was rinsed thoroughly with de-ionized water and air dried. Dow Corning vacuum grease

was applied to the O-ring and the steel block was clamped between the acrylic viewing plate and the copper grooves.

The FHP was vacuumed for two hours so that the materials could properly out-gas and all remaining liquid had been evaporated due to the low pressure. The seal in the FHP was tested by measuring the leak rate of the system before charging. The Omega pressure transducer in the charging station had a range of 0-5 PSI over 100 mV so that small leaks could be detected. An Agilent multimeter was used for precise microvolt readings. If the pressure reading did not change in 15 minutes the chamber was charged. Once the flat heat pipe was charged, the setup was inclined to the proper angle using a digital angle gauge.

The heater was adjusted to various heat fluxes based on the electrical resistance of the heater and measured voltage. The actual heat input was calculated from the temperature measurements on the heater stem. The heat input was kept constant until the flat heat pipe reached steady state. The heat pipe was considered to be steady if none of the temperatures changed by more than one degree Celsius in 15 minutes. During the test, the guard heater on the viewing window kept at the measured saturation temperature to prevent condensation. Condensation of even a few droplets was very problematic in preliminary testing due to the low total volume of fluid in the heat pipe. The input power was incrementally increased until dry-out of the evaporation region occurred. This performance failure was determined by several criteria. The microscope camera was used to view the grooves through the acrylic cover plate to determine dry-out. This condition also caused a sharp increase in the temperature difference between thermocouples on the plate. Thermal resistance was calculated from the input power and the average temperature difference of the evaporator and condenser. The temperature difference between thermocouple #1 and the average

of thermocouple #9 and #10 as seen in Figure 25 was used for the first wick. Dry-out of the wick was also identified by the presence of an inflection point in the thermal resistance of the heat pipe ($R = \Delta T / Q_{in}$).

5.2   Results and Discussion (Experimental Results for IAS 2 in Grooved Wick #1)

The experimental results for the first wick with the large grooves is presented in the next section. The repeatability of the experiment with water as a working fluid is first discussed. Two IAS fluids, #2.1 and #2.2, shown in Table 7, were tested. The details of the performance comparison, images of the coating deposition, and experimental uncertainty are also presented.

5.2.1   Preliminary Tests and Repeatability

The first experiments used water as a working fluid in order to obtain baseline data to compare with the performance of the advanced working fluids, as well as check for repeatability. The preparation and procedure detailed above was followed for each water test. An inclination angle of three degrees was chosen after some preliminary testing. The low capillarity of the large grooves required a low angle to be initially fully wetted. The thermal resistance values and temperature differences for all three runs are shown in Figure 31 and Figure 32.

A third order trend line was used to plot the data in Figure 31. The resistance value at each point along the lines were all within five percent each other demonstrating excellent repeatability. Details regarding the uncertainty analysis used for the error bars is discussed in Section 5.2.4. The values in Figure 32 for temperature difference appear even closer together.
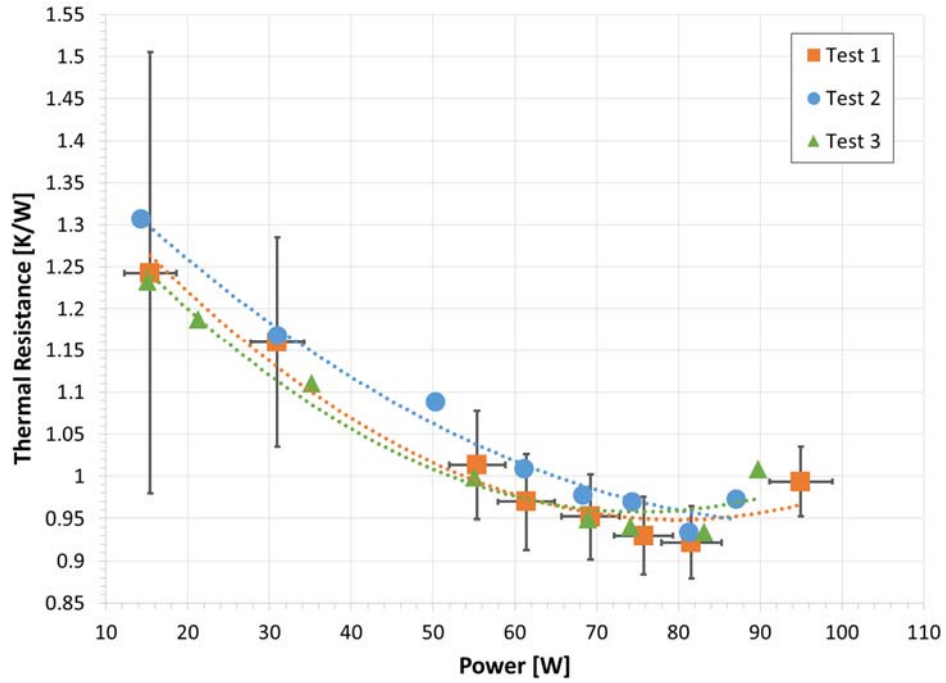
Figure 31: Overall flat heat pipe thermal resistance of grooved wick #1 for three different water tests to examine repeatability

Approved for public release: distribution is unlimited.
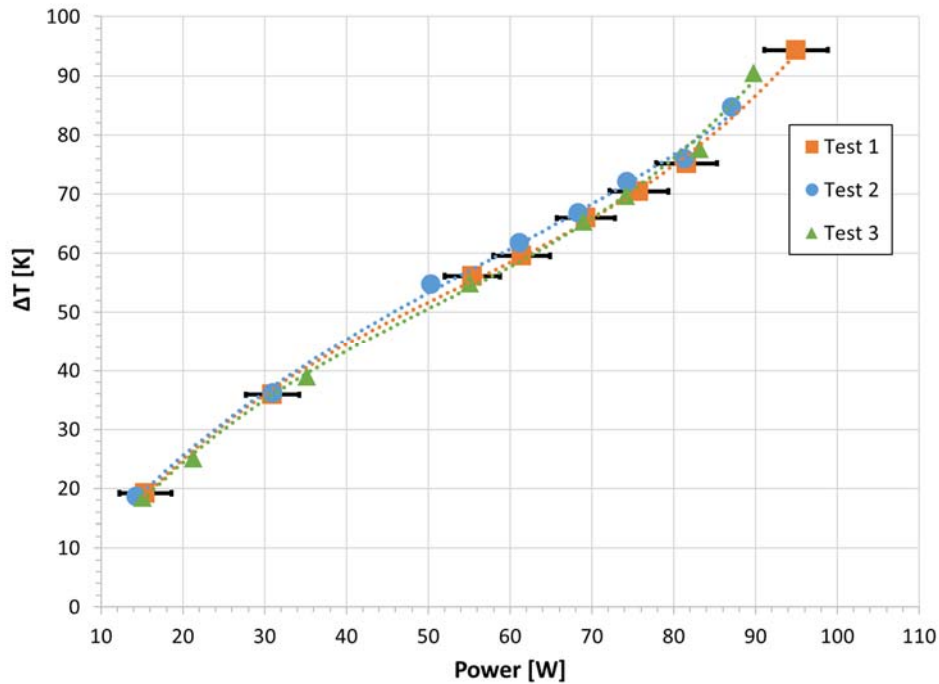
Figure 32: FHP test repeatability for temperature difference measurements

The resistance values are more scattered because the plotted values were calculated based on other measured data and not just temperature difference alone. The resistance measurement accrues the inherent uncertainty in the temperature difference measurement as well as the uncertainty in the input power measurement, systematically increasing the inherent total uncertainty. Even so, the flat heat pipe testing procedure was considered repeatable. A more detailed uncertainty analysis is described in Section 5.2.4.

As each test progressed the thermal resistance decreased steadily until approximately 85 W. The resistance values at powers at and above 85 W increased sharply and generally did not reach steady state as rapidly as at lower powers. This inflection point in the resistance measurements was identified as the point of dry-out. The evaporator section at the top of the grooves was also physically observed through the acrylic cover plate to be dry at these powers.

76

Though the inflection point occurred near 85 W, nucleation was observed in the range 60-80 W. Bubbles in the grooves expanded to the liquid-vapor interface intermittently. Below 80 W, the nucleation did not cause dry-out. Liquid was pushed from the groove by the bubbles but was able to re-wet the surface. However, the nucleation frequency eventually became large enough to eventually cause catastrophic dry-out. Nucleation is typically considered a cause of dry-out in a variety of wicks and referred to as the boiling limit [3]. However, several studies have shown that nucleation in grooved wicks does not constitute an operation limit and may even increase the performance of the heat pipe [90, 91]. Chen et al. [92] studied capillary and boiling limits in 200-500 μm square cooper grooves. A small 1 cm^2 heater area was utilized to create nucleation at very low heat fluxes but did not cause dry-out. In the current work, differences in heater area, tilt angle, and groove size, and wettability of the wick surface may have contributed to dry-out from nucleation.

5.2.2   IAS Fluid Performance

To investigate the effect of the designer fluid IAS 2.1 on the performance of a FHP, the fluid was tested at inclination angles of three, five, six, and seven degrees and the results are shown in Figure 33. For direct comparison, IAS 2.1 was first tested at an inclination angle of three degrees to compare thermal resistance and the point of dry-out with water. The thermal resistance was shifted down by approximately 0.25 K/W or 20%. Considering the 5% scatter in the three water tests, this was a significant improvement. At lower powers the changes are within the estimated uncertainty. However, it was clear the improvements were significant at power above 40 W.
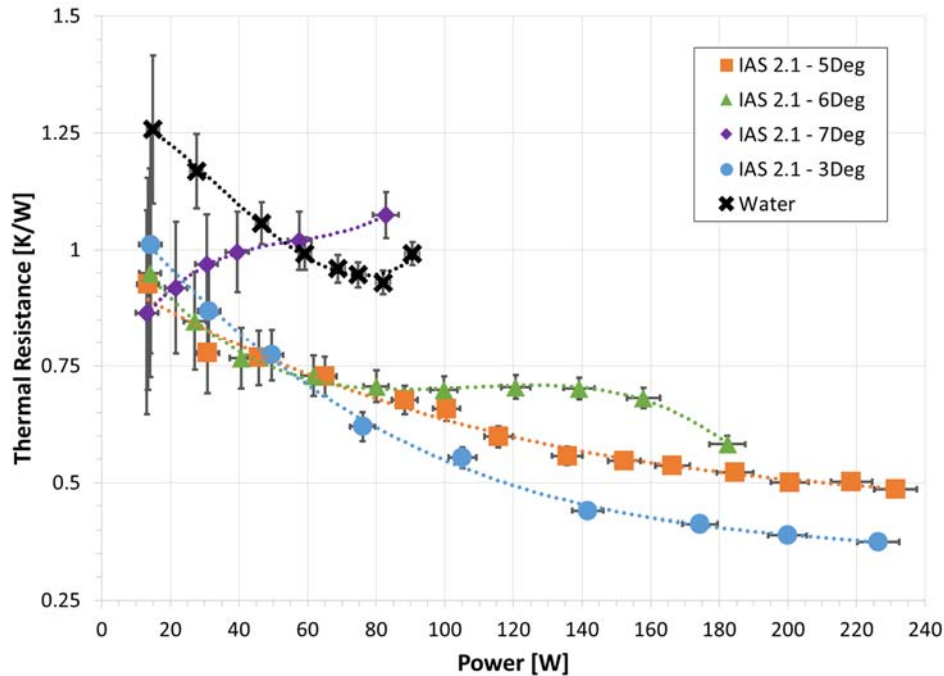
Figure 33: Performance dependency on inclination angle of IAS 2 in Grooved Wick #1

At a three-degree inclination and low power, the grooves were completely full of liquid regardless of the working fluid. Theoretically there should not have been any exposed coating, no additional wicking, and thus no additional evaporative surface area and decrease in thermal resistance. However, IAS deposits began to appear on the tops of the grooves as soon as the test was initiated. The early deposits were unexpected based on the early solubility analysis done by Yao et al. [55] in which coating generation was predicted at much higher temperatures. Initial deposits were a result of increases in local concentrations due to the strong advection along the grooves. Higher local concentrations decreased the temperature in which the solubility limits were reached. In addition, these deposits allowed liquid to be wicked out of the groove and evaporated. This phenomenon explained the decrease in resistance at low powers. A magnified image of the several grooves viewed from above, Figure 34, shows the deposits after 15 minutes at a power of

78

15 W. At this early stage of operation, the fluid was purple due to the permanganate ions that have yet to react with the copper surface.
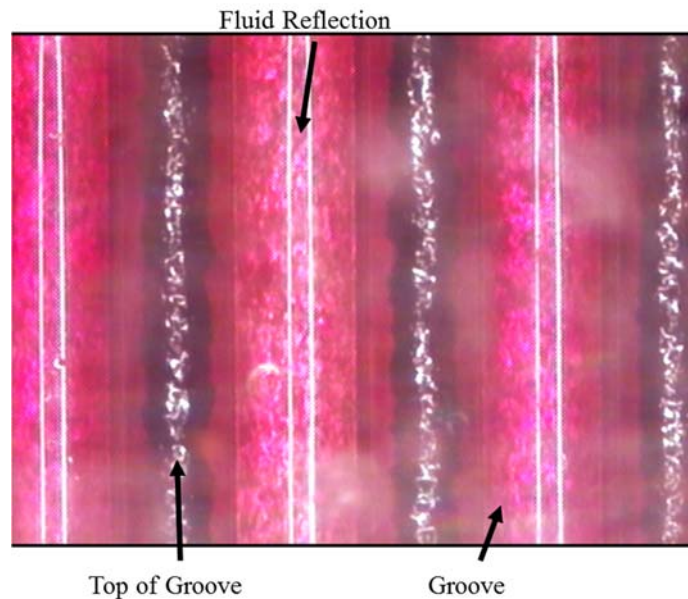
Figure 34: IAS 2.1 coating near the beginning of the test. The white lines are reflections of the light from the microscope optics due to the curved liquid/vapor interface.

As the power increased to 80 W and beyond, no inflection point, or dry-out, was observed. Nucleation began to occur around 60 W but the resistance continued to drop and eventually reached values lower than 0.4 K/W. The test was finally stopped at 230 W due to limits in the apparatus. Temperatures in the heater block reached the melting temperature of the solder. The test was stopped to avoid fundamentally changing the system for further testing.

The results at a five degree inclination angle in Figure 32 followed a similar trend. The thermal resistance exhibited a similar downward shift though the values were slightly higher at larger heat fluxes. Again, no dry-out was reached at this angle before the system temperature limits were reached.

79

At an inclination of six degrees, the grooves were not initially full. The bulk liquid in the groove receded about 1cm down the plate though smaller menisci filled the corners of the grooves. The trend in thermal resistance differed slightly from the lower angles. Around 85 W, the resistance curve flattens out at 0.7 K/W. This coincides with the dry-out point of water at an inclination of only three degrees. However, the thermal resistance is maintained and no inflection in resistance is observed. Even though the bulk liquid meniscus had receded slightly, the deposits continually wicked liquid up toward the evaporator. A picture of the grooves during operation is shown in Figure 35. The thick deposits on the top of the groove remained wet during the test as seen on the bottom right. Inside the groove, shown on the bottom left, the remaining liquid is spread out in a thin film over more coarse deposits. The different types and magnitudes of coating in each area of the grooves is an interesting effect that should be further investigated. The color of the fluid is also important to note. Its yellow color signified that most, if not all, the permanganate had fully reacted out of solution. The yellow/orange color was due to the remaining chromate ions in solution.
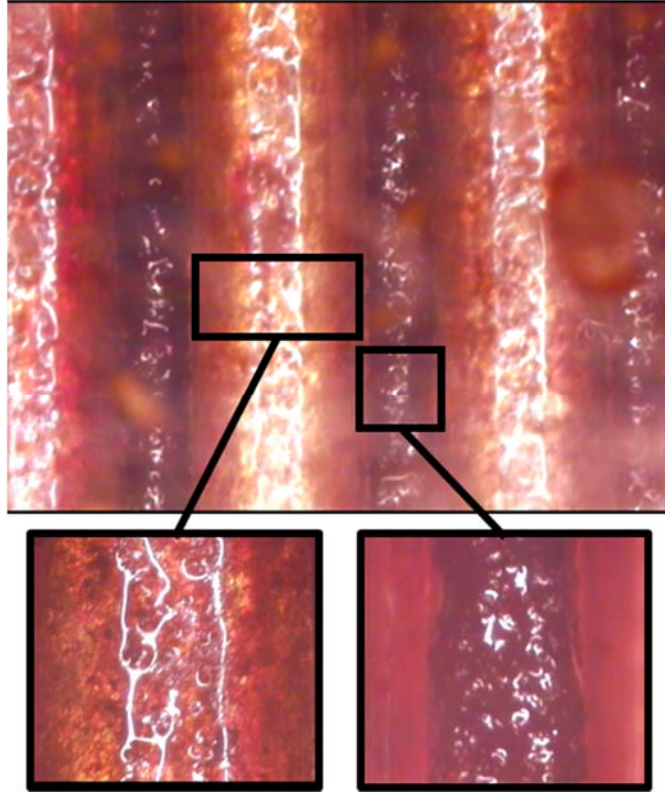
Figure 35: Heat pipe wick after boiling limit

At approximately 150 W, the resistance begins to decrease until the test was stopped due to reaching the system temperature limits. The drop in resistance was possibly due to different evaporative heat transfer coefficients for the grooves and the coating. If evaporation was more efficient from the coating, perhaps due to the larger area covered by thin liquid film, the thermal resistance would decrease as the bulk liquid receded and more coating was exposed. This of course is a hyporeport that must be tested in further experiments.

At an inclination angle of seven degrees, a limit in the previous performance trend of the IAS fluid was reached. At this angle the resistance began to increase immediately as the heat flux was increased. The initial thermal resistance was still lower than for water. The wetting ability of

the coating was enough to lower the initial thermal resistance but could not sustain a completely wetted surface.

At the end of each test, after the temperature limits of the set-up were reached, the power was switched off and the inclination angle was increased to keep the coating intact. The final dry coating is shown in Figure 36.
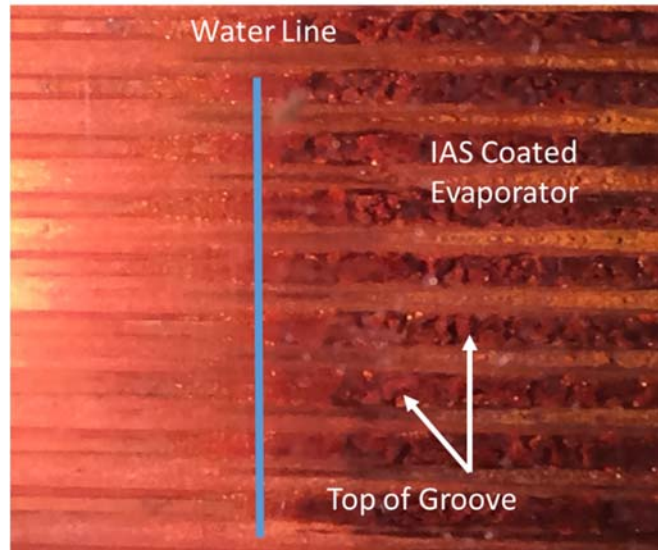
Figure 36: Surface augmentation resulting from designer working fluid

The plate was then imaged in a Hitachi S-4700 Scanning Electron Microscope (SEM). The top of the groove is shown in Figure 37. The structures are highly irregular and porous. However, these structures may not be representative of the coating during operation. The deposits in Figure 34 and Figure 35 were not dry and were covered by a continuous thin film.

Approved for public release: distribution is unlimited.
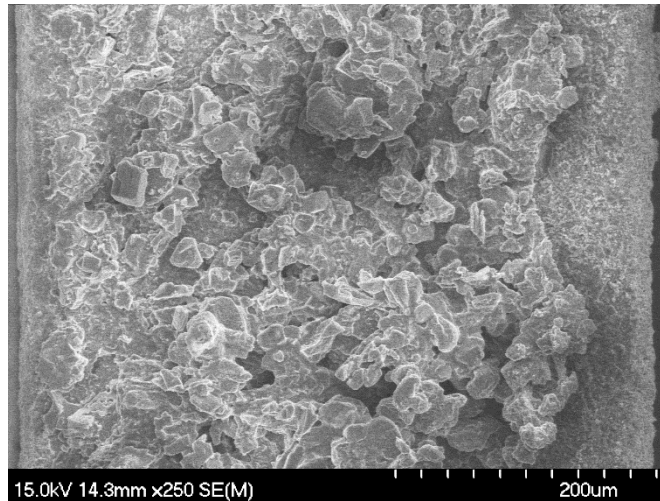
Figure 37: SEM of top of a single groove after the plate was completely dry

Without reaching the capillary limit in any of the tests with the designer fluid, a conclusion can't be made on the geometry or structure of the coating in a device that could reach this limit. The structures inside the groove clearly helped spread the liquid but it was unclear whether the coating on the top of the groove aided in capillarity or if it simply increased the evaporative surface area.

5.2.3   Effect of IAS Concentration

Though the system limits prevented observation of dry-out for the IAS 2.1 designer fluid, IAS 2.2, containing twice the concentration of IAS 2.1, was tested. IAS 2.2 was tested at six and seven degrees as shown in Figure 38 and Figure 39.
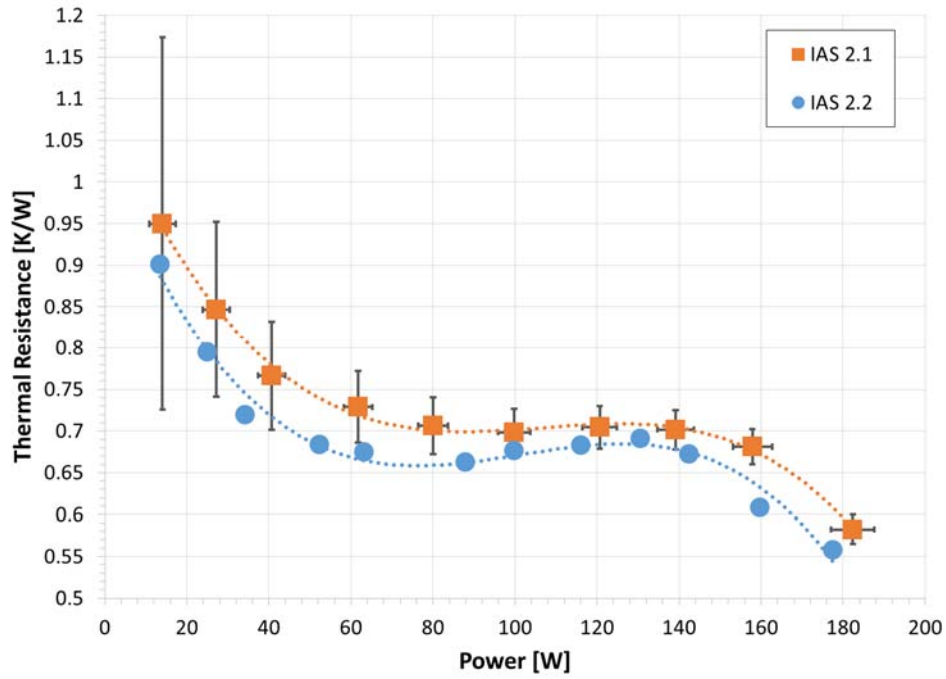
Figure 38: Effect of concentration of the designer fluid on thermal resistance at six degrees inclination
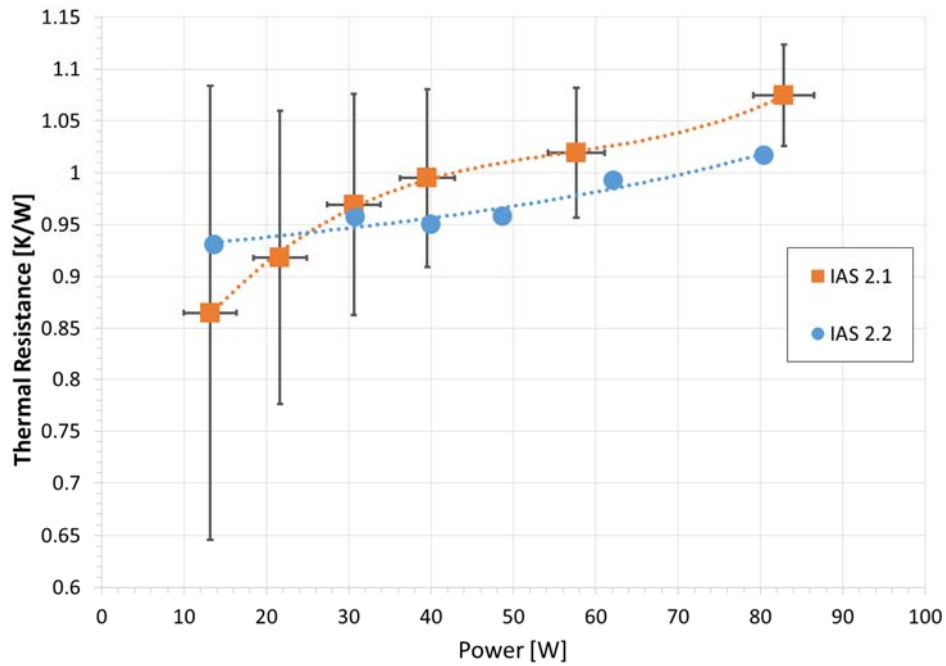
Figure 39: Effect of concentration of the designer fluid on thermal resistance at seven degrees inclination

84

Approved for public release: distribution is unlimited.

The results for IAS 2.2 at either inclination angle were very similar to that of IAS 2.1. The thermal resistances are lower at most heat fluxes but within 5%. This difference was not significant enough to confirm any performance enhancement.

5.2.4   Uncertainty Analysis

Uncertainty in the input heat flux was calculated with the RSS method propagated through Fourier's Law shown below,

$$\frac{\delta q_{in}}{q_{in}} = \left\{ \left(\frac{\delta k}{k} \right)^2 + \left(\frac{\delta A_s}{A_s} \right)^2 + \left(\frac{\delta \Delta T_s}{\Delta T_s} \right)^2 + \left(\frac{\delta x_s}{x_s} \right)^2 \right\}^{1/2}$$

(25)

The thermal conductivity of 110 copper alloy (391 W/m^2-K) was assumed to have a ±2% uncertainty. The uncertainty in the heat stem dimensions were estimated from the resolution of the digital callipers used for the measurements. The uncertainty of the distance between stem thermocouples, x_s, and stem cross sectional area, A_s, was assumed to be ±0.1 mm and ±0.01 mm^2 respectively. The uncertainty in the temperature difference was calculated to be ±0.81 °C. For the water tests, the maximum uncertainty in the input power was calculated to be ±3.8 W. At the first few input powers, 15-30W, this uncertainty was about ±10-20% of the input power. At larger powers the percentage uncertainty decreased to ±4%. The uncertainty in the input power for the IAS tests reached ±6.17 W due to the much larger values for input power. However, the percentage uncertainty was similar to water, ±10-20% at low powers and ±3% at higher powers.

The resistance uncertainty was calculated by combining the uncertainty in the input power and the temperature difference of the plate between thermocouple #1 and the average of thermocouples #9 and #10.

$$\frac{\delta R_{FHP}}{R_{FHP}} = \left\{ \left(\frac{\delta \Delta T_{FHP}}{\Delta T_{FHP}} \right)^2 + \left(\frac{\delta q_{in}}{q_{in}} \right)^2 \right\}^{1/2} \tag{26}$$

The maximum uncertainty was ±0.26 K/W at 15 W, slightly over 26%. The uncertainty decreased to 0.041 K/W at larger input powers lowering the uncertainty to ±4.5%. For IAS, the resistance uncertainty was ±.22 K/W (11%) at 15 W and below ±0.03 K/W (2.4%) at higher powers.

5.2.5   Discussion

The decrease in thermal resistance and increase in operational limit found when using the advanced working fluid are obvious advantages. In addition, the IAS enabled the flat heat pipe to maintain superior performance at larger angles of inclination. This feature is beneficial for applications that require the phase change devices to operate against gravity.

The surface coating increased the surface wetting and capillarity limit of the device by keeping the surface of the evaporator covered with liquid. The IAS fluids decreased the thermal resistance by approximately 30% and more than tripled the capillary limit. The surface structures created by the working fluid also allowed the heat pipe to operate at higher inclination angles. Interestingly, the bulk IAS in the groove seemed to recede close to when nucleation caused water to fail. Dry-out was postponed by wetting the surface with a thin film, not by maintaining a fully saturated groove.

Another interesting characteristic of the coating deposition was that it creeped up on top of the groove fin. As discussed in Section 3.1.2, grooves suffer from lack of evaporative surface area. The addition of evaporative surface area on top of the fin drastically reduced the overall thermal resistance. The creeping behaviour of permanganate, discussed in Section 4.5 might have been responsible though far more evidence was needed to make any conclusions.

86

The nucleation and absence of capillary limit also created difficulty in fully analyzing the IAS fluids. The grooves were simply too large and sensitive to gravity to find a perfect inclination angle to reach the capillary limit at reasonable temperatures and heat fluxes. Nucleation added uncertainty into how the designer fluid would perform in capillarity limited situation. The next set of experiments incorporated a wick geometry that allowed the capillary limit to be reached in order to more fully understand how the designer fluids perform.

5.3   Results and Discussion (Experimental Results for IAS 3 with Grooved Wick #2)

The experimental results for the second wick with IAS 3 is presented in the next section. The repeatability of the experiment with water as a working fluid is first discussed and then the 3 series of IAS fluids, shown in Table 8, were tested. The details of the performance comparison, images of the coating deposition, and experimental uncertainty are also presented.

The flat heat pipe experiment was continued based the results obtained for the large grooves. Insight gained about the fluid concentration, uncertainty in the experimental data, and performance limits of the heat pipe were considered.

The boiling limit was reached before the capillary limit when the large grooves and testing conditions. In order to study the capillary limit and the effect of the designer fluids on this limit, several adjustments were made to the grooved wick and evaporator region. The size of the grooves was reduced to 500 μm x 500 μm in the second grooved plated described in Section 5.1.1. These dimensions were chosen to allow them to be milled and reduce cost. The thickness of the plate below the grooves was reduced to 1 mm to decrease axial conduction in the plate. The reduction in groove size significantly increased the boiling limit relative to the capillary limit. The smaller

groove, which provided a larger capillary force, allowed the heat pipe to be inclined at a higher angle. This helped find an inclination angle that had a reasonable capillary limit.

The evaporator area was also a factor in the performance limits. To decrease the heat flux, and thus the boiling limit, the evaporator area was increased to 3 cm x 3 cm. The thermocouples locations were also modified. An additional thermocouple was mounted under the evaporator. The adjustments made to the evaporator area and thermocouple placement are shown in Figure 25.

The heater stem was 2.5 cm x 1 cm for Wick #1, so another piece of copper was used to spread the heat over the entire evaporator for Wick #2. This piece of copper was 5 mm thick. To ensure a uniform flux over the entire evaporator, a simulation was conducted using SolidWorks Simulation. The heat flux was found to vary by less than 5% at 100 W. The updated apparatus is shown below in Figure 40.
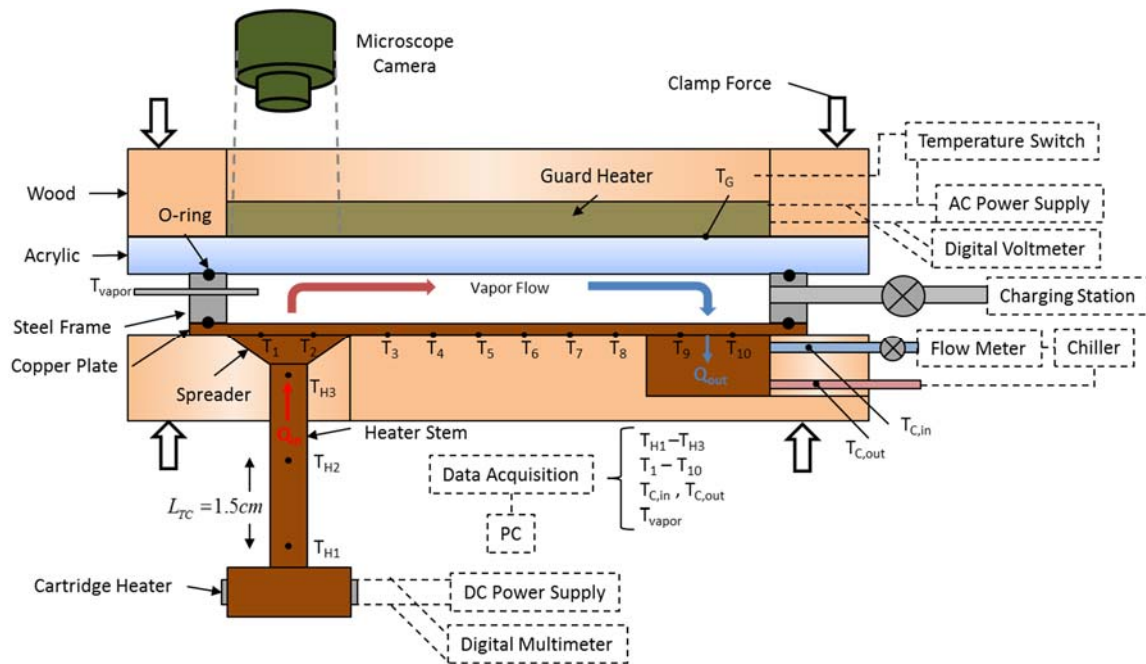
Figure 40: Flat heat pipe apparatus for the second grooved wick

Approved for public release: distribution is unlimited.

The coolant loop was replaced. A precision thermostat, Lauda Integral XT 150, was used to keep the condenser block inlet temperature constant. The chiller pumped silicon oil at 0 °C. Silicon oil preferred since it was capable of a true 0 °C temperature and a much lower specific heat. This allowed for a larger temperature difference between the inlet and outlet coolant temperatures, and better calorimetric accuracy. A precision needle valve and flow meter were used to monitor the flow rate, seen in Figure 41. The flow meter was an Omega flow meter with a narrow range of $0.2 - 2.0$ mL/min for better accuracy. The first set of tests showed that the previous volumetric flow rate of 3.47 mL/s was too low to adequately remove heat from the heat pipe. For the new heat pipe, flow rates of 750 mL/min and 1500 mL/min were utilized.
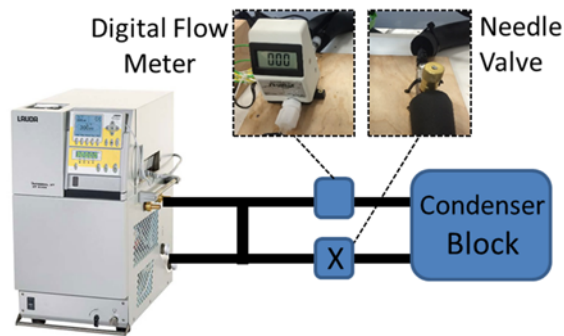
Figure 41: Updated cooling system for second wick
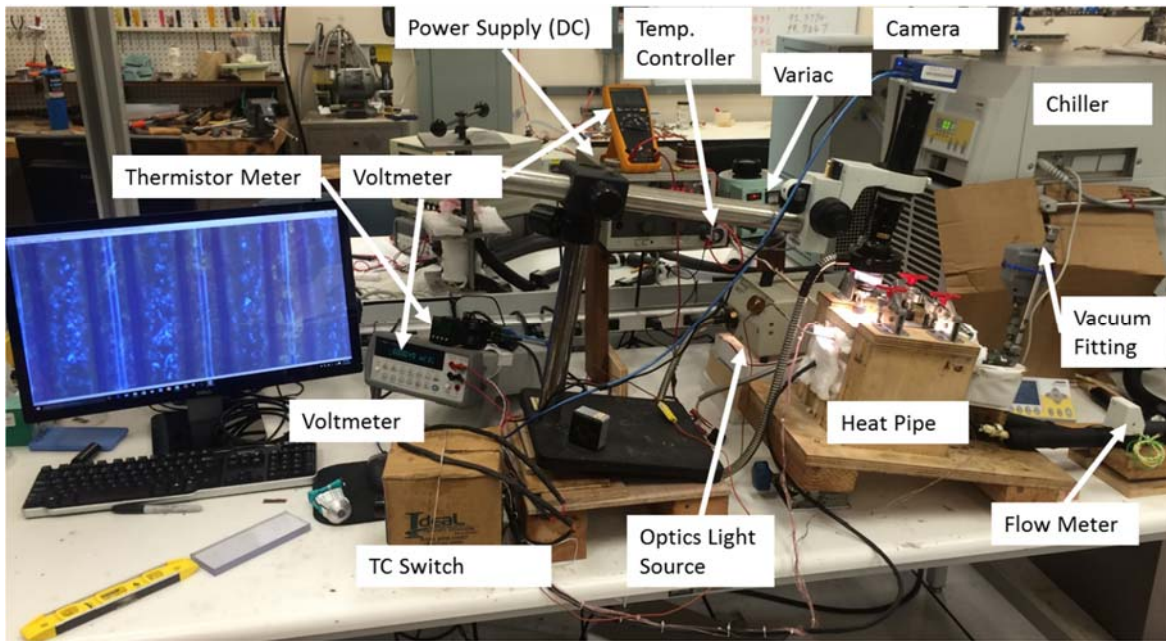
Figure 42: Physical Test setup

The physical experiment is shown in Figure 42 with the updated equipment. The preliminary testing method to check for repeatability is described in the next section.

5.3.1 Preliminary Tests and Repeatability

Preliminary tests with water were done to demonstrate repeatability and identify a inclination angle to use for the rest of the IAS testing. The flow rate for the first set of tests with the Lauda chiller used a flow rate of 750 mL/min. Water was tested at an inclination angle of 10°, 10.5°, and 11°. Two runs were completed for each angle. The resulting temperature, measured input power, and thermal resistance were averaged between two runs for each angle, shown in Figure 43. The estimated uncertainty was calculated as a weighted average. The maximum difference between two consecutive runs at the same angle was 0.0134 K/W, well within the estimated uncertainty for a single test.
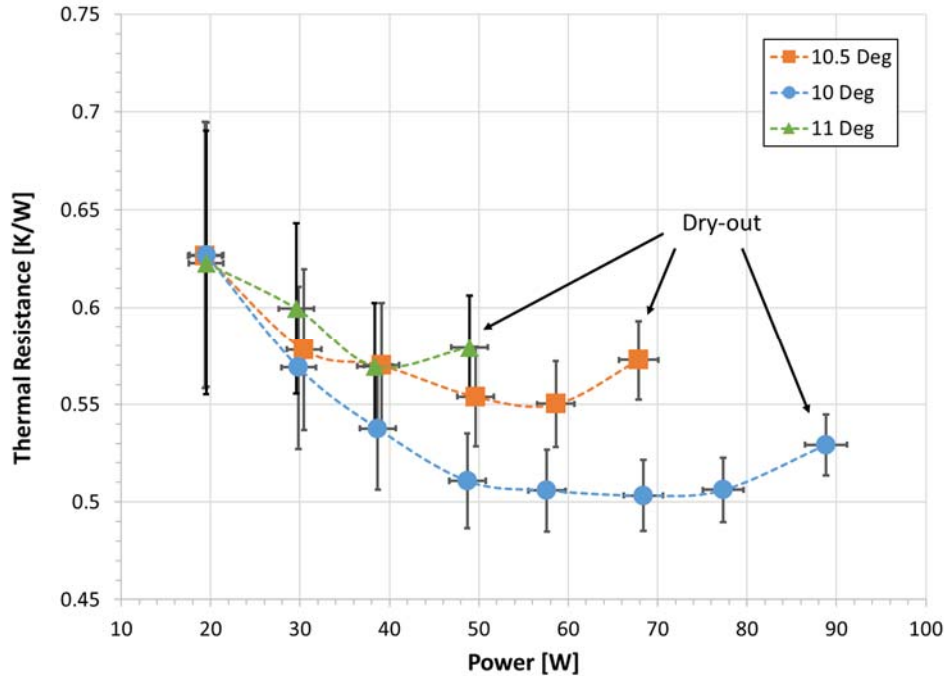
Figure 43: Averaged FHP results for Wick #2 with water at various angles

The overall trend for thermal resistance was to decrease as power increased, until the heat pipe reached the capillary limit. The heat pipe reached its maximum heat transport at a lower power at higher inclination angle due to the additional gravitational pressure drop. The point noted as dry-out in Figure 43 was not necessarily the actual dry-out point, considering the resolution of the input power was ~10 W. The actual capillary limit somewhere between the last two data points.

91
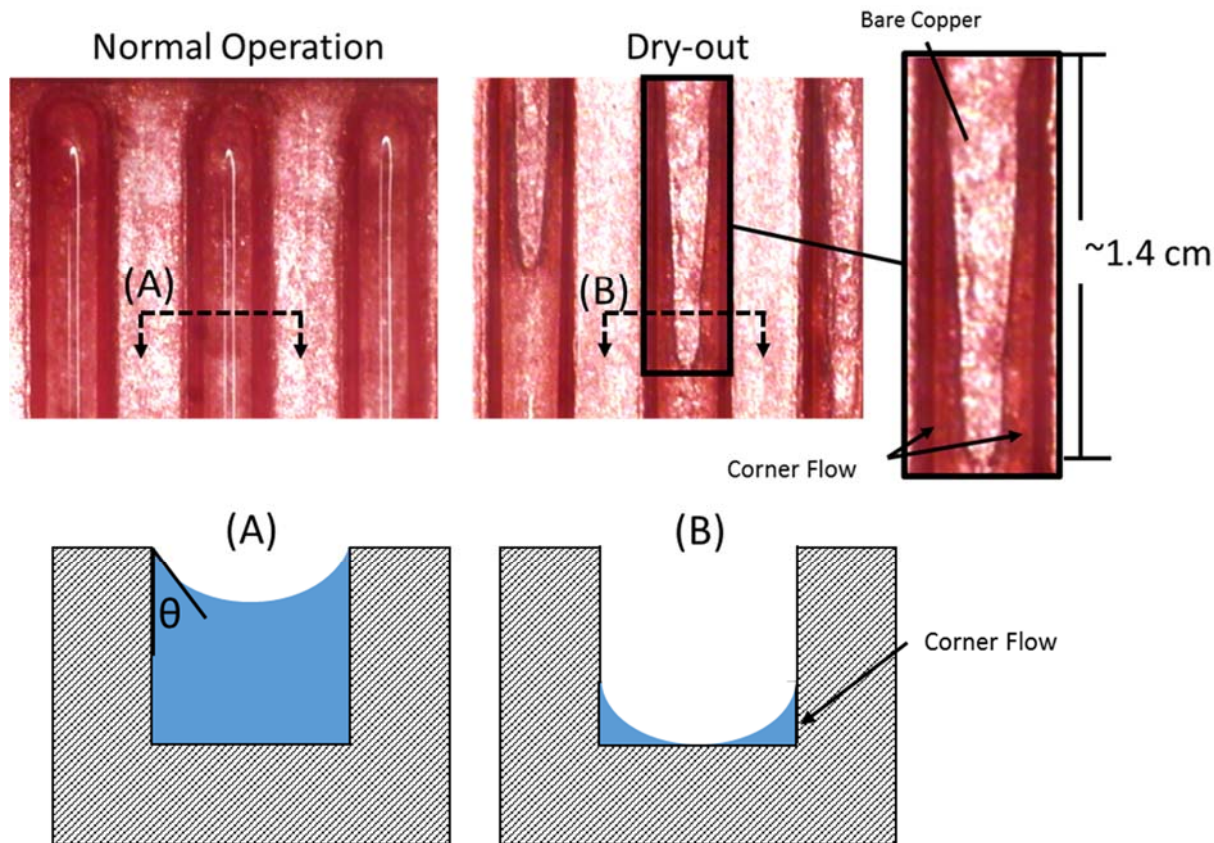
Figure 44: Meniscus shape in a groove during operation stages of the flat heat pipe (top), and schematics of the groove cross-section (bottom)

As the meniscus in the groove reached its minimum contact angle and curvature, the bulk liquid de-pinned from the top of the groove and receded. Liquid filled the corners of the groove forming two triangular grooves. This process has been referred to as "corner flow," and is the primary capillary mechanism behind micro-heat pipes [93]. Once the minimum contact angle in a saturated groove is reached, the curvature is further reduced by forming the minimum contact angle with the bottom of the groove. As the liquid flows in the triangular corner, the contact angle remains constant and the curvature varies with the height of the liquid meniscus. In the present work, the corner flow existed over a very short length.

92

5.3.2   Performance of Different IAS Concentrations

The preliminary water tests were successful as a baseline for repeatability. An inclination of 10.5° was chosen as the base angle for the IAS comparison tests. The flow rate in the condenser was increased to 1500 mL/min to reduce temperatures along the heat pipe and alleviate concerns about the structural integrity of some of the flat heat pipe materials such as the acrylic cover and O-ring. Water were repeated at an angle 10.5° and the new flow rate to confirm the water baseline. The thermal resistance values differed from the two tests at the previous flow rate only slightly. The maximum difference was 0.0134 K/W. The rest of the IAS tests used the 1500 mL/min flow rate.

Two tests were completed and averaged for each of the five concentrations of IAS. The thermal resistance results are shown in Figure 45. The thermal resistance of the IAS fluids seemed to shift to lower values for every power as the concentration increased. However, the uncertainty at the lower powers seem to overlap several of the concentrations. It was unclear whether the higher concentration fluids actually reduced the thermal resistance significantly more. At the higher input powers the trend was more clear. Differences in thermal resistance are outside of the estimated uncertainty. In addition, differences between tests with the same fluid differed by at most 0.02 K/W, significantly lower than the estimated uncertainty. Analyzing the data while considering the smaller variation between repeated tests, helped reach a conclusion about the trend in thermal resistance. Also, the differences in dry-out power extend far beyond the uncertainty of the input powers. The highest concentration IAS fluid was able to enhance the thermal performance by about 50% in input power and decrease the thermal resistance by approximately 30%.
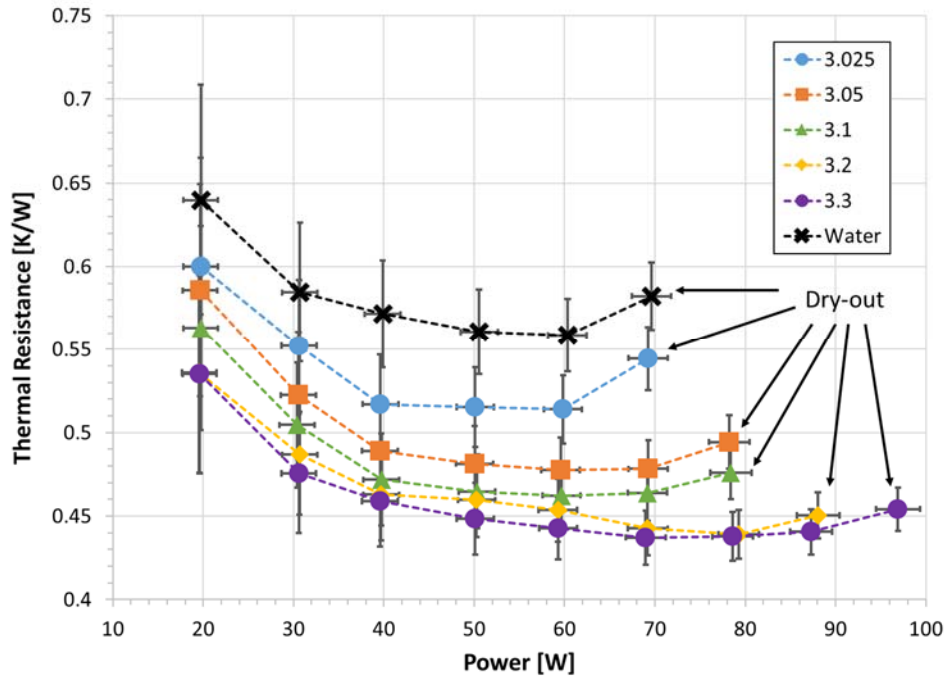
Figure 45: Performance comparison for different concentrations of IAS 3 in Wick #2

5.3.2.1 Coating Deposition

The coating deposition was observed for the different fluid concentrations. The same images were taken for every concentration for direct comparison. To capture the dry-out dynamics of the groove, the microscope camera was positioned at the very tip of the evaporator, looking down perpendicular at the plate through the acrylic plate. The first image labeled, "Initial Heating," was taken five minutes after the start of the test at a power of about 20W. The "Normal Operation" image was taken at steady state at approximately 40W. The "Groove Dry-out" image was captured once the bulk meniscus de-pinned and receded into the groove. Images of the IAS 3.025 deposits are shown in Figure 46

94
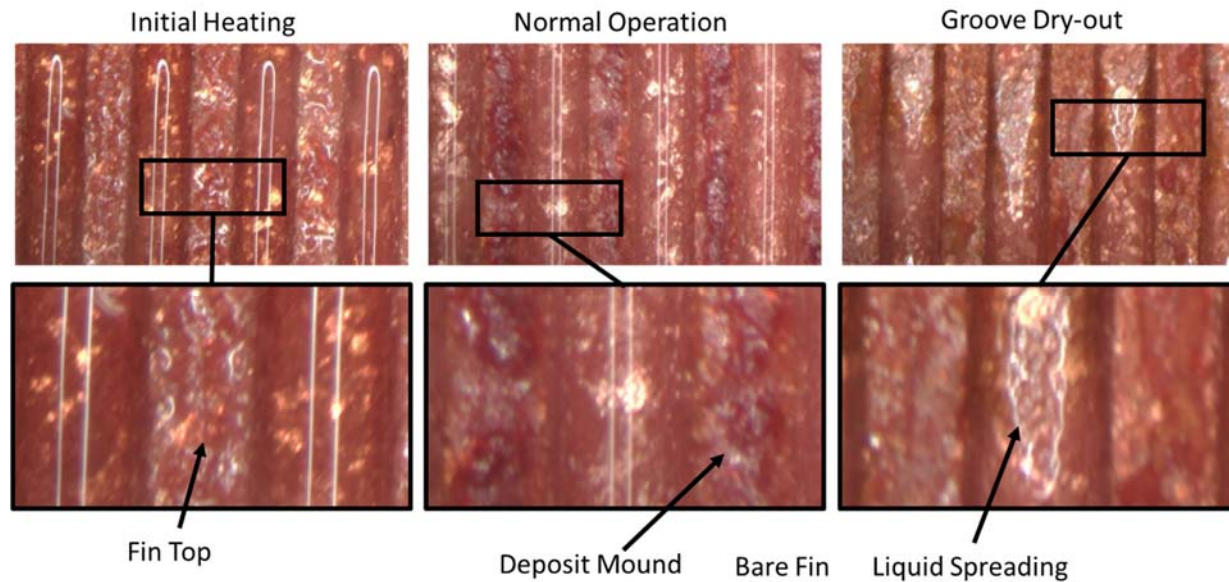
Figure 46: IAS 3.025 deposition on Wick #2

Immediately upon heating, deposits began to form on top of the groove fin. The deposits are much smaller in magnitude compared to the previous tests with the first grooved plate. Some of the fin top was still visible. The drop in thermal resistance was again attributed to the additional evaporative surface area on the top of the fin. When the heat pipe began to dry-out the fluid formed corner flow, just as water did. However, the liquid seemed to spread over the bare copper surface, where water had a clear dry-spot. However, the flat heat pipe failed in the same heat flux range as water. Any improvements in wetting were not enough to significantly postpone dry-out.

The coating deposits for IAS 3.05 is shown in Figure 47. Slightly more deposition was present on the fin top, though parts of the fin were still visible. As the bulk liquid receded from the groove, the liquid spread throughout instead of only filling the corners. Some small deposits were left at the bottom of the groove but there was a clear difference from the deposits on the fin top. It is important to note that the bulk meniscus de-pinned at the same input power for both water and IAS 3.05, though the resistance did not increase for IAS 3.05. The spreading of liquid in the bottom

95

of the groove maintained a wetted surface over the evaporator as pictured on the right of Figure 47. This secondary flow along the deposits prevented the sharp increase in thermal resistance due to the dry evaporator area seen with corner flow.
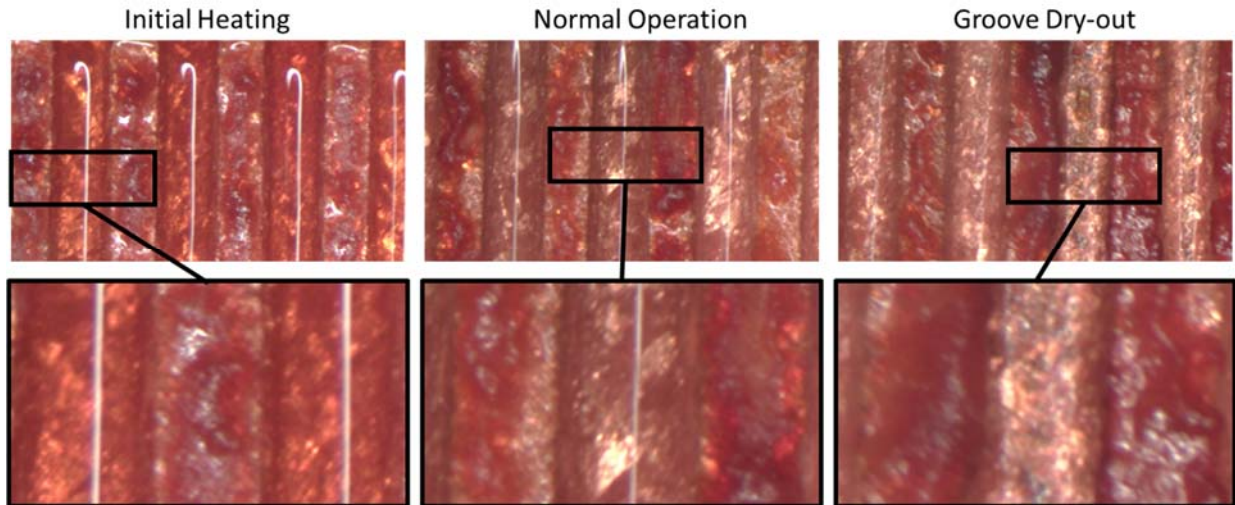
Figure 47: IAS 3.05 deposition on Wick #2

The same deposition process was increasingly apparent at the higher concentration of the base fluid IAS 31, shown in Figure 48. The fluid appeared much darker initially, and the deposits on the fin top were more uniform and covered almost the entire fin top. The additional decrease in thermal resistance at this concentration was most likely due to the additional coverage and thus evaporative surface area on the fin top. The change in fluid color was also telling. By the second power level, the fluid was nearly transparent. The reactions, and solubility related deposits occurred relatively quickly, removing the most of the chemical mass from the liquid. Without analyzing the final fluid sample no quantitative conclusion could be made about the remaining concentration. However, even minute concentrations, a few milligrams, for example, of the ions present in IAS, such as permanganate and chromate turn the liquid bright purple or yellow respectively.
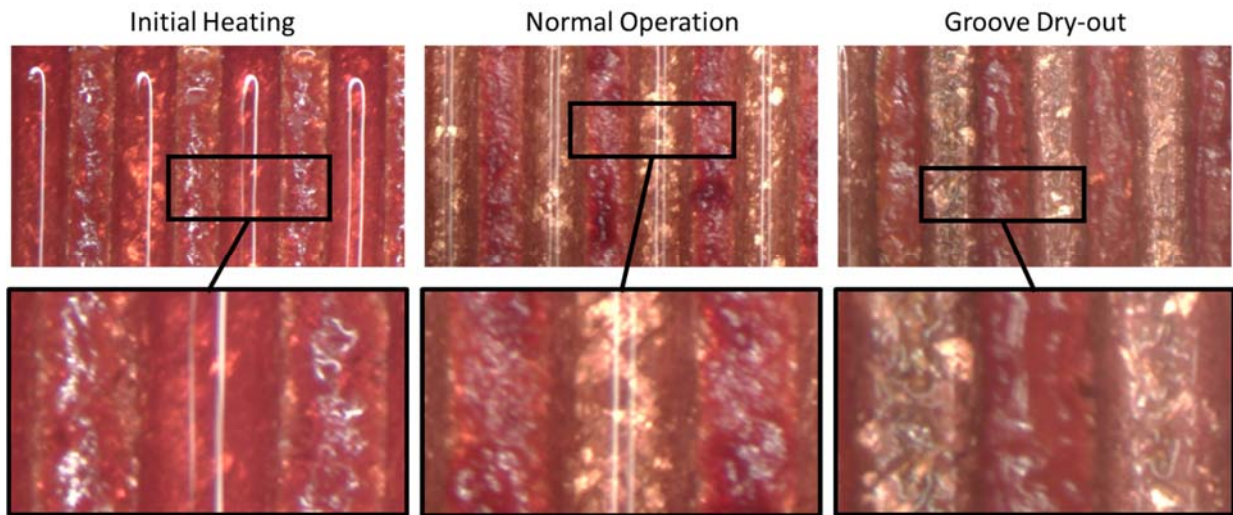
Figure 48: IAS 3.1 deposition on Wick #2

The coating on the film top continued to increase in thickness and coverage for the IAS 3.2 fluid, pictured in Figure 49. The fluid still became transparent and more noticeable deposits were left on the groove interior. The coating on the fin top resembled a super-saturated media in the form of a slurry, as opposed to a solid porous structure. The deposits on the bottom of the groove by contrast resembled mounds that created a 2-D surface roughness that created liquid menisci between features. The final dry-out point of the heat pipe was further extended due to the additional deposits inside the groove.
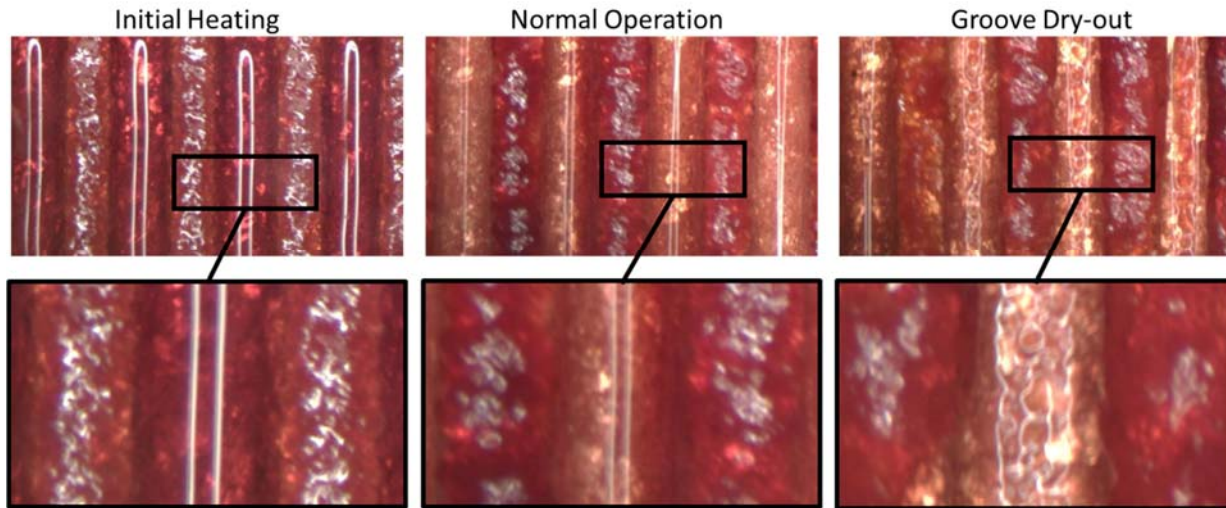
Figure 49: IAS 3.2 deposition on Wick #2

The deposits of the most concentrated fluid tested, IAS 3.3, are shown in Figure 50. The fluid was very dark red color initially. At 40 W, shown in the middle images, the fluid was not observed to be transparent as it was for the other concentrations. The increase in concentration required a longer time interval (~1hr) to react with the copper surface or deposit enough chemical mass to achieve the same optical transparency seen in the other fluids at this point. The thickness of the coating on the fin top was comparable in size to the groove itself. The deposits protruded out over the groove, seen on the right of Figure 50. The magnitude of the deposits on the interior of the groove also increased. The enhanced liquid spreading was apparent and allowed the liquid to travel a longer distance along the groove after the bulk fluid receded.
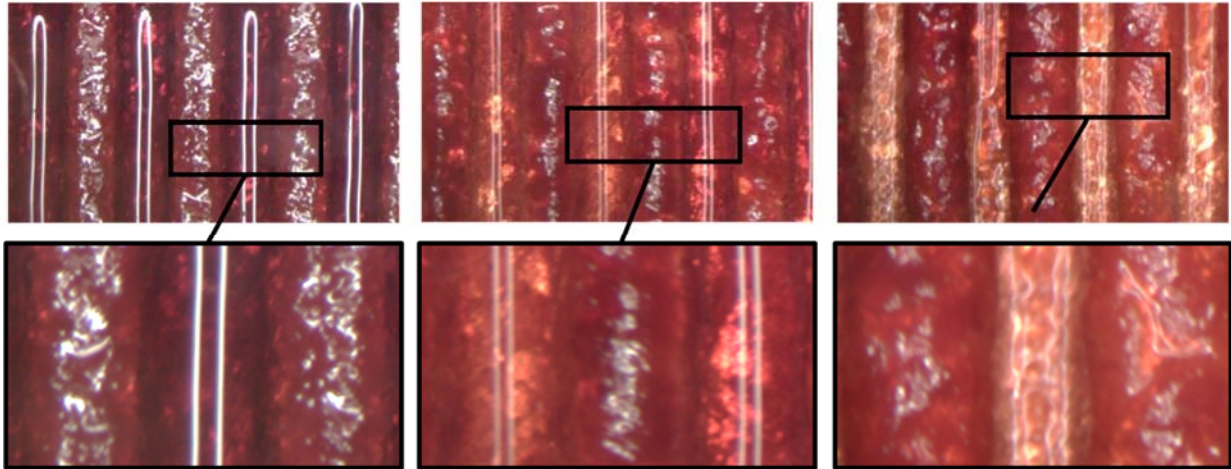
Figure 50: IAS 3.3 deposition on Wick #2

5.3.2.2   Discussion

Overall, the IAS fluids exhibited similarities in deposition and followed a basic trend as the concentration was increased. Observations summarizing the IAS deposition in the flat heat pipe experiments are listed below.

1. The deposits formed immediately upon heating.

2. The majority of the coating formed on the top of the groove fin due creeping of the deposits, extending the evaporative surface area of the wick and lowering the overall thermal resistance of the heat pipe

3. The fluid became transparent within the first hour of testing for all concentrations signaling the deposition of most of the chemical constituents in the fluid.

4. The bulk meniscus de-pinned and receded in the groove in the same input power range as water.

5. Deposits left in the interior of the groove enhanced liquid spreading and maintained a wetted evaporator, postponing dry-out.

The benefit of the coating on the top of the fin is best explained by returning the groove example in Chapter 2. A similar illustration of the heat flow path for IAS is shown in Figure 51. The addition of the coating on top of the fin was represented as a simple conduction thermal resistance in parallel with the thin film thermal resistance. Regardless of the thickness or thermal conductivity, adding a resistance in parallel always reduces the overall thermal resistance. This is especially effective for grooves due to conjugate problem.
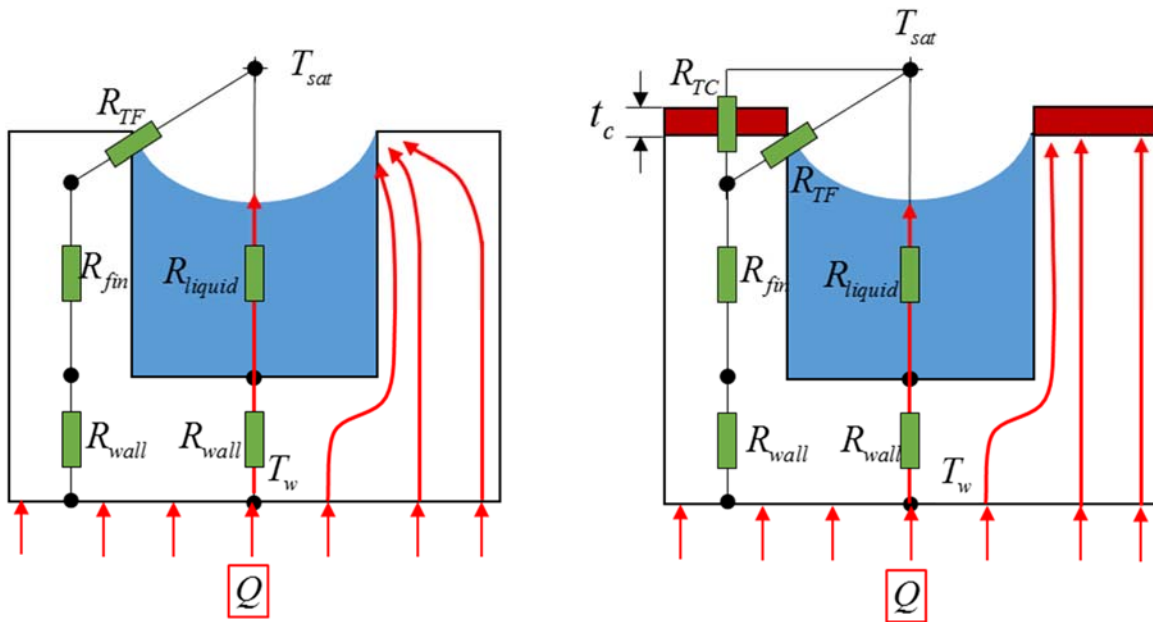
Figure 51: Illustration of the heat flow path for water (left) and IAS (right) in a single groove cross-section

Though the addition of a parallel path reduced the thermal resistance achieved by water, a thicker coating should have created a larger thermal resistance compared to a coating with a lower thickness. One would expect the fluids with higher concentrations and thicker deposits on the fin top to have a larger thermal resistance than the lower concentration fluids, even if it was lower still and improvement over water. This contradiction is explored further in Section 5.3.4.
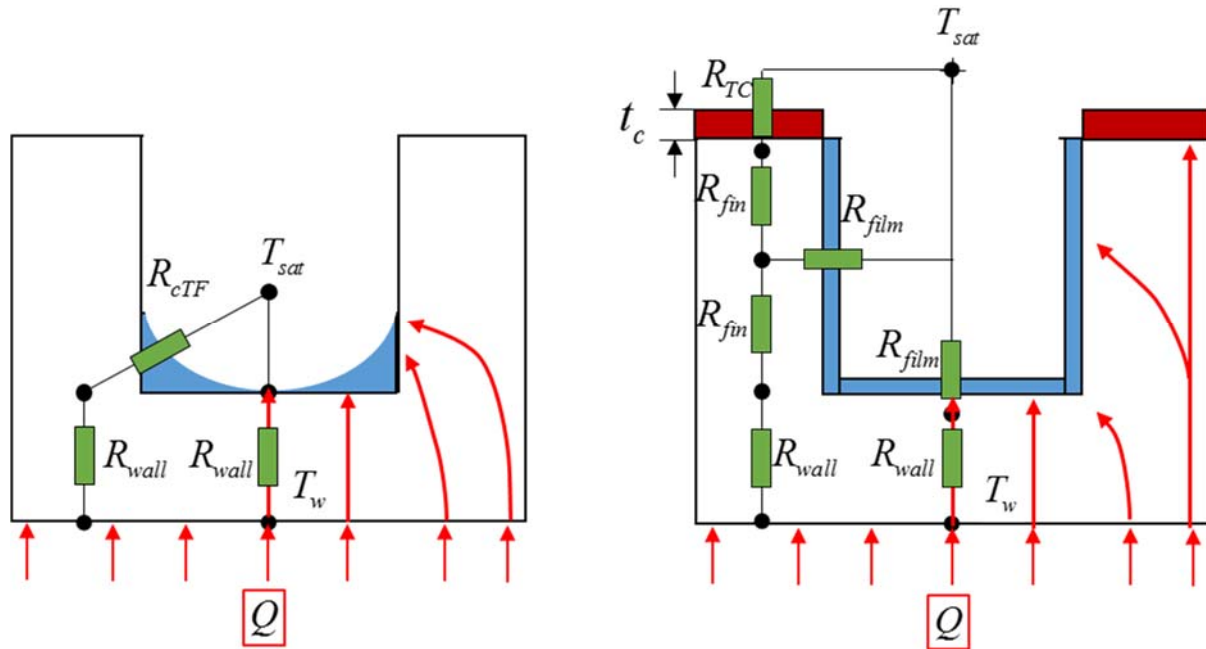
Figure 52: Illustration of the heat flow path for water (left) and IAS (right) in a single groove cross-section after the bulk meniscus has receded

During bulk meniscus recession the advantages of enhanced liquid distribution are more obvious. A representation of the heat flow paths is shown in Figure 52. For water, the formation of corner flows reduces the overall thermal resistance by removing the large conductive resistance of the bulk liquid. However, the majority of the groove is bare. With IAS the situation can still be improved through increases in evaporative surface area. The liquid spread on the interior of the groove allows for evaporation along the entire surface of the groove. The actual thermal resistances are of course dependent on the thickness of the liquid film as well as the unknown thermal conductivity of the deposits on the top of the fin.

5.3.3 The Role of Permanganate

The following section discusses the results of the permanganate-only and chromate-only fluids. IAS 3.2 was chosen as the base concentration based on observations from the experiments

discussed above. IAS 3.2 had significant deposition on the grooved wick, decrease in thermal resistance and extension of dry-out. These tests were intended to be purely investigative. The purpose of this work was primarily to examine the deposition mechanisms of the complete IAS fluid. The thermal resistance measurements are plotted in Figure 53 with water and IAS 3.2 for comparison.
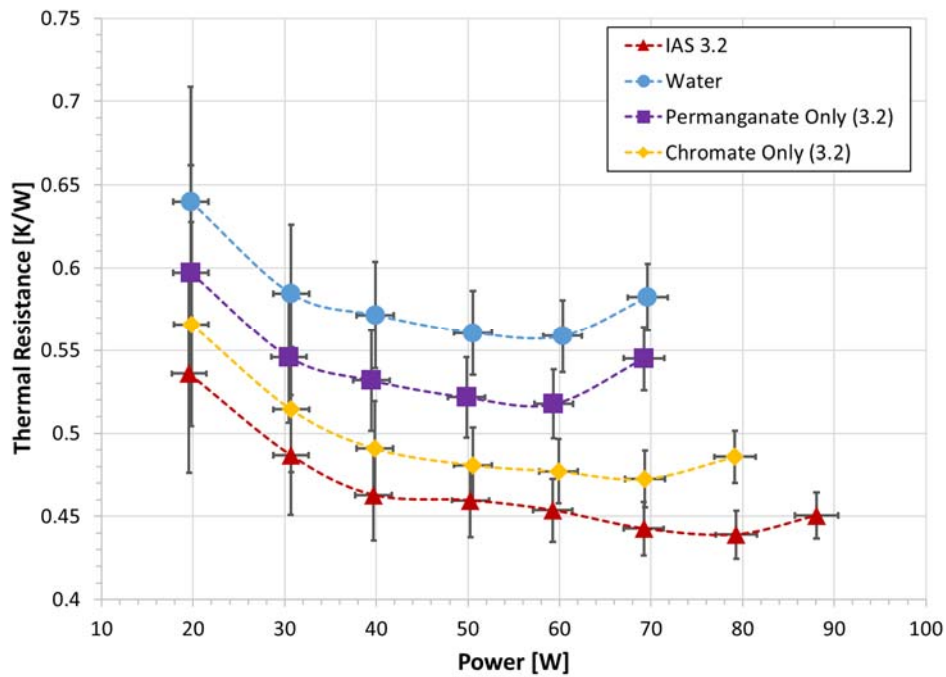
Figure 53: Performance comparison of different fluid components

The thermal resistance of the permanganate-only fluid slightly decreased thermal resistance compared to water and reached dry-out in the same range. The chromate-only fluid provided a larger decrease in thermal resistance and extended the dry-out to the next 10W input power range. Neither fluid achieved performance of the complete IAS 3.2 fluid in thermal resistance or dry-out extension. The small overall variation of thermal resistance between water and IAS 3.2 and uncertainty in the resistance measurements made a reliable conclusion about

thermal performance difficult. In addition, only one base concentration of the fluid was used to test the different constituent groups.

5.3.3.1   Coating Deposition

Similar images for the fluids in this section were captured. The deposition with the permanganate-only fluid is shown in Figure 54. The fluid appeared purple due to the permanganate in solution. Black deposits formed upon heating on the fin tops as with the complete IAS fluid. However, the deposits were very thin and sparse. As the input power was increased the deposits on the fin top were not able to sustain a wetted surface, which explained why the thermal resistance was not significantly decreased. Deposits left on the groove interior still enhanced liquid spreading, though dry-out was not extended.
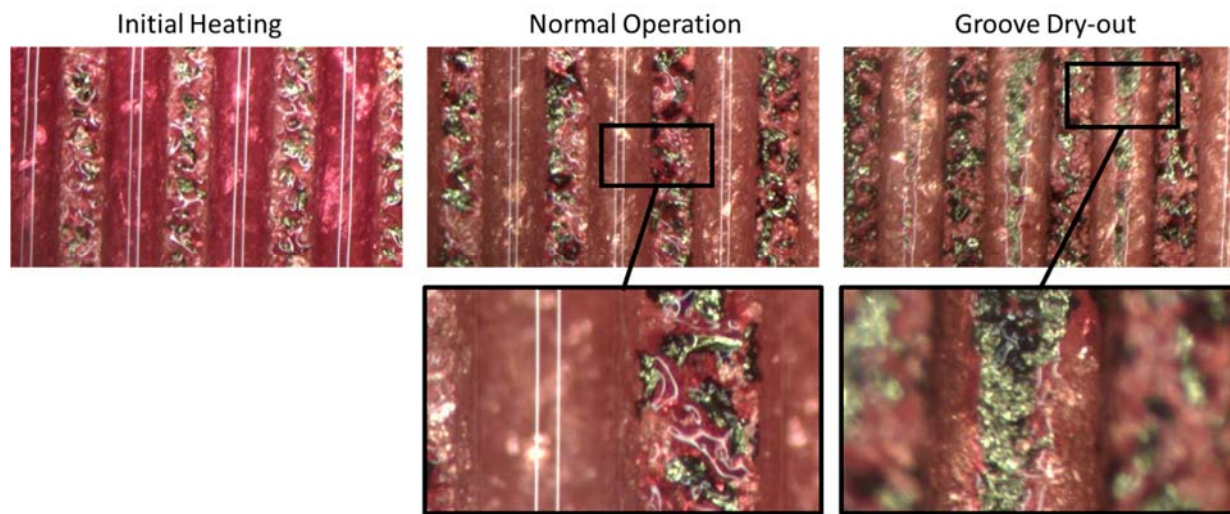
Figure 54: Permanganate-only deposition

The chromate-only fluid behaved much differently, shown in Figure 55. The fluid was yellow initially due to the chromates in solution. The coating thickness on the fin top was comparable to the complete fluid. It was clear that the majority of the deposition in the IAS fluid was comprised of chromate salts. Though the salts formed on top of the fin, the coating was not

103

uniform. The deposits were concentrated near the edge of the groove, forming distinct mounds, seen in the middle image of Figure 55. In some areas of the fin, bare copper surface was visible between the mounds. The chromate-only fluid seemed to lack the spreading capability of the permanganate-only fluid.
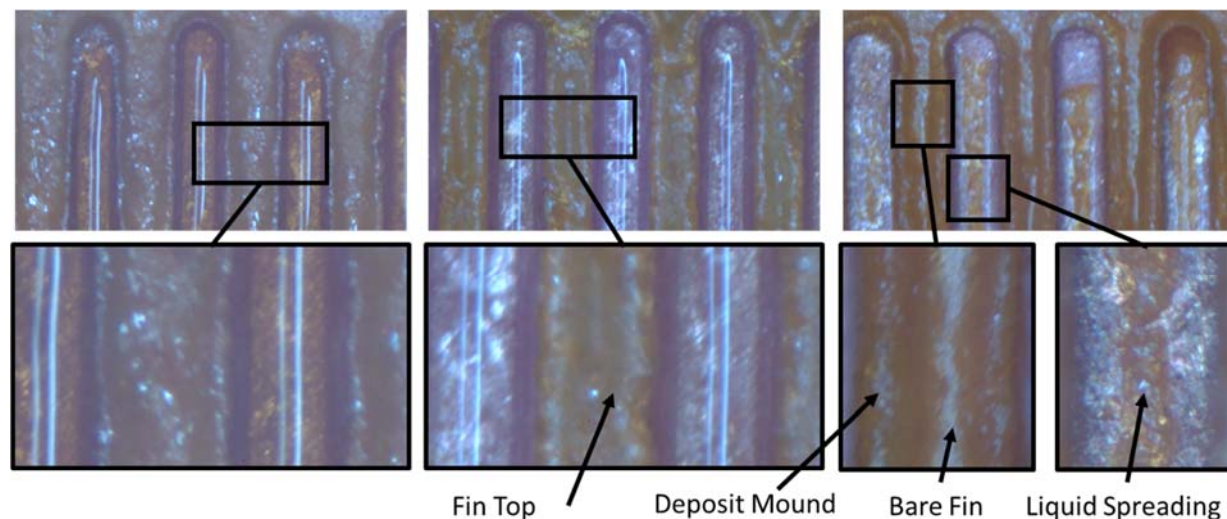
Figure 55: Chromate Only Deposits

5.3.3.2   Discussion

These observations were supported by the droplet investigations in Section 4.5. The magnified images of the droplet edge deposits are reproduced below in Figure 56. The creeping of liquid caused by the permanganate reaction with copper caused protruding branches of deposits. For the potassium chromate solution, a mound was created along the edge of the droplet and no liquid spreading was observed.
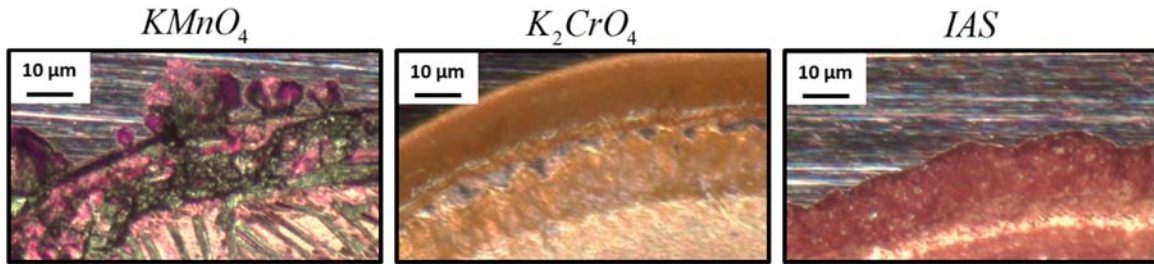
Figure 56: Magnified images of the droplet edge for different fluid constituents from Section 4.5

Inclusion of permanganate in the flat heat pipe allowed the working fluid to creep over the entire fin. However, the result of the reaction did not leave deposits thick enough to remain wet. The mass of the deposits in the form of chromate salts provide the deposit volume and liquid transport capability to effectively lower the thermal resistance. In addition, the thicker deposits in the interior of the groove from the chromate salts were responsible for the enhanced liquid spreading and extension of dry-out limits.

Though much more testing is needed to conclude on the role of each constituent, observations from the droplet test and the heat pipe experiments demonstrated that a combination of the different constituent groups is necessary to maximize liquid spreading and thermal performance enhancement.

5.3.4 Coating Measurements

In this section, measurements of the coating geometry are presented and discussed. The goal of these measurements was to further investigate the effect of fluid concentration and coating geometry on thermal performance in the flat heat pipe as well as obtain some experimental closure for modeling in Chapter 5.

5.3.4.1 Coating Thickness
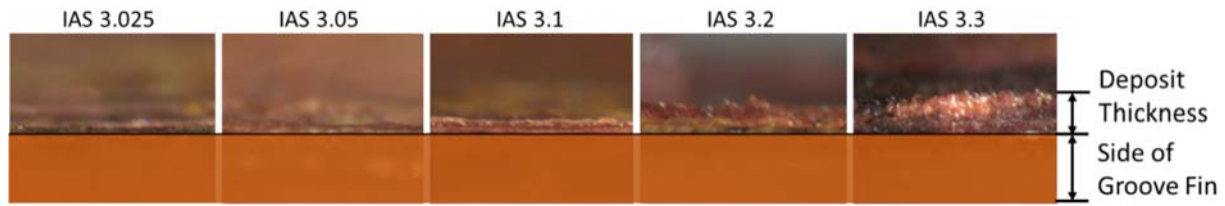
Figure 57: Side view of the coating thickness of the deposits on the top of the groove fin

A side view of the coating thicknesses for the different IAS fluids are shown in Figure 57. These images were taken at the tip of the evaporator. The thickness was measured using the MATLAB Image Tool. Ten measurements were taken and averaged. The reported uncertainty was the standard deviation of the data set. The thicknesses are tabulated in Table 11.

Table 11: Thickness of the coating on top of the groove fin

IAS Fluid	Fin Coating Thickness [μm]
3.025	33 ± 9
3.05	71 ± 16
3.1	141 ± 16
3.2	223 ± 12
3.3	302 ± 19

The coating thickness varied significantly even in the short length shown in Figure 57, creating large standard deviations. The coating reached a thickness of over 300 μm for the highest concentration, IAS 3.3. This thickness was comparable in size to the 500 μm groove.

5.3.4.2 Film Length at Dry-out

The images of the coating thickness and images taken during operation in Section 5.3.2.1 only showed the coating at the top of the evaporator. However, the coating was not uniform and varied in coverage along the evaporator. Images of the coating deposition in the evaporator are shown in Figure 58.
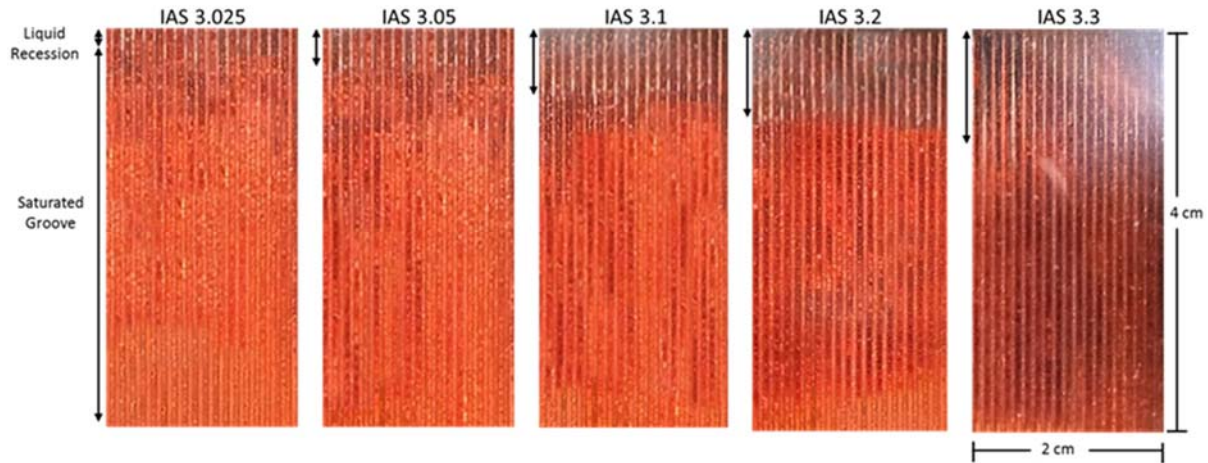
Figure 58: Deposit coverage and dry-out length for the different IAS concentrations (top)

The section of the wick shown is 4 cm long and 2cm wide. Though the heater block was only 3cm long, axial conduction in the plate caused evaporation in the first part of the adiabatic region. One side of the evaporator was cropped because the thermocouple used to measure the vapor temperature interfered with processing the images. The images were captured right before the dry-out point for each concentration, which was different for each fluid. At this point, the bulk meniscus had receded leaving the thin liquid film in the interior of the groove. The white lines at the top of the images are the reflections from this region. The length is marked by the black arrow next to the image of each plate. The same measurement and uncertainty procedure as the coating thickness data was used.

IAS 3.025, which was observed in corner flow, had a measured length close to that measured for the corner flow with water. The lengths of the film region for the other fluids increased well beyond corner flow. IAS 3.3 was able to sustain a wetted length almost ten times that of pure water.

107

5.3.4.3 Resistance Number

As mentioned in 5.3.2.2, the decrease of thermal resistance with increased concentration was a difficult trend to explain if only the thickness of the coating was considered. Two other parameters were defined and measured using the evaporator images in Figure 58. The rationale behind these two parameters was derived from studying the deposition pattern for each concentration and identifying possible effects of those pattern on thermal resistance. Two observations were prominent. The first and obvious observation was that the total coverage increased with concentration. Full cover of the evaporator would have a greater effect on thermal resistance. The second observation was mostly evident in lower concentrations where the coating was concentrated near the top of the heat pipe due to the strong advective flow. It was assumed that for the fin top to be wetted, the coating had to be adequately covered, and that beyond some effective length the grooves could be considered to perform the same as water (i.e. no coating exists).

The first parameter, the Total Fin Coverage (TFC), was simply the percentage of the fin tops covered with IAS deposits. The second parameter, the Effective Length Coverage (ELC), was defined as the maximum length along the heat pipe (starting in the evaporator), where more than 25% of the fin tops were covered with IAS deposits. While increasing the coating thickness would have a negative impact on the thermal resistance (larger conductive resistance), increasing the TFC and ELC would decrease the thermal resistance. These three parameters were combined into a "Resistance Number," defined below.

$$RN = \frac{t_c}{TFC \times ELC} \tag{27}$$

108

To measure the TFC and ELC, the evaporator images were converted to greyscale in an image processing program call ImageJ. A threshold was used to identify the IAS coating and convert the image to binary. The number of black pixels (IAS coating) was compared the number of pixels that represent to fin tops (half of the total) to determine the coverage percentage. This threshold was determined based on the IAS 3.3 fluid which, from observation had 100% coverage. The threshold that calculated 100% coverage for IAS 3.3 was used for the rest of the fluids.
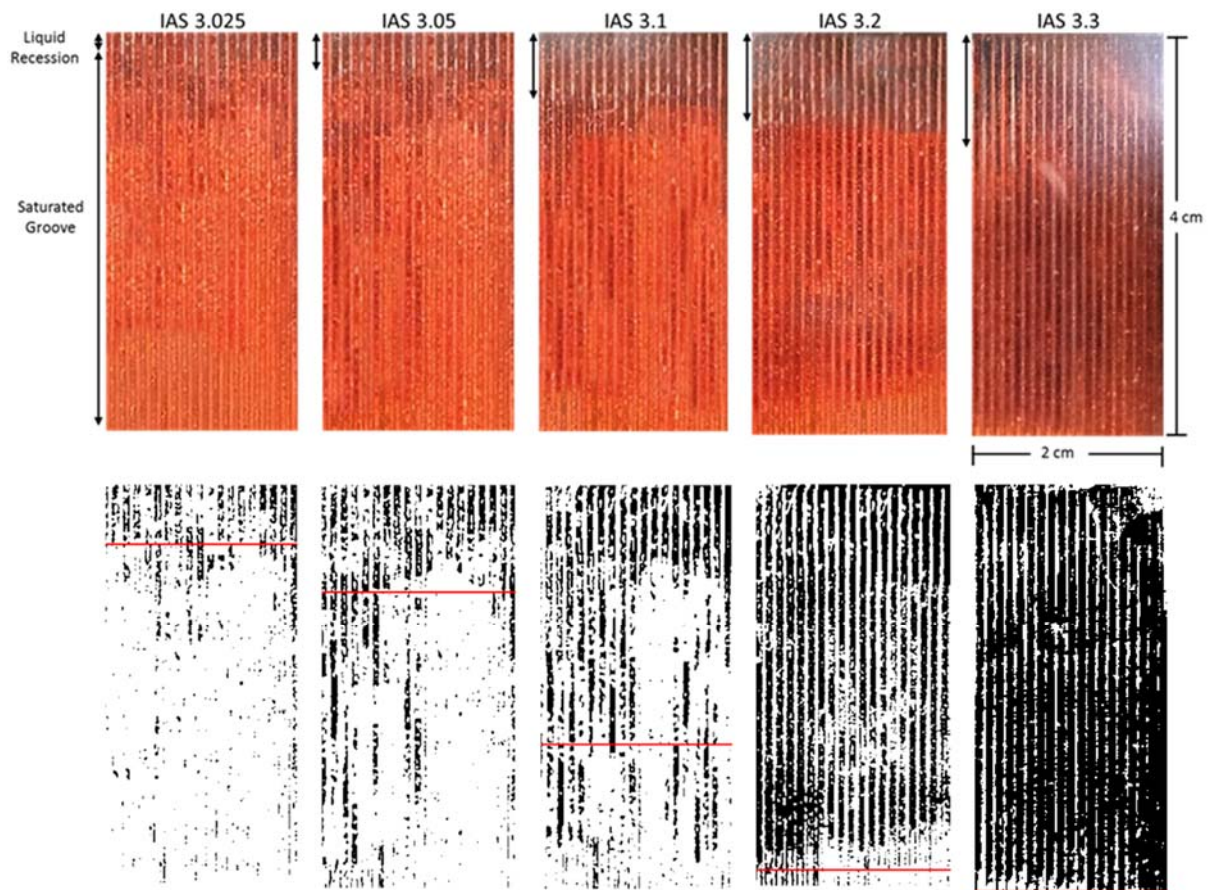
Figure 59: Image processing example for calculating TTFC and ELC

An example of the image processing results are shown in   Figure 59. To calculate ELC, a MATLAB script was written to count to percentage of pixels at each location along the

109

evaporator. When the percentage was calculated to be below 25%, the ELC was returned. The data

for TFC, ELC, and RN can be found in Table 12.

Table 12: Coating measurement data.

IAS	Dryout Length [mm]	Fin Coating Thickness [μm]	Total Fin Coverage [%]	Effective Length Coverage [%]	Resistance Number [μm]
3.025	1.6 ± 0.3	33 ± 9	15 ± 5	15 ± 17	1449 ± 675
3.05	3.8 ± 0.5	71 ± 16	31 ± 5	27 ± 28	864 ± 287
3.1	6.7 ± 0.4	141 ± 16	45 ± 5	65 ± 19	481 ± 121
3.2	8.9 ± 0.5	223 ± 12	96 ± 5	96 ± 8	242 ± 26
3.3	11.4 ± 0.4	302 ± 19	100 ± 5	100 ± 3	302 ± 25

The uncertainty of the TFC was assumed to be 5%, and the ELC uncertainty was estimated

by using different percentages and comparing the results. The ELC was also calculated by using

20% and 30% minimum coverage. The difference in ELC between 30% and 25% and the

difference between 20% and 25% was averaged. This average variation was reported as the

uncertainty in Table 12. The Resistance Number is plotted in Figure 60. The uncertainty of the

resistance number was calculated using the RSS method and propagating the uncertainty of

the three parameters used to calculate it.
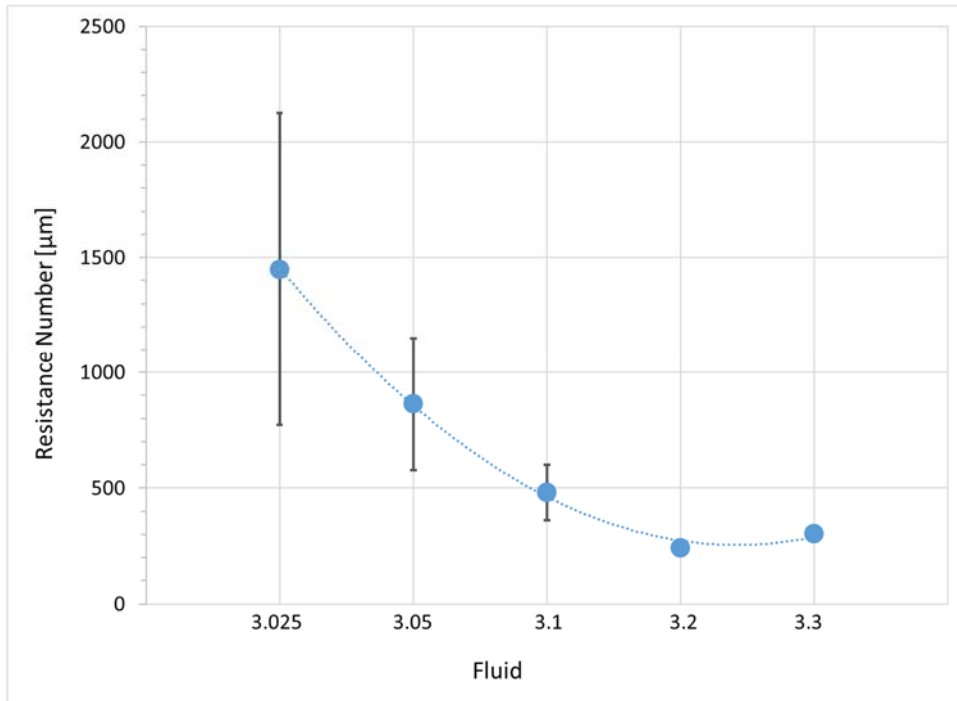
Figure 60: Resistance Number for the IAS fluids

The resistance number was meant to serve as a metric for evaluating the thermal resistance of a given fluid. A higher RN would create a larger overall heat pipe thermal resistance. A clear trend was observed in the results. The RN decreased as concentration increased until it reached a minimum at IAS 3.2. The resistance number (RN) for IAS 3.3 was slightly larger.

This analysis demonstrated the competing effects of coating thickness and coating coverage. A thin coating was more favorable for thermal resistance, as long as it was thick enough to remain wetted. However, the coverage of the wick was just as important. The existence of the parallel pathway through the coating reduced the thermal resistance significantly even if the coating was thick.

The next step to understanding IAS deposition and performance enhancement was to use these experimental observations and measurements in a theoretical heat pipe model. In the next

chapter, a flat heat pipe model is developed to help explain the performance enhancement of a heat

pipe using IAS.

6   Heat Pipe Model

This chapter covers the development of a flat heat pipe model used to analyze the fluid dynamics and heat transfer of water and IAS as heat pipe working fluids. The goal of the model was to better understand the thermal performance enhancement and delay of dry-out achieved by IAS. An immense amount of research has been devoted to understanding and modeling the physical mechanisms that contribute to capillary flow and heat transfer in heat pipes. However, additional development was needed to implement the unique characteristics of the IAS deposits.

The dry-out dynamics of capillary flow in grooves needed to be addressed to account for the secondary flow regimes that appear as the bulk meniscus recedes into the groove before dry-out. Typical heat pipe models don't include corner flow and only consider a saturated groove with a pinned meniscus with a variable solid-liquid contact angle [94, 95]. The symmetry and quasi 1-D flow in axial grooves reduces the liquid/vapor interface to a single radius of curvature. The axial component of curvature of the meniscus can be neglected since it is much larger than the curvature in the longitudinal direction (perpendicular to the flow direction). Corner flows have been investigated primarily for micro heat pipes, which only operate in corner flow due to their small size and fully enclosed channel [96]. A schematic of a triangular micro heat pipe is shown in Figure 61. The curvature varies due to gradual changes in meniscus height whereas a pinned meniscus in an open groove varies curvature with contact angle.
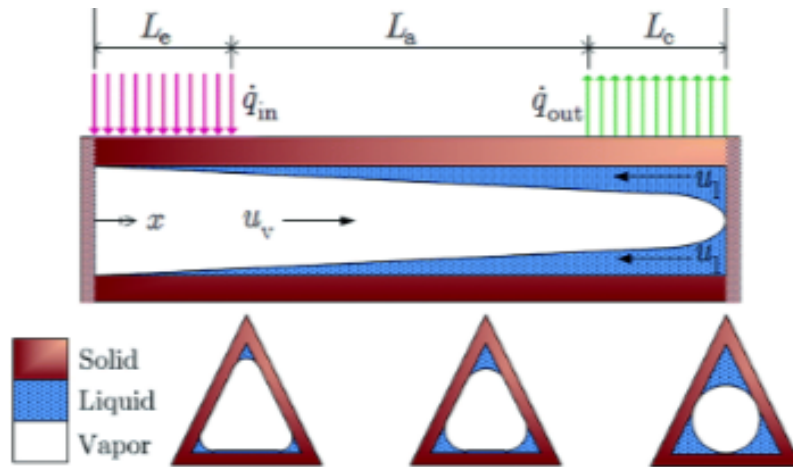
Figure 61: Schematic of a triangular micro heat pipe[97]

In a typical heat pipe groove the bulk meniscus transitions from its pinned height to corner flow in a more complex process, discussed in detail in Section 6.2. Hopkins et al. [91] and Kim et al. [98] successfully modeled the two regions separately in heat pipes with trapezoidal grooves. However, the transition region in a rectangular groove is unique (see Section 6.2). Transition models that have dealt specifically with rectangular grooves were developed for uniformly heated grooves in open air fed by a liquid reservoir and don't consider the evaporation and condensation effects that are present in a heat pipe [99, 100]. Another important feature of a heat pipe model is the treatment of excess charge. Surplus working fluid that pools over the condenser can have significant effects on the overall resistance of a heat pipe [101, 102].

Flow models can predict the maximum heat transport and capillary limit of heat pipes without considering detailed heat transfer analysis. However, Do et al. [95] demonstrated that axial conduction in a flat grooved heat pipe significantly affected the evaporative heat flux profile along the heat pipe. Accounting for axial conduction and non-uniform thermal resistance along the heat pipe were important in correctly predicting heat pipe performance. In order to calculate the axial temperature distribution along a heat pipe, conservation of energy analysis is needed in the solid

114

wall domain. Heat transfer in the transverse direction (perpendicular to the wick) at each axial location must be determined. As discussed above, the formation of distinct thin film regions on the groove wall creates a complicated conjugate heat transfer problem. Do to the high percentage of heat transfer that occurs in the thin film region, some models calculated the heat transfer coefficient of the entire groove by modeling flow in the thin film region at each point along the axial direction of the heat pipe [94]. Others have utilized thermal resistance networks to calculate heat transfer [98, 103, 104].

In this work, a flat heat pipe with axial rectangular grooves and a liquid pool over the condenser was investigated. The model focused on macro-scale fluid flow and heat transfer. A quasi 1D model was developed for water first by solving the mass, momentum, and energy conservation equations of liquid and vapor phases along the different flow regimes of heat pipe. The transition between different flow regimes in the heat pipe (e.g. corner flow to accommodation flow) required special treatment do to non-negligible inertial effects. A nodal thermal resistance network model was also developed to account for axial conduction and coupled with the flow model. The thermal resistance of the wick was estimated at each location along the heat pipe as network.

The base model for water was then adapted to address the effects of the IAS fluid. Discoveries and a variety of unknowns with the IAS deposits, including thermophysical properties, geometry, surface chemistry, etc., made a quantitative model doubtful. Simplified geometrical representations of the deposits made by the fluid with the addition of experimental measurements were utilized to estimate the thermal resistances in the flat heat pipe. Since some properties of the coating, such as permeability, were still unknown these properties were determined as closure to

match the experimental data. This method allowed the study of the thermal performance and dry-out dynamics of the fluid.

6.1 Grooved Heat Pipe Domain

Modeling of a heat pipe requires coupled treatment of momentum transfer in the liquid and vapor domains along with heat transfer in solid heat pipe wall. The evaporative mass flow rate is integrated into the conservation of mass and energy analysis over the entire heat pipe domain. The flow in the liquid and vapor phases is coupled to the heat transfer in the wall through evaporation and condensation. A differential form of the Young-Laplace equation is utilized to determine the variation in curvature from the liquid and vapor pressure drops.

A schematic of the axially grooved heat pipe domain for the model is shown at the top in Figure 62. The z-axis represents the axial length and starts in the evaporator section. Heat is applied to the evaporator section (L_e), which evaporates the working fluid, and removed in the condenser section (L_c), as the vapor condenses. No heat is applied or removed in the adiabatic region (L_a) though axial conduction can cause evaporation and condensation inside the heat pipe. The sections described above only refer to external heating and cooling. Flow of the liquid from condenser to evaporator is countercurrent to the vapor flow but are coupled through phase change at the interface. The liquid and vapor flow along the heat pipe creates frictional losses that are compensated by changes in the curvature of the liquid/vapor interface in the groove. The excess working fluid pools in the condenser region due to gravity.
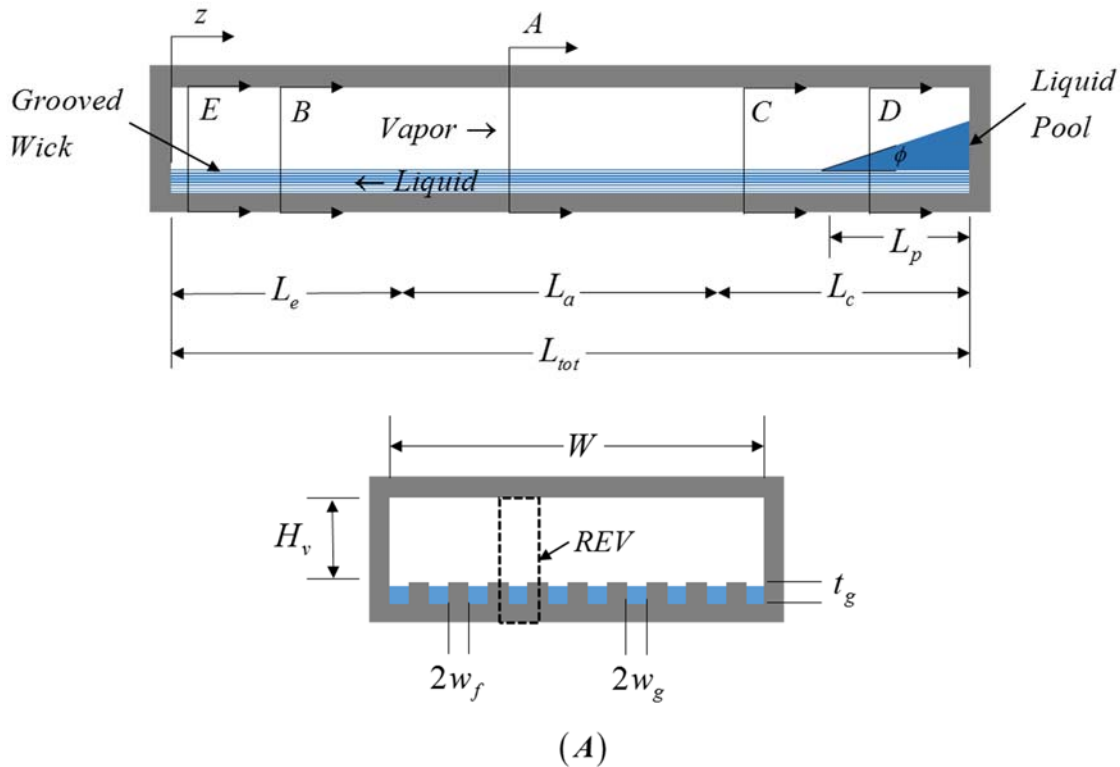
Figure 62: Heat pipe schematic and single groove cross-sections

6.2 Flow Regimes in a Capillary Groove

Stroes and Catton [105] developed a semi-analytical model to predict dry-out in triangular channels. They argued that when a liquid reservoir is present (in this case a liquid pool), there is an accommodation region where the meniscus deforms from its flat inlet condition to the minimum curvature associated with the minimum contact angle. In the accommodation region, the meniscus remains attached to the upper corners of the groove. After this region, the meniscus recedes in the groove with a constant contact angle providing a monotonic decrease in curvature to compensate for the liquid pressure gradient. Stroes and Catton [100] investigated rectangular channels with similar analysis. They argued that once the curvature of the accommodation regime reaches the minimum curvature of the groove, the meniscus de-pins, recedes down to the bottom of the groove,

117

and forms two corner flow regions. The formation of a solid/liquid interface at the bottom of the groove reduces the meniscus curvature. However, they argued that at a constant contact angle, meniscus recession in the groove does not change the curvature of the meniscus like it does for the triangular groove. This transition was referred to as the "dead zone." When modeling capillary flow in a groove, only the curvature perpendicular to the flow is considered. Assuming the channel is uniform width, the meniscus will have no variation in curvature as it recedes. Without axial variation in curvature no pressure gradient or flow can theoretically occur over a finite length. The authors were not able to theoretically determine the length of the transition region or "dead zone." Illustrations of the meniscus shapes in a triangular groove and a rectangular groove are shown in Figure 63.
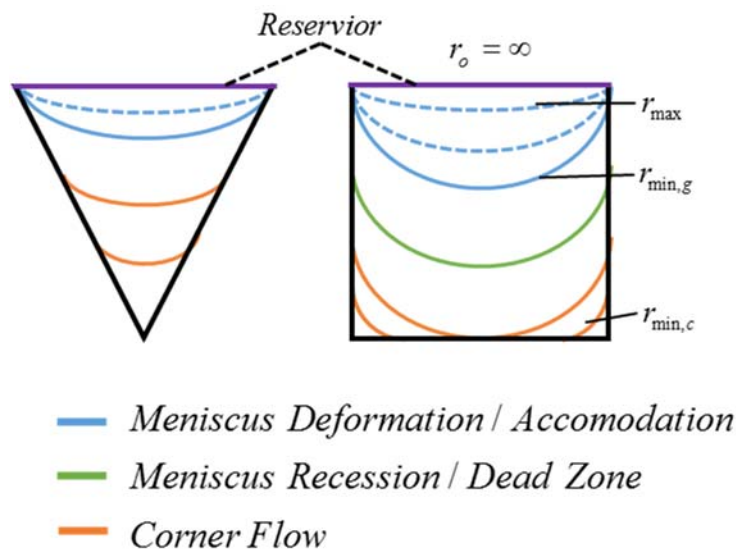
Figure 63: Flow regimes in different capillary grooves

Nilson [106] developed a mathematical model to address the axial extent transition region and argued that the transition region is characterized by a discontinuous saturation gradient. He notes that in the real case, saturation jumps will occur over some finite length due to other physical

processes like variation in the other curvature component or thin film adhesion forces. He used scaling arguments to compare the total possible capillary pressure derived from the longitudinal and axial curvature components to estimate the axial extent of the transition region can be expressed using the nomenclature in this work as,

$$\frac{L_{trans}}{L} \approx \left(\frac{w_f t_g}{L^2}\right)^{\frac{1}{3}} \tag{28}$$

The transition region was calculated to be less than 2% of the total length for Wick #2.

6.3 Flow Regions in a Grooved Heat Pipe

The liquid flow in the heat pipe varies along the axial direction due to evaporation and condensation. Examples at various locations are shown in Figure 64. The liquid pool, shown in (D) forms over the condenser due to an excess liquid charge. The pool levels with the horizontal, at the angle of heat pipe inclination from grooves. Thus, the gravitational pressure gradient in the z-direction was considered to be zero. In the condenser region (C), a condensate film forms over the groove fin and drains into the groove which is discussed in detail later. In the evaporator section (B) the groove is fully saturated with liquid with a pinned meniscus at the top of the fin. During dry-out corner flow (E) occurs as the liquid recedes into the corners of the groove. These regions were defined at a specific location z based on the size of the liquid pool, and whether there was evaporation or condensation. The evaporator (B) and condenser (C) regions, are not confined to the evaporator (L_e) and condenser (L_c) sections.
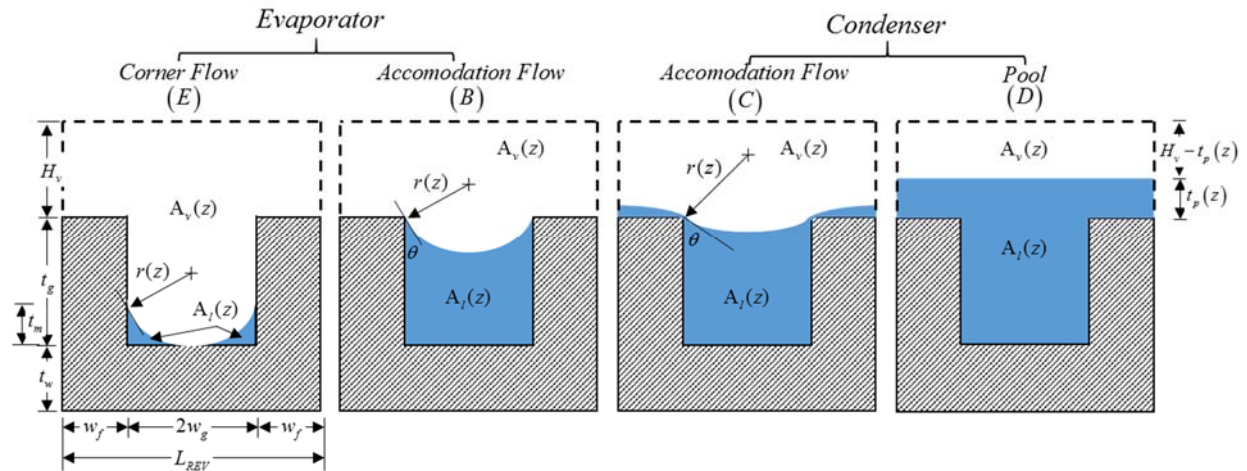
Figure 64: Regions of the flat heat pipe

As mentioned before, capillary flow requires a variation in curvature at the liquid/vapor interface. In the liquid pool, the interface is flat and the curvature is infinite. The curvature decreases to some minimum at the beginning of the evaporator section of the heat pipe to create sufficient capillary force to overcome the frictional losses. The axial variation of the liquid shape in a single groove from the liquid pool (dotted line) to the tip of the evaporator is pictured in Figure 65. The regions in this picture represent the flow regimes, wetting geometries, and mechanism for curvature variation. The accommodation regime occupies the majority of the axial length. The curvature was chosen to vary in this region from some r_{max} to $r_{min,g}$. The transition region between accommodation flow was neglected. A step change from the pinned meniscus to corner flow was modeled instead. The repercussions of this are discussed later.

In the studies discussed above the maximum curvature was taken to be the curvature of the reservoir, which was infinity. These models were developed for open grooves that did not have condensation. In this study, the condensate film that forms near the meeting point of the reservoir and the groove was assumed to create a transition region where the flat interface of the liquid pool conforms (pins) to some maximum radius of curvature over a small length. In heat pipe models

120

the maximum curvature in the condenser is commonly equated to the hydraulic radius of the vapor core [44]. This also allowed for more effective treatment of the change in flow regime there.
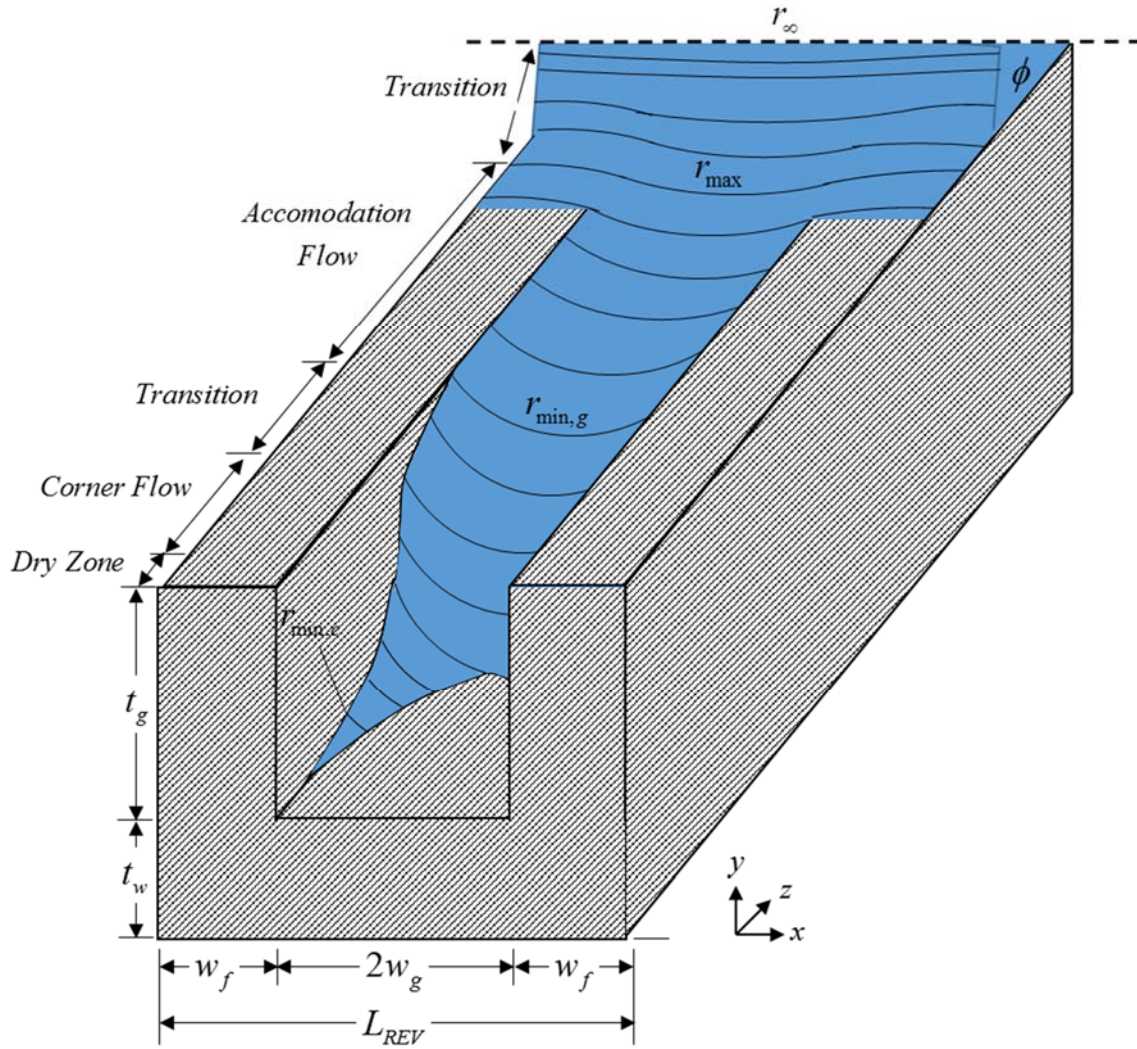
Figure 65: Flow regime transitions in a groove

6.4 Flow Model Governing Equations

This section covers the development of the governing equations and assumptions used to model the hydrodynamics in a flat heat pipe.

6.4.1 Assumptions

The mass, momentum, and energy equations were derived for the control volume shown in Figure 66.
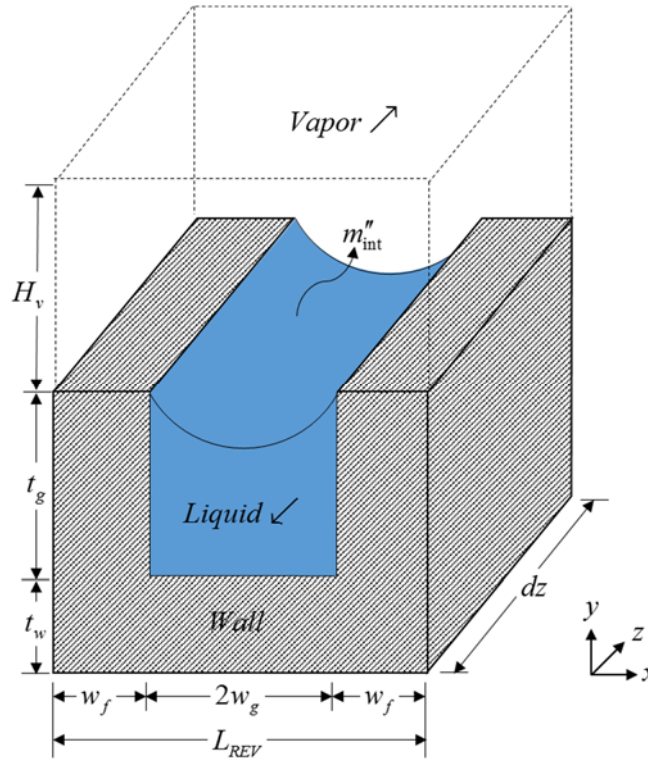
Figure 66: Control volume for a single heat pipe groove

The control volume contains one groove and one half fin on each side of the groove. The conservation equations are derived separately for the vapor, liquid, and solid phases. The following fundamental assumptions are used in deriving the equations in the hydrodynamic model:

1. Steady state operation

2. Constant fluid properties evaluated at the working fluid saturation temperature

3. Laminar, incompressible flow in the liquid and vapor phase

    - The calculated Reynolds number did not exceed 50 for each phase and the vapor and the Mach number was $\ll 1$ for the vapor flow.

122

4. Quasi 1-D flow

5. Negligible viscous dissipation

6. Negligible convection heat transfer in the liquid and vapor phases

7. The meniscus curvature can be approximated by the curvature in the axial direction, r(z).

   - (Curvature of meniscus in x-direction is much larger than in axial direction

8. Radius of curvature is constant at each z-location

   - The variation of curvature in the thin film region only occurs over several microns which was two orders of magnitude smaller than the groove width.

9. Gravity body force is neglected for vapor

Additional assumptions will be addressed as needed in the following sections.

6.4.2   Conservation of Mass

Control volumes for mass and energy transfer in the groove control volume are shown in Figure 67. The liquid and solid phase are coupled at the interface. The transverse heat flux for each control volume (output of thermal model) is assumed to be known before solving the equations.
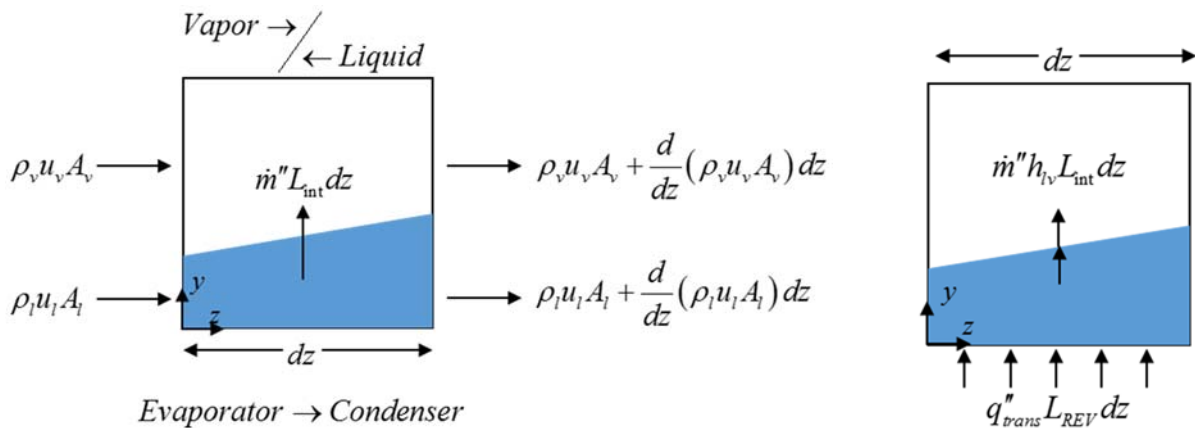
Figure 67: Control volume schematic for conservation of mass (left) and conservation of energy (right)

The mass evaporated from the liquid in the groove is equal to the mass gained by the vapor phase. The coupled mass and energy equations for the vapor and liquid phase are,

$$\rho_v \frac{d(u_v A_v)}{dz} = \frac{q''_{trans} L_{REV}}{h_{lv}}$$ (29)

$$\rho_l \frac{d(u_l A_l)}{dz} = \frac{-q''_{trans} L_{REV}}{h_{lv}}$$ (30)

The total mass in the liquid and vapor phases must equal the charge mass of the working fluid.

$$m_{tot} = N \left[\int_0^{L_{tot}} \rho_l A_l dz + \int_0^{L_{tot}} \rho_v A_v dz \right] = m_{charge}$$ (31)

6.4.3   Conservation of Momentum

A control volume for the conservation of momentum is shown in Figure 68.
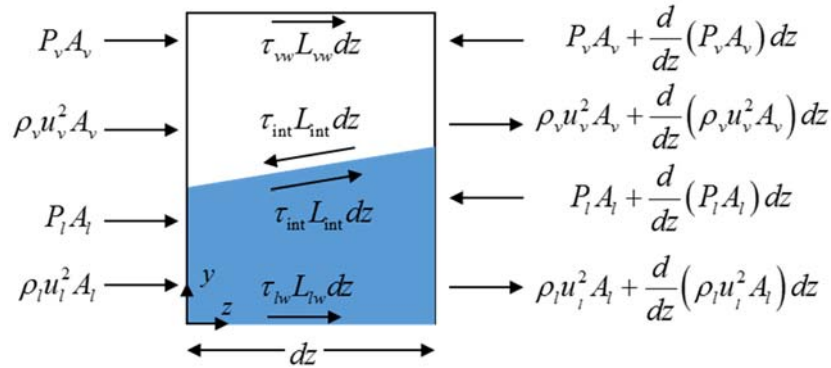
Figure 68: Control volume schematic for conservation of momentum

The momentum equations for the vapor and liquid phases were,

$$\rho_v \frac{d(u_v^2 A_v)}{dz} = -A_v \frac{dP_v}{dz} - |\tau_{vw}| L_{vw} - |\tau_{int}| L_{int}$$ (32)

124

Approved for public release: distribution is unlimited.

$$\rho_l \frac{d\left(u_l^2 A_l\right)}{dz} = -A_l \frac{dP_l}{dz} + \rho_l g A_l \sin\phi + |\tau_{lw}| L_{lw} + |\tau_{int}| L_{int} \tag{33}$$

where the gravitation effect in the vapor phase is neglected. The shear stresses are the most important aspect of the momentum equations which need to be evaluated. The liquid velocity is very low compared to the vapor velocity so the liquid/vapor interface can be considered stationary for calculation of the vapor shear stress [2, 95]. The methodology for calculating shear stress developed by Lips et al. [107] and Rulliere et al. [108] for both phases was adopted. Separating the wall and interfacial shear stresses show equality of the interfacial shear stress in the liquid and vapor phase. The shear stress is expressed in terms of the friction factor,

$$\tau_w = \frac{1}{2}\rho u^2 f \quad , \quad f = \frac{Po}{\mathrm{Re}} \tag{34}$$

The hydraulic diameter is calculated using the true cross-sectional area of the liquid,

$$D_h = \frac{4A}{L_{wet}} \quad , \quad \mathrm{Re} = \frac{u D_h}{v} \tag{35}$$

For a rectangular channel with laminar flow, the Poiseuille number was calculated with the Shah and London correlation,

$$Po = 24\left(1 - 1.3553C + 1.9467C^2 - 1.7012C^3 + 0.9564C^4 - 0.2537C^5\right) \tag{36}$$

where C is the minimum aspect ratio of the channel. The vapor Poiseulle number was calculated considering the vapor space as a single rectangular channel of thickness H_v, and width NL_{REV}, where N was the number of grooves. Because of the stationary liquid assumption, the liquid-wall shear stress was equal to the vapor-wall shear stress. In the liquid phase, the liquid-wall shear stress was calculated considering a free liquid-vapor surface. The Poiseuille number was determined by

125

considering a channel of height $2t_g$ and width $2w_g$ In corner flow, Poiseulle number for triangular flow should be used. The value from the numerical solution of Ayyaswamy et al. [109] for a 90° triangular groove with a 35° contact angle was used (Po ≈ 54). A schematic highlighting the wetted perimeters used for the shear stress calculations is shown in Figure 69.
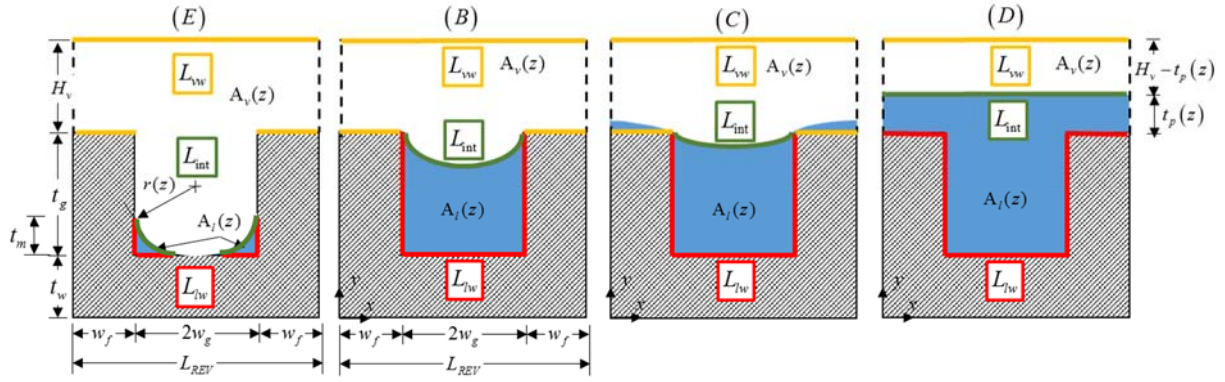
Figure 69: Schematic for the wetted perimeters of the liquid and vapor phases for each region of the heat pipe

The true cross-sectional area can be expressed as a function of the curvature and contact angle along the heat pipe for each regime. In corner flow, where the contact angle is fixed,

$$A_v = H_v L_{REV} \tag{37}$$

$$A_l = r^2 \cos 2\theta - \frac{r^2}{2}\left(\sin 2\theta + \frac{\pi}{2} - 2\theta \right) \tag{38}$$

$$t_m = r(\cos\theta - \sin\theta) \tag{39}$$

The liquid area in Equation (38) is only for one corner. In accommodation flow the area of the liquid and vapor are expressed as,

$$A_l = 2w_g t_g - r^2\left[\tfrac{\pi}{2} - \theta - \sin\theta \cos\theta \right] \tag{40}$$

$$A_v = H_v L_{REV} \tag{41}$$

126

It was assumed that the condensate film did not contribute to axial flow of liquid or disturb axial flow of vapor. In the liquid pool region, the area and the area gradient are simply,

$$A_v = \left[H_v - t_p \right] L_{REV} \tag{42}$$

$$A_l = 2 w_g t_g + t_p L_{REV} \tag{43}$$

$$t_p = \left[L_p - \left(L_{tot} - z \right) \right] \tag{44}$$

6.4.4 Young-Laplace Equation

The cross sectional area and pressures depend on the liquid-vapor interface curvature. The differentia Young-Laplace equation couples the pressures to the curvature of the groove meniscus.

$$\frac{dP_v}{dz} - \frac{dP_l}{dz} = \frac{d}{dz}\left(\frac{\sigma_{lv}}{r} \right) \tag{45}$$

6.5 Solution Procedure

The mass, momentum, energy, and Young-Laplace equation constitute five first order, nonlinear, coupled ordinary differential equations of five unknowns: r, u_v, u_l, P_v, P_l . The equations are integrated with the Euler Method shown below,

$$\begin{bmatrix} r \\ u_v \\ u_l \\ P_v \\ P_l \end{bmatrix}_{i+1} = \begin{bmatrix} r \\ u_v \\ u_l \\ P_v \\ P_l \end{bmatrix}_i + \frac{d}{dz}\begin{bmatrix} r \\ u_v \\ u_l \\ P_v \\ P_l \end{bmatrix}_i \Delta z \tag{46}$$

This simple method was chosen to integrate the equations in the flow model in order to deal with the step transition region between flow regimes, discussed in the next section.

127

6.5.1 Boundary Conditions

The equations were integrated from the start of the evaporator region to the end of the heat pipe. A schematic of the curvature boundary conditions for a scenario when corner flow is present is shown in Figure 70.
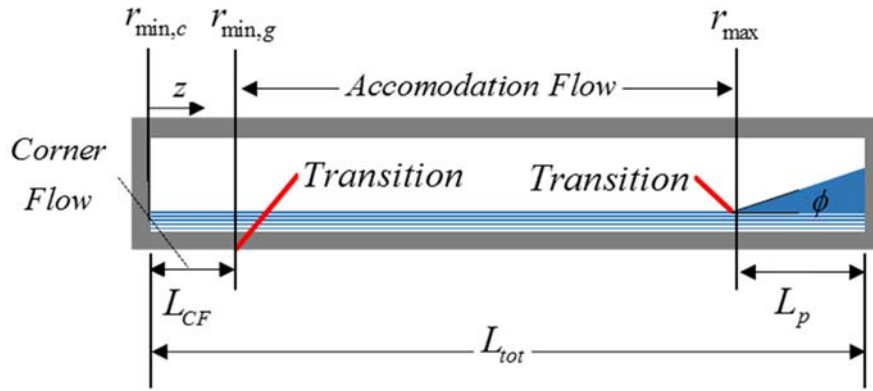
Figure 70: Schematic of boundary condition locations

The boundary conditions at the beginning of the heat pipe are,

$$u_v \big|_{z=0} = 0$$
$$u_l \big|_{z=0} = 0$$
$$r \big|_{z=0} = r_{min} \tag{47}$$
$$P_v \big|_{z=0} = P_{sat}(T_{sat})$$
$$P_l \big|_{z=0} = P_{sat} - \frac{\sigma}{r_{min}}$$

At z = 0 the pressure is taken to be the saturation pressure of vapor and the liquid and vapor velocities are zero due to the no-flow through condition at the heat pipe wall. The Young-Laplace equation was used to define the initial liquid pressure. The minimum curvature varies during the solution of the equation based on the applied heat flux. If, for example, the heat pipe is at the maximum heat transport limit, the minimum curvature will be the minimum curvature defined for

128

corner flow. However, corner flow isn't required for lower heat fluxes. If the heat pipe is capable of transporting the applied heat flux with only accommodation flow, the minimum curvature can be greater than the minimum curvature defined for a saturated groove. The minimum curvature for corner flow and the saturated groove are discussed later in Section 6.9.1.1. The curvature at the beginning of the liquid pool (r_{max}), discussed in Section 6.3, was used as the convergence condition. Following Do et al. [95] and Anand et al. [110], the maximum curvature in a flat grooved heat pipe was approximated as the hydraulic radius of the vapor core,

$$r\big|_{z=L_{tot}-L_p} = r_{max} = \frac{D_h}{2} \tag{48}$$

Although the necessary information about convergence was achieved at the start of the liquid pool, the integration continued to the end of the heat pipe to allow calculation of temperature along the entire heat pipe.

The step changes from corner flow to accommodation flow required a special boundary condition and numerical treatment. The step change in cross-sectional area as the groove becomes saturated was problematic. The inertial terms in the mass and momentum equation account for rapid changes in velocity or area. However, the location of the transition region was not known *a priori* during the integration along the heat pipe. The expressions for area gradient in corner flow, for example, would not be used until after the transition had occurred. The late application of the correct geometrical expressions caused large spikes in velocity and unstable results. Changes in algorithm, illustrated in Figure 71, were implemented to avoid this problem.
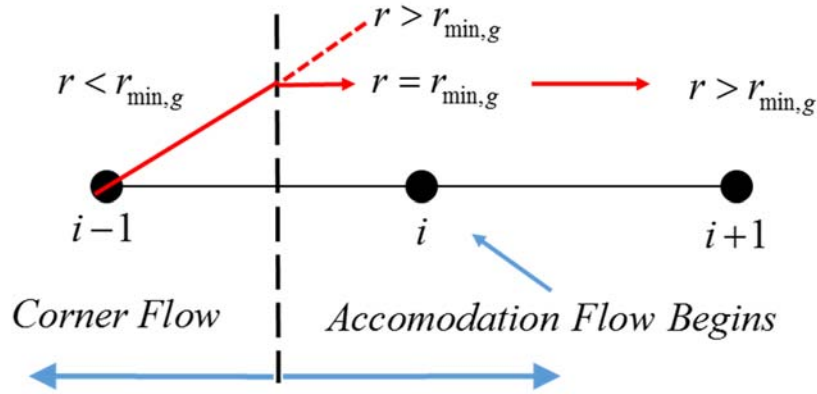
Figure 71: Example of force setting boundary condition at the start of the accommodation flow

After each calculation at z_{i-1}, the curvature at z_i was checked to determine if the accommodation

region had been reached, which was identified by comparing the minimum curvature of the pinned

meniscus in accommodation flow. If the accommodation region was reached at that i^{th} node, a

boundary condition was enforced there to account for the step transition at the $i-1$ node that

should have used different expressions for area gradients. The boundary condition is shown below,

$$u_{v,i} = u_{v,i}$$
$$u_{l,i} = u_{l,i-1} \frac{A_{l,i-1}}{A_{l,i}} + \frac{q_{trans,i-1}}{\rho_l h_{lv} A_{l,i-1}}$$
$$r_i = r_{min,g} \tag{49}$$
$$P_{v,i} = P_{v,i}$$
$$P_{l,i} = P_{v,i} - \frac{\sigma}{r_{min,g}}$$

The curvature was set to the minimum value for the saturated groove. This was used to

then calculate the liquid cross-sectional area and liquid pressure. Because the transition in the

groove doesn't affect the vapor phase, the previous calculations were kept. Since everything was

130

known at the previous node, the continuity equation was solved for liquid velocity directly. The integration procedure was then continued. Implementing the correct area gradient had a huge effect on the velocity spike generated at the transition. Details are discussed in Section 6.9.1.

6.5.2   Grid

The axial lengths and gradients of the different flow regimes varied by orders of magnitude. The numerical grid was refined differently for each type of flow to accurately capture the hydrodynamics and heat transfer. The numerical solutions depended on the axial length increment as well as the increment in curvature. The grid data used is shown in Table 13.

Table 13: Grid information for axial length for different flow regimes and number of steps

	Grid Refinement Length [mm]	h_1	h_2
		500	2000
		Δz [μm]	Δz [μm]
Accomodation Only	-	-	65
Corner Flow	1	2	64.5
Coating Flow	15	30	57.5

Depending on the flow, a small region was refined near the beginning of the evaporator. Refinement was especially important for corner flow which had a large mass flow rate and velocity gradient.

6.6 Thermal Model

6.6.1 Assumptions

Some additional assumptions for the thermal model are listed below,

1. Uniform external heat flux in the evaporator

   - The thermal resistance did not vary much in the evaporator.

2. Convection boundary condition for external heat flux in the condenser (See Section 6.6.2)

3. Constant vapor temperature, T_{sat}

4. Negligible axial vapor thermal resistance due to pressure drop

5. Negligible conduction and convection in the fluid or vapor in the axial direction

   1. The thermal conductivity of the wall material (copper) was much greater than the thermal conductivity of the working fluid

6. The wall represented by a single temperature T_w, at each axial location. (i.e T_w=T_w(z))

6.6.2 Nodal Model

To solve for the temperature profile along the heat pipe, a nodal model was used similar to Rulliere et. al [108] as shown in Figure 72. The energy equation was first derived as a differential equation,

$$k_w A_w \frac{d^2 T_w}{dz^2} = q''_{trans} L_{REV} - q''_w L_{REV} \tag{50}$$
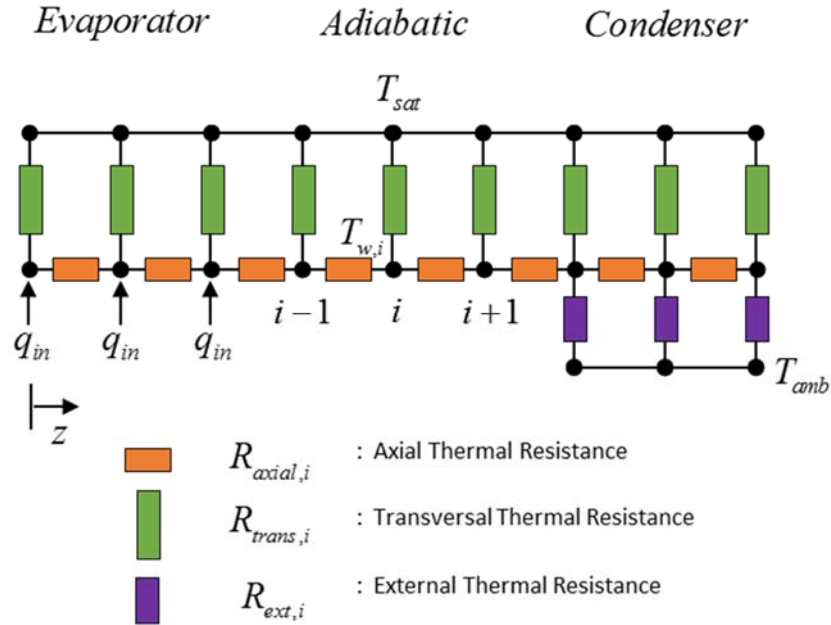
Figure 72: Nodal thermal model axial wall temperature distribution with a uniform heat flux in the evaporator and a fixed external thermal resistance in the condenser

Applied heat can travel in two different pathways, through axial conduction, or through conduction and evaporation in the transverse direction. The axial conduction thermal resistance is constant throughout the heat pipe but the transverse thermal resistance varied along z. A uniform heat flux was applied to the evaporator section. This is a valid assumption if the thermal resistance is also uniform. In the condenser the liquid pool created an extremely large thermal resistance compared to the rest of the condenser section due to the additional layer of working fluid. Therefore, it was unreasonable to assume that heat was rejected uniformly along the condenser. To overcome this obstacle, an external thermal resistance and fixed ambient temperature to calculate the external heat removal from the temperature difference between the wall and the ambient. The external heat flux profile was represented as a piecewise function,

$$q''_w(z) = \begin{cases} q_{in}/A_{evap} & 0 \le z \le L_e \\ 0 & L_e \le z \le L_e + L_a \\ -(T_w - T_{amb})/A_{cond}\,\mathrm{R}_{ext} & L_e + L_a \le z \le +L_e + L_a + L_c \end{cases} \quad (51)$$

The external thermal resistance was calculated from the average heat transfer coefficient estimated from the experimental flat heat pipe data. For every test, and every power, the external heat transfer coefficient was calculated by,

$$\bar{h}_{ext} = \frac{q_{in}}{A_{cond}\left(\bar{T}_{cond} - \bar{T}_{amb}\right)} \quad , \quad \bar{R}_{ext,i} = \frac{1}{\bar{h}_{ext}A_{REV}} \quad (52)$$

The average external heat transfer coefficient was calculated to be 2170 W/m² for the tests run with the flow rate of 0.75 L/min and 3300 W/m² for the 1.5 L/min tests. An effective representative elementary volume (REV) for the thermal model is shown in Figure 73.
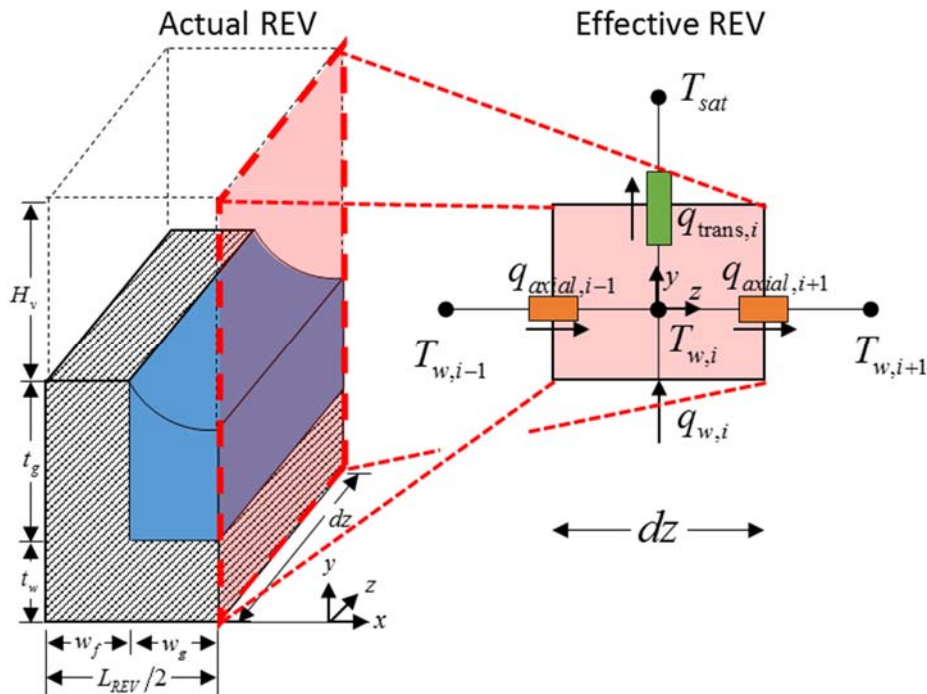
Figure 73: Thermal model REV

The energy equation can be expressed in nodal form in terms of the axial and transverse thermal resistances,

$$\frac{T_{w,i+1} - 2T_{w,i} + T_{w,i-1}}{R_{axial}} = \frac{T_{w,i} - T_{sat}}{R_{trans,i}} - q_{w,i} \tag{53}$$

for each section of the heat pipe:

Evaporator

$$\left(\frac{1}{R_{axial}}\right)T_{w,i+1} - \left[\frac{2}{R_{axial}} + \frac{1}{R_{trans,i}}\right]T_{w,i} + \left(\frac{1}{R_{axial}}\right)T_{w,i-1} = -\frac{T_{sat}}{R_{trans,i}} - q_w \tag{54}$$

Adiabatic

$$\left(\frac{1}{R_{axial}}\right)T_{w,i+1} - \left[\frac{2}{R_{axial}} + \frac{1}{R_{trans,i}}\right]T_{w,i} + \left(\frac{1}{R_{axial}}\right)T_{w,i-1} = -\frac{T_{sat}}{R_{trans,i}} \tag{55}$$

Condenser

$$\left(\frac{1}{R_{axial}}\right)T_{w,i+1} - \left[\frac{2}{R_{axial}} + \frac{1}{R_{trans,i}} + \frac{1}{R_{ext,i}}\right]T_{w,i} + \left(\frac{1}{R_{axial}}\right)T_{w,i-1} = -\frac{T_{sat}}{R_{trans,i}} - \frac{T_{amb}}{R_{ext,i}}$$

$$\tag{56}$$

These equations form a tri-diagonal matrix and were solved simultaneously with the boundary conditions.

$$\left.\frac{dT_w}{dz}\right|_{z=0} = \left.\frac{dT_w}{dz}\right|_{z=L_{tot}} \tag{57}$$

The use of the external thermal resistance does not ensure conservation of energy. The saturation temperature was varied until the net heat transfer along the heat pipe was zero, calculated as,

135

$$q_{net} = N \int_0^{L_{tot}} q_w'' L_{REV} dz = 0 \tag{58}$$

6.6.3   Thermal Resistance

To solve the thermal model, the thermal resistance of each control volume was calculated. The region was determined by the sign of the evaporative mass flux. This accounted for evaporation and condensation in the adiabatic region due to axial conduction. This was also necessary due to the variation of the liquid pool length.

6.6.3.1   Axial Conduction

The thermal resistance for axial conduction in the heat pipe wall was constant along the heat pipe do to the uniform cross-sectional area of the grooved wick. The resistance is,

$$R_{axial} = \frac{dz}{k_w A_w} \quad , \quad A_w = 2t_g w_f + t_w L_{REV} \tag{59}$$

where the entire cross-section of the heat pipe wall was used, following Lefevre et al. [111]. This analysis was based on the assumption that the wall could be represented by a single axial temperature due to the high thermal conductivity of copper.

6.6.3.2   Evaporator

The true heat transfer problem is a complicated conjugate problem combined with thin film evaporation. To use a thermal resistance model shown in Figure 74, an approximation by Chi [3, 112] was utilized.
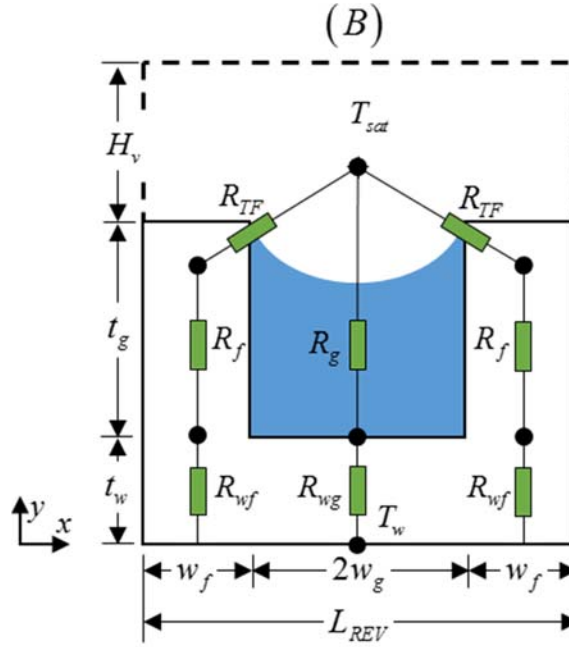
Figure 74: Thermal resistance network in evaporator

Chi estimated the conjugate resistance by solving 2-D conduction in liquid with uniform wall temperature on three sides and a flat meniscus at T_{sat}. The analytical summation solution was correlated with the groove aspect ratio. The other resistances are simple typical conduction expressions. The approximation for the resistance through the thin film is,

$$R_{TF} = \frac{0.185 \tanh\left(5.4\left(\dfrac{t_m}{2w_g}\right)\right)}{k_l dz} \tag{60}$$

$$R_{wf} = \frac{t_w}{k_w w_f dz} \qquad R_{wg} = \frac{t_w}{k_w 2w_g dz} \qquad R_f = \frac{t_g}{k_w w_f dz} \qquad R_g = \frac{t_g}{k_l 2w_g dz} \tag{61}$$

The resistance for the corner flow scenario was approximated using the same expression. The assumptions break down here as the meniscus touches the bottom of the groove. However, the approximation was kept for simplicity as an initial estimation.
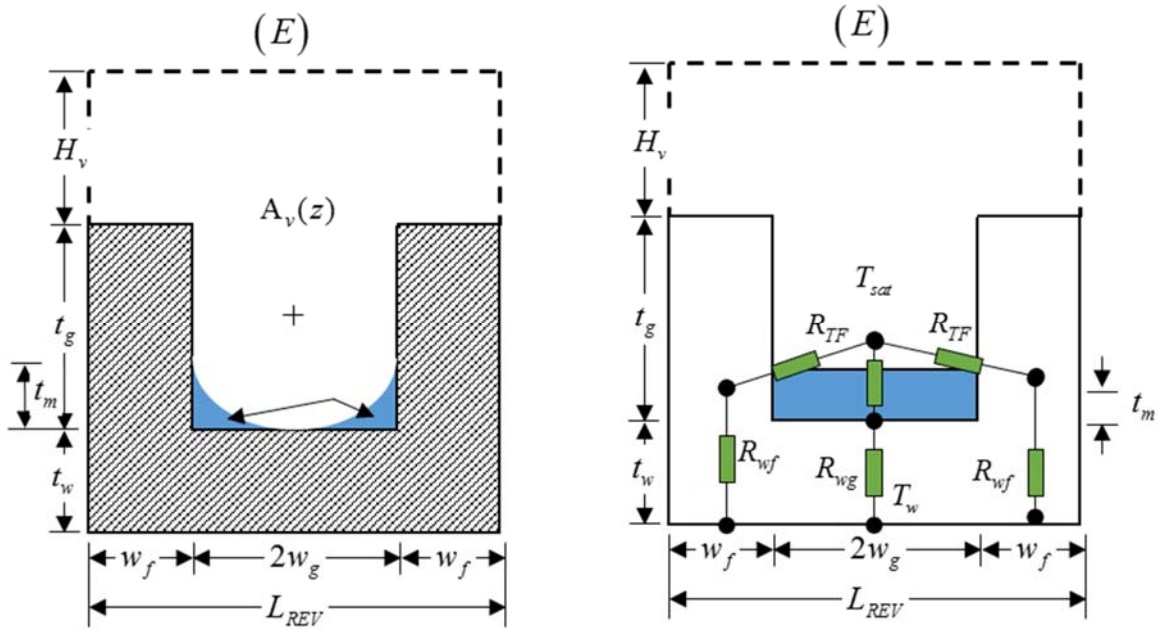
Figure 75: Thermal resistance network for corner flow

6.6.3.3 Condenser

In the condenser a film is formed on top of the fin due to the larger thermal conductivity of the metal. Faghri [113] demonstrated this behavior with a detailed numerical approach. Jiao [114] approximated the film with a uniform thickness. Do et al. [95] used an integral approach and approximated the film as a 4th order polynomial using the curvature, contact angle, and flow velocity boundary conditions. This method was adopted in this work. A schematic of the condensate film is shown in Figure 76.
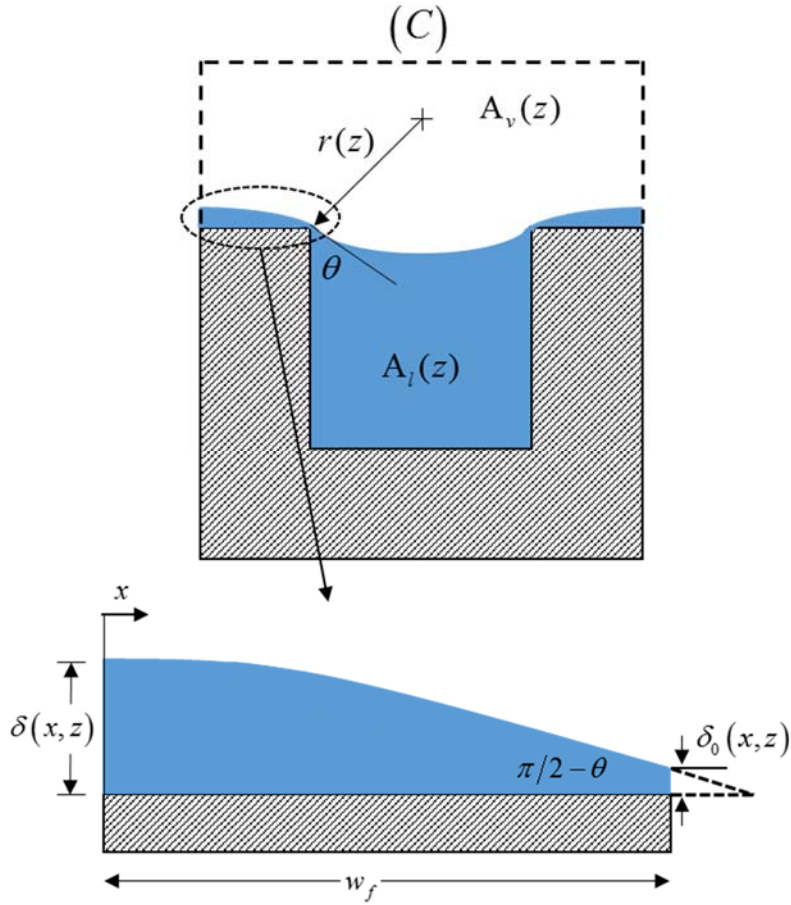
Figure 76: Condensate film formed on the fin tops in the condenser section

The 4th order polynomial for fin thickness with the suggested boundary conditions is written below,

$$\delta(x) = C_0 + C_1(x - w_f) + C_2(x - w_f)^2 + C_3(x - w_f)^3 + C_4(x - w_f)^4$$

(62)

$$\left.\frac{d\delta}{dx}\right|_{x=0} = 0, \quad \left.\frac{d^2\delta}{dx^2}\right|_{x=0} = \frac{1}{r}, \quad \left.\frac{d^3\delta}{dx^3}\right|_{x=0} = 0, \quad \left.\frac{d\delta}{dx}\right|_{x=w_f} = -\tan(\pi/2 - \theta)$$

Applying the boundary conditions yields,

$$C_1 = -\tan\left(\pi/2 - \theta\right), \quad C_2 = \frac{1}{2r}, \quad C_3 = 4C_4 w_f, \quad C_4 = \frac{2C_2 w_f - C_1}{\left(2w_f\right)^3} \quad (63)$$

C_0 was found by equating the mass flow rate of the total condensed liquid and the flow rate in the groove. The velocity of the fluid was calculated in the flow model.

$$\delta_0(z) = \frac{q''_{trans}\left(w_f + w_g\right)}{\rho_l h_{lv} u_l(z)} \quad (64)$$

The condenser film adds and additional thermal pathway over the fin that can be combined in parallel with the resistance through the thin film, shown in Figure 77. The average condensate film thickness was used to calculate the thermal resistance,

$$R_{CF} = \frac{\delta_{avg}}{k_l w_f dz} \quad (65)$$

The rest of the thermal resistances were the same as the evaporator.

140
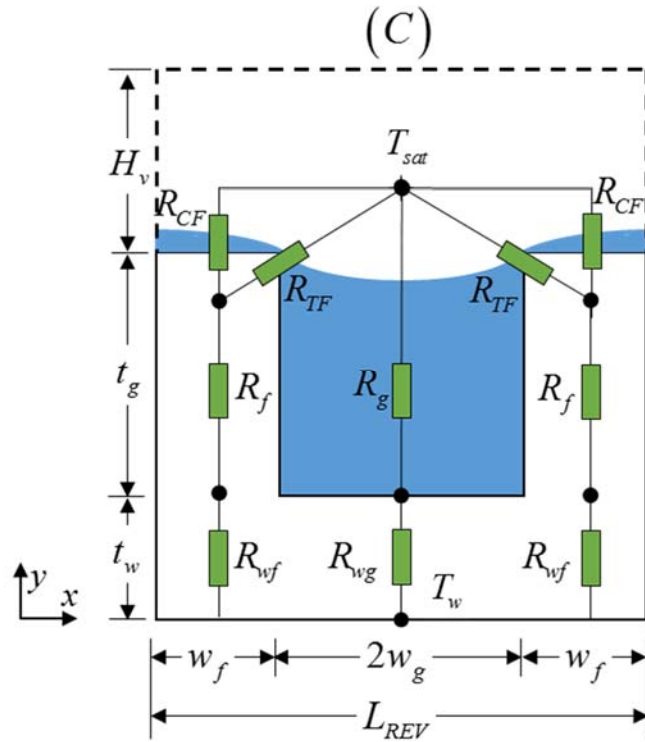
Figure 77: Thermal resistance network in the condenser with a condensate film

6.6.3.4 Liquid Pool

The liquid pool thermal resistance was dependent on the pool thickness. The thermal resistance network is shown in Figure 78. The two additional resistances that haven't been listed yet are shown below,

$$R_{pf} = \frac{t_p}{k_l w_f dz}, \qquad R_{pg} = \frac{t_p}{k_l 2 w_g dz} \tag{66}$$
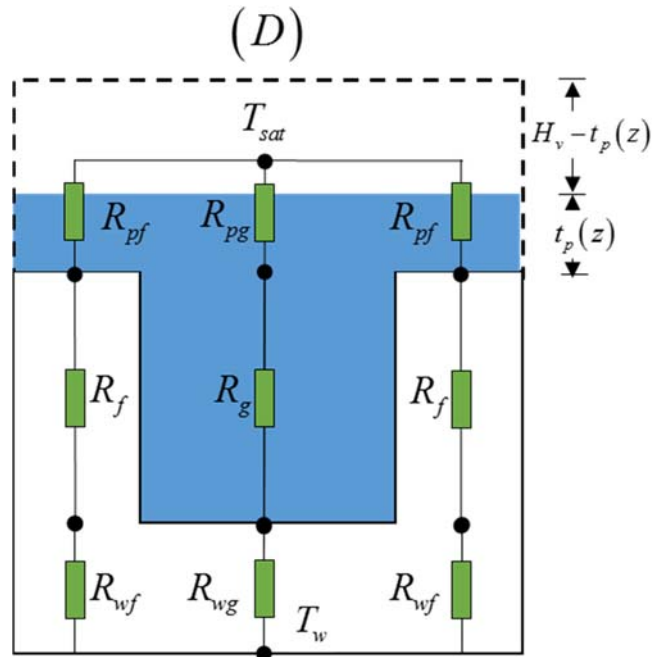
Figure 78: Thermal resistance network in the liquid pool

6.7 IAS

The geometric representations of the IAS deposits are shown in Figure 79. These portrayals were based on the visual observations made during the flat heat pipe experiments in Chapter 4. The two flow regimes were treated similar to water vs. corner flow. During the accommodation stage, the only difference was the additional evaporative surface area. This was realized through updating the thermal resistance network in the evaporator section. The second flow regime, referred to in this work as "coating flow," required completely different treatment than corner flow.

1. A thick coating formed on the top of the groove fin in the evaporator region during normal operation while the bulk meniscus was pinned at the top of the groove.

2. After the meniscus began to recede from the evaporator, a wetting film was present the bottom and sides of the groove due to deposits left on the interior of the groove.

142

3. Liquid was transported axially through the coating on the top of the fins during coating flow only.
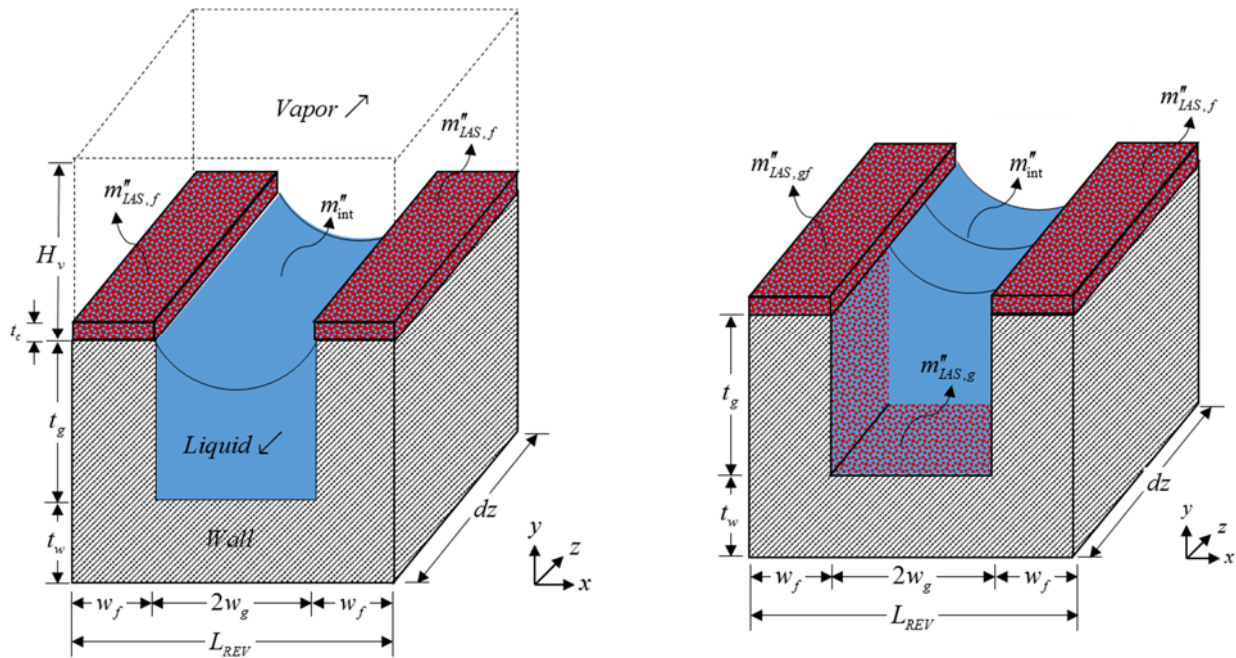
Figure 79: Representation of IAS during accommodation flow (left), and coating flow after meniscus recession (right)

6.7.1 Conservation of Momentum

The momentum analysis was re-visited for the coating flow regime. Closure was needed for the friction factor. The coating was treated as a porous media with an effective permeability to represent the complex wetting and surface chemistry processes that transported liquid. The coating and interior film were combined into a single media. Darcy's Law was used to represent the frictional losses due to transport of liquid through the media. The cross-sectional area of the coating was considered to be uniform.
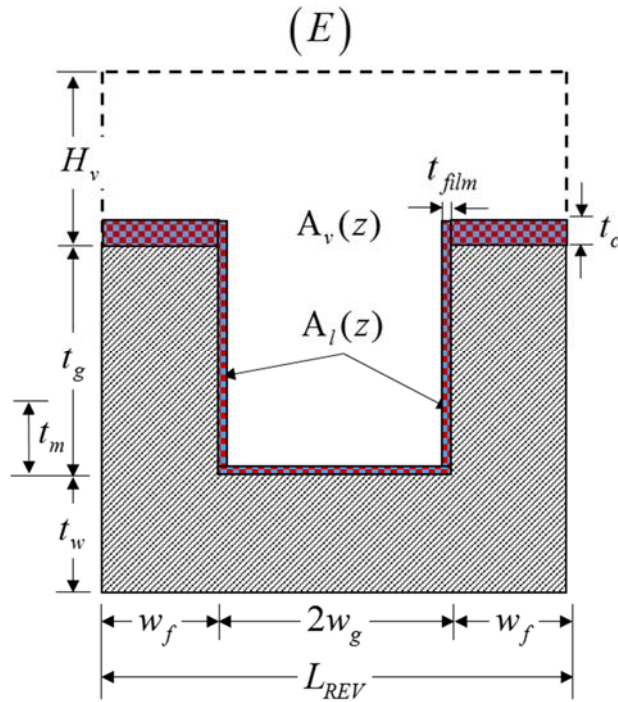
Figure 80: Effective medial representation of the IAS coating

The pressure drop in the IAS media was calculated directly from Darcy's Law

$$\frac{dP_l}{dz} = -\frac{\mu_l u_l}{K} \qquad (67)$$

6.7.2   Thermal Resistance

The thermal resistance networks defined for water were updated for IAS. The coating thickness measurements as well as coverage percentages from Chapter 4 were utilized to define some of the geometry. The representative thermal resistance networks are shown in Figure 81.
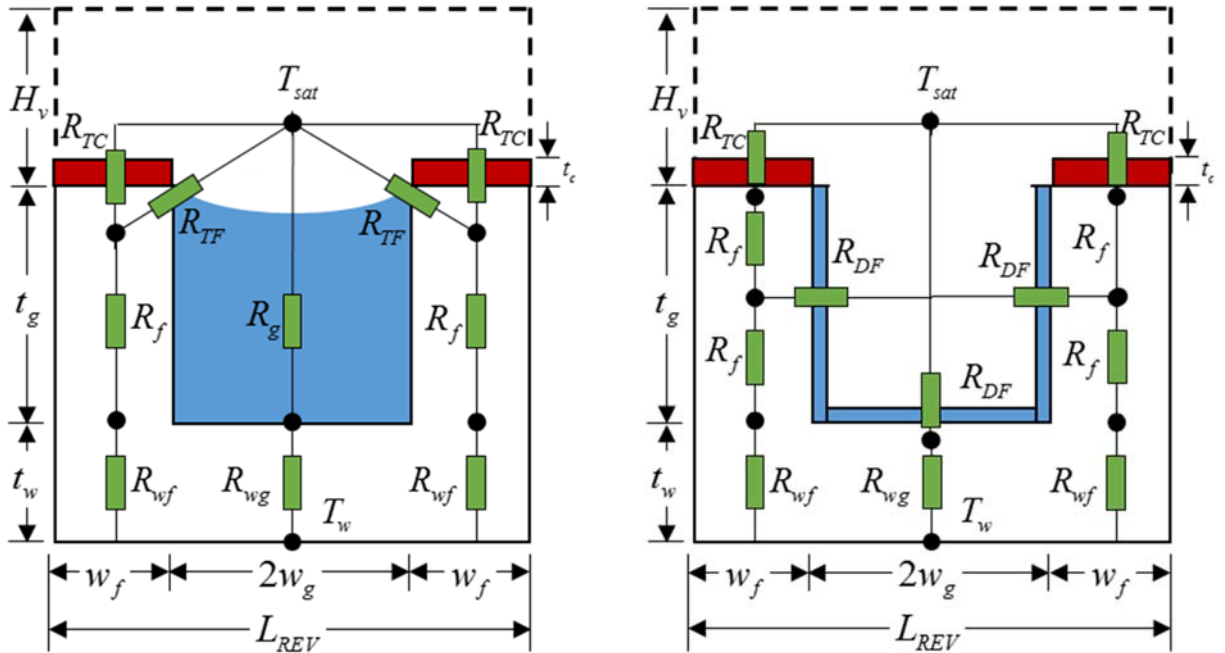
Figure 81: Thermal resistance network for accommodation flow (left), and coating flow (right)

The network for accommodation flow was very similar to that of the condenser section of water with the condensate film. The coating thermal resistance was added as a parallel pathway to the thin film resistance. The Effective Length Coverage (ELC) was also implemented in the model. If the location along the heat pipe was greater than the ELC, the thermal resistance expressions for water were used.

The uncertainty regarding the geometry of the coating flow made it much more difficult to treat. The thickness of the interior film was not measured. The treatment of the film thickness and other known properties such as thermal conductivity are discussed in Section 6.9.2.1.

6.8 Coupled Flow and Thermal Solution Algorithm

A flow chart of the solution procedure is shown in Figure 82.
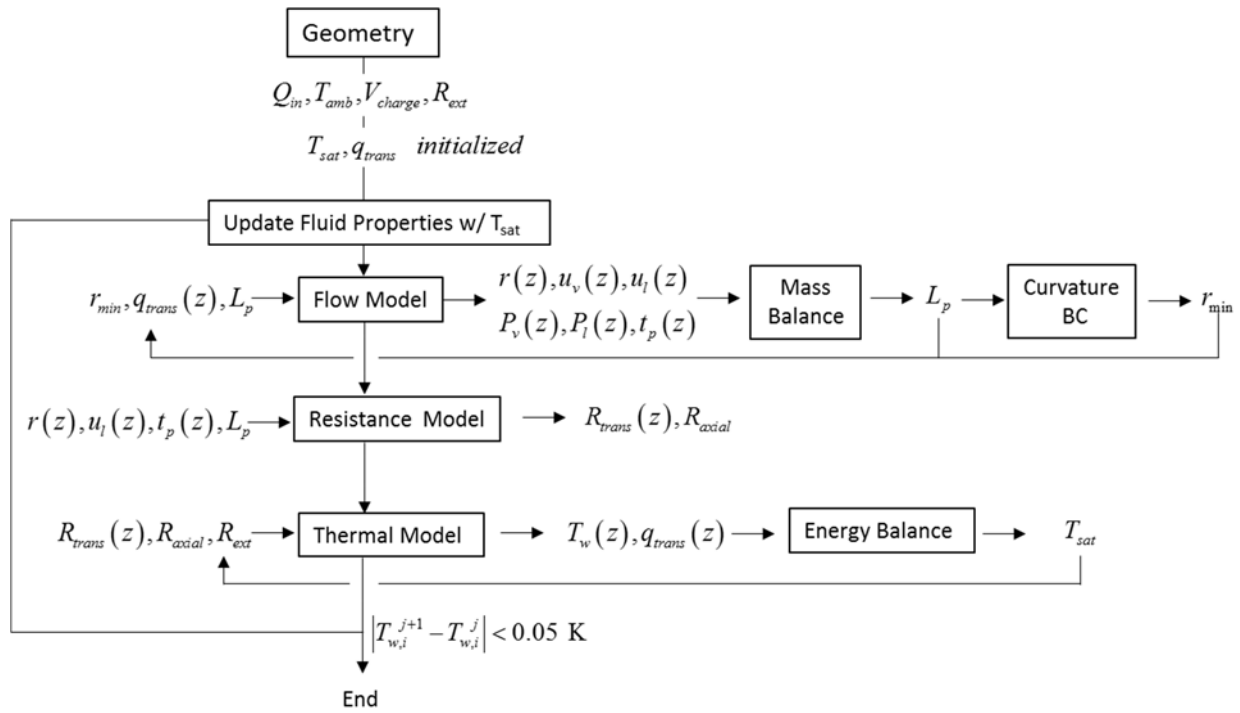
Figure 82: Flow chart of solution procedure

6.9 Results

The following section contains a discussion of results generated by the flat heat pip model developed above. The process of obtaining critical inputs and other specific information necessary to use the model was relied heavily on empirical data. The details regarding closure properties for water and IAS deposits is presented. The model data was compared to the flat heat pipe experiments in Chapter 4 for validation. The coupled hydrodynamic and thermal effects of the secondary flow regimes seen near dry-out are analyzed. The model was used to gain insight into how coatings and wetting films change the dynamics of heat transfer and flow in a grooved wick.

6.9.1 Water

Results and closure for water as a working is presented first as a basis for the much more complex interactions of IAS.

6.9.1.1 Closure

The minimum contact angle is an important closure parameter, especially with large grooves that have low capillarity. Wong and Lin [115] studied the effect of copper surface wettability on the evaporation performance and observed significant differences in thermal resistance and capillary limit. They noted that the minimum wetting contact angle is different that the contact angle of a sessile droplet, though they are related. The minimum wetting contact angle varies in heat pipe literature and is difficult to measure. Stepanov [116] measured the minimum wetting contact angle of various liquid/solid systems and reported 33° for a copper/water system. This work was heavily referenced by Faghri [2]. In one heat pipe study, Hopkins [91] investigated using both 0° and 33° for copper flat heat pipes and argued that the micro roughness's in manufactured devices can't be assumed to have the same wetting and contact angles as those

147

predicted in controlled environments . Chen [104] used 40° for milled copper grooved wicked plates, a result of measuring contact angle of a water droplet on the plate and disregarding the distinction between the two types of contact angles

Since the goal of the modeling in this work was to study IAS, and the actual surface properties of the wick are very difficult to determine, the minimum contact angle was used as a fitting parameter. The water experiments at the lower condenser flow rate (0.75 L/min) were completed at three angles of inclination, which provided an opportunity to fit one set of data that could be validated against other tests. The strategy was to find the minimum contact angle to achieve dry-out for the accommodation model without corner flow. The lower bound of the possible dry-out range for the 10.5° inclination angle was used for the fitting. The lower bound was chosen so that adding the corner flow regime could be validated in the correct range with the most room for error.

The reported dry-out for the water experiments were the averages of the last two powers. The resolution of the averaged range ($\sim \pm 5W$) was combined with the uncertainty of a single heat flux measurement to account for the fact that the true dry-out point could be anywhere in that range. A minimum contact angle of 36.5° was found cause dry-out at the lower bound, 58.61W for water at 10.5° inclination. This angle was used to find the dry-out point for accommodation flow at other angles of inclination as well as the dry-out point predicted by the corner flow model.

The minimum curvature for corner flow was also unknown. A cross-section of a milled groove was investigated (See Appendix 0) and the minimum curvature of the grooved wicks was estimated to be 40μm.

6.9.1.2   Dry-out Validation

The results for the predicted dry-out points for the accommodation model and corner flow model are shown in Figure 83.
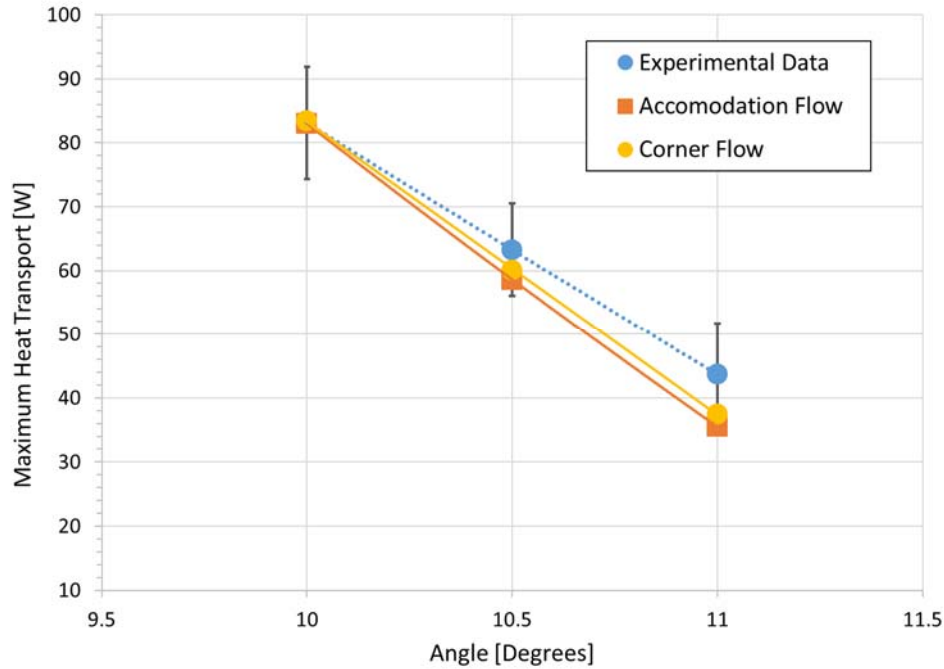
Figure 83: Predicted dry-out of accommodation flow and corner flow for different angles using a minimum contact angle of 36.5°

The predicted dry-out points are just within the experimental uncertainty. The slope of the predicted line was slightly steeper but followed the same trend. The corner flow did not aid much in extending dry out or performance. The existence of corner flow allowed the heat pipe to increase maximum heat transport by less than 2 W. The length of the corner flows at dry-out and dry-out data plotted above are tabulated below,

149

Table 14: Dry-out data for flat heat pipe with water at different inclination angles, (*10.5 was tested with 1.5L/min condenser flow rate)

Inclination Angle	Maximum Heat Transport [W]			Corner Flow Length [mm]
	Experiment (Average)	Model (Accomodation)	Model (Corner)	
10	83.08	83.00	83.38	0.674
10.5	63.25	58.61	60.05	0.715
11	43.65	35.49	37.41	0.787
*10.5	64.46	63.73	64.42	0.644

The corner flow length achieved was very small. Any performance improvement from having a lower liquid level was lost due to the negligible area that was covered. Once the correct closure property was implemented, the model adequately predicted the dry-out of the flat heat pipe. Using the standard contact angle of 33° overestimated the maximum heat transport of the heat pipe by approximately 50%. Thought the dry-out was directly dependent on the minimum contact angle in the flow, the thermal model was not. The next section presents the thermal model results.

6.9.1.3   Axial Temperature Profile

The model was useful in that it could determine the axial temperature profile, heat flux, without fixing any internal parameters. A heat flux was applied to the heat pipe and the wall temperatures and the saturation temperature were free to vary. One reason this type of model was possible was the ability to evaluate the properties of the working fluid automatically using X Steam [117], an open source data base of saturated properties for water that can be easily loaded into MATLAB. The axial temperature profiles for the water tests are shown below,

The inclination angle 10°, 10.5°, and 11° are shown in Figure 84, Figure 85, and Figure 86 respectively. The 10.5° water test at the second flow rate (1.5 L/min) and is shown in Figure 87.
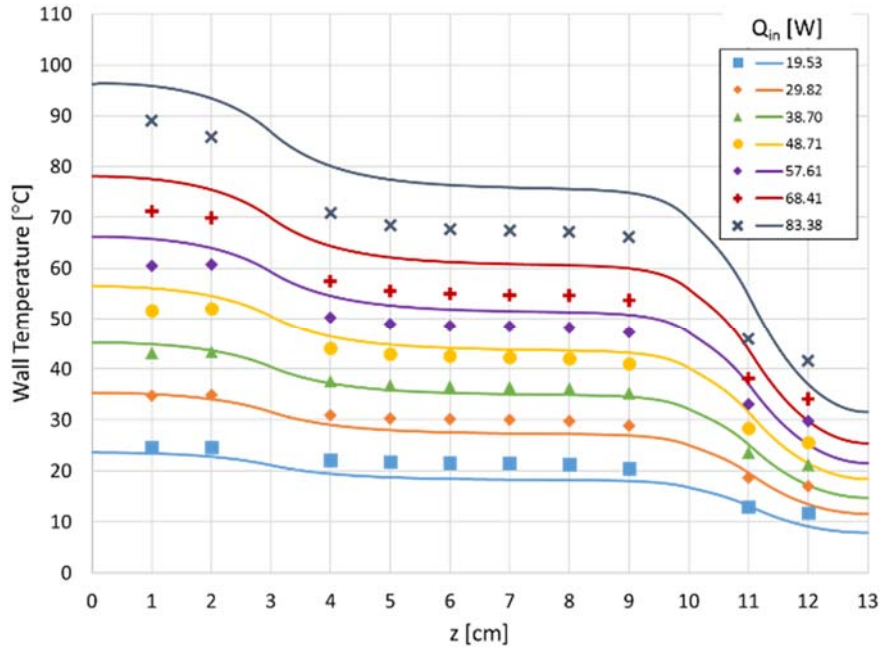
Figure 84: 10 degrees
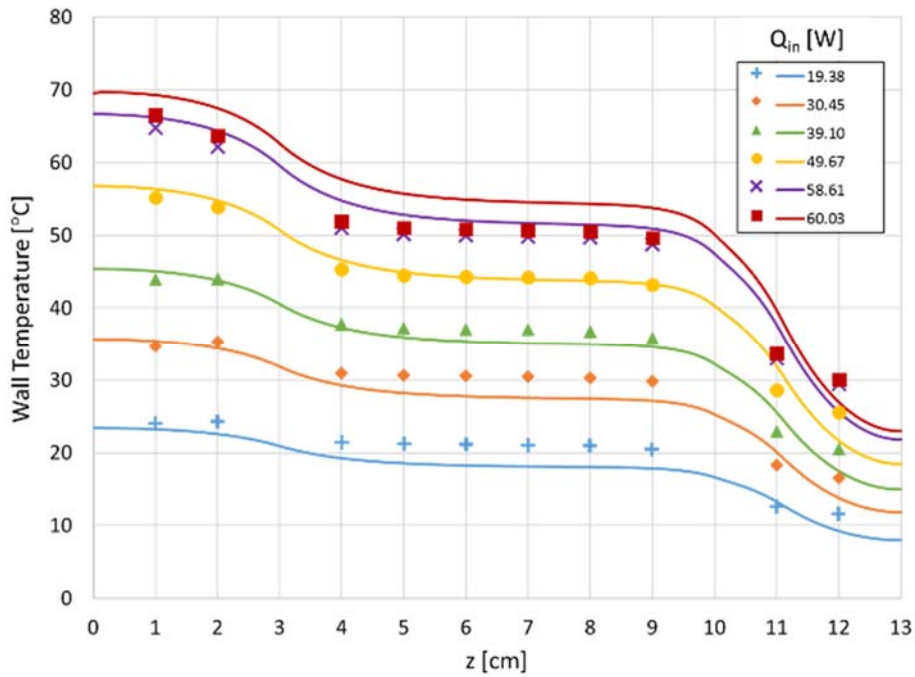
Figure 85: 10.5 degrees (0.75 L/min)

151
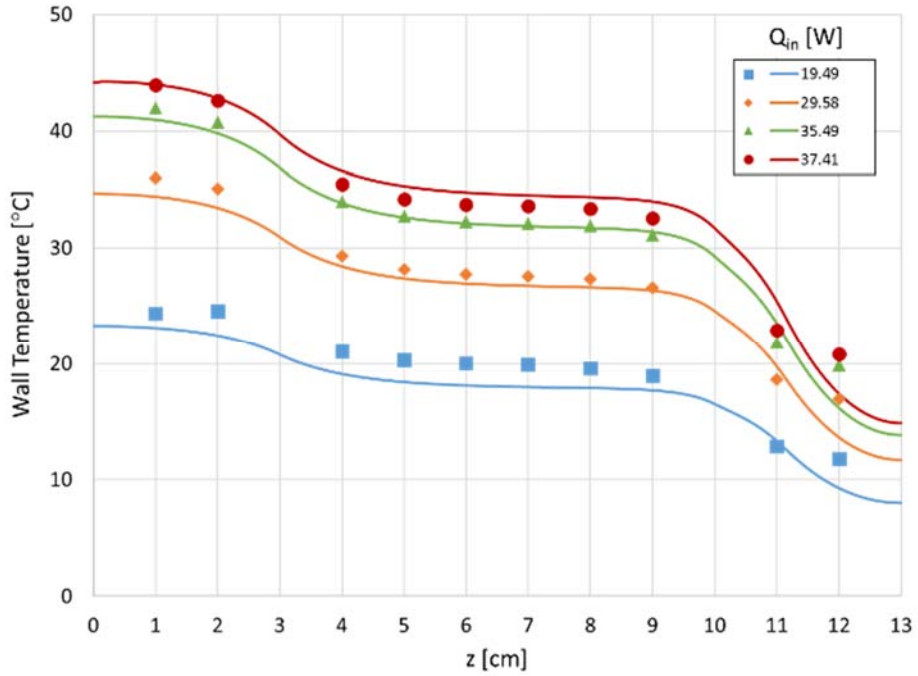
Figure 86: 11 Degrees
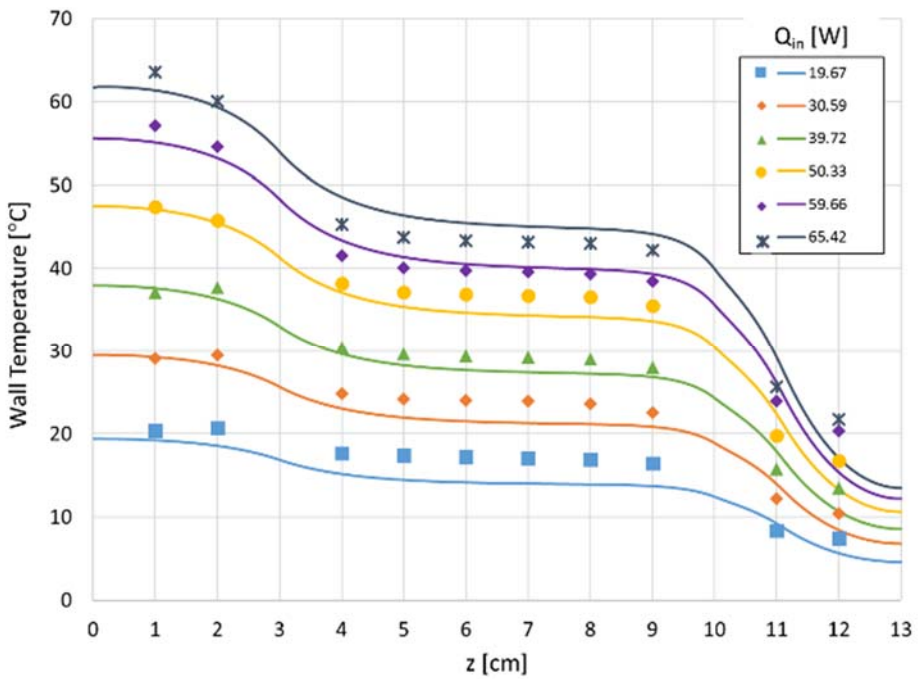
Figure 87: 10.5 (1.5 L/min)

152

The temperature profiles also demonstrate the importance of accounting for axial conduction. The relatively smooth blending of the evaporator and condenser temperatures with the adiabatic section was evidence of this. The steep temperature gradient in the condenser was due to the larger thermal resistance of the liquid pool. Liquid pool length data and an example axial thermal resistance profile can be found in the appendix. The temperature profiles model followed the experimental data fairly well, but less so at higher powers. These results were encouraging considering the modular type of heat pipe tested.

6.9.1.4   Corner Flow Dynamics

The heat flux profiles and liquid velocity profiles for water at 10.5° (1.5 L/min) are shown in Figure 88.
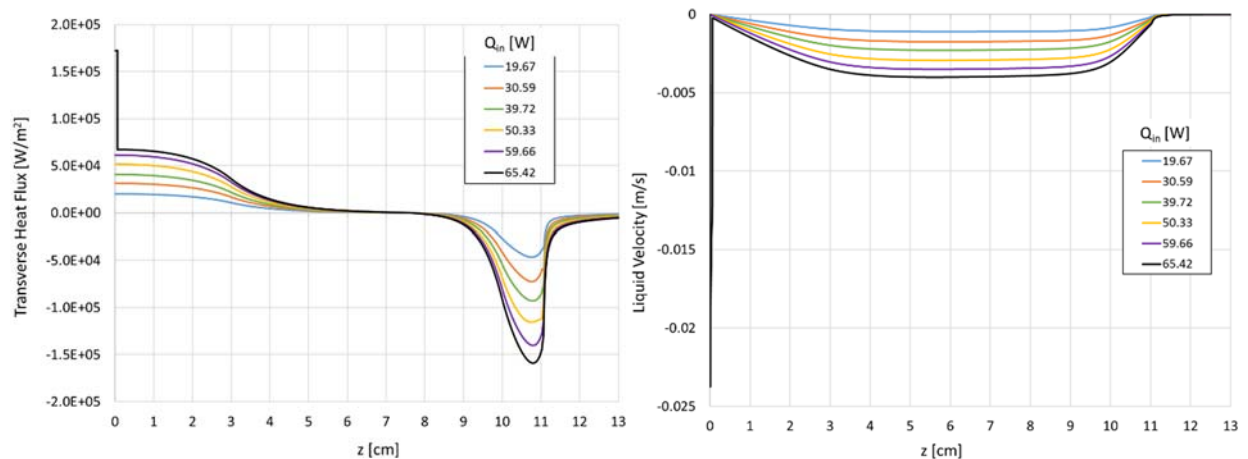
Figure 88: Transverse Heat flux profile (left) and liquid velocity (right) for water at 10.5°

There was a clear difference between the heat flux in the evaporator and condenser. The evaporator was fairly uniform until dry-out while the condenser had a peak just before the liquid pool. The combination of the steep temperature gradient in that region and the nearly step change in thermal resistance created a large peak heat flux. The consequence of the heat flux spike in the

153

corner flow region was obvious in the liquid velocity profile. The large heat flux spike in the corner flow region was due to a decrease in thermal resistance from liquid recession. The estimated thermal resistance of the corner flow region was approximately 30% that of accommodation flow.

To gain insight into the dynamics of dry-out in grooved wicks, short section of corner flow was analyzed. The steep velocity gradient and step change transition region hinted that inertial effects need conside ration. The two terms contributing to the velocity gradient in the continuity equation are shown below,

$$\frac{du_l}{dz} = \underbrace{\frac{-m'' L_{REV}}{\rho_l A_l}}_{\text{Evaporation Term}} - \underbrace{\frac{u_l}{A_l}\frac{dA_l}{dz}}_{\text{Area Gradient Term}} \tag{68}$$

Figure 89 shows the axial distribution of these two terms during accommodation flow. The area gradient term was negligible until the liquid pool. Here the sharp increase in area strongly reduces the liquid velocity.
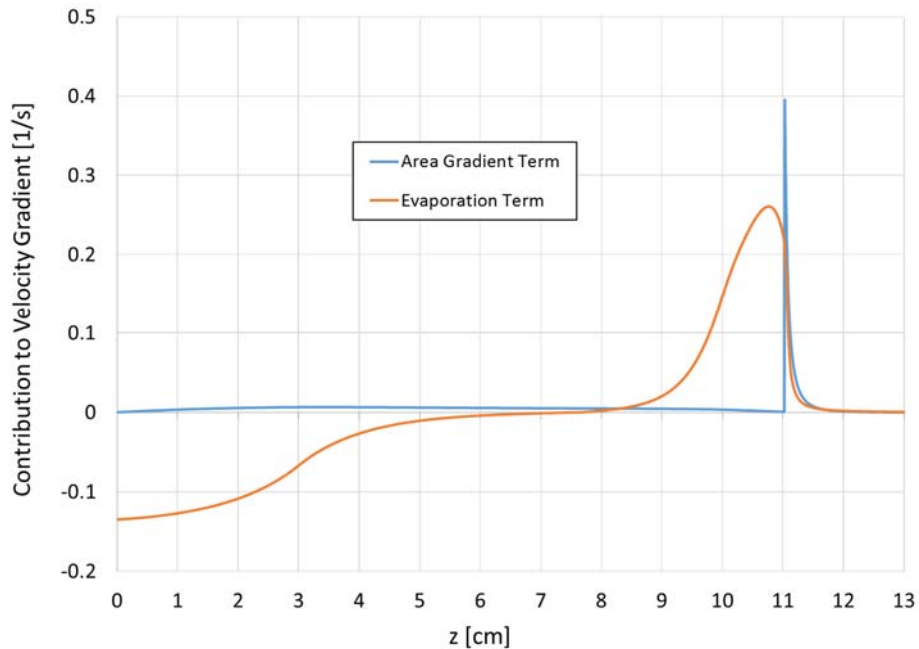
Figure 89: Comparison of terms in continuity equations for accommodation flow

In Section 6.5.1, a change in flow regime needed special treatment due to inertial effects. This procedure wasn't necessary in the liquid pool. The liquid area gradient in the pool was constant, large, and not discontinuous so that any error in velocity calculations were mitigated at each subsequent point along the pool. The area gradient in the accommodation region was negligible, and could not compensate for the error created at the transition without special treatment. Figure 90 shows the same continuity terms in the corner flow region at the predicted maximum heat transport for the same 10.5° water case.
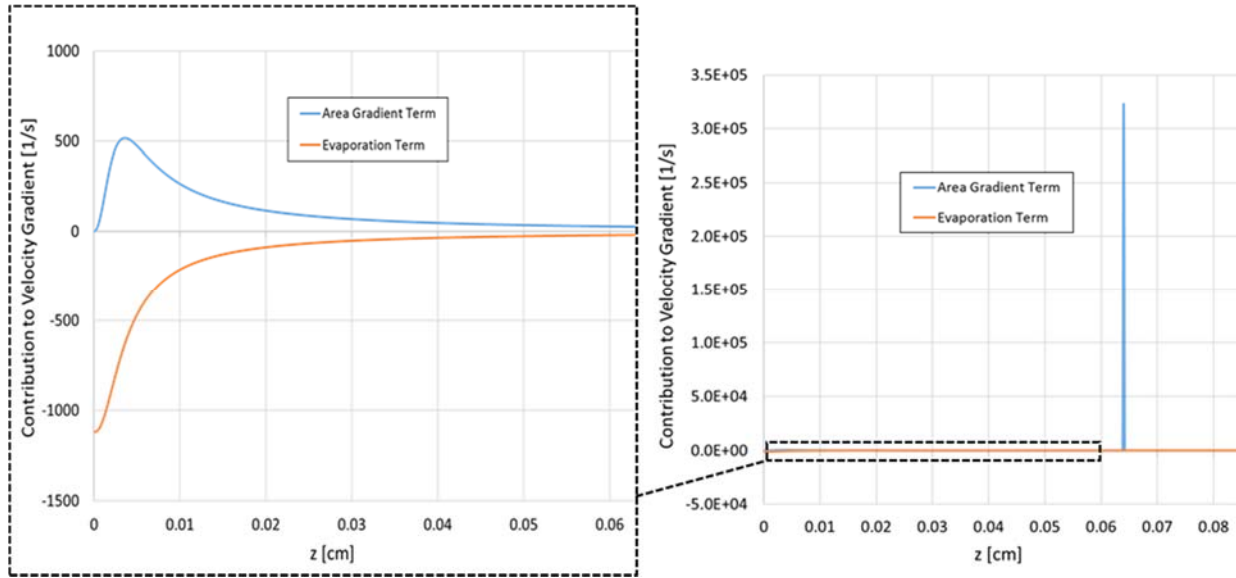
Figure 90: Comparison of continuity terms in corner flow

On the right of the figure, the large spike from the area gradient term completely dominates. The values are also six orders of magnitude greater that the spike in the liquid pool. This spike was due to the imposed boundary condition at the transition region. Large velocities created in the corner flow region due to high heat fluxes and small cross-sectional are reduced by the large change in area. The extremely large magnitude of this spike was due in part to the fact that the transition region was confined to one single length increment. Instead of a gradual process the full transition was forced to occur all at once. On the left of Figure 90, the area gradient term was clearly significant even before the transition region. This was due to the fact that corner flow changes curvature by changing its receded distance into the groove corner. The cross-sectional area and curvature have a greater impact on each other. The contributions to the pressure gradient of different terms were also analyzed and shown below,

$$\frac{dP_l}{dz} = -\underbrace{\frac{\rho_l u_l^2}{A_l}\frac{dA_l}{dz}}_{\text{Area Gradient}} - \underbrace{\rho_l 2u_l\frac{du_l}{dz}}_{\text{Velocity Gradient}} + \underbrace{\frac{1}{A_l}\Big[|\tau_{lw}|L_{lw} + |\tau_{\text{int}}|L_{\text{int}}\Big]}_{\text{Shear Stress}} + \underbrace{\rho_l g \sin\phi}_{\text{Gravity}} \qquad (69)$$

156

Figure 91 shows three of the four terms (gravity was left out of the analysis since it is constant).
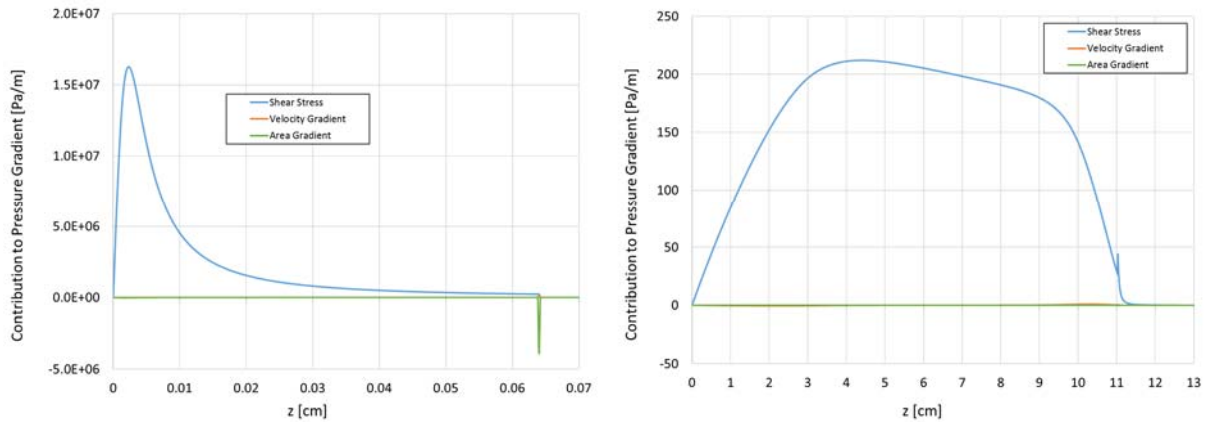
Figure 91: Corner flow dry-out on (left) and accommodation flow (right)

The shear stress term was obviously dominant in accommodation flow. In corner flow, the shear stress was still dominant except at the transition region. The magnitude of the shear stress in the corner flow region was also five orders of magnitude greater than anywhere in the accommodation region.

This analysis helped explain why the corner flow region was so short in the experiments. Not only does it inherently have higher friction (Po =54 vs. Po≈16 for a rectangular channel), but it has a much smaller, by two orders of magnitude, cross-sectional area. This added flow resistance was magnified by non-uniform evaporation due to a lower thermal resistance.

6.9.2   IAS

6.9.2.1   Closure

Simplified representations of the deposits were strategically developed to analyze their effect on heat pipe performance. Experimental measurements helped estimate the thermal resistances in the flat heat pipe. Since some properties of the coating, such as permeability, were still unknown these properties were determined as closure to match the experimental dry-out data. The goal was to understand how liquid transport in a coating effects a heat pipe, not necessarily how the coating actually transports the liquid. This method allowed the study of the thermal performance and dry-out dynamics of the fluid.

The thermal conductivity of the effective IAS media was chosen to be 1 W/m·K, for simplicity and to be close to that of water. The minimum pore size used in the water modeling was also copied for a more direct comparison with water. The two flow regimes, corner flow and coating flow, were also assigned the same overall possible capillary pressure difference (same r_{min} and r_{max}) to delineate performance enhancement mechanisms.

The remaining unknowns in the model were, the film thickness t_{film} and the permeability, K. A similar strategy to the water closure method was adopted. The goal of the closure strategy was to find a film thickness and permeability that fit perfectly for one fluid concentration and then use those values for the other concentrations. IAS 3.1 was chosen as the closure fluid, being the middle data set like 10.5° was for water. However, the fit was done so that IAS 3.1 reached dry-out with coating flow at the very end of its possible experimental range. This change was made because the adjacent concentration 3.05 reached dry-out in the same range. It was assumed 3.05

158

underperformed 3.1, so this would allow both fluids to fit in the same range. The two unknown parameters had to be iterated manually. The process is outlined below,

Procedure

1. Start with a t_{film}

2. Find permeability, K, for IAS 3.1 to achieve dry-out at the end the experimental range.

3. Calculate other concentrations dry-out in their respective experimental ranges

4. If not, adjust $t_{film,}$ and find new permeability

After several attempts, a successful set was obtained. The values are printed below,

$$K = 2.19 \times 10^{-12} m^2$$
$$t_{film} = 5 \mu m$$

(70)

6.9.2.2 Dry-out Validation

The effect of the film thickness was immediately apparent during the iterations. The film thickness primarily affected the thermal resistance of the groove. A thinner film reduced the thermal resistance in the coating flow compared to the accommodation flow and causing non-uniform evaporation similar to corner flow. The effects of non-uniform evaporation are discussed later in this section.

The dry-out predictions for the accommodation model and the coating flow model are shown in Figure 92.
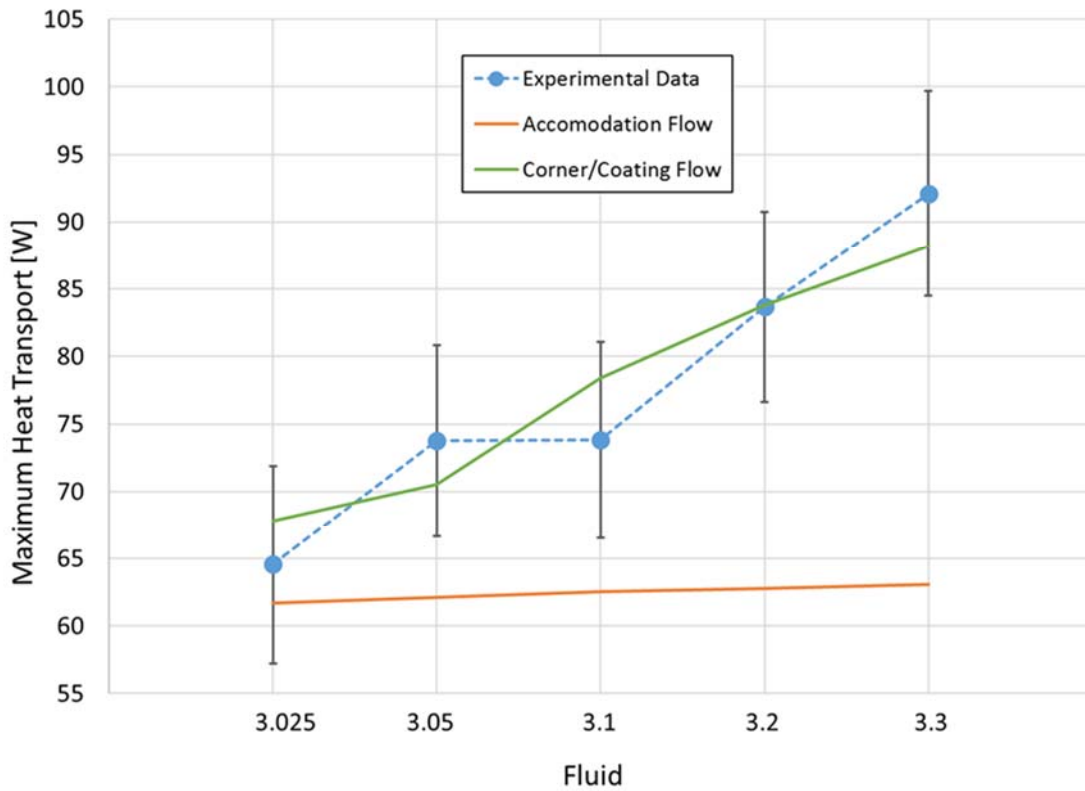
Figure 92: Validation of maximum heat transport using closure properties for different IAS fluids

The dry-out data and length of the coating flow is tabulated below in Table 15. Although the dry-out points were fitted, the maximum length of the coating predicted by the model was short by 50%. However, the lengths of these coatings are significantly longer than for corner flow due to the large flow area in the coating. Another important observation was that the maximum heat transport of the accommodation flow was actually less than it was for water. The reasons for this behavior was explored and the analysis is discussed in the following sections.

*Table 15: Dry-out data for IAS fluids (*This water test was at 10.5 and cooling flow rate 1.5L/min)*

Fluid	Maximum Heat Transport [W]			Max Coating Length [mm]	
	Experiment (Average)	Model (Accomodation)	Model (Corner/Coating)	Experiment	Model (Corner/Coating)
Water*	64.46	63.73	65.42	1.4	0.6
3.025	64.55	61.72	67.80	1.6	1.3
3.05	73.75	62.11	70.50	3.8	2.1
3.1	73.80	62.53	78.42	6.7	3.2
3.2	83.68	62.80	83.80	8.9	4.3
3.3	92.10	63.05	88.20	11.4	5.2

6.9.2.3   Axial Temperature Profiles

The axial temperature profiles for IAS utilized the coating thickness and Effective Length Coverage to estimate thermal resistance. The experimental temperature profiles for all five IAS fluids were compared with model predictions. Figure 93 through Figure 97 show the comparison for the five IAS concentrations. The temperature profiles at the higher fluxes for every concentration surprisingly had positive temperature gradients at the beginning of the evaporator which peaked and then resumed the normal negative gradient. At lower concentrations, such as IAS 3.025 in Figure 93, the initial positive gradient appears at every power level. At higher concentrations, such as IAS 3.3 in Figure 97. There was a clear transition between extremely flat evaporator temperatures at lower heat fluxes and rounded profile at higher fluxes in the coating flow regime. The temperature profiles were much less accurate at the higher fluxes possibly due to error in estimations of the thermal resistance. The temperature profile match in the accommodation models demonstrates a thick, low conductivity coating can still improve thermal resistance.
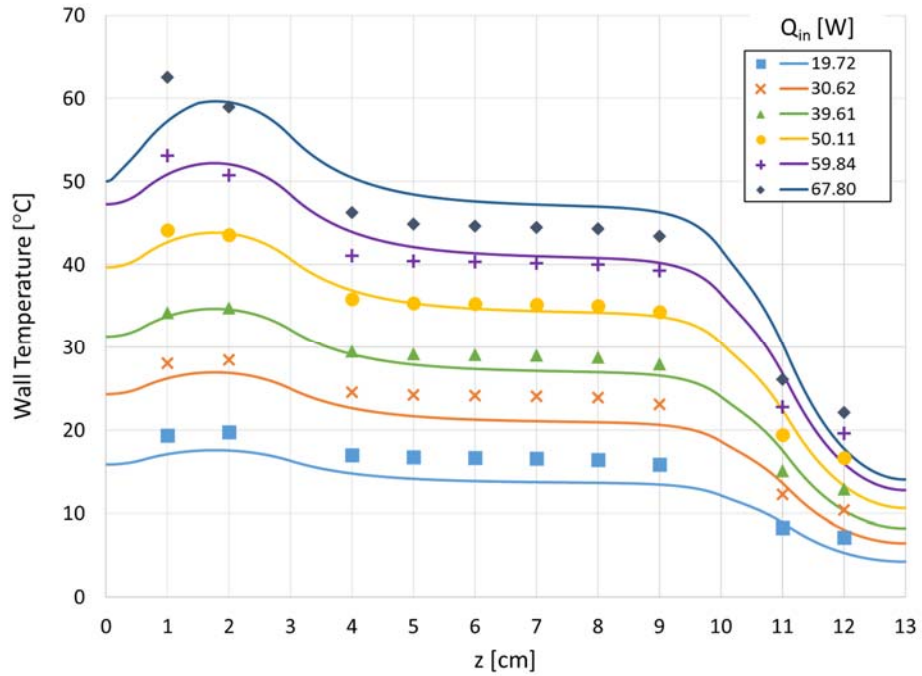
Figure 93: Model predictions of axial temperature profiles for IAS 3.025 for various experimental input powers.
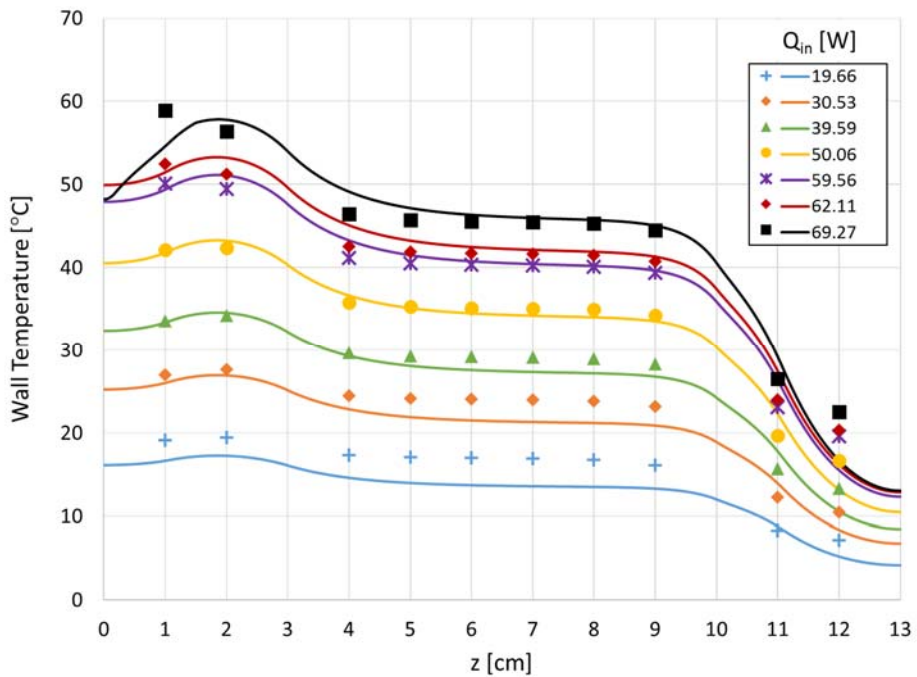
Figure 94: Model predictions of axial temperature profiles for IAS 3.05 for various experimental input powers.

162
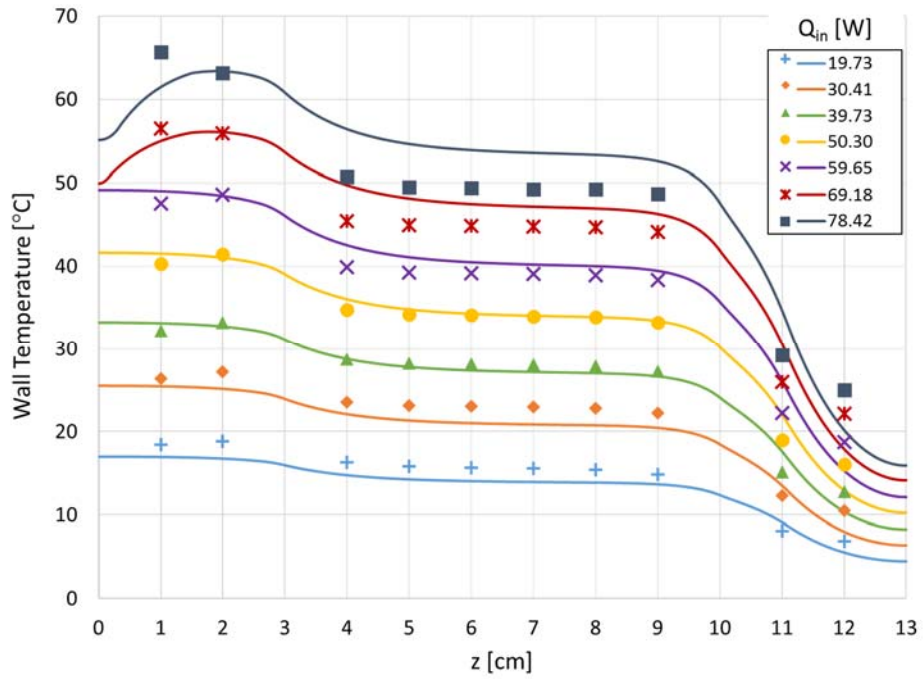
Figure 95: Model predictions of axial temperature profiles for IAS 3.1 for various experimental input powers.
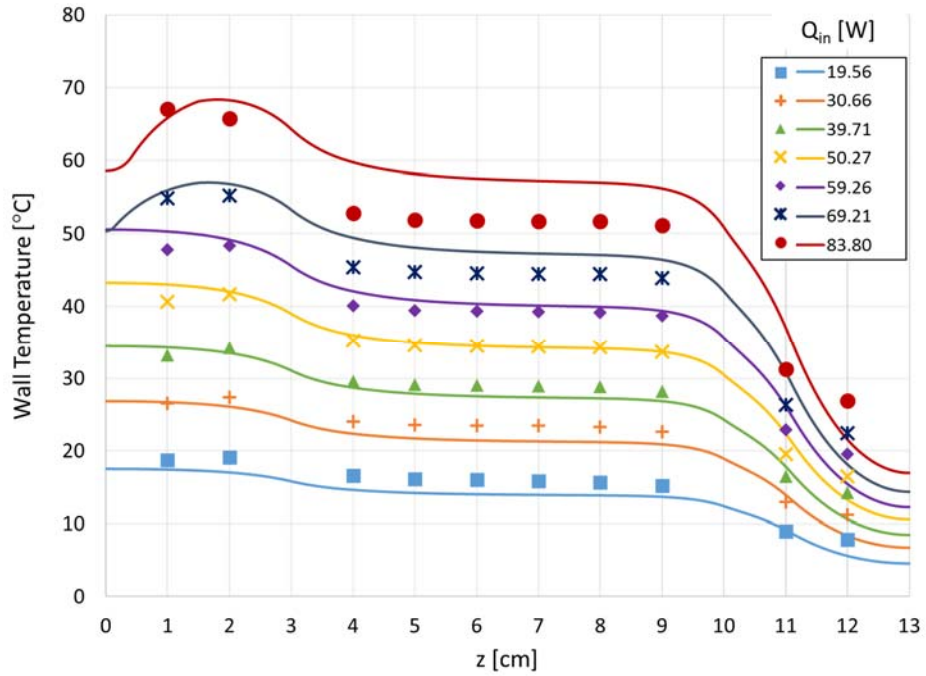
Figure 96: Model predictions of axial temperature profiles for IAS 3.2 for various experimental input powers.
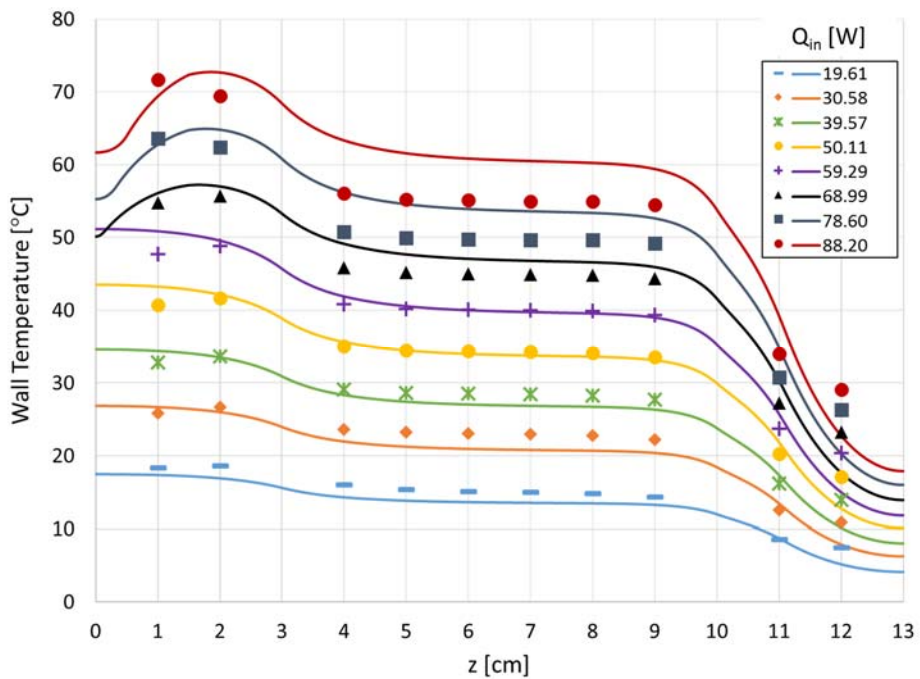
Figure 97: Model predictions of axial temperature profiles for IAS 3.3 for various experimental input powers.

6.9.2.4   Thermal Resistance

The axial thermal resistance per unit length for the different IAS concentrations in accommodation flow is shown in Figure 98. The effect of the coating and effective coverage length portrays the coating analysis done in Chapter 4. The lower concentrations, with lower coating thicknesses reached the lowest thermal resistance. However, this region only exists over a small region. The thermal resistance profiles in Figure 99 are for dry-out of each concentration. The addition of a third step in resistance, also the lowest resistance, is visible due to the exposer of the coating flow. The positive gradients in the temperature profiles were clarified. The low thermal resistance in coating flow was responsible for the profile at higher powers. At lower powers, however, the lower concentration 3.025, has a curved profile in the evaporator because of its non-uniform *and* thin coating. This shifts heat toward that region.
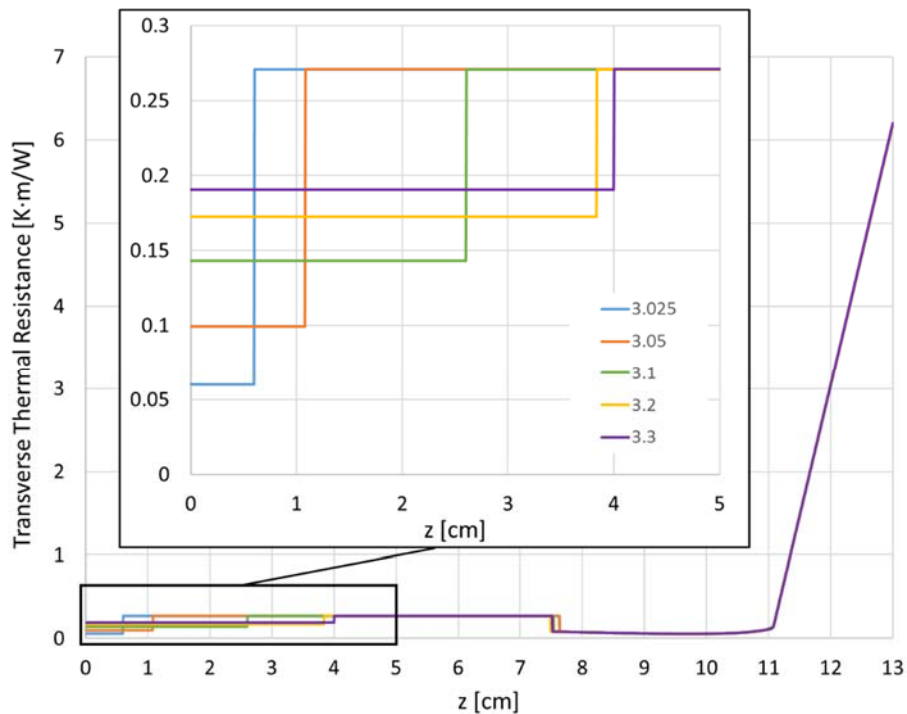
Figure 98: Thermal resistance at the same power
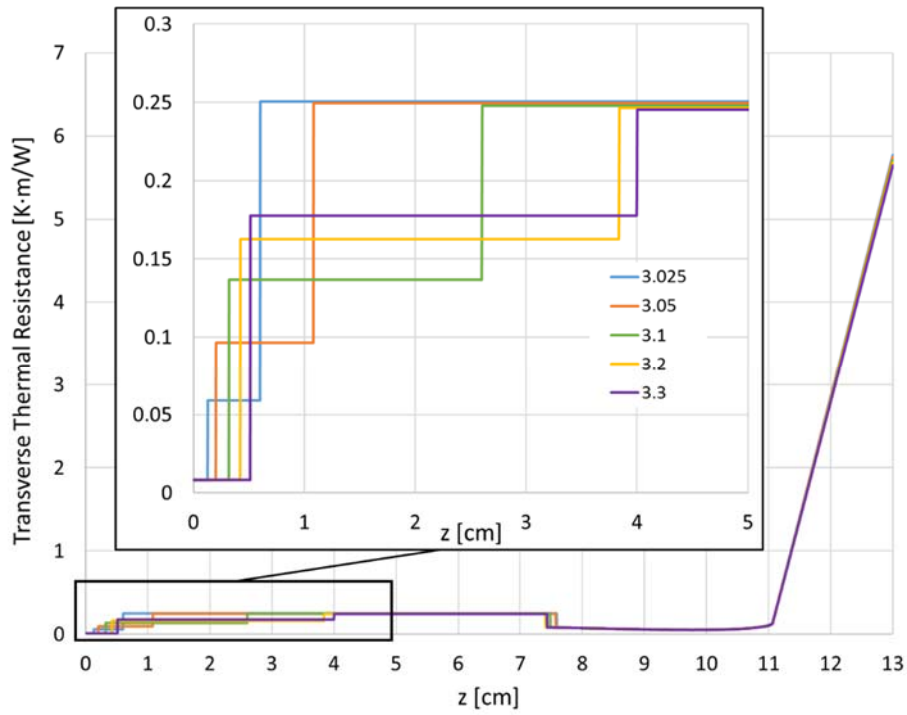
Figure 99: Thermal resistance at dry-out

6.9.2.5   Heat Flux

The effects of the different thermal resistance profiles, which was a result of the coating, was observed in the transverse heat flux profiles. Figure 100 shows the heat flux profiles for the IAS fluids at dry-out.

166
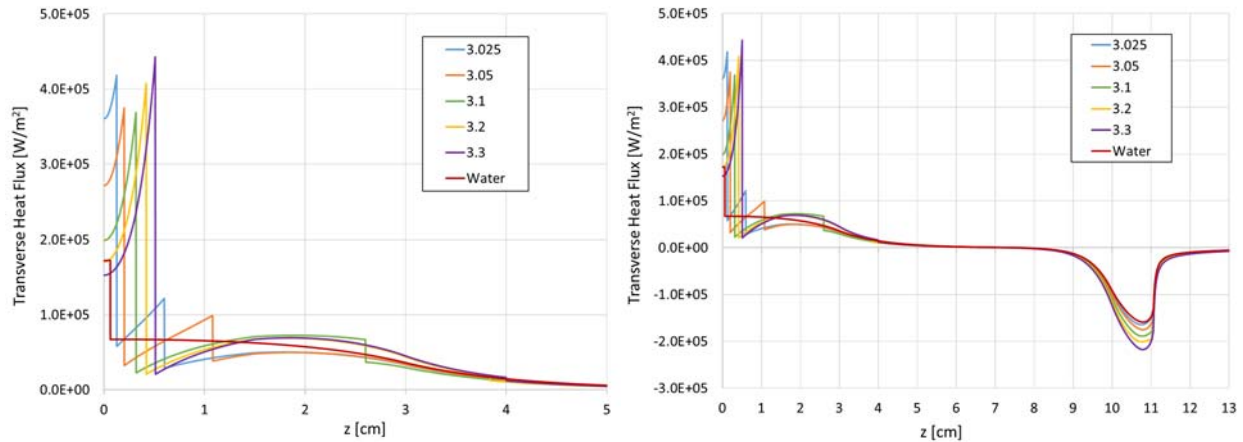
Figure 100: Heat fluid profiles for dry-out for IAS of different concentrations

Each fluid was capable of generating the same maximum capillary pressure difference across the heat pipe. However, the liquid pressure drop that was generated along the heat pipe was not the same. Pressure drop is cumulative from the beginning of the evaporator to the end of the condenser. Shifting evaporation towards the start of the evaporaror, seen with the low concnetration fluids, creates large velocity spikes and pressure drops, since the pressure drop is proportional to the velocity squared. Velocity profiles for the IAS fluids are shown in Figure 101.
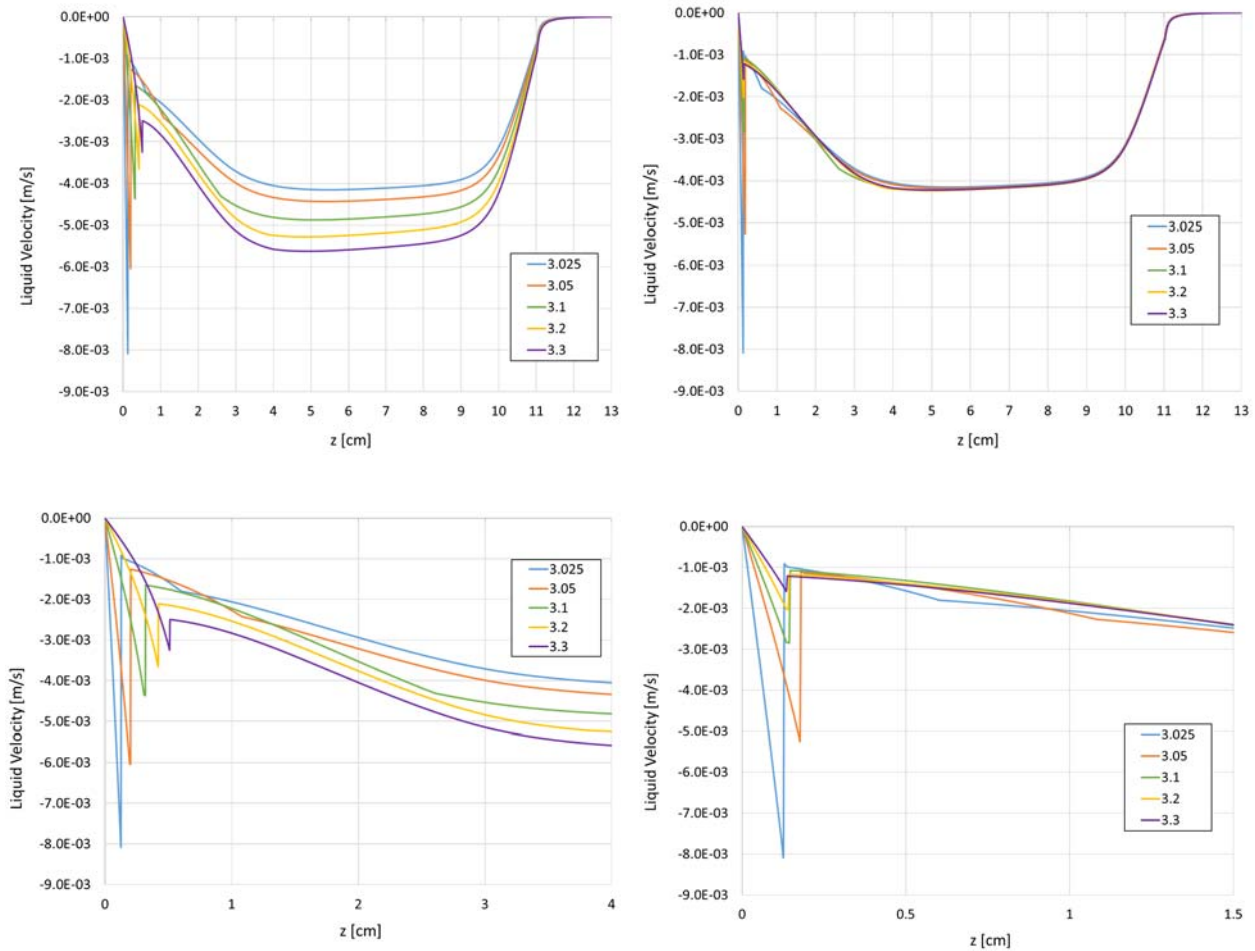
Figure 101: Velocity profiles for the IAS fluids at dry-out (left) and for the same power in corner flow (right)

On the right, the heat transferred was the same for each fluid. However, the lower thermal resistances created by coating flow in the low concentration fluid spike the velocity. The fluids with uniform coatings don't have as large of a difference in thermal resistance as a coating with pore coverage. In the profiles on the left, again, each fluid was generating the same maximum capillary pressure. The velocity was greater for IAS 3.3 for example over most of the heat pipe. However, pressure drop generated in the coating early, due to lower flow area and higher velocity, causes the flow regime to transition to accommodation flow, effectively increasing the capillary

168

length of that region. So, not only was the accommodation region longer, the groove was forced to transport a larger mass flow rate to supply liquid to the enhanced evaporation there.

6.9.3   Summary of Findings

A coupled hydrodynamic and thermal model was developed to study the effects of the IAS coating on capillary flow in a rectangular groove. Experimental closure was used to help set the coating geometry, but the permeability and film thickness were fit to the dry-out data. The dry-lengths were 50% lower that the experimental values but still up to 10 times that of that of water. The temperature profiles matched well for the accommodation flow regime. In corner or coating flow the model over predicted the temperatures.

6.9.3.1   Water

The findings from analysis of the water model are listed below.

1. Using minimum wetting angle as closure helped validate the dry-out data and did not have any effect on the temperature profiles due to the simplicity the nodal network.

2. Evaporation and condensation occurs over the entire length of the heat pipe. There is no true internal adiabatic region.

3. Rectangular channels are chosen over triangular channels because they have twice the cross sectional and inherently less shear stress. The short transition from across the "dead zone" to corner flow creates a larger gradient in thermal resistance and heat flux.

4. Non-uniform heat transfer away from the adiabatic region increases pressure drop accumulated in the accommodation region. Because corner flow occurs at the tip of the evaporator, a larger pressure drop is created over the accommodation regions and reduces

the total capillary length. Corner flow is essentially self-limiting in rectangular grooves that have a heated accommodation region.

5. The conditions in the flat heat pipe caused the area gradient term to be very significant due to the high velocities, large friction factor, and small cross-sectional area.

6. The error at higher powers could be due to the breakdown of the uniform heat flux assumption due to the large difference in heat transfer coefficients for corner and accommodation flow.

6.9.3.2 IAS

The trends seen in corner flow were highlighted by the analysis of IAS which is summarized below.

1. Positive temperature gradients in the first half of the evaporator were observed due to the incredibly high evaporation in the coating flow. As a check, the effect of a heat transfer boundary condition should be investigated.

2. Non-uniform evaporation during the accommodation region causes premature dry-out.

3. During the coating flow, the accommodation region has fixed curvature at its boundaries, r_{ming} and $r_{max,}$, so the pressure drop along the accommodation region must be constant. Its length varies based the mass flux profile along the groove which is linked to the corner flow.

4. The large flow area in the coating helped lower the velocity spike at the transition.

5. Thick coatings increase the maximum heat transport for several reasons. 1) The area ratio in the transition is much closer to unity 2) A uniform coating prevents non-uniform mass flux even with coating flow. Since the thermal resistance on the top of the fin is more

170

comparable to the coating flow that a bare groove. 3) The coating flow thermal resistance is larger because of the coating on the fin top.

7 Conclusions and Recommendations

7.1 Conclusions

The stated goal of this report was to study the deposition mechanisms of IAS in an *operating* heat pipe and to use that information to represent IAS surface coatings in a heat pipe. The dry-out dynamics of IAS deposits could then be investigated through hydrodynamic and thermal modeling. These goals were accomplished and embodied by the following results.

1. A flat grooved heat pipe experiment was designed successfully and provided reliable performance data for different IAS concentrations, through careful consideration of instrumentation and vacuum charging.

2. Surprising observations of the deposition patterns in a grooved wick yielded valuable insight into the fundamental heat transfer concepts in which the fluid enhances heat pipe thermal performance, such as addition of evaporative surface area on the groove fins and enhanced wetting during dry-out.

3. The flat heat pipe observations were complimented with individual evaporating droplet studies. The role of interesting dynamics of the fluid, including the role of advective flow in a heat pipe, or the creeping nature of salt deposits, in enhancing heat transfer were identified.

4. These observations were then utilized to develop a heat pipe model to study the effects of the deposition on heat pipe thermal resistance and dry-out limit theoretically.

5. Strategic application of experimental closure to the model as well as clever treatment of different flow regimes and boundary conditions lead to understanding of the effects of coating thickness and coverage in the evaporator.

6. Detailed analysis of hydrodynamics of corner flows revealed why they failed to provide any capillary length and the detrimental effects non-uniform heat transfer on the maximum heat transport capability of a heat pipe.

7.2 Recommendations

The broad scope of IAS research, was overwhelming. The tendency of past researchers, including the author of this work, to attempt to develop novel heat pipe concepts or modeling techniques *while* investigating the intricate complexities of a fluid of IAS can obscure the benefit of both. In general, IAS research has taken a top down approach due to its mystery. After several recent reports on IAS and affiliates, enough is known about the fluid to now take a bottom-up approach. Heat pipe performance enhancement with salt deposits has potential but needs to be simplified before to can ever be practically developed. Recommendations for future work presented here follow the same outline as this report.

7.2.1 IAS Deposition

The delineation of deposition characteristics of different constituents in IAS was only qualitatively addressed in this work but the observations hinted that not all of chemicals in IAS are necessary and merely distract. In addition, some compounds that have unique qualities, particularly hygroscopic sodium chromate are underrepresented in IAS and should be investigated individually. Segregation of IAS into "chromates" and "permanganates" was useful but its

173

recommended that study of combinations of compound be postponed until equal parts of individual components are understood. Sodium chromate clearly doesn't belong with the other chromates and would be a good candidate for further investigation.

7.2.2   Experiments

Modular heat pips are very useful for research that requires constant reproduction of experimental conditions. Having a reliable, vapor chamber that can be fitted with modular wicks is convenient. Taking the time to build an accurate and re-usable testing device saves valuable time and helps reduce inconclusive work. Unlike wick research, advanced working fluids are more quickly and cheaply obtained and easily modified. The advanced manufacturing techniques needed to make a wick prevent volume testing. Development of methods to accomplish high volume testing of working fluids would take advantage full advantage of this.

Charging advanced working fluids presents a lot of challenges in terms of contamination for subsequent tests, cleaning time, and wear on equipment. A smart compliment to a modular heat pipe experiment would be development of a charging station designed for this purpose.

7.2.3   Modeling

The model developed in this work can easily be applied to other advanced working fluids or porous coatings. This model can be easily further developed if applied to a heat pipe where the working fluid properties or porous layer geometry is known. The secondary flow regime and moving boundary condition could be used for a nanofluid coating for example. The treatment of the transition region could be improved by extending it over a longer region defined by the scaling argument by Nilson [106].

Thermal resistance network models are limited to homogenous domains or domains where there are distinct boundaries between different geometries. Study of different flow regimes, especially if they vary significantly in the axial direction require more advance thermal modeling. In addition, the prescription of a convention boundary condition in the evaporator (as was done in the condenser in this work) may be required if the differences in heat transfer coefficient are large.

The work done in this report provided a new look into modifications of current experimental and theoretical investigations that have to be made when studying advanced working fluids in phase change devices.

References

[1] Reay, D., McGlen, R., and Kew, P., <u>Heat pipes: Theory, design and applications</u>, 6th ed., Butterworth-Heinemann publisher, 2013.

[2] Faghri, A., <u>Heat pipe science and technology</u>, Global Digital Press, 1995.

[3] Chi, S., <u>Heat pipe theory and practice</u>, McGraw-Hill Inc., U.S., 1976.

[4] http://www.frostytech.com/articleview.cfm?articleID=2466, "Heatpipe Wick Structures Exposed: Sintered, Groove, and Mesh," accessed prior to 12/13/2016. (author's name unavailable).

[5] Faghri, A., "Review and advances in heat pipe science and technology," *Journal of Heat Transfer,* 134(12), p. 123001, 2012.

[6] Carey, V. P., *Liquid-vapor phase-change phenomena*, 1st Edition, Taylor & Francis, Inc 1992.

[7] Wayner, P., Kao, Y., and LaCroix, L., "The interline heat-transfer coefficient of an evaporating wetting film," *International Journal of Heat and Mass Transfer*, 19(5), pp. 487-492, 1976.

[8] Schonberg, J., DasGupta, S., and Wayner Jr, P., "An augmented Young-Laplace mod el of an evaporating meniscus in a microchannel with high heat flux," *Experimental thermal and fluid science*, 10(2), pp. 163-170, 1995.

[9] Mirzamoghadam, A., and Catton, I., "A physical model of the evaporating meniscus," *Journal of Heat Transfer*, 110(1), pp. 201-207, 1988.

[10] Wang, H., Garimella, S. V., and Murthy, J. Y., "Characteristics of an evaporating thin film in a microchannel," *International Journal of Heat and Mass Transfer*, 50(19-20), pp. 3933-3942, 2007.

[11] Stephan, P. C., and Busse, C. A., "Analysis of the Heat-Transfer Coefficient of Grooved Heat Pipe Evaporator Walls," International Journal of Heat and Mass Transfer, 35(2), pp. 383-391, 1992.

[12] Cheng, P., Dong, J., Thompson, S., and Ma, H., "Heat transfer in the bulk and thin film fluid regions of a rectangular micro groove," *J Thermophys Heat Tr*, 26(1), pp. 108-114, 2012.

[13] Prasher, R. S., "A simplified conduction based modeling scheme for design sensitivity study of thermal solution utilizing heat pipe and vapor chamber technology," *Journal of Electronic Packaging*, 125(3), pp. 378-385, 2003.

[14] Plawsky, J., Fedorov, A., Garimella, S., Ma, H., Maroo, S., Chen, L., and Nam, Y., "Nano- and Microstructures for Thin-Film Evaporation—A Review," *Nanoscale and Microscale Thermophysical Engineering*, 18(3), pp. 251-269, 2014.

[15] Li, Y., He, H.-f., and Zeng, Z.-x., "Evaporation and condensation heat transfer in a heat pipe with a sintered-grooved composite wick," *Applied Thermal Engineering*, 50(1), pp. 342-351, 2013.

[16] Deng, D., Tang, Y., Huang, G., Lu, L., and Yuan, D., "Characterization of capillary performance of composite wicks for two-phase heat transfer devices," *International Journal of Heat and Mass Transfer*, 56(1), pp. 283-293, 2013.

[17] Franchi, G., and Huang, X., "Development of composite wicks for heat pipe performance enhancement," *Heat Transfer Engineering*, 29(10), pp. 873-884, 2008.

[18] Hwang, G., Kaviany, M., Anderson, W., and Zuo, J., "Modulated wick heat pipe," *International Journal of Heat and Mass Transfer*, 50(7), pp. 1420-1434, 2007.

[19] Xu, J., Ji, X., Yang, W., and Zhao, Z., "Modulated porous wick evaporator for loop heat pipes: Experiment," *International Journal of Heat and Mass Transfer*, 72(0), pp. 163-176, 2014.

[20] Hwang, G., Fleming, E., Carne, B., Sharratt, S., Nam, Y., Dussinger, P., Ju, Y., and Kaviany, M., "Multi-artery heat-pipe spreader: Lateral liquid supply," *International Journal of Heat and Mass Transfer*, 54(11), pp. 2334-2340, 2011.

[21] Hwang, G., Nam, Y., Fleming, E., Dussinger, P., Ju, Y., and Kaviany, M., "Multi-artery heat pipe spreader: experiment," *International Journal of Heat and Mass Transfer*, 53(13), pp. 2662-2669, 2010.

[22] Min, D., Hwang, G., and Kaviany, M., "Multi-artery, heat-pipe spreader," *International Journal of Heat and Mass Transfer,* 52(3), pp. 629-635, 2009.

[23] Ponnappan, R., Ramalingam, M., Johnson, J., and Mahefkey, E., "Evaporator critical heat flux in the double-wall artery heat pipe," *Experimental Thermal and Fluid Science*, 2(4), pp. 450-464, 1989.

[24] Khrustalev, D., and Faghri, A., "Enhanced flat miniature axially grooved heat pipe," *Journal of Heat Transfer*, 118(1), pp. 261-264, 1996.

[25] Vasil'ev, L., Grakovich, L., Rabetskii, M., and Tulin, D., "Investigation of heat transfer by evaporation in capillary grooves with a porous coating," *Journal of Engineering Physics and Thermophysics*, 85(2), pp. 407-414, 2012.

[26] Wang, J., and Catton, I., "Enhanced evaporation heat transfer in triangular grooves covered with a thin fine porous layer," *Applied Thermal Engineering*, 21(17), pp. 1721-1737, 2001.

[27] Cai, Q., and Chen, Y.-C., "Investigations of biporous wick structure dryout," *Journal of Heat Transfer,* 134(2), p. 021503, 2012.

[28] Reilly, S., "Optimization of Phase Change Heat Transfer in Biporous Media," UCLA Ph.D. report, University of California at Los Angeles, 2013, http://escholarship.org/uc/item/59k9m9bt.

[29] Vadnjal, A., and Catton, I., "Heat Removal Model for a Thin Bi-Porous Wick," *Proc. International Heat Transfer Conference 13*, Sydney, Australia, Begel House Inc., 13-19 August 2006.

[30] Semenic, T., and Catton, I., "Experimental study of biporous wicks for high heat flux applications," *International Journal of Heat and Mass Transfer*, 52(21), pp. 5113-5121, 2009.

[31] Ranjan, R., Garimella, S. V., Murthy, J. Y., and Yazawa, K., "Assessment of nanostructured capillary wicks for passive two-phase heat transport," *Nanoscale and Microscale Thermophysical Engineering*, 15(3), pp. 179-194, 2011.

[32] Ranjan, R., Patel, A., Garimella, S. V., and Murthy, J. Y., "Wicking and thermal characteristics of micropillared structures for use in passive heat spreaders," *International Journal of Heat and Mass Transfer*, 55(4), pp. 586-596, 2012.

[33] Nam, Y., and Ju, Y. S., "Fabrication and characterization of superhydrophilic Cu microposts for micro heat pipes," *Proc. PowerMEMS*, Washington, D.C., pp. 1-4, 2009.

[34] Weibel, J. A., Kim, S. S., Fisher, T. S., and Garimella, S. V., "Experimental characterization of capillary-fed carbon nanotube vapor chamber wicks," *Journal of Heat Transfer,* 135(2), p. 021501, 2013.

[35] Cleveland, C., Moghaddam, S., and Orazem, M. E., "Nanometer-Scale Corrosion of Copper in De-Aerated Deionized Water," *Journal of The Electrochemical Society*, 161(3), pp. C107-C114, 2014.

[36] Kiatsiriroat, T., Nuntaphan, A., and Tiansuwan, J., "Thermal performance enhancement of thermosyphon heat pipe with binary working fluids," *Experimental Heat Transfer*, 13(2), pp. 137-152, 2000.

[37] Savino, R., Cecere, A., and Di Paola, R., "Surface tension-driven flow in wickless heat pipes with self-rewetting fluids," *International Journal of Heat and Fluid Flow*, 30(2), pp. 380-388, 2009.

[38] Wu, J., and Zhao, J., "A review of nanofluid heat transfer and critical heat flux enhancement—research gap to engineering application," *Progress in Nuclear Energy*, 66, pp. 13-24, 2013.

[39] Ahn, H. S., and Kim, M. H., "A review on critical heat flux enhancement with nanofluids and surface modification," *Journal of Heat Transfer*, 134(2), p. 024001, 2012.

[40] Kim, H. D., and Kim, M. H., "Effect of nanoparticle deposition on capillary wicking that influences the critical heat flux in nanofluids," *Applied Physics Letters*, 91(1), p. 014104, 2007.

[41] Sureshkumar, R., Mohideen, S. T., and Nethaji, N., "Heat transfer characteristics of nanofluids in heat pipes: A review," *Renewable and Sustainable Energy Reviews*, 20, pp. 397-410, 2013.

[42] Liu, Z.-H., Li, Y.-Y., and Bao, R., "Thermal performance of inclined grooved heat pipes using nanofluids," *International Journal of Thermal Sciences,* 49(9), pp. 1680-1687, 2010.

[43] Solomon, A. B., Ramachandran, K., and Pillai, B., "Thermal performance of a heat pipe with nanoparticles coated wick," *Applied Thermal Engineering*, 36, pp. 106-112, 2012.

[44] Do, K. H., and Jang, S. P., "Effect of nanofluids on the thermal performance of a flat micro heat pipe with a rectangular grooved wick," *International Journal of Heat and Mass Transfer*, 53(9), pp. 2183-2192, 2010.

[45] Amouzegar Ashtiani, L., "A Multi-scale Study of Inorganic Aqueous Solution (IAS) for Advanced Heat Pipe Applications," Ph.D. Report, University of California at Los Angeles, 2015, http://escholarship.org/uc/item/2pb9s92v.

[46] Qu, Y., "Superconducting heat transfer medium," U.S. Patent 6,132,823, Oct 17, 2000.

[47] Yao, Q. "Investigation of the Use of an Inorganic Aqueous Solution (IAS) in Phase Change Heat Transfer Devices," Ph.D. report, University of California at Los Angeles, 2016, http://escholarship.org/uc/item/805215b9#page-1.

[48] Amouzegar, Ladan, "A Multi-scale of Inorganic Aqueous Solution (IAS) for Advanced Heat Pipe Applications," Ph.D. thesis, University of California at Los Angeles, 2015.

[49] Catton, I., Tao, H. T., Reilly, S. W., Amouzegar, L., Yao, Q., Stubblebine, M. J., and Supowit, J., "Inorganic aqueous solution (ias) for phase-change heat transfer medium," U.S. Patent Application US201400090817, 3 Apr 2014.

[50] Reilly, S. W., and Catton, I., "Utilization of advanced working fluids with biporous evaporators," *Journal of Thermal Science and Engineering Applications,* 3(2), p. 021006, 2011.

[51] Karimi, A., Reilly, S., and Catton, I., "Enhanced performance of a thermal ground plane utilizing an Inorganic Aqueous Solution," *Proc. Thermal and Thermomechanical Phenomena in Electronic Systems (ITherm),* pp. 1235-1243, 2014.

[52] Stubblebine, M., Reilly, S., Yao, Q., and Catton, I., "Use of an Inorganic Aqueous Solution to Prevent Non-Condensable Gas Formation in Aluminum Heat Pipes," *Proc. ASME 2013 Heat Transfer Summer Conference collocated with the ASME 2013 7th International Conference on Energy Sustainability and the ASME 2013 11th International Conference on Fuel Cell Science, Engineering and Technology, American Society of Mechanical Engineers,* Minneapolis, MN, 2013.

[53] Tandon, R., Crisp, P., Ellis, J., and Baker, R., "Effect of pH on chromium (VI) species in solution," *Talanta,* 31(3), pp. 227-228, 1984.

[54] Brito, F., Ascanio, J., Mateo, S., Hernandez, C., Araujo, L., Gili, P., Martin-Zarza, P., Dominguez, S., and Mederos, A., "Equilibria of chromate (VI) species in acid medium and ab initio studies of these species," *Polyhedron,* 16(21), pp. 3835-3846, 1997.

[55] Yao, Q., Stubblebine, M., Reilly, S., Amouzegar, L., and Catton, I., "Using an Inorganic Aqueous Solution (IAS) in Copper and Aluminum Phase Change Heat Transfer Devices," *Proc. ASME 2013 International Mechanical Engineering Congress and Exposition, American Society of Mechanical Engineers*, Minneapolis, MN, 2013.

[56] Lide, D. R., CRC Handbook of Chemistry and Physics, CRC press, 2004.

[57] Supowit, J., Reilly, S., Amouzegar, L., and Catton, I., "*A Novel Inorganic Aqueous Solution and its Effect on Liquid Spreading and Freeze/Thaw Processes," Proc. ASME 2013 Heat Transfer Summer Conference collocated with the ASME 2013 7th International Conference on Energy Sustainability and the ASME 2013 11th International Conference on Fuel Cell Science, Engineering and Technology, American Society of Mechanical Engineers*, San Diego, CA, 2013.

[58] Bico, J., Thiele, U., and Quéré, D., "Wetting of textured surfaces," *Colloids and Surfaces A: Physicochemical and Engineering Aspects*, 206(1), pp. 41-46, 2002.

[59] Hay, K., and Dragila, M., "Physics of fluid spreading on rough surfaces," *Int J Numer Anal Mod*, 5, pp. 85-92, 2008.

[60] Deegan, R. D., Bakajin, O., Dupont, T. F., Huber, G., Nagel, S. R., and Witten, T. A., "Capillary flow as the cause of ring stains from dried liquid drops," *Nature*, 389(6653), pp. 827-829, 1997.

[61] Bourges-Monnier, C., and Shanahan, M., "Influence of evaporation on contact angle," *Langmuir*, 11(7), pp. 2820-2829, 1995.

[62] Deegan, R. D., Bakajin, O., Dupont, T. F., Huber, G., Nagel, S. R., and Witten, T. A., "Contact line deposits in an evaporating drop," *Physical Review E*, 62(1), p. 756, 2000.

[63] Maenosono, S., Dushkin, C., Saita, S., and Yamaguchi, Y., "Growth of a semiconductor nanoparticle ring during the drying of a suspension droplet," *Langmuir*, 15(4), pp. 957-965, 1999.

[64] Adachi, E., Dimitrov, A. S., and Nagayama, K., "Stripe patterns formed on a glass surface during droplet evaporation," *Langmuir*, 11(4), pp. 1057-1060, 1995.

[65] Hu, H., and Larson, R. G., "Analysis of the microfluid flow in an evaporating sessile droplet," *Langmuir*, 21(9), pp. 3963-3971, 2005.

[66] Ristenpart, W., Kim, P., Domingues, C., Wan, J., and Stone, H., "Influence of substrate conductivity on circulation reversal in evaporating drops," *Physical Review Letters*, 99(23), p. 234502, 2007.

[67] Chon, C. H., Paik, S., Tipton, J. B., and Kihm, K. D., "Effect of nanoparticle sizes and number densities on the evaporation and dryout characteristics for strongly pinned nanofluid droplets," *Langmuir*, 23(6), pp. 2953-2960, 2007.

[68] Berteloot, G., Hoang, A., Daerr, A., Kavehpour, H. P., Lequeux, F., and Limat, L., "Evaporation of a sessile droplet: Inside the coffee stain," *Journal of Colloid and Interface Science*, 370(1), pp. 155-161, 2012.

[69] Bhardwaj, R., Fang, X., and Attinger, D., "Pattern formation during the evaporation of a colloidal nanoliter drop: a numerical and experimental study," *New Journal of Physics*, 11(7), p. 075020, 2009.

[70] Bonn, N. S., Bertrand, F., and Bonn, D., "Damage due to salt crystallization in porous media," arXiv preprint arXiv:0906.2502, https://arxiv.org/abs/0906.25022009, accessed prior to 19 Dec 2016.

[71] Flatt, R. J., "Salt damage in porous materials: how high supersaturations are generated," *Journal of Crystal Growth*, 242(3), pp. 435-454, 2002.

[72] Winkler, E. M., and Singer, P. C., "Crystallization pressure of salts in stone and concrete," *Geological Society of America Bulletin*, 83(11), pp. 3509-3514, 1972.

[73] Shahidzadeh-Bonn, N., Rafaı, S., Bonn, D., and Wegdam, G., "Salt crystallization during evaporation: impact of interfacial properties," *Langmuir*, 24(16), pp. 8599-8605, 2008.

[74] Shahidzadeh, N., Schut, M. F., Desarnaud, J., Prat, M., and Bonn, D., "Salt stains from evaporating droplets," *Scientific Reports 5, Nature*, 10335, 2015.

[75] Nikolov, A., Kondiparty, K., and Wasan, D., "Nanoparticle self-structuring in a nanofluid film spreading on a solid surface," *Langmuir*, 26(11), pp. 7665-7670, 2010.

[76] Washburn, E. R., "The creeping of solutions," *The Journal of Physical Chemistry*, 31(8), pp. 1246-1248, 1927.

[77] Hazlehurst Jr, T., Martin, H., and Brewer, L., "The Creeping of Saturated Salt Solutions," *The Journal of Physical Chemistry*, 40(4), pp. 439-452, 1936.

[78] Langer, J., "Instabilities and pattern formation in crystal growth," *Reviews of Modern Physics*, 52(1), p. 1, 1980.

[79] van Enckevort, W. J., and Los, J. H., "On the creeping of saturated salt solutions," *Crystal Growth & Design*, 13(5), pp. 1838-1848, 2013.

[80] Yuan-Hui, L., and Gregory, S., "Diffusion of ions in sea water and in deep-sea sediments," *Geochimica et cosmochimica acta*, 38(5), pp. 703-714, 1974.

[81] Wong, S. C., and Chen, C. W., "Visualization experiments for groove-wicked flat-plate heat pipes with various working fluids and powder-groove evaporator," *International Journal of Heat and Mass Transfer*, 66(0), pp. 396-403, 2013.

[82] Liou, J. H., Chang, C. W., Chao, C., and Wong, S. C., "Visualization and thermal resistance measurement for the sintered mesh-wick evaporator in operating flat-plate heat pipes," *International Journal of Heat and Mass Transfer*, 53(7-8), pp. 1498-1506, 2010.

[83] "Parker O-Ring Handbook," Parker Hannifin Corporation, Cleveland, Ohio, https://www.parker.com/literature/ORD%205700%20Parker_O-Ring_Handbook.pdf, accessed prior to 14 Dec 2016.

[84] "Practical Temperature Measurements," 2012, http://cp.literature.agilent.com/litweb/pdf/5965-7822E.pdf, accessed prior to 14 Dec 2016.

[85] Burns, G. W., Scroger, M., Strouse, G., Croarkin, M., and Guthrie, W., "Temperature-electromotive force reference functions and tables for the letter-designated thermocouple types based on the ITS-90," *NIST, Monograph 175*, p. 630, 1993.

[86] Kline, S. J., and McClintock, F., "Describing uncertainties in single-sample experiments," *Mechanical Engineering*, 75(1), pp. 3-8, 1953.

[87] Ababneh, M., "Novel Charging Station and Computational Modeling for High Thermal Conductivity Heat Pipe Thermal Ground Planes," Ph.D. Report, University of Cincinnati, 2012, https://etd.ohiolink.edu/pg_10?0::NO:10:P10_ACCESSION_NUM:ucin1353950640.

[88] de Bock, H. P. J., Chauhan, S., Chamarthy, P., Weaver, S. E., Deng, T., Gerner, F. M., Ababneh, M. T., and Varanasi, K., "On the Charging and Thermal Characterization of a micro/nano structured Thermal Ground Plane," *Proc. Thermal and Thermomechanical Phenomena in Electronic Systems (ITherm), 2010 12th IEEE Intersociety Conference,* Las Vegas, NV, 2010.

[89] Gao, M., Cao, Y., and Zampino, M. A., "Ceramic Miniature Heat Pipes and Liquid Charging Methods," *Heat Transfer Engineering,* 31(7), pp. 564-569, 2010.

[90] Lefèvre, F., Lips, S., Rullière, R., Conrardy, J.-B., Raynaud, M., and Bonjour, J., "Flat plate heat pipes: from observations to the modeling of the capillary structure," *Frontiers in Heat Pipes (FHP)*, 3(1), 2012.

[91] Hopkins, R., Faghri, A., and Khrustalev, D., "Flat miniature heat pipes with micro capillary grooves," *Journal of Heat Transfer*, 121(1), pp. 102-109, 1999.

[92] Chen, S. W., Hsieh, J. C., Chou, C. T., Lin, H. H., Shen, S. C., and Tsai, M. J., "Experimental investigation and visualization on capillary and boiling limits of micro-grooves made by different processes," *Sensor Actuat a-Phys*, 139(1-2), pp. 78-87, 2007.

[93] Faghri, A., and Khrustalev, D., "Micro/Miniature Heat Pipe Technology for Electronic Cooling," WL-TR-97-2085, Department of Mechanical and Materials Engineering, Wright State University, Dayton, OH, July 1997.

[94] Khrustalev, D., and Faghri, A., "Thermal characteristics of conventional and flat miniature axially grooved heat pipes," *Journal of Heat Transfer*, 117(4), pp. 1048-1054, 1995.

[95] Do, K. H., Kim, S. J., and Garimella, S. V., "A mathematical model for analyzing the thermal characteristics of a flat micro heat pipe with a grooved wick," *International Journal of Heat and Mass Transfer*, 51(19), pp. 4637-4650, 2008.

[96] Chaker, Z. M., Samah, M., and Jed, M., "Theoretical and Experimental Analysis of Flows and Heat Transfer Within Flat Mini Heat Pipe Including Grooved Capillary Structures," *InTech Open Science Publisher*, Chapter 5, 2011, Zaghdoudi Mohamed Chaker, Maalej Samah and Mansouri Jed (2011). http://www.intechopen.com/books, DOI: 10.5772/19533.

[97] Longtin, J., Badran, B., and Gerner, F., "A one-dimensional model of a micro heat pipe during steady-state operation," *Journal of Heat Transfer*, 116(3), pp. 709-715, 1994.

[98] Kim, S. J., Seo, J. K., and Do, K. H., "Analytical and experimental investigation on the operational characteristics and the thermal optimization of a miniature heat pipe with a grooved wick structure," *International Journal of Heat and Mass Transfer*, 46(11), pp. 2051-2063, 2003.

[99] Guo, C., Yu, D., Wang, T., Jiang, Y., and Tang, D., "Theoretical and experimental analysis of the evaporating flow in rectangular microgrooves," *International Journal of Heat and Mass Transfer*, 84, pp. 1113-1118, 2015.

[100] Stroes, G., Rohloff, T., and Catton, I., "The Dependence of Capillary Force in Rectangular Channels on Heat Input from Below," NASA-CR-203804, Mechanical, Aerospace and Nuclear Engineering Department, University of California, Los Angeles, CA, 1991.

[101] Chen, J.-S., and Chou, J.-H., "Cooling performance of flat plate heat pipes with different liquid filling ratios," *International Journal of Heat and Mass Transfer*, 77(0), pp. 874-882, 2014.

[102] Lips, S., Lefevre, F., and Bonjour, J., "Combined effects of the filling ratio and the vapour space thickness on the performance of a flat plate heat pipe," *International Journal of Heat and Mass Transfer*, 53(4), pp. 694-702, 2010.

[103] Gillot, C., Avenas, Y., Cezac, N., Poupon, G., Schaeffer, C., and Fournier, E., "Silicon heat pipes used as thermal spreaders," *IEEE Transactions on Components and Packaging Technologies*, 26(2), pp. 332-339, 2003.

[104] Chen, S.-W., Hsieh, J.-C., Chou, C.-T., Lin, H.-H., Shen, S.-C., and Tsai, M.-J., "Experimental investigation and visualization on capillary and boiling limits of micro-grooves made by different processes," *Sensors and Actuators A: Physical*, 139(1), pp. 78-87, 2007.

[105] Stroes, G. R., and Catton, I., "A Semi-analytical Model to Predict the Dryout Point in Heated Inclined Triangular Capillary Grooves," *ASME-PUBLICATIONS-HTD*, 357, pp. 107-116, 1998.

[106] Nilson, R., Tchikanda, S., Griffiths, S., and Martinez, M., "Steady evaporating flow in rectangular microchannels," *International Journal of Heat and Mass Transfer*, 49(9), pp. 1603-1618, 2006.

[107] Lips, S., Lefèvre, F., and Bonjour, J., "Physical mechanisms involved in grooved flat heat pipes: experimental and numerical analyses," *International Journal of Thermal Sciences*, 50(7), pp. 1243-1252, 2011.

[108] Rullière, R., Lefèvre, F., and Lallemand, M., "Prediction of the maximum heat transfer capability of two-phase heat spreaders–Experimental validation," *International Journal of Heat and Mass Transfer*, 50(7), pp. 1255-1262, 2007.

[109] Ayyaswam.Ps, Catton, I., and Edwards, D. K., "Capillary Flow in Triangular Grooves," *J Appl Mech-T Asme*, 41(2), pp. 332-336.

188

[110] Anand, S., De, S., and Dasgupta, S., "Experimental and theoretical study of axial dryout point for evaporation from V-shaped microgrooves," *International Journal of Heat and Mass Transfer*, 45(7), pp. 1535-1543, 2002.

[111] Lefèvre, F., Rullière, R., Pandraud, G., and Lallemand, M., "Prediction of the temperature field in flat plate heat pipes with micro-grooves–Experimental validation," *International Journal of Heat and Mass Transfer*, 51(15), pp. 4083-4094, 2008.

[112] Chi, S., "Mathematical modeling of high and low temperature heat pipes. Final report," Publisher: School of Engineering and Applied Science, George Washington Univ., Washington, DC (USA), 1971.

[113] Faghri, Y. Z., Amir, "Numerical simulation of condensation on a capillary grooved structure," *Numerical Heat Transfer: Part A: Applications*, 39(3), pp. 227-243, 2001.

[114] Jiao, A. J., Riegler, R., Ma, H. B., and Peterson, G. P., "Thin film evaporation effect on heat transport capability in a grooved heat pipe," *Microfluid Nanofluid*, 1(3), pp. 227-233, 2005.

[115] Wong, S. C., and Lin, Y. C., "Effect of copper surfa*ce wettability on the evaporation performance: Tests in a flat-plate heat pipe with visualization," International Journal of Heat and Mass Transfer*, 54(17-18), pp. 3921-3926, 2011.

[116] Stepanov, V., Volyak, L., and Tarlakov, Y. V., "Wetting contact angles of certain systems," *Journal of Engineering Physics*, 32(6), pp. 646-648, 1977.

[117] Holmgren, M., "X Steam for Matlab," www. x-eng. com, accessed October, 21, p. 2006.

[118] Taylor, J., Introduction to error analysis, the study of uncertainties in physical measurements, 2nd Edition, University Science Books; ISNB-13: 978-0935702750, 1996.

189

Appendix A: Validation of Testing Method

Concerns regarding corrosion of the grooved plate due to repeated use with the IAS fluids were discussed in Section 5.1.4. In order to confirm that the corrosion did not affect performance of subsequent tests, a water test was repeated after all the IAS fluids had been tested. A comparison between the average of the two baseline tests and the test done after the IAS experiments is shown in Figure A-1.
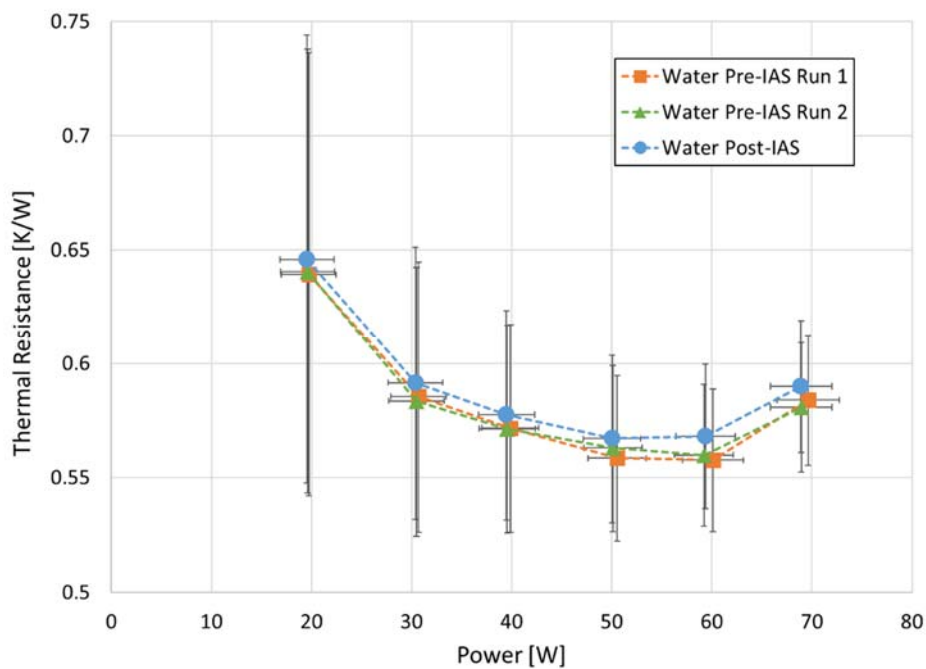
Figure A-1: Comparison of the thermal resistance of water at (10.5°-1.5L/min) before and after the IAS fluids were tested in the grooved wick

The thermal resistance data matched very well between the three tests. A before and after picture of the grooved wick is shown in Figure A-2.
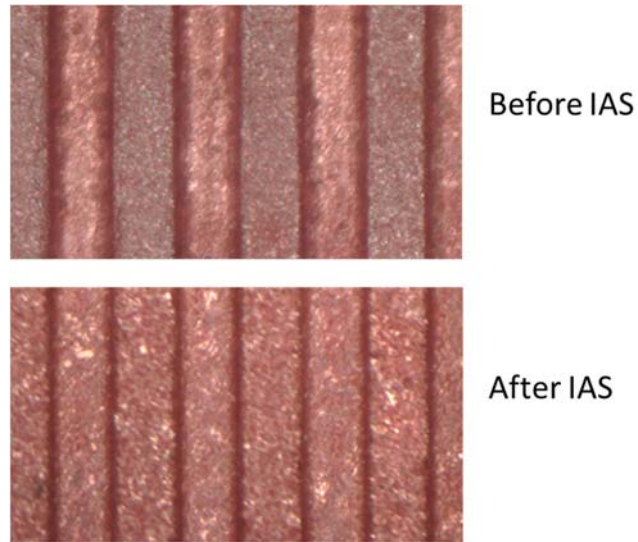
Figure A-2: Image of the grooved wick before and after IAS corrosion

Some corrosion was clearly evident in the image. However, the performance test confirmed that there was no difference in performance and the size of the groove remained the same to within measurement (Figure A-3).

$$r_{min} \approx 40 \mu m$$
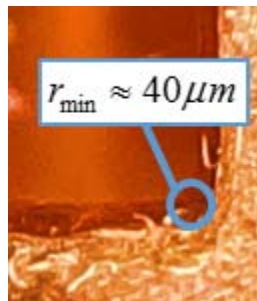
Figure A-3: Minimum radius of curvature for corner flow

Appendix B: Model Data

Water
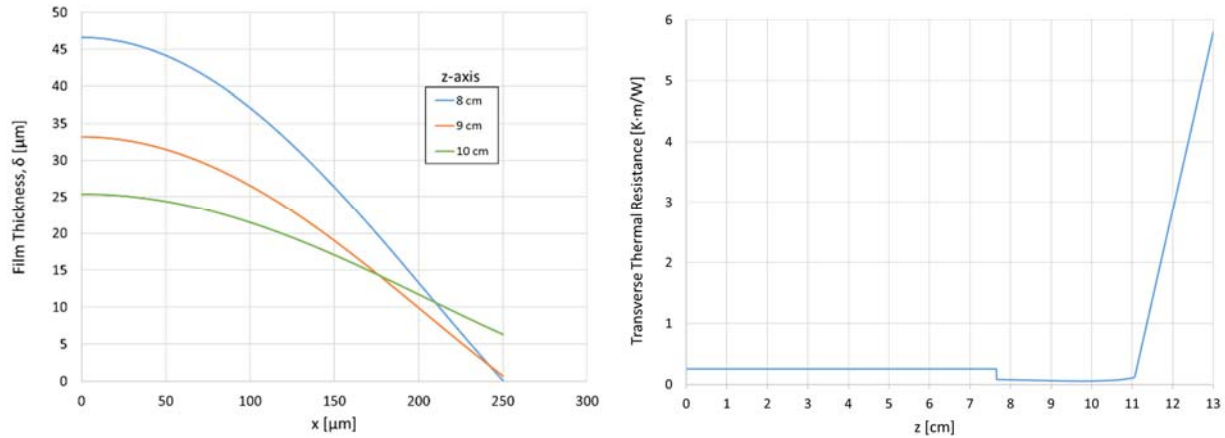
Figure B-1: Example of the condensate film thickness in the condenser at three different axial locations (left) and the thermal resistance per unit length for water (10.5°) at 59.66W

Thermal Resistance Tables

Two thermal resistances were calculated in the model for comparison. R_{th} was calculated from taking the average of the entire evaporator and condenser. R_{ec} was calculated from only the temperatures at the experimental thermocouple locations on the heat pipe. This resistance was the fairest comparison. The tables also include calculated saturation temperature, liquid pool length and the corner or coating flow length (Table B-1, Table B-2, and Table B-3).

Table B-1: Experimental and theoretical comparison of thermal resistance for water

10 Degrees							
Q_{in} [W]	T_{sat} [C]	R_{exp} [K/W]	R_{ec} [K/W]	R_{th} [K/W]	$T_{sat,ec}$ [C]	L_p [mm]	L_{CF} [mm]
19.53	21.65	0.627	0.612	0.586	18.25	20.145	-
29.82	30.28	0.569	0.603	0.578	27.28	20.145	-
38.70	36.75	0.538	0.596	0.570	34.95	20.145	-
48.71	42.82	0.511	0.590	0.565	43.72	20.145	-
57.61	48.90	0.506	0.585	0.560	51.35	20.145	-
68.41	55.48	0.503	0.579	0.555	60.65	20.145	-
77.35	62.20	0.506	0.576	0.551	68.30	20.145	-
83.00	68.07	0.518	0.574	0.550	73.18	20.145	-
83.38	68.47	0.518	0.585	0.574	75.70	20.214	0.674

10.5 Degrees							
Q_{in} [W]	T_{sat} [C]	R_{exp} [K/W]	R_{ec} [K/W]	R_{th} [K/W]	$T_{sat,ec}$ [C]	L_p [mm]	L_{CF} [mm]
19.38	21.14	0.627	0.600	0.576	18.04	19.660	-
30.45	30.60	0.578	0.590	0.566	27.45	19.660	-
39.10	37.23	0.570	0.586	0.562	35.00	19.725	-
49.67	44.53	0.554	0.580	0.556	43.78	19.725	-
58.61	50.16	0.550	0.574	0.551	51.52	19.725	-
60.05	51.02	0.554	0.583	0.575	54.40	19.742	0.715

11 Degrees							
Q_{in} [W]	T_{sat} [C]	R_{exp} [K/W]	R_{ec} [K/W]	R_{th} [K/W]	$T_{sat,ec}$ [C]	L_p [mm]	L_{CF} [mm]
19.49	20.14	0.623	0.590	0.567	17.90	19.245	-
29.58	28.01	0.599	0.582	0.560	26.65	19.245	-
35.49	32.60	0.579	0.579	0.557	31.76	19.275	-
37.41	34.09	0.573	0.588	0.581	34.40	19.314	0.787

10.5 Degrees							
Q_{in} [W]	T_{sat} [C]	R_{exp} [K/W]	R_{ec} [K/W]	R_{th} [K/W]	$T_{sat,ec}$ [C]	L_p [mm]	L_{CF} [mm]
19.67	17.14	0.640	0.586	0.561	13.95	19.660	-
30.59	23.99	0.584	0.577	0.553	21.20	19.660	-
39.72	29.45	0.571	0.575	0.551	27.30	19.725	-
50.33	37.00	0.561	0.568	0.545	34.20	19.725	-
59.66	39.83	0.559	0.564	0.540	40.00	19.725	-
63.73	42.32	0.569	0.563	0.540	42.80	19.740	-
65.42	43.36	0.573	0.568	0.560	44.90	19.742	0.644
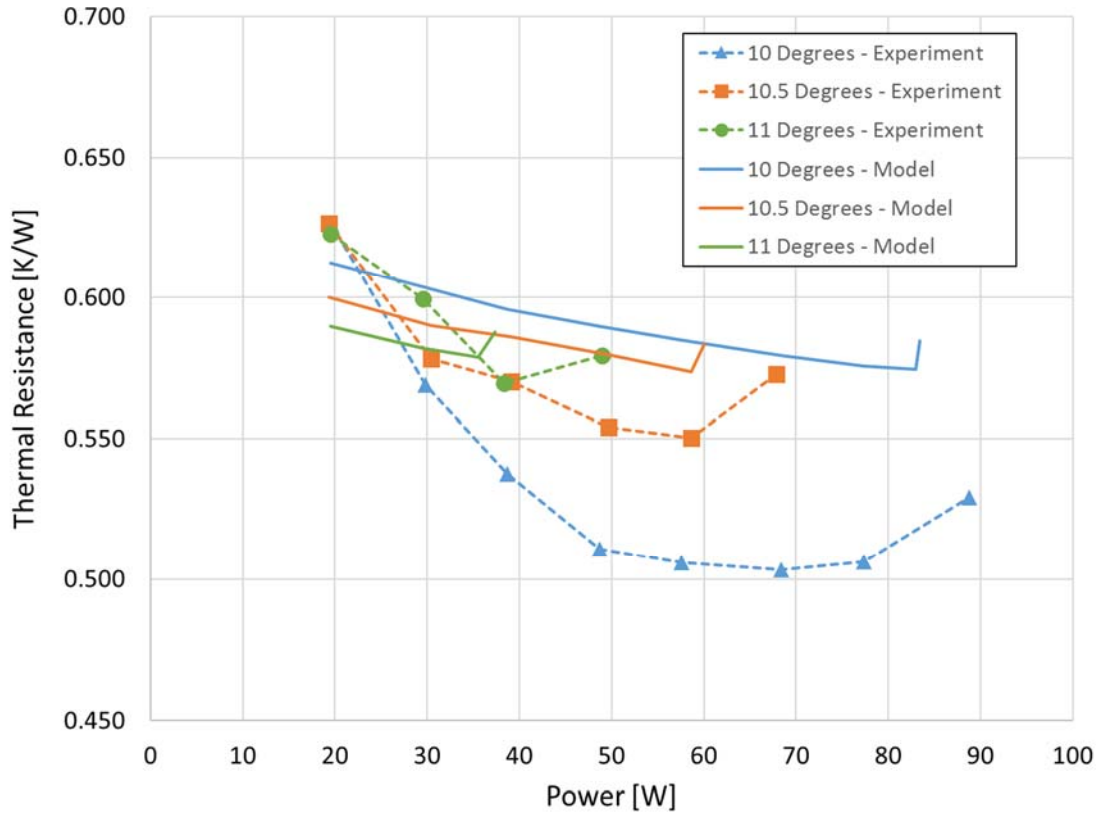
Figure B-2: Comparison of experimental and theoretical thermal resistances for water at three different angles

IAS

Thermal Resistance Tables

Table B-2: Experimental and theoretical comparison of thermal resistance (3.025 through 3.2)

IAS 3.025							
Q_{in} [W]	T_{sat} [C]	R_{exp} [K/W]	R_{ec} [K/W]	R_{th} [K/W]	$T_{sat,ec}$ [C]	L_p [mm]	L_{CF} [mm]
19.72	16.73	0.600	0.518	0.485	13.70	19.660	-
30.62	24.23	0.552	0.513	0.480	21.00	19.660	-
39.61	29.21	0.517	0.510	0.478	27.05	19.725	-
50.11	35.47	0.515	0.506	0.473	34.30	19.725	-
59.84	40.57	0.514	0.502	0.470	40.90	19.725	-
61.72	41.65	0.520	0.501	0.469	42.10	19.725	-
67.80	45.14	0.540	0.506	0.460	47.10	19.813	1.32

IAS 3.05							
Q_{in} [W]	T_{sat} [C]	R_{exp} [K/W]	R_{ec} [K/W]	R_{th} [K/W]	$T_{sat,ec}$ [C]	L_p [mm]	L_{CF} [mm]
19.66	17.07	0.586	0.506	0.480	13.55	19.660	-
30.53	24.20	0.522	0.501	0.476	21.25	19.660	-
39.59	29.36	0.489	0.499	0.474	27.25	19.725	-
50.06	35.41	0.481	0.495	0.470	34.10	19.725	-
59.56	40.66	0.478	0.492	0.467	40.30	19.725	-
62.11	42.04	0.478	0.491	0.466	42.00	19.725	-
69.27	45.91	0.478	0.493	0.449	45.84	19.813	1.83
70.50	46.41	0.480	0.492	0.448	49.35	19.813	2.07

IAS 3.1							
Q_{in} [W]	T_{sat} [C]	R_{exp} [K/W]	R_{ec} [K/W]	R_{th} [K/W]	$T_{sat,ec}$ [C]	L_p [mm]	L_{CF} [mm]
19.73	15.84	0.563	0.482	0.464	13.90	19.660	-
30.41	23.18	0.505	0.478	0.459	20.80	19.660	-
39.73	28.34	0.472	0.476	0.457	27.10	19.725	-
50.30	34.31	0.465	0.472	0.454	33.95	19.725	-
59.65	39.40	0.462	0.469	0.451	40.10	19.725	-
62.53	41.12	0.463	0.468	0.450	42.05	19.725	-
69.18	45.08	0.464	0.452	0.420	47.05	19.755	1.5
78.42	49.79	0.476	0.446	0.409	53.45	19.813	3.24

IAS 3.2							
Q_{in} [W]	T_{sat} [C]	R_{exp} [K/W]	R_{ec} [K/W]	R_{th} [K/W]	$T_{sat,ec}$ [C]	L_p [mm]	L_{CF} [mm]
19.56	15.37	0.536	0.503	0.481	13.90	19.660	-
30.66	23.26	0.487	0.497	0.476	21.25	19.660	-
39.71	28.71	0.463	0.496	0.474	27.30	19.725	-
50.27	34.66	0.460	0.492	0.470	34.25	19.725	-
59.26	40.36	0.454	0.488	0.467	40.05	19.725	-
62.80	41.30	0.450	0.487	0.466	42.35	19.725	-
69.21	44.69	0.443	0.462	0.427	47.20	19.755	1.47
79.30	49.82	0.439	0.454	0.414	54.00	19.813	3.39
83.80	51.95	0.445	0.450	0.409	57.15	19.813	4.26

Table B-3: Experimental and theoretical comparison of thermal resistance for IAS 3.3

IAS 3.3							
Q_{in} [W]	T_{sat} [C]	R_{exp} [K/W]	R_{ec} [K/W]	R_{th} [K/W]	$T_{sat,ec}$ [C]	L_p [mm]	L_{CF} [mm]
19.61	15.37	0.535	0.519	0.496	13.50	19.660	-
30.58	23.26	0.476	0.512	0.490	20.75	19.660	-
39.57	28.71	0.459	0.511	0.489	26.80	19.725	-
50.11	34.66	0.448	0.506	0.485	33.70	19.725	-
59.29	40.36	0.443	0.503	0.482	39.65	19.725	-
63.05	42.29	0.440	0.502	0.480	42.10	19.725	-
68.99	45.34	0.434	0.472	0.436	46.70	19.755	1.41
78.60	50.12	0.438	0.461	0.419	53.50	19.755	3.33
87.30	55.01	0.441	0.455	0.411	59.75	19.813	4.98
88.20	55.42	0.442	0.454	0.410	60.40	19.813	5.16
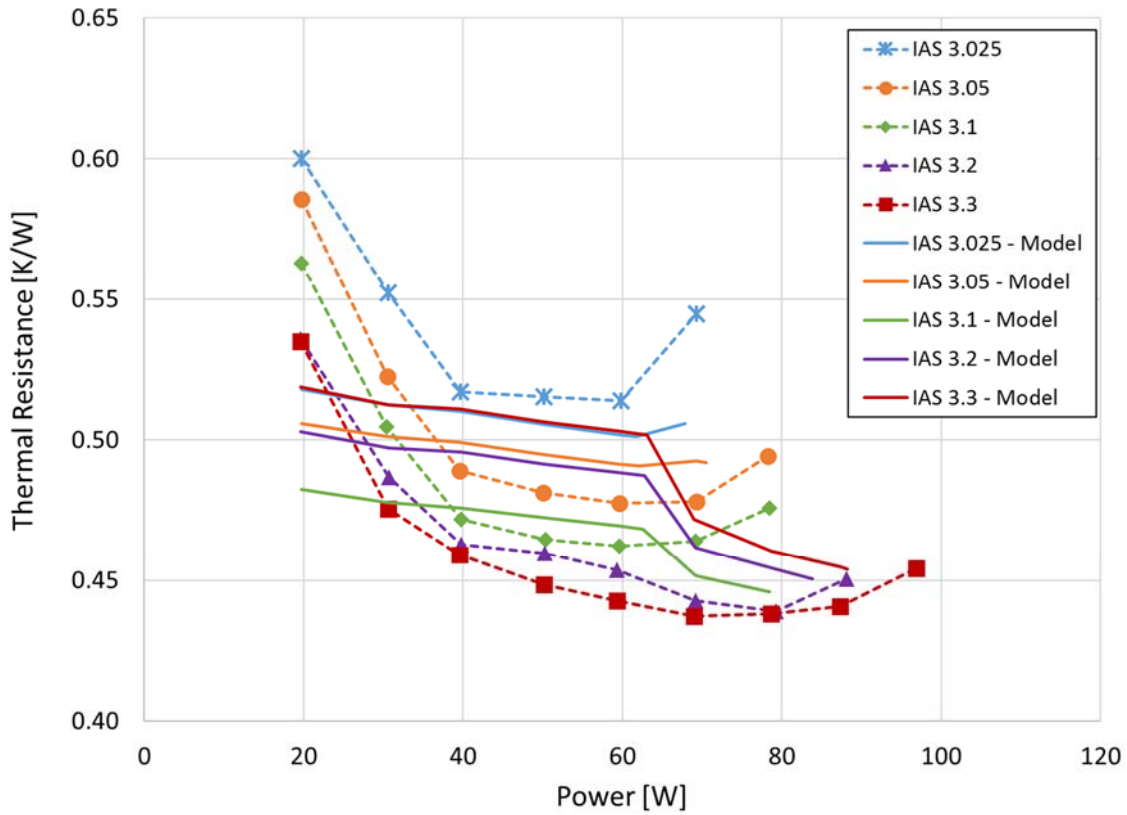
Figure B-3: Comparison of experimental and theoretical thermal resistances for the IAS fluids

196

Appendix C: Uncertainty

Analysis of calibration and measurement uncertainty was performed based on the Root of Sum of Squares (RSS) method developed by Kline and Mclintock (see reference 86). The NIST ITS-90 Type-T calibration curve was utilized for the thermocouple measurements (see reference 85).

$$\frac{\delta R}{R} = \left\{ \left(a \frac{\delta X_1}{X_1} \right)^2 + \left(b \frac{\delta X_2}{X_2} \right)^2 + ... + \left(m \frac{\delta X_M}{X_M} \right)^2 \right\}^{1/2} \tag{C-1}$$

The uncertainty in the input power, output power and thermal resistance was calculated using the following equations to propagate uncertainty,

$$\frac{\delta q_{in}}{q_{in}} = \left\{ \left(\frac{\delta k}{k} \right)^2 + \left(\frac{\delta A}{A} \right)^2 + \left(\frac{\delta \Delta T}{\Delta T} \right)^2 + \left(\frac{\delta \Delta x}{\Delta x} \right)^2 \right\}^{1/2} \tag{C-2}$$

$$\frac{\delta q_{out}}{q_{out}} = \left\{ \left(\frac{\delta \dot{m}}{\dot{m}} \right)^2 + \left(\frac{\delta c_p}{c_p} \right)^2 + \left(\frac{\delta \Delta T}{\Delta T} \right)^2 \right\}^{1/2} \tag{C-3}$$

$$\frac{\delta R_{FHP}}{R_{FHP}} = \left\{ \left(\frac{\delta \Delta T}{\Delta T} \right)^2 + \left(\frac{\delta q_{in}}{q_{in}} \right)^2 \right\}^{1/2} \tag{C-4}$$

The fluid properties used for the calculations as well as the differences in heat stem geometry are tabulated in Table C-1. The thermocouple distance reported in the table was the distance between the first and third thermocouple, so each one was actually spaced at half that distance. The cooling fluid and stem material properties were assumed to have a 2% uncertainty, and the estimated uncertainty for the distance between stem thermocouples, x_s, and stem cross sectional area, A_s, was assumed to be ±0.1 mm and ±0.01 mm². The digital flowmeter reported a

1% of FS uncertainty for volumetric flow rate which was combined (RSS) with the resolution uncertainty of the gauge. The total uncertainty in volumetric flow rate was 3.47e-7 m³/s. To calculate mass flow rate, volumetric flow rate was multiplied by density. The uncertainty of density and volumetric flow rate were then combined (RSS) to get the uncertainty in mass flow rate.

Table C-1: Properties of coolant fluids and heater stem materials

Water Properties [4°C]		
Density	1000	kg/m^3
Specific Heat	4179	J/kg-K
Mass Flow Rate	0.00347	kg/s
Volumetric Flow Rate (Paristaltic)	0.00000347	m^3/s

**Silicon Oil Properties [4°C]		
Density	933	kg/m^3
Specific Heat	1450	J/kg-K
Mass Flow Rate	0.0116625	kg/s
Volumetric Flow Rate (750 mL/min)	0.0000125	m^3/s
Volumetric Flow Rate (1500 mL/min)	0.000025	m^3/s
**Properties for Lauda Brinkman Kryo-70 Fluid		

Heater and Stem Properties		
Thermal Conductivity (Copper) [W/m-K]	391	W/mK
TC Distance	0.03	m
Cross Sect. Area (1.5mm Groove)	0.0003	m^2
Cross Sect. Area (0.5mm Groove)	0.00025	m^2

Temperature Measurement Uncertainty

This section was meant to supplement the uncertainty discussion in Section 0. These equations are used in the calculations done in Table C-2.

198

$$\delta T_{total}^2 = \delta T_{DMM}^2 + \delta T_{cal}^2 + \delta T_{CJ}^2$$

$$\delta T_{DMM} = \frac{\partial T}{\partial V} \delta V_{DMM} \qquad\qquad\text{(C-5)}$$

$$\delta T_{CJ}^2 = \delta T_{meter}^2 + \delta T_{Therm}^2$$

Table C-2: Uncertainty budget for temperature measurement

Uncertainty Budget		
Cold Juction		
	%	±[°C]
Thermistor Meter		0.2
Thermistor		0.2
	Total	0.2828
Thermocouples		
Seebeck Coefficient (20°C)	40	µV/°C
	%	±[°C]
Type T (Special Limit Error)		0.5
NIST Calibration		0.03
	Total	0.5009
DMM		
	%[Voltage]	±[°C]
Voltage	0.0035	0.0088
Resolution (±0.005µV)		0.0001
	Total	0.0088
System Total	0.5753	±[°C]
ΔT	0.8136	±[°C]

Combining Independent Data Sets

Two tests were completed for each fluid/angle combination. The results and uncertainty of these two independent tests were combined as a weighted average as done by Taylor [118] for separate measurements: $x_1 \pm \sigma_1, \; x_2 \pm \sigma_2 \ldots x_N \pm \sigma_N$

$$x_{wav} = \frac{\sum w_i x_i}{\sum w_i}, \quad w_i = \frac{1}{\sigma_i^2} \tag{C-6}$$

This rule is valid as long as the difference between measurements is not significantly larger than the single uncertainties. The thermal resistances, input power, etc. from two similar tests was combined in this manner. Since the uncertainties for every test were almost the same, using the average values essentially divided the uncertainty by the square root of two. Example calculations are shown in Table C-3 and Table C-4.

Uncertainty Example Calculation

Table C-3: Example uncertainty for example FHP data – water (10.5) (1.5L/min)

Qin	δQin	%	Qout	δQout	%	R	δR	%
19.73	2.72	0.14	17.50	27.52	157%	0.639	0.097	15%
30.71	2.77	0.09	29.72	27.53	93%	0.585	0.059	10%
39.88	2.83	0.07	38.46	27.54	72%	0.572	0.045	8%
50.54	2.92	0.06	47.18	27.56	58%	0.558	0.036	6%
60.12	3.01	0.05	57.68	27.58	48%	0.558	0.031	6%
69.62	3.12	0.04	66.44	27.60	42%	0.584	0.029	5%

Qin	Qout	%Diff
19.73	17.50	11%
30.71	29.72	3%
39.88	38.46	4%
50.54	47.18	7%
60.12	57.68	4%
69.62	66.44	5%

Table C-4: Example FHP data for water (10.5) (1.5 L/min)

HEATER STEM	T1	29.63	43.54	55.99	69.74	83.26	96.77
	T2	26.60	38.84	49.91	62.10	74.11	86.16
	T3	23.63	34.22	43.87	54.38	65.00	75.62
EVAPORATOR	T4	20.35	29.08	37.12	47.32	57.06	67.23
	T5	20.64	29.47	37.72	45.70	54.39	63.30
ADIABATIC	T6	17.66	24.85	30.49	38.23	41.33	47.48
	T7	17.41	24.19	29.62	37.13	39.91	45.81
	T8	17.26	23.99	29.40	36.87	39.55	45.41
	T9	17.11	23.89	29.27	36.75	39.55	45.29
	T10	16.94	23.62	29.03	36.53	39.31	45.13
	T11	16.41	22.59	27.98	35.50	38.47	44.33
CONDENSER	T12	8.39	12.21	15.78	19.78	23.93	26.67
	T13	7.37	10.39	13.47	16.79	20.48	22.57
INLET	T14	0.82	0.92	0.91	0.92	0.67	0.40
OUTLET	T15	1.34	1.80	2.05	2.32	2.38	2.37
Tsat	T16	17.24	24.10	29.57	37.12	39.96	45.86
EVAPORATOR AVERAGE		20.49	29.28	37.42	46.51	55.73	65.27
CONDENSER AVERAGE		7.88	11.30	14.62	18.28	22.21	24.62
COOLANT AVEARGE		1.08	1.36	1.48	1.62	1.53	1.38
PLATE TEMP DIFFERENCE		12.61	17.98	22.80	28.23	33.52	40.65
HEAT IN	Qin12	19.91	30.95	40.03	50.26	60.22	69.79
	Qin23	19.55	30.46	39.73	50.83	60.01	69.44
	Qin13	19.73	30.71	39.88	50.54	60.12	69.62
CALORIMETRY	Qout	17.50	29.72	38.46	47.18	57.68	66.44
THERMAL RESISTANCE		0.639	0.585	0.572	0.558	0.558	0.584

201

List of Symbols, Abbreviations, and Acronyms

Variables

A area $[m^2]$

c total mole density $[kmol/m^3]$

C minimum aspect ratio

D diameter $[m]$: diffusion coefficient $[m^2/s]$

ELC Effective Length Coverage

f friction factor

g gravitational acceleration $[m/s^2]$

h heat transfer coefficient $[W/m^2]$

H height $[m]$

h_{lv} enthalpy $[J/kg]$

L length $[m]$

k thermal conductivity $[W/m \cdot K]$

K permeability $[m^2]$

N total molar flux $[kmol/m^2]$

P pressure $[Pa]$

Po Poiseuille number

q heat transfer rate $[W]$

r radius of curvature $[m]$

Re Reynolds number

RN resistance number $[\mu m]$

t   thickness [m]

T   temperature [K]

TFC   Total Fin Coverage

u   velocity [m/s]

v   velocity [m/s]

V   volume [m^3]

w   width [m]

W   heat pipe width [m]

x   mold fraction

x, y, z coordinates [m]

<u>Subscripts</u>

a   adiabatic

amb   ambient

c   condenser or capillary or coating

ext   external

e   evaporator

f   fin

g   groove

h   hydraulic

i   node

int   interfacial

l   liquid

p   pool

m   meniscus

s   stem

sat   saturation

trans   transverse or transition

tot   total

TF   thin film

v   vapor

w   wall

Greek Symbols

δ condensate film thickness [m]

θ contact angle [rad]

μ dynamic viscosity [Pa·s]

τ shear stress [N/m2]

ε porosity

ρ density [kg/m3]

σ surface tension [N/m]

ϕ inclination angle [rad]

υ kinematic viscosity [m^2/s]

Abbreviations

AC   Alternate current

BSC   Bottom supplied creeping

CCD   Charged-coupled devices

CHF   Critical Heat Flux

CJC   Cold junction compensation

DAQ   Data acquisition

DC   Direct current

FHP   Flat heat pipe

FTÅ   First Ten Angstroms

IAS   Inorganic Aqueous Solution

NCG   Non-condensable gas

NIST   National Institute of Standards and Technology

NRL   Naval Research Laboratory

REV   Representative elementary volume

RSS   Root Sum of Squares

SEM   Scanning Electron Microscope

TSC   Top supplied creeping

UCLA   University of California, Los Angeles

DISTRIBUTION LIST

DTIC/OCP
8725 John J. Kingman Rd, Suite 0944
Ft Belvoir, VA 22060-6218   1 cy

AFRL/RVIL
Kirtland AFB, NM 87117-5776   2 cys

Official Record Copy
AFRL/RVSV/Andrew Williams   1 cy